THE UNIVERSITY OF ADELAIDE
SCHOOL OF CHEMISTRY AND PHYSICS
DISCIPLINE OF PHYSICS

# Chiral Effective Field Theory
# Beyond the Power-Counting Regime

Jonathan Michael MacGillivray Hall

Supervisors: Prof. Derek B. Leinweber, Dr. Ross D. Young

*Special Research Centre for the*

*Subatomic Structure of Matter*

and

*Department of Physics,*

*University of Adelaide,*

*Australia*

June 2011

# Abstract

Chiral effective field theory complements numerical simulations of quantum chromodynamics on a spacetime lattice. It provides a model-independent formalism for connecting lattice simulation results at finite volume, and at a variety of quark masses, to the physical region. Knowledge of the power-counting regime of chiral effective field theory, where higher-order terms of the expansion may be regarded as negligible, is as important as knowledge of the expansion. Through the consideration of a variety of renormalization schemes, techniques are established to identify the power-counting regime. Within the power-counting regime, the results of extrapolation are independent of the renormalization scheme.

The nucleon mass is considered as a benchmark for illustrating this approach. Because the power-counting regime is small, the numerical simulation results are also examined to search for the possible presence of an optimal regularization scale, which may be used to describe lattice simulation results outside of the power-counting regime. Such an optimal regularization scale is found for the nucleon mass. The identification of an optimal scale, with its associated systematic uncertainty, measures the degree to which the lattice QCD simulation results extend beyond the power-counting regime, thus quantifying the scheme-dependence of an extrapolation.

The techniques developed for the nucleon mass renormalization are applied to the quenched $\rho$ meson mass, which offers a unique test case for extrapolation schemes. In the absence of a known experimental value, it serves to demonstrate the ability of the extrapolation scheme to make predictions without prior phenomenological bias. The robustness of the procedure for obtaining an optimal regularization scale and performing a reliable chiral extrapolation is confirmed.

The procedure developed is then applied to the magnetic moment and the electric charge radius of the isovector nucleon, to obtain a consistent optimal regularization scale. The consistency of the results for the value of the optimal regularization scale provides strong evidence for the existence of an intrinsic energy scale for the nucleon-pion interaction.

# Statement of Originality

This work contains no material which has been accepted for the award of any other degree or diploma in any university or other tertiary institution to Jonathan Hall and, to the best of my knowledge and belief, contains no material previously published or written by another person, except where due reference has been made in the text.

I give consent to this copy of my thesis, when deposited in the University Library, being available for loan and photocopying, subject to the provisions of the Copyright Act 1968.

I also give permission for the digital version of my thesis to be made available on the web, via the University's digital research repository, the Library catalogue and also through web search engines, unless permission has been granted by the University to restrict access for a period of time.

# Acknowledgments

Thank you to Professor Derek Leinweber, for his patient and intelligent supervision and his sense of humour expressed during our enjoyable discussions. Also thank you to Doctor Ross Young for his explanations of theory, his patience, and for our numerous, informative conversations. Ross' generosity with his time for me has been exemplary, and in many cases, an essential component of our successes.

I also thank Doctor Rod Crewther, who has been very informative in the fields of physics and education, and Doctor James Zanotti, who has helped marvellously with collaboration and support.

Thank you to the staff of the School of Chemistry and Physics for their general assistance, and more specifically to Professor Anthony Thomas and the staff of the Special Research Centre for the Subatomic Structure of Matter.

I give my thanks to my loving family for their support.

It is with hope and faith that we endeavour to extend our learning to reach new insights just beyond our present reach.

# Contents

# Chapter 1

# Introduction

*"One measure of the depth of a physical theory is the extent to which it poses serious challenges to aspects of our worldview that had previously seemed immutable."* (Greene, B. 1999. *The Elegant Universe* p.386) [Gre99]

## 1.1 Prologue

The theoretical physicist challenges previous theory, using original research that enables alternative coherence to emerge, as outlined by Bohm [Boh92] (p.223). The underlying theory behind the strong force of particle interactions, which is the force responsible for the binding of protons and neutrons together in atomic nuclei, had been a persistent mystery throughout the first half of the Twentieth Century. This hitherto unknown force acts in opposition to the electric Coulomb force that repels positively charge protons from each other, but is at least two orders of magnitude stronger at the distance scale of an atomic nucleus. The strong interaction between protons and neutrons, or nucleons, is currently most successfully described by the theory of quantum chromodynamics (QCD). The advent of the quark model, and the theory of the colour force by which the quarks interact, opened a new field of research into the internal structure of matter.

In 1964, Gell-Mann and Zweig independently proposed the existence of a new constituent particle, the quark, in order to classify the bewildering array of subatomic

particles called hadrons [GM64]. It was discovered that the hadrons can be arranged into families that correspond to representations of the group SU(3), and that three quark types, or flavours, were required to form the fundamental representation of this group. It was not until 1968 that the results of deep inelastic scattering experiments provided the first evidence of the existence of these new elementary particles. As more hadrons were discovered, additional quark flavours were proposed. It is currently accepted that six flavours of quark are required to produce the full range of hadrons observed in particle accelerator experiments. Their names, in ascending order of mass, are: up, down, strange, charm, bottom and top. Of the six flavours, the most recent to be discovered experimentally was the top quark, in 1995 at Fermilab, with a mass of 172 GeV [Pro96].

Each quark has a unit of charge equal to $+2/3$ or $-1/3$ times the charge of a proton (units of $+e$). An an example, the proton consists of two up quarks and a down quark for a total charge of $+1 e$, whereas a neutron consists of two down quark and an up quark for a total charge of zero. However, because quarks have a certain spatial distribution inside the nucleon, or indeed any hadron, the internal, high energy dynamics as described by the behaviour of quarks gives rise to properties such as non-zero magnetic moments for the neutron and anisotropic momentum distributions. It is clear that in order to describe the internal behaviour of a hadron, one cannot assume that a quark behaves as a static source. Instead, the dynamics of quarks must be described by a theory, the most successful of which is QCD.

QCD connects the quark model of nuclear physics to quantum gauge field theories by introducing the quarks as the relevant degrees of freedom inside a hadron. The hadrons are formed by confined colour singlets of three quarks called baryons, or quark-antiquark pairs, known as mesons. Quarks are spin-1/2 fermions, which also have the properties of colour and approximate flavour symmetry. Since fermions, by definition, must satisfy Fermi-Dirac statistics, the fact that each baryon contains three bound quarks in the same state violates the Pauli Exclusion Principle. Therefore, it was necessary to suppose an the existence of an additional quantum number, known as colour charge, so that each quark may be assigned one of three, orthogonal

basis states, labelled red, green and blue. Colour is mediated by the related gauge particles of the strong force; the gluons, and the quarks also form a representation of the colour gauge group $SU(3)_c$, with eight group generators.

Mathematically, QCD is a non-Abelian theory. That is, the gauge connection of the gluons is non-commutative. The fact that isolated, unbound quarks are never found in experiment is one of the striking consequences of a non-Abelian theory. Confinement of the quarks within a hadron is a result of the gluon fields exerting a linear potential that increases with distance between quarks [Wil74]. That is, for a large distance scale, the strong coupling parameter $\alpha_s$ also becomes large. This behaviour contrasts with electromagnetism, where the electric Coulomb force diminishes as two charged particles are separated. However, quarks experience only a small force from the gluon fields as $\alpha_s$ becomes small at short distances [GW73b, Pol73, GW73a, GW74]. This asymptotic freedom is observed when probing the internal structure of hadron at high energies, where the small de Broglie wavelength of the probe is able to resolve the short distances within the composite particle. Near this asymptotically free regime, the methods of perturbative quantum field theory are suitable for constructing amplitudes, cross-sections and scattering matrices. However, it leads to a difficulty in finding an appropriate method for performing a calculation with QCD in the low-energy region. Two of the most successful methods that will be discussed in this thesis are chiral effective field theory ($\chi$EFT) and lattice QCD.

Using $\chi$EFT, one is able to encapsulate the dynamics of a quantum system by writing down an 'effective' action of low-energy degrees of freedom. By imposing symmetries satisfied by QCD, one can expand out the formula for an observable property into a series of quantum amplitudes that can be arranged in order of the importance of their contribution by a choice of power-counting scheme: usually in increasing powers of mass/energy. These amplitudes can alter, or renormalize the calculation of an observable from its naïve value, and landmark success has been made in confirming these real and measurable effects by experiment. For example, the value of the anomalous magnetic dipole moment of the electron agrees with ex-

periment to better than twelve significant figures. The Casimir effect (1948), which describes the forces arising from the quantum vacuum fluctuations, were successfully predicted by the gauge field theory of quantum electrodynamics (QED). In the low-energy, non-perturbative region of QCD, many phenomena can be explained by the emergent properties of quark confinement and the behaviour of their bound states as hadrons. For example, the proton and neutron also have a large anomalous component of their magnetic moment. This is due to the cloud of interacting fields, which renormalize the core of the observable. This 'hadron cloud' is one of the unique properties of a quantum field theory. Of the available low-energy effective theories of QCD, chiral perturbation theory ($\chi$PT) is the most notable, in its careful incorporation of the fundamental symmetries of QCD. However, the robustness of $\chi$PT is confined only to a restrictive region called the power-counting regime. Within the power-counting regime, the perturbative expansions that occur in $\chi$PT are convergent; the terms of the expansion series are ordered such that higher-order terms are sufficiently smaller than lower-order terms. The details of the power-counting regime are discussed in more detail in Chapter 3.

Lattice QCD is a discretized version of QCD, where the dynamics are evaluated on a finite-sized box with only certain allowed values of position (or momentum) separated by a fixed spacing. Thus, lattice QCD is equivalent to QCD in the limit of infinite box size and vanishing lattice spacing. Using lattice QCD, one is able to access the non-perturbative, low-energy regime of QCD and provide reliable predictions of hadronic behaviour. In addition, lattice QCD simulations do not suffer from the common problems of quantum field theory associated with renormalization. The discrete lattice spacing and the finite box size of the lattice act as an ultraviolet and infrared regulator, respectively. Thus, observable quantities evaluated on the lattice are finite and calculable. Nevertheless, it can be computationally expensive to evaluate observables at large box sizes, small lattice spacings and physical quark masses. To be able to obtain a result using quark masses as small as their physical values, an extrapolation is a practical alternative to a brute-force approach. In addition, the corrections to finite-volume effects ought also to be calculated for a realistic comparison

with experiments.

## 1.2    Overview and Aims

The framework of QCD provides a rich selection of possibilities for inquiry. Among these, the low-energy, chiral dynamics of hadrons provides us with a uniquely successful understanding of many of their imporant properties.

This thesis explores the properties of the aforementioned power-counting regime by considering how low-energy constants, which occur in a calculation using the methods of $\chi$PT, are renormalized, or altered, at different energy scales. This knowledge of the power-counting regime, in turn, yields insight into the repercussions of chiral symmetry breaking in QCD.

The results of lattice QCD simulations provide an important application for the investigation into $\chi$PT and the power-counting regime. Lattice QCD results are typically produced at a variety of quark masses larger than the physical quark mass. As such, a chiral extrapolation to the physical point is required before the result can be compared to experiment. In addition, experimental results are not constrained by the boundaries of a small box only a few fermi in length. It is important to be able to quantify how the finite-volume nature of lattice QCD affects calculations. Analysis shows that the finite-volume behaviour of QCD on the lattice can affect the result of a calculation in non-trivial ways. Being able to perform an extrapolation that takes into account finite-volume effects is also an important step in understanding the effects of a finite-volume box on the dynamics of QCD.

The investigation of the power-counting regime has additional importance. Few lattice QCD results in the literature are evaluated at quark masses that lie within the power-counting regime. As such, the powerful tools associated with $\chi$PT may not be used legitimately, since the chiral power-counting expansion of an observable would not be convergent. If higher-order terms in the series expansion are not small with respect to some power-counting scheme, the result of an extrapolation will be scheme-dependent. This thesis describes the construction of an extended effective

field theory that can be applied outside the power-counting regime by extracting a quantative estimate of the extent of the energy scale-dependence, associated with the process of regularization in $\chi$PT calculations. It is discovered that lattice simulation results themselves can provide guidance on an optimal choice of regularization scale. This optimal scale indicates a possible connection with the finite-size of the hadron cloud in the form of an intrinsic scale.

Thus, by analyzing the results from the supercomputer simulations of lattice QCD, an intrinsic scale will be discovered that characterizes the finite size of the interaction between the hadron cloud and the core of the hadron.

# Chapter 2

# Lattice QCD

*"While the classical vision of the world is intrinsically limited, nothing restricts the scientific representation. During the conception stage, the method is free to consider all hypotheses, even the most far-fetched, in order to mimic Reality."* (Omnès, R. 2002. *Quantum Philosophy: Understanding and Interpreting Contemporary Science* p.268) [Omn02]

The inception of a discrete, lattice approach to quantum chromodynamics (QCD) in 1974 by Wilson marked the beginning of a robust, investigative technique into the previously inaccessible low-energy region of strong force interactions [Wil74]. By simulating the behaviour of quarks on a lattice, bound states of hadrons are formed, exhibiting confinement, and the behaviour of particle interactions is correctly predicted: a testament to the achievement of QCD as a theory of the strong force.

Lattice QCD provides non-perturbative techniques for obtaining results from the low-energy, chiral dynamics of hadrons. It involves the construction of a finite-volume box of discrete momenta, with calculations performed from first principles. The finite box size of the lattice removes any infrared divergences that would occur in infinite-volume QCD, and the lattice spacing acts to regulate the ultraviolet behaviour of observable quantities by limiting the lattice momenta to discrete values.

In lattice QCD, a Euclidean hypercube is constructed with finite length and discrete lattice spacing. The quantum field theory can then be represented by the functional integrals defined on such a box. The momenta can only take the discrete values

in the four-box:

$$k_\mu = \frac{2\pi}{aN} n_\mu,\tag{2.1}$$

where $a$ is the lattice spacing, $n_\mu$ is an integer array representing the lattice sites, and $N$ is the number of lattice sites in each direction, such that $-N/2 < n_\mu \leq N/2$. Thus, the maximum value $k_\mu$ can take is $\pi/a$. This means that the ultraviolet physics included in our lattice is entirely determined by the lattice spacing, which thus acts to regulate arbitrarily hard momentum contributions to quantum field theoretical quantities. The real-world dynamics of QCD are recovered in the limit of vanishing lattice spacing (the continuum limit) and the infinite-volume limit.

The dynamics of QCD are encoded in the QCD Lagrangian: a quantity in quantum field theory that extends the classical notion of the difference between the kinetic and potential energy terms to a density in spacetime. The generalized kinetic and potential terms are constructed from the relevant degrees of freedom: quantum fields [Wei95]. The QCD Lagrangian includes a sum of Fermi-Dirac Lagrangians for all quark flavours, an interaction term and a Yang-Mills term. In tensor form (and summing over repeated indices), the Lagrangian reads:

$$\mathcal{L}_{\text{QCD}} = \mathcal{L}_{\text{Dirac}} + \mathcal{L}_{\text{int}} + \mathcal{L}_{\text{YM}}\tag{2.2}$$

$$= \sum_q \left\{ \bar{\psi}_q^i (\gamma^\mu \overset{\leftrightarrow}{\partial}_\mu - m_q) \psi_q^i - \alpha_s \bar{\psi}_q^i \gamma^\mu J_a^{ij} \mathcal{A}_\mu^a \psi_q^j \right\} - \frac{1}{4} G_{\mu\nu}^a G_a^{\mu\nu}.\tag{2.3}$$

The fields $\psi_q$ and $\bar{\psi}_q$ are Dirac spinors representing different quark flavours and colours, with mass $m_q$. (Dirac spinor algebra was introduced in References [Dir28b, Dir28a], and some of the basic properties of a Dirac spinor can be found in Appendix A.3.) The fields $G_{\mu\nu}^a$ are the non-Abelian field strength tensors corresponding to the gluon field $\mathcal{A}_\mu^a$, via the equation:

$$G_{\mu\nu}^a = \partial_\mu \mathcal{A}_\nu^a - \partial_\nu \mathcal{A}_\mu^a - i\alpha_s f_{abc} \mathcal{A}_\mu^b \mathcal{A}_\nu^c,\tag{2.4}$$

where the structure constants $f_{abc}$ are defined in Appendix A.2. The Yang-Mills term describes the self-interaction of the gluon fields, such that the result is invariant with

respect to a special type of symmetry known as the gauge symmetry. In QCD, the gauge symmetry is realized in the Lagrangian by forming represenions of a mathematical group, in this case, $SU(3)_c$ (where $c$ stands for 'colour'). Each term in the Lagrangian must be invariant under transformations involving this group. The quark spinors form a basis for the fundamental representation of the group. The gluon fields, however, are defined in the eight-dimensional representation of $SU(3)$, and the index $a$ runs from 1 through 8. The matrices $J_a^{ij}$ are the generators of the gauge group $SU(3)$. A detailed review of the symmetries of QCD is included in Chapter 3. Suffice to say, the Lagrangian in Equation (2.3) will be assumed in defining the QCD Action in the following Section.

## 2.1    Functional Methods

Lattice QCD relies on a variety of techniques to obtain information about the dynamics of QCD. In particular, the path integral method of quantization serves as a starting point, where complex valued Grassmann fields are used to represent the quark spinors $\psi$ and their adjoints $\bar{\psi}$. (For a short summary on the properties of Grassmann algebra and Berezin integrals, refer to Appendix A.3.) Before introducing the procedure for calculating the expectation values of observables using lattice QCD, it is helpful to review the functional methods required for defining the generating functionals and the $n$-point Green's Functions. In the following Section, use is made of the functional derivative $\frac{\delta}{\delta \mathcal{J}(x)}$, the properties of which follow analogously from the standard derivative of a function [RS80].

Consider the generating functional technique, choosing a set of fields $\Phi = \{\mathcal{A}_\mu^a, \psi, \bar{\psi}\}$, defined by a set of gauge fields $\mathcal{A}_\mu^a$ and Dirac spinors $\psi$ & $\bar{\psi}$, and integrating over all possible paths. In general, for a Lagrangian $\mathcal{L}(\Phi, \partial^\mu \Phi)$, the corresponding action can be written as follows:

$$S[\Phi] = \int \mathrm{d}^4x \, \mathcal{L}(\Phi(x), \partial^\mu \Phi(x)) \,. \tag{2.5}$$

The generating functional with source terms $\mathcal{J}(x_i)$ takes the form:

$$\mathcal{Z}[\mathcal{J}(x_i)] = \frac{1}{N} \int \mathcal{D}\Phi \exp\left\{ iS[\Phi] - \int d^4x\, \mathcal{J}(x_i)\Phi(x_i) \right\}, \quad \int \mathcal{D}\Phi \equiv \prod_{i=1}^{\infty} \int d\Phi_i, \quad (2.6)$$

with normalization:

$$N = \int \mathcal{D}\Phi \exp\left\{ iS[\Phi] \right\}. \quad (2.7)$$

The calculation of the $n$-point Green's Functions is performed by taking functional derivatives of the generating functional with respect to sources $\mathcal{J}(x_i)$, and then setting each source to zero:

$$\tau^{(n)}(x_1, \cdots, x_n) = \frac{1}{N} \int \mathcal{D}\Phi\, \Phi_1 \cdots \Phi_n \exp\left\{ iS[\Phi] \right\}. \quad (2.8)$$

In order to obtain only the connected diagrams for the generating functional, one can define the connected generating functional $\mathcal{W}$:

$$\mathcal{W}[\mathcal{J}] = -i\log \mathcal{Z}[\mathcal{J}]. \quad (2.9)$$

The connected (or irreducible) $n$-point Green's Functions can then be calculated as the time-ordered vacuum expectation values of the fields, with respect to the interacting vacuum $|\Omega\rangle$:

$$G^{(n)}(x_1, \cdots, x_n) = \langle\Omega| \, \mathcal{T}[\Phi(x_1) \cdots \Phi(x_n)] \, |\Omega\rangle = \frac{1}{i^n} \frac{\delta^{(n)}\mathcal{W}[\mathcal{J}]}{\prod_{i=1}^{n} \delta\mathcal{J}(x_i)}\bigg|_{\mathcal{J}=0}. \quad (2.10)$$

The generating functional of Equation (2.6) is useful for constructing an expansion of amplitudes. This expansion is obtained from the Schwinger-Dyson equations, the set of differential equations satisfied by the generating functional:

$$\frac{\delta}{\delta\Phi(x_i)} S\left[\frac{1}{i}\frac{\delta}{\delta\mathcal{J}}\right] \mathcal{Z}[\mathcal{J}(x_i)] + \mathcal{J}(x_i)\mathcal{Z}[\mathcal{J}] = 0. \quad (2.11)$$

The Schwinger-Dyson Equations are simply the Euler-Lagrange equations of motion for the $n$-point Green's Functions of the gauge field theory. They provide a

continuum persective to the challenging problems of non-perturbative QCD, as summarized by Roberts and Williams [RW94]. The investigation of the analytic properties of these equations form a crucial component of the study of quark confinement: where the strong coupling parameter becomes large. The Schwinger-Dyson Equations also shed light onto the process of dynamical chiral symmetry breaking, discussed in detail in Chapter 3.

Physical observables of a system can be obtained conveniently using Equation (2.10). To evaluate expectation values $\langle O \rangle$ numerically, it is common practice to remove the difficulties of Minkowski spacetime by an analytic continuation to imaginary Euclidean time, or a Wick rotation, $t \rightarrow -it$, and $S = iS_E$. Thus the expectation values become numerically soluble, since the highly oscillatory behaviour of the $n$-point Green's Functions have been exponentially damped. Thus:

$$\langle O \rangle = \frac{\int \mathcal{D}\Phi \, O \exp\{-S_E[\Phi]\}}{\int \mathcal{D}\Phi \, \exp\{-S_E[\Phi]\}} \, , \tag{2.12}$$

which is of the same form as the correlation function in statistical mechanics. Using the Euclidean Action, the fermionic part of the partition function can be calculated explicitly, leaving an expression in terms of a fermion correlation matrix $\mathcal{M}$:

$$\mathcal{Z} = \int \mathcal{D}\mathcal{A}_\mu^a \, \det(\mathcal{M}[\mathcal{A}_\mu^a]) \exp\{-S_E[\mathcal{A}_\mu^a]\} \, . \tag{2.13}$$

### 2.1.1   Wilson Fermions

In constructing an action on the lattice, such as that of Equation (2.5), there is a difficulty in implementing the fermion field. This difficulty is known as the fermion doubling problem. The problem occurs when solving the kinetic part of the Dirac Equation of motion, $(i\slashed{\partial} - m)\psi = 0$, on the lattice. The derivative $\partial$ is taken as an average (or a forward-backward average so that the result is Hermitian), and the propagator derived is of the form: $\sin(\slashed{p} + m)^{-1}$. The correct behaviour of the Green's Function is exhibited as $p \rightarrow 0$, but as $p \rightarrow \pi$ the propagator also vanishes at the edge of the Brillouin Zone: the fundamental cell of a lattice theory with a periodic bound-

ary.  Thus for $\sin(p\!\!\!/) = 0$ there are $2^{dim}$ degenerate quarks for each flavour, which corresponds to sixteen degenerate quarks in four-space. In order to amend this, Wilson introduced a five-dimensional operator, which increases the mass of the doubler species proportional to lattice spacing $a$ [Wil74].  Note that as $a \to 0$ in the continuum limit, the Wilson term disappears and does not alter the dynamics of QCD. However, the Wilson Action violates chiral symmetry. This important symmetry ensures the consistent renormalization of the low-energy constants of the Lagrangian via the chiral Ward Identities, which describe the conservation of a symmetry as applied to quantum amplitudes. Chiral symmetry is described in more depth in Chapter 3. Additionally, a so-called Clover term is often added to the Lagrangian, which is proportional to $\bar{\psi} J^a G^a_{\mu\nu} \psi$. This term is also a five-dimensional object, and, like the Wilson Action, is suppressed in the continuum limit.  In addition, errors of $O(a)$ can be removed, and higher-order errors of $O(a^2)$ can be suppressed by using non-perturbatively improved actions [NN95, LSSW96, Z$^+$02].  Lattice QCD simulation results relying on a variety of actions are presented in Chapters 4 through 7, and the benefits and shortcomings of each one will be addressed as they arise.

### 2.1.2   Correlation Functions and the Effective Mass

Consider the following example regarding the construction of a correlation matrix element, and the extraction of the effective mass.  In applying lattice QCD to the extraction of the mass of the nucleon, one defines interpolating fields $\chi$ and $\bar{\chi}$, which incorporate the structure of a nucleon in terms of its constituent quarks.  For example, in the case of a proton, $\chi = \varepsilon^{abc}(u_a^T C \gamma_5 d_b) u_c$ is a suitable choice, since the maximally anti-symmetric Levi-Civita symbol $\varepsilon$ ensures a colour-singlet state, and the Dirac spin matrix $\gamma_5$ (defined in Appendix A.1) preserves the spinor properties of the interpolating field. The fields $u$, $d$ are Dirac spinors representing the up and down quarks, respectively, and the charge conjugation matrix $C = i\gamma_0\gamma_2$ ensures that the product of a spinor and its transpose satisfies Lorentz invariance.

The two-point Green's Function for a proton, or more generally, the nucleon, can be expanded by inserting both a complete set of momentum- and spin-dependent

eigenstates $|A(q,s)\rangle$, and a translation operator on the $\chi$ field:

$$G^{(2)}(\vec{x},t) = \langle\Omega|\chi(\vec{x},t)\,\bar{\chi}(0)|\Omega\rangle, \tag{2.14}$$

$$G^{(2)}(\vec{p},t) = \sum_{\vec{x},A,\vec{q},s} e^{-i\vec{p}\cdot\vec{x}}\langle\Omega|e^{-iq\cdot x}\chi(0)\,e^{iq\cdot x}|A(q,s)\rangle\langle A(q,s)|\bar{\chi}(0)|\Omega\rangle \tag{2.15}$$

$$= \sum_{\vec{x},A,\vec{q},s} e^{-i(\vec{p}-\vec{q})\cdot\vec{x}}e^{-E_A(\vec{q})t}\langle\Omega|\chi(0)|A(q,s)\rangle\langle A(q,s)|\bar{\chi}(0)|\Omega\rangle \tag{2.16}$$

$$= \sum_{A,\vec{q},s} \delta(\vec{p}-\vec{q})e^{-E_A(\vec{q})t}|\langle\Omega|\chi(0)|A(q,s)\rangle|^2 \tag{2.17}$$

$$= \sum_{A,s} |\lambda_{A,p,s}|^2 e^{-E_A(\vec{p})t}\psi(\vec{p},s)\,\bar{\psi}(\vec{p},s), \tag{2.18}$$

for complex-valued scalar coefficients $\lambda_{A,p,s}$, $\lambda^*_{A,p,s}$ and spinor fields $\psi$, $\bar{\psi}$ defined by the matrix elements:

$$\lambda_{A,p,s}\psi = \langle\Omega|\chi(0)|A(p,s)\rangle; \qquad \lambda^*_{A,p,s}\bar{\psi} = \langle A(p,s)|\chi(0)|\Omega\rangle. \tag{2.19}$$

The mass of the nucleon can then be extracted from the two-point Green's Function at zero 3-momentum, that is, $E_A(\vec{p}=0) = M_A$. To obtain a measure of this quantity from the exponential, one defines the effective mass $M_{\text{eff}}$ by comparing the behaviour of the Green's Function at times $t$ and $t+1$:

$$M_{\text{eff}} = \log\left(\frac{G_2(0,t)}{G_2(0,t+1)}\right). \tag{2.20}$$

Note that $M_{\text{eff}}$ is a dimensionless quantity, and the calculation of the mass of the nucleon must involve the conversion to physical units from lattice units by dividing by the lattice spacing $a$. Since the Green's Function incorporates the full quantum mechanical spectrum of modes, the behaviour of $M_{\text{eff}}$ is strongly influenced by the excited states of the nucleon at small $t$. In the limit of large $t$, however, the ground-state nucleon mass can be recovered:

$$M_N = \lim_{t\to\infty}\frac{M_{\text{eff}}}{a}. \tag{2.21}$$

### 2.1.3    Quenching and Computational Alternatives

Computing the quantity $\det(\mathcal{M}[\mathcal{A}_\mu^a])$ is the most time-consuming operation in the calculation of the partition function in Equation (2.13). For this reason, calculations are performed at fermion masses larger than their physical value, thus decreasing the Compton wavelength of a fermion and significantly reducing the computational resource requirement of the summation over all paths and the time required to execute all the necessary fermion matrix inversion algorithms. Usually, results from lattice QCD are obtained at multiple fermion masses, so an extrapolation can be used to obtain the result at the physical value, or at zero mass (the chiral limit). A complementary computational simplification known as quenching exists, whereby $\det(\mathcal{M}[\mathcal{A}_\mu^a])$ is set equal to a constant. This has the effect of removing from the theory all vacuum polarization diagrams, changing the dynamics of the quantum field theory in a non-trivial way. For this reason, quenched QCD (QQCD) should be considered, in essence, a different theory from QCD. The results from QQCD calculations can nonetheless be interesting points of investigation, as they offer a unique testing ground for extrapolation schemes. This is because results from the unphysical QQCD calculation cannot be known in advance from experiment.

Several other alternatives to quenching have been used in the literature to date. Sometimes, the vacuum polarizations, normally omitted in QQCD, are calculated for a different (usually larger) quark mass than the valence quarks, which couple to external sources. The quarks that appear in the disconnected loops are known as sea quarks. This distinction between sea quark mass and valence quark mass provides some of the dynamics of QCD, albeit altered, whilst still ameliorating the computational intensity of the calculation of $\det(\mathcal{M}[\mathcal{A}_\mu^a])$. An alternative, particularly used in electromagnetic contributions to QCD, is to omit diagrams that include indirect couplings, that is, external fields coupling to sea quark-antiquark pairs, as shown in Figure 2.1. The computation of the indirect couplings to disconnected quark loops is by far the most time-consuming portion of the calculation of a diagram. Valence QCD (VQCD) therefore only includes diagrams where any external particles, such as incoming photons, couple directly to valence quarks in the relevant hadron. Al-
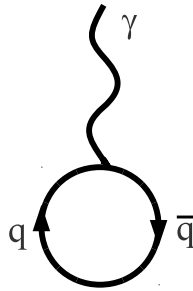
Figure 2.1: An external photon coupling to a sea quark-antiquark pair. Diagrams including this kind of coupling are omitted in Valence QCD.

though the resulting theory differs from full QCD, often properties of particles are calculated using an isovector combination. In the case of an isovector, a linear combination of isospin partners is formed so that the resultant combination transforms as a vector in isospin space. For example, in the case of the nucleon, the combination of the fermion fields: $p - n$ (proton minus neutron) is isovectorial with total isospin of 1, and all diagrams containing indirect couplings cancel. This is because diagrams that contain indirect couplings to disconnected loops are exactly the same for the proton and neutron, and thus disappear in the combination: $p - n$. It is only the valence quark composition that differs between the proton ($uud$) and the neutron ($ddu$). Thus the distinction between full QCD and VQCD disappears for this observable, and the calculations of its properties are less computationally intensive.

## 2.2   Lattice QCD Applicability and Issues

It is important to identify clearly the constraints of lattice gauge theory. Lattice QCD is well defined over all box sizes, lattice spacings and quark masses, and it is also infinitely scalable. However, the computational cost of the calculation of an observable is generally proportional to the square of the lattice volume and inversely proportional to the sixth power of the lattice spacing. To avoid major finite-volume effects, the literature suggests that the lattice box length should be about 2.5 to 3.0 fm [SW85, LTTW00, FKOU95, DLL96, LS96]. This is the typical size of most current lattice QCD calculations. Nevertheless, finite-volume effects can still be significant

at these box sizes, and ought not to be neglected. In fact, for many observables, a box length of 3.0 fm is insufficient to avoid large finite-volume corrections at physical quark masses. This will be demonstrated in Chapters 4 through 7 for a variety of observables.

While continued supercomputing advances in numerical simulations of lattice QCD are important, one ought to recognize its limitations in providing a thorough understanding of the internal structure of hadrons, which can be aided, in part, by complementary techniques such as chiral perturbation theory ($\chi$PT). For example, consider the effects of the mesons known as kaons, vital for understanding strangeness in the nucleon, which appear in the meson octet (see in Appendix A.4). One must either use $\chi$PT calculated to significantly high order in the relevant perturbative expansion, or develop new non-perturbative approaches which utilize the non-perturbative information expressed in the lattice simulation results. Since the former is likely to be compromised by the asymptotic nature of the expansion, attention is given to the latter approach in Chapter 4.

The computation of observables in lattice QCD provides great insight into the non-perturbative region of QCD. As long as one can account for finite-volume and momentum discretization effects, lattice QCD provides excellent predictions of the behaviour of quarks at low-energy. In simulating the interactions of hadrons, and demonstrating confinement, lattice QCD is a landmark achievement in the realm of chiral dynamics.

The complementary methods obtained from effective field theory offer guidance in the calculation of observables on the lattice. They provide estimates of finite-volume effects and extrapolations to physical quark masses, and providing a deeper understanding of the applicable regions of lattice QCD. This can serve to ameliorate the otherwise unseen difficulties encountered in a brute-force approach to calculation by considering symmetries, renormalization, power-counting, and other techniques built into the formalism of chiral effective field theory. Each method presents its own challenges, but also brings enlightenment through the significantly different approaches to a given problem.

# Chapter 3

# Chiral Effective Field Theory

*"Everything can be tried, a bold abstraction of something that has succeeded else-where, the exploration of the faintest clue, or a leap through empty spaces...*

*Thus, the method exists, boundless, its ultimate foundation being the freedom of the mind."* (Omnès, R. 2002. *Quantum Philosophy: Understanding and Interpreting Contemporary Science* p.268) [Omn02]

In an effective field theory, one identifies the relevant degrees of freedom at a particular energy, and encodes the behaviour of these degrees of freedom in a suitable Lagrangian. For a low-energy effective field theory corresponding to quantum chromodynamics (QCD), such as chiral effective field theory ($\chi$EFT), effective Lagrangians may take on different forms to the QCD Lagrangian, but the physics of the strong interaction must remain the same in each case. That is, results for calculating elements of the S-matrix must agree among effective field theories, up to some order. In order to construct such a theory, terms in the effective Lagrangian are chosen so that they satisfy the fundamental symmetries of QCD. The coefficients of the terms in the effective Lagrangian are new coupling constants, the values of which are determined from experiments.

The method of effective Lagrangians provides alternative machinery to lattice QCD for understanding the low-energy behaviour of QCD, and physical theories in general at a specific energy level. The dynamics of the low-energy degrees of freedom, such as mesons and baryons in the case of $\chi$PT, are incorporated directly into

17

the Lagrangian, whereas very massive particles are treated as static sources [DGH96, Bor07]. Examples of important effective field theories include the Sigma Model and its various instructive representations, the MIT Bag Model [CJJ$^+$74, Joh78] and Cloudy Bag Model [MTT80], as well as quantum electrodynamics (QED) and QCD themselves [Wei95].

Recall that the QCD Lagrangian comprises a Yang-Mills term involving vector potentials $\mathcal{A}_\mu^a$, their field strength tensors $G_{\mu\nu}^a = \partial_{[\mu}\mathcal{A}_{\nu]}^a - i\alpha_s f_{abc}\mathcal{A}_\mu^b\mathcal{A}_\nu^c$ and a Dirac term of quark spinors $\psi$ corresponding to a mass matrix $\mathcal{M}$. The spinors and the mass matrix are extended to contain the six flavour and three colour components of QCD. Using the slash-notation $\gamma^\mu D_\mu \equiv \slashed{D}$, the QCD Lagrangian may written out conveniently in matrix form[1]:

$$\mathcal{L}_{\text{QCD}} = \bar{\psi}(i\overset{\leftrightarrow}{\slashed{D}} - \mathcal{M})\psi - \frac{1}{2}\text{Tr}\left[\bar{G}_{\mu\nu}\bar{G}^{\mu\nu}\right], \tag{3.1}$$

where the trace acts over colour indices for the matrix-valued versions of the gluon field strength tensor $\bar{G}_{\mu\nu}$, defined by summing over the generators $J^a$ of SU(3):

$$\bar{G}_{\mu\nu} = J^a G_{\mu\nu}^a = \partial_{[\mu}\bar{\mathcal{A}}_{\nu]} + i\alpha_s[\bar{\mathcal{A}}_\mu, \bar{\mathcal{A}}_\nu]. \tag{3.2}$$

The generators $J^a$ in the eight-dimensional representation of SU(3) are related to the Gell-Mann matrices $\lambda^a$, defined in Appendix A.2, by a factor of a half:

$$J^a = \frac{\lambda^a}{2}. \tag{3.3}$$

The quark-gluon interaction vertex is incorporated into the covariant derivative, defined as:

$$D_\mu = \partial_\mu + i\alpha_s\frac{\lambda^a}{2}\mathcal{A}_\mu^a, \tag{3.4}$$

which acts as a parallel transport in gauge-space, so that the QCD Lagrangian of Equation (3.1) is gauge-invariant. By substituting into Equation (3.2), it can be seen

---

[1]The double-headed arrow indicates the difference between the derivative acting to the right and to the left. i.e. $\overset{\leftrightarrow}{D} = \overset{\rightarrow}{D} - \overset{\leftarrow}{D}$.

that the anti-symmetrization of the covariant derivative is the field strength tensor. This is a consequence of the gauge connection $\bar{\mathcal{A}}_\mu$ lacking torsion:

$$\bar{G}_{\mu\nu} = \frac{i}{\alpha_s}[D_\mu, D_\nu].$$  (3.5)

The fundamental symmetries of QCD are built into the QCD Lagrangian of Equation (3.1). In particular, chiral symmetry will be important in the subsequent analyses of observables using $\chi$EFT. The consequences of chiral symmetry breaking ultimately have a profound effect on the behaviour of subatomic particles, their masses, magnetic moments and other properties. Therefore, it will be beneficial to describe some of the subtleties of chiral symmetry with care in the discussion below.

## 3.1 Chiral Symmetry

In general, a symmetry, or an invariance of a dynamical quantity under a transformation of one of its parameters, leads to important physical insights into a system. Noether's Theorem demonstrates that a conserved current can always be constructed from a (non-anomalous) symmetry of a field theory.

Chirality is defined as the handedness of the representations of the Poincaré group (which encodes the isometries of Minkowski spacetime) under which the quark spinors transform. It is related to the helicity of a particle: the projection of its spin on its direction of linear momentum, which is equivalent to chirality if the quarks are massless. Helicity is not in general a Lorentz-invariant quantity. Its value in one frame may be flipped with respect to its value in a boosted frame.

The QCD Lagrangian in Equation (3.1) can be split into separate left- and right-handed chiral states under the projections $\Gamma_{L,R} = \frac{1}{2}(1 \pm \gamma_5)$. The left- and right-handed spinors are written as:

$$\psi_{L,R} = \Gamma_{L,R}\psi.$$  (3.6)

Note that the resultant chirality of the quark fields is decoupled only for zero mass

[DGH96]:

$$\mathcal{L}_{\text{QCD}} = \mathcal{L}_L + \mathcal{L}_R + \mathcal{L}_{\text{YM}} + \mathcal{L}_{\text{mass}}$$
$$= i\bar{\psi}_L \overset{\leftrightarrow}{\slashed{D}} \psi_L + i\bar{\psi}_R \overset{\leftrightarrow}{\slashed{D}} \psi_R - \frac{1}{2}\text{Tr}\left[\bar{G}_{\mu\nu}\bar{G}^{\mu\nu}\right] - (\bar{\psi}_L \mathcal{M}\psi_R + \bar{\psi}_R \mathcal{M}\psi_L). \quad (3.7)$$

The quark fields transform under the chiral rotations $L$ and $R$, which are elements of the left- and right-handed Lie Algebra, respectively, defined for the group generators $Q_{L,R}^a$ and arbitrary, continuous, real parameters $\alpha_{L,R}^a$:

$$L = \exp(i\alpha_L^a Q_L^a) \in SU(3)_L, \quad (3.8)$$

$$R = \exp(i\alpha_R^a Q_R^a) \in SU(3)_R. \quad (3.9)$$

The transformation laws for each of the spinor fields can thus be written:

$$\psi_L \to L\psi_L = \psi_L + \delta\psi_L, \quad (3.10)$$

$$\psi_R \to R\psi_R = \psi_R + \delta\psi_R. \quad (3.11)$$

Noether's Theorem allows one to construct the left and right symmetry currents, with the corresponding time-independent charges forming the eight unique invariants of the group. These invariants are the generators, and are found by integrating over a spacelike surface $\sigma$. Note that in the case of $SU(3)_{L,R}$ the generators are related to the previously mentioned Gell-Mann matrices $\lambda^a$, after chiral projection by the group elements (up to a minus sign and a factor of a half, by convention):

$$J_{L,R}^{\mu a} = \frac{\partial \mathcal{L}_{\text{QCD}}}{\partial \partial_\mu \bar{\psi}_L}\delta\bar{\psi}_L = \frac{1}{2}\bar{\psi}_{L,R}\gamma^\mu \frac{\lambda^a}{2}\psi_{L,R}, \quad (3.12)$$

$$Q_{L,R}^a = \int d\sigma_\mu J_{L,R}^{\mu a} = \int d^3x\, J_{L,R}^{0a} = -\Gamma_{L,R}\frac{\lambda^a}{2}. \quad (3.13)$$

An equivalent convention to that of left/right chirality is the construction of vector and axial vector transformations. The group action can be written out explicitly for either convention, using the definition of a Lie group with continuous group parameters $\alpha_{V,A}^a$. The charges $Q_V^a$ and $Q_A^a$ simply count the sum and the difference of

left- and right-handed fermions, respectively:

$$V = \exp(i\alpha_V^a Q_V^a) \in \text{SU}(3)_V,\tag{3.14}$$

$$A = \exp(i\alpha_A^a Q_A^a) \in \text{SU}(3)_A,\tag{3.15}$$

$$Q_V^a = Q_L^a + Q_R^a = -\frac{\lambda^a}{2},\tag{3.16}$$

$$Q_A^a = Q_L^a - Q_R^a = -\frac{\lambda^a}{2}\gamma_5.\tag{3.17}$$

These sets of rotations are the most convenient for asserting the invocation of an important theorem known as Goldstone's Theorem. Goldstone's Theorem, described below, is crucial in understanding the connection between axial charges $Q_A^a$ and the origin of mesons in QCD.

### 3.1.1   Spontaneous Symmetry Breaking

In QCD, particles are believed to utilize the Nambu-Goldstone mode of spontaneous breaking of a continuous global gauge symmetry. This symmetry breaking occurs in flavour space, and only the lightest three quark flavours will be considered: up, down, strange. Since the up and down quarks have relatively low mass ($m_{u,d} \sim$ 2-6 MeV, $m_s \sim$ 100 MeV) compared to the other quarks ($m_c \sim$ 1.3 GeV), they contribute the most strongly to symmetry breaking effects.

Goldstone's Theorem states that the symmetry group $\text{SU}(3)_V \otimes \text{SU}(3)_A$ is not respected by the (no-particle) vacuum state $|0\rangle$, even though this group is a symmetry of the massless QCD Lagrangian. One might naïvely expect that the vacuum state is invariant under the group transformations:

$$V|0\rangle = A|0\rangle = |0\rangle.\tag{3.18}$$

Noether's Theorem entails that the symmetry charges are time-independent:

$$\frac{\mathrm{d}}{\mathrm{d}t}Q_{V,A}^a = 0 = [\mathcal{H}_{\text{QCD}}, Q_{V,A}^a]. \tag{3.19}$$

This means that the charges should annihilate the vacuum state $|0\rangle$, since the QCD Hamiltonian $\mathcal{H}_{\text{QCD}}$ annihilates the vacuum state. In 1984, Witten and Vafa proved this result for vector charges even without assuming chiral symmetry [VW84]. However, were this the case for axial charges, a spectrum of mass-degenerate partners with opposite parity would be expected to exist for all hadrons. This is because the axial charges are odd under parity transformations, and any state acted on by the axial charges will also retain the same energy eigenvalue (but with a flipped parity eigenvalue), because of the commutation relation in Equation (3.19). There is a stark lack of experimental evidence for such particles [Y$^+$06]. Thus, physical hadrons merely observe the symmetry group $\text{SU}(3)_V$.

Instead of annihilating the vacuum state, the axial charges transform it to an element of a new Hilbert space:

$$Q_V^a|0\rangle = 0, \tag{3.20}$$

$$Q_A^a|0\rangle = q_A|\pi^a(\vec{p})\rangle \neq 0. \tag{3.21}$$

This new state (with axial eigenvalue $q_A$) has the same energy as the vacuum state as long as the symmetry is not also explicitly broken by terms in the Lagrangian. Goldstone's Theorem states that new particles are created, the number of which corresponds to the number of generators for the relevant representation of $\text{SU}(3)_A$. These new particles must be massless and spinless pseudoscalar mesons, called Goldstone bosons.

If the physical manifestation of a symmetry of a Lagrangian involves the spontaneous breaking of one or several local continuous transformations, the theory predicts a massive spin zero boson called a Higgs field, and the Higgs mode is said to be realized. Although the Higgs mode is not expected to occur in the strong nuclear force sector of the Standard Model, its actualization in the electroweak sector would

result in a mass term for the $\{W^{\pm}, Z\}$ weak gauge bosons. Such a mass is observed in experiments, and also explains how the charged fermion fields gain mass, through the following argument. By considering the Lagrangian for an SU(2) complex doublet of bosons, which can be expanded about its minimum potential energy in the same manner as the Goldstone bosons, one must arbitrarily choose a direction in isospin space in which to expand. Three of the Higgs degrees of freedom combine to become the longitudinal spin modes of the three weak gauge bosons, and the mass of the fermions is produced by the vacuum expectation value of the remaining Higgs boson, which remains in the theory [GHK64]. It should be noted that the Higgs mechanism contributes only a small amount to the mass of hadrons in QCD, and that the dominant process for their mass acquisition is dynamical chiral symmetry breaking [GN74, RCR10]. A more detailed analysis of the consequences of dynamical chiral symmetry breaking for the mass of the nucleon is discussed in Chapter 4, in the context of varying quark masses in lattice QCD results.

## 3.1.2   Partial Conservation of the Axial Current

Before discussing the powerful techniques associated with effective Lagrangians, a brief overview is now presented for the current algebra method for obtaining the low-energy matrix elements of pion decay. It is known that the SU(3) axial currents $J_A^{\mu a}$ are non-zero. But in order to know exactly how these matrix elements vary and how they depend on the octet meson masses, one requires a current algebra technique known as Partial Conservation of the Axial Current (PCAC). The statement of Goldstone's Theorem in Equation (3.21) can be re-expressed as a matrix element:

$$\langle 0|J_A^{\mu a}|\pi^b(\vec{p})\rangle = i f_\pi p^\mu \delta^{ab} \,, \qquad (3.22)$$

from which follows the divergence:

$$\langle 0|\partial_\mu J_A^{\mu a}|\pi^b(\vec{p})\rangle = f_\pi m_\pi^2 \delta^{ab} \,. \qquad (3.23)$$

Equation (3.22) serves as a suitable definition of the pion decay constant $f_\pi$. Taking the value from experiment: $f_\pi \approx 92.4$ MeV.

Equation (3.23), together with the Haag Theorem, forms the principal statement of PCAC, that either $\pi^a$ or $\partial_\mu J_A^{\mu a}$ can be used equivalently, and that if the pion mass becomes zero then the axial current is totally conserved. Thus the following relation may be written:

$$\pi^a = \frac{1}{f_\pi m_\pi^2} \partial_\mu J_A^{\mu a} \,. \tag{3.24}$$

This situation is a special case of the Soft-Pion Theorem for a matrix element involving a general local operator $O$ :

$$\lim_{p^\mu \to 0} \langle \pi^a(\vec{p})\beta | \, O \, |\alpha\rangle = -\frac{i}{f_\pi} \langle\beta| \, [J_A^a, O] \, |\alpha\rangle \,. \tag{3.25}$$

While they are useful in obtaining specific information about the low-energy matrix elements of pion decay, the methods of PCAC can be subtle in determining possible momentum dependence in an amplitude of a low-energy process.  One must also make the assumption that matrix elements vary continuously in taking the soft pion limit, $p^\mu \to 0$. The method of effective Lagrangians is less awkward in obtaining the appropriate momentum dependence and any quantum corrections to a low-energy amplitude. This is because the effective Lagrangians are ordered by a systematic expansion in momentum or mass, which encodes the relative importance of corrections to an amplitude in question.

### 3.1.3   The Sigma Model

The Linear Sigma Model [GML60] is a useful pedagogical tool, because with it important theoretical techniques such as the construction of symmetry currents, spontaneous symmetry breaking and changes in parameterization can be demonstrated easily [DGH96]. First, consider an $SU(2)$ Sigma Model Lagrangian consisting of a massless spinor field $\psi$, a so-called pion field $\vec{\pi}$ spanning the triplet representation of $SU(2)$ and a massive scalar field $\sigma$. The consideration of isospin symmetry in $SU(2)$ provides a simple and instructive example for investigating symmetries [DGH96].

The Lagrangian takes the following form:

$$\mathcal{L}_\sigma = \bar{\psi} i \overleftrightarrow{\partial} \psi + \frac{1}{2} \partial_\mu \vec{\pi} \cdot \partial^\mu \vec{\pi} + \frac{1}{2} \partial_\mu \sigma \partial^\mu \sigma - g \bar{\psi} (\sigma - i \vec{\tau} \cdot \vec{\pi} \gamma_5) \psi + \frac{\mu^2}{2} (\sigma^2 + \vec{\pi}^2) - \frac{\lambda}{4} (\sigma^2 + \vec{\pi}^2)^2 ,$$

(3.26)

(for constant coupling parameters $g$, $\mu$ and $\lambda$, and SU(2) Pauli Spin matrices $\vec{\tau}$ defined in Appendix A.1).

Spontaneous symmetry breaking occurs in the Lagrangian of Equation (3.26) for $\mu^2 > 0$. In minimizing the potential:

$$V(\sigma, \vec{\pi}) = -\frac{\mu^2}{2} (\sigma^2 + \vec{\pi}^2) + \frac{\lambda}{4} (\sigma^2 + \vec{\pi}^2)^2 ,$$

(3.27)

a ground state is found that is non-trivial (unlike the case $\mu^2 < 0$, for which the only ground state solution is: $\sigma = \vec{\pi} = 0$). This ground state is defined by:

$$\sigma^2 + \vec{\pi}^2 = \frac{\mu^2}{\lambda} .$$

(3.28)

By redefining the $\sigma$ field and expanding the Lagrangian about the new ground state $\langle \sigma \rangle_0 \equiv v$, the Linear Sigma Model exhibits spontaneous symmetry breaking, evident in the acquisition of mass for the $\tilde{\sigma}$ field:

$$\tilde{\sigma} = \sigma - v,$$

(3.29)

$$\mathcal{L}_{\tilde{\sigma}} = \bar{\psi} (i \overleftrightarrow{\partial} - gv) \psi + \frac{1}{2} \partial_\mu \vec{\pi} \cdot \partial^\mu \vec{\pi} + \frac{1}{2} (\partial_\mu \tilde{\sigma} \partial^\mu \tilde{\sigma} - 2\mu^2 \tilde{\sigma}^2) - g \bar{\psi} (\tilde{\sigma} - i \vec{\tau} \cdot \vec{\pi} \gamma_5) \psi$$
$$- \lambda v \tilde{\sigma} (\tilde{\sigma}^2 + \vec{\pi}^2) - \frac{\lambda}{4} [(\sigma^2 + \vec{\pi}^2)^2 - v^4].$$

(3.30)

Nevertheless, SU(2) isospin symmetry is preserved in this Lagrangian.

The active degrees of freedom in an effective field theory do not necessarily correspond to elementary particles of nature, and so it is expected that changes in the representation do not alter the outcome of physical processes. This notion is formalized in the Haag Theorem [Haa58], which states that for two field variables derived from (unitarily) equivalent representations, if one is a free field, then the other is also free, regardless of how they are related and whether the associated diagrams

and Lagrangian vertices change [Gue66]. As a corollary, an interacting quantum field theory 'does not exist', in the sense that its fields do not transform covariantly under the interacting Poincaré group. Weinberg suggested that only free fields are required to construct the S-matrix from the relativistic Hamiltonians in QED, but in QCD one must simply resort to writing down the most general Lagrangian [Wei95]. An alternative approach demonstrates that an interaction picture can be constructed consistently if time evolution is taken to be only locally unitarily implementable [Gue66].

By redefining the scalar field in either linear or non-linear combinations of the other involved fields, different sets of interaction vertices can be assembled. For example, using the Linear Sigma Model, two particularly instructive representations are considered for later adaptation to low-energy QCD. By rewriting the heavy $\sigma$ field and pion triplet as a matrix quantity $\Sigma \equiv \sigma + i\vec{\tau} \cdot \vec{\pi}$, the resultant new field $\Sigma$ transforms as an object in the adjoint representation, which forms left cosets of the group $SU(2)_L \otimes SU(2)_R$, as described by Scherer [SS05]:

$$\Sigma \to L\Sigma R^\dagger. \tag{3.31}$$

In this representation, the Lagrangian becomes:

$$\mathcal{L}_\Sigma = \bar{\psi}_L i \overleftrightarrow{\partial} \psi_L + \bar{\psi}_R i \overleftrightarrow{\partial} \psi_R + \frac{1}{4}\mathrm{Tr}\,[\partial_\mu \Sigma \partial^\mu \Sigma^\dagger] + \frac{1}{4}\mu^2 \mathrm{Tr}\,[\Sigma^\dagger \Sigma] - \frac{\lambda}{16}\mathrm{Tr}\,[\Sigma^\dagger \Sigma]^2$$
$$- g\left(\bar{\psi}_L \Sigma \psi_R + \bar{\psi}_R \Sigma^\dagger \psi_L\right). \tag{3.32}$$

This form is useful because it allows one to identify easily the terms involved in spontaneous chiral symmetry breaking ($\sim \mathrm{Tr}\,[\Sigma^\dagger \Sigma]$). Terms responsible for explicit chiral symmetry breaking (eg. $\sigma \sim \mathrm{Tr}\,[\Sigma + \Sigma^\dagger]$) do not occur in this case, but will be considered in the context of $\chi$PT, in Section 3.2.

The exponential representation is most commonly employed for its application to low-energy QCD. By defining a matrix-valued field $U \equiv \exp(i\vec{\tau} \cdot \vec{\pi}/v)$ that transforms the same way as the previous $\Sigma$ field, and a massive scalar field $S$, the Lagrangian

becomes:

$$\mathcal{L}_U = +\bar{\psi}_L i \overleftrightarrow{\partial} \psi_L + \bar{\psi}_R i \overleftrightarrow{\partial} \psi_R + \frac{1}{2}\left((\partial_\mu S)^2 - 2\mu^2 S^2\right) + \frac{(v+S)^2}{4}\mathrm{Tr}\left[\partial_\mu U \partial^\mu U^\dagger\right]$$

$$- \lambda v S^3 - \frac{\lambda}{4}S^4 - g(v+S)\left(\bar{\psi}_L U \psi_R + \bar{\psi}_R U^\dagger \psi_L\right),\tag{3.33}$$

for an arbitrary coupling constant $v$. This representation combines the matrix form with a heavy scalar degree of freedom, which can be integrated out of the theory easily using the prescription provided by Donoghue, Golowich and Holstein [DGH96]. This is exactly the form needed to construct a low-energy effective field theory.

## 3.2   Chiral Perturbation Theory

The formalism of chiral perturbation theory ($\chi$PT) will take advantage of Goldstone's Theorem and the study of symmetries discussed in the previous section. In this case, however, the global gauge group considered is flavour SU(3). In order for the effective field theory to emulate physical results, one must write down the mechanics of a Lagrangian field theory incorporating the necessary symmetries and degrees of freedom at the observed scale. To represent particles such as pions and kaons obeying Bose-Einstein statistics, one can write the standard massless scalar Lagrangian:

$$\mathcal{L}_{\mathrm{eff}} = \frac{1}{2}\partial_\mu \pi^a \partial^\mu \pi^a + O(\pi^4),\tag{3.34}$$

and interpret $\pi^a$ as the octet of Goldstone bosons (whose explicit form can be found in Appendix A.4). By defining a matrix-valued function $U$, and its transformation law, one can collect together the interaction terms in the exponential representation in a similar way to the Sigma Model:

$$U = \exp\left(\frac{i}{f}\pi^a \lambda^a\right),\tag{3.35}$$

$$U \to LUR^\dagger,\tag{3.36}$$

with constant $f$. Now the effective Lagrangian can be written down as an expansion of successive orders of momenta. The two derivatives in the scalar Lagrangian mean that only even chiral powers are admitted for particles such as mesons. For the lowest-order free mesonic Lagrangian, there is only one low-energy coupling constant, $f$:

$$\mathcal{L}_{\text{eff}}^{(2)} = \frac{f^2}{4} \text{Tr} \left[ \partial_\mu U \partial^\mu U^\dagger \right]. \qquad (3.37)$$

(Higher-order mesonic Lagrangians can be found in References [SS05, Bor07, Ber08].) The coefficient $f$ from the definition of the field $U$ appears here as a low-energy constant (LEC), since it is expected that the expanded effective Lagrangian for the pseudo-Goldstone fields will have the standard normalization for bosons, $\mathcal{L}_{\text{eff}} = \frac{1}{2} \partial_\mu \pi^a \partial^\mu \pi^a + O(\pi^4)$. This LEC can further be identified with the pion decay constant $f_\pi$ by first considering the Fermi weak interaction Lagrangian as a left-handed source field and computing the decay rate from the resultant invariant S-matrix element [DGH96, SS05].

The second-order Lagrangian of Equation (3.37) will be the starting place for the consideration of the low-energy meson sector of QCD.

### 3.2.1   Meson Sector

In the theory of mesons, one considers a set of Goldstone boson fields and interprets them as the meson sector of QCD. One can use the knowledge of explicit symmetry breaking from Section 3.1.1 to provide the fields with a (small) mass. Using the exponential representation, $U(x)$ can be systematically expanded in powers of its small momentum and mass with respect to some energy scale $\Lambda_\chi$. In 1984, Manohar *et al.* identified this scale of chiral symmetry breaking as $\Lambda_\chi \sim 4\pi f \approx 1$ GeV [MG84]. In renormalization, this is the scale at which the next-order loop contribution retains the same effective coupling strength (see Section 3.3).

The total mesonic Lagrangian can be written out in the expanded form of even

chiral powers [Bor07]:

$$\mathcal{L}_\pi(U(x),\mathcal{M}) = \sum_{i=1}^{\infty} \mathcal{L}_\pi^{(2i)}(U(x),\mathcal{M}). \tag{3.38}$$

In order to quantify the extent of the chiral symmetry breaking caused by the mass terms in the expansion, initially let $\mathcal{M}$ transform as a field ($\mathcal{M} \to L\mathcal{M}R^\dagger$), so that the Lagrangian will remain invariant under global $SU(3)_L \otimes SU(3)_R$. At lowest non-trivial order:

$$\begin{aligned}
\mathcal{L}_\pi^{(2)} &= \mathcal{L}_\pi^{\mathrm{kin}} + \mathcal{L}_\pi^{\mathrm{mass}} \\
&= \frac{f_\pi^2}{4}\mathrm{Tr}\,[\partial_\mu U \partial^\mu U^\dagger] + \frac{f_\pi^2 B_0}{4}\mathrm{Tr}\,[\mathcal{M}U^\dagger + U\mathcal{M}^\dagger],
\end{aligned} \tag{3.39}$$

where $B_0$ is a constant (with dimensions of mass) included for generality. Chiral symmetry breaking then results from imposing the Hermitian condition for the quark mass matrix $\mathcal{M} = \mathcal{M}^\dagger$. Thus the constant $B_0$ directly corresponds to the extent of chiral symmetry breaking [SS05, Bor07].

Some terms in the Lagrangians of either QCD or $\chi$PT explicitly break chiral symmetry. For example, $\mathcal{L}_{\mathrm{mass}}$ involving the quark mass in Equation (3.7) is invariant under an axial group action $A = \exp(-\frac{i}{2}\alpha_A^a \lambda^a \gamma_5)$. The associated axial Noether currents $J_A^{\mu a}$ encountered in PCAC will not be conserved, but diverge according to the equation:

$$\partial_\mu J_A^{\mu a} = 2i\bar{\psi}\mathcal{M}\gamma_5 \frac{\lambda^a}{2}\psi. \tag{3.40}$$

To relate the meson masses to the quark masses, consider chiral SU(3). It is expected that the vacuum expectation values of the scalar quark densities are the same in each theory: QCD and $\chi$PT. That is, the quark condensate $\langle \bar{q}q \rangle$, where $q$ stands for $u$, $d$ or $s$ quarks, should be an observable independent of representation. Consider the explicit chiral symmetry breaking terms of each Lagrangian, namely, $\mathcal{L}_{\mathrm{mass}}$ defined in Equation (3.7) for QCD, and the mass term $\mathcal{L}_\pi^{\mathrm{mass}}$ of Equation (3.39)

for χPT. By expanding out the exponential field $U$ in $\mathcal{L}_\pi^{\text{mass}}$, one obtains:

$$\mathcal{L}_\pi^{\text{mass}} = B_0 f_\pi^2 \text{Tr}[\mathcal{M}] - \frac{1}{2} B_0 \text{Tr}[\mathcal{M}\pi^2] + O(\pi^4). \tag{3.41}$$

For approximate isospin symmetry $m_u \approx m_d \approx \frac{1}{2}(m_u + m_d) \equiv \hat{m} \neq m_s$, expanding the first of these terms yields the relations:

$$\langle \bar{q}q \rangle = -\langle 0| \frac{\partial \mathcal{L}_{\text{mixed}}}{\partial \hat{m}} |0\rangle = -\langle 0| \frac{\partial \mathcal{L}_\pi^{\text{mass}}}{\partial \hat{m}} |0\rangle = -B_0 f_\pi^2. \tag{3.42}$$

Thus there is a profound connection between quark condensation and the process of dynamical chiral symmetry breaking. The second term yields the Gell-Mann−Oakes−Renner Relations [GMOR68] relating meson masses to quark masses:

$$m_\pi^2 = 2B_0 \hat{m}, \tag{3.43}$$

$$m_K^2 = B_0(m_d + m_s), \tag{3.44}$$

$$m_\eta^2 = \frac{2}{3} B_0(\hat{m} + 2m_s). \tag{3.45}$$

Just like PCAC, Equation (3.43) shows that if the light quark masses are zero, then the pion mass must also be zero, and thus chiral symmetry holds. This leads to the Gell-Mann−Okubo Mass Relation:

$$3m_\eta^2 = 4m_K^2 - m_\pi^2. \tag{3.46}$$

By additionally enforcing local chiral symmetry, the set of all chiral Ward Identities become an invariant of the generating functional encountered in Section (2.1), as long as no anomalies are present [SS05]. The chiral Ward Identities simply encode the statement of symmetry preservation and the existence of conserved quantities as a consequence, much like Noether's Theorem; but applied to quantum amplitudes. Consider QED, a U(1) gauge theory, as an example. The Ward Identity amounts to a statement of charge conservation, and the existence of a conserved electric current. In QCD, to be able to generate all the Green's Functions for the theory, the

Lagrangian must include pseudo-scalar ($p$) and vector ($l_\mu$, $r_\mu$) source fields, which vanish to recover the standard QCD Lagrangian in Equation (3.1), and a scalar field ($s$) that assumes the role of the quark masses $\mathcal{M}$. This is known as the method of external sources. This generalization of the QCD Lagrangian is vital for calculating the divergence of Green's Functions. These fields obey the following transformation laws for the local chiral rotations $L(x), R(x) \in SU(3)_{L,R}$:

$$l_\mu \to L(x)\, l_\mu L^\dagger(x) + i(\partial_\mu L(x)) L^\dagger(x)\,, \tag{3.47}$$

$$r_\mu \to R(x)\, r_\mu R^\dagger(x) + i(\partial_\mu R(x)) R^\dagger(x)\,, \tag{3.48}$$

$$(s + ip) \to L(x)(s + ip) R^\dagger(x)\,. \tag{3.49}$$

The QCD Lagrangian, invariant under local $SU(3)_L \otimes SU(3)_R$, becomes:

$$\mathcal{L}_{QCD}^{local} = i\bar\psi \overleftrightarrow{\partial\!\!\!/} \psi - \frac{1}{2}\mathrm{Tr}\left[\bar{G}_{\mu\nu}\bar{G}^{\mu\nu}\right] - \bar\psi_L(s + ip)\psi_R - \bar\psi_R(s + ip)\psi_L$$
$$- \bar\psi\gamma_\mu\Gamma_L l^\mu\psi - \bar\psi\gamma_\mu\Gamma_R r^\mu\psi\,. \tag{3.50}$$

In the case of the low-energy effective Lagrangian, one must define a covariant derivative with transformation law:

$$\nabla_\mu U = \partial_\mu U + il_\mu U - iU r_\mu\,, \tag{3.51}$$

$$\nabla_\mu U \to L(x)\nabla_\mu U R^\dagger(x)\,. \tag{3.52}$$

Therefore, the lowest-order non-trivial Lagrangian for mesons obeying local chiral symmetry can now be written with mass source defined using the convention $\chi = 2B_0(s + ip)$, functioning as a field, as before:

$$\mathcal{L}_\pi^{(2)} = \frac{f_\pi^2}{4}\mathrm{Tr}\left[\nabla_\mu U \nabla^\mu U^\dagger + \chi U^\dagger + U\chi^\dagger\right]. \tag{3.53}$$

## 3.2.2   Baryon Sector

Since the Lagrangian of a low-energy theory can be expanded out in a convergent series of small momenta $p/\Lambda_\chi$, the mass of the baryons themselves cannot be treated as an expansion parameter, since their mass and momenta are of the same order of magnitude as the scale $\Lambda_\chi$; thus the perturbation theory diverges. That is, the mass of a baryon $M_B \sim \Lambda_\chi$, so the expansion parameter $M_B/\Lambda_\chi$ cannot be small. To overcome this difficulty in ordering the chiral series in the baryon sector of $\chi$PT, consider the heavy-baryon approximation.

Define some alternative fields $B_v(x)$ to the SU(3) octet baryons $B(x) = B^a(x)\lambda^a$, with velocity $v_\mu$ largely unchanged by pion interactions [Geo90, JM91a, JM91b]. These fields $B_v(x)$ are only just off-shell by a small amount $k \cdot v$:

$$p_B^\mu = M_B v^\mu + k^\mu. \tag{3.54}$$

A perturbation theory about this small momentum $k_\mu$ can now be constructed. In addition, the difficult spin structure of the new fields $B_v$ can be handled by using the particle projection operator $P_v = \frac{1}{2}(1 + \slashed{v})$, thus absorbing the effects of virtual baryon loops into higher chiral orders of the theory:

$$B_v(x) = P_v\, e^{iM_B \slashed{v} v \cdot x} B(x). \tag{3.55}$$

This procedure can be repeated in exact analogy for the totally symmetric Rarita-Schwinger tensor $T_v^{\mu abc}(x)$, which represents the spin-3/2 decuplet fields, as long as all spin-1/2 components are removed ($\gamma \cdot T_v^{abc} = 0$). It is defined by:

$$T_v(x) = P_v\, e^{i(M_B + M_T)\slashed{v} v \cdot x} T(x). \tag{3.56}$$

The sum of the octet and decuplet masses is used, by convention, in the exponential in order to avoid extra factors of mixed octet-decuplet fields in the final Lagrangian. This results in a positive term proportional to the mass splitting $\Delta = |M_T - M_B|$ [JM91a]. (The explicit representation of these fields in SU(3) can be found in

Appendix A.4).  Treating the mass splitting $\Delta \ll \Lambda_\chi$ as a small perturbation, the new velocity-dependent fields $B_v$ and $T_v$ (indices suppressed) obey a massless Dirac Equation, and a Dirac Equation with small mass splitting, respectively:

$$i\slashed{\partial} B_v(x) = 0, \tag{3.57}$$

$$(i\slashed{\partial} - \Delta)T_v(x) = 0. \tag{3.58}$$

To write out a completely velocity-dependent Lagrangian for baryons and their interactions with mesons, it now remains to rewrite all Dirac bilinears in terms of a covariant spin operator $S_v^\mu = -\frac{1}{8}\gamma_5[\gamma^\mu, \gamma^\nu]v_\nu$, which has the useful property that its commutation and anti-commutation rules depend only on the four-velocity $v_\mu$. The meson interactions are incorporated into the theory by coupling baryon fields to the axial current encountered in PCAC (Section (3.1.1)), which is equivalent to the Goldstone bosons as per the Haag Theorem. The convention is to define exponential fields $\xi^2 \equiv U$, which follow the transformation rule [JM91b]:

$$\xi \to L\xi H^\dagger(x) = H(x)\xi R^\dagger. \tag{3.59}$$

The transformation matrix $H = H(x)$ is a spacetime dependent combination of the chiral transformation matrices and the Goldstone bosons themselves. This means that the octet and decuplet fields' transformation rules also involve $H$, and in fact, the axial current $A_\mu$ and the octet baryon field $B_v$ are exactly analogous to the $\xi$ field in their transformations. The additional subtlety with the decuplet field is that each of its three indices transforms separately:

$$B \to HBH^\dagger, \tag{3.60}$$

$$T_\mu^{abc} \to H^{aa'}H^{bb'}H^{cc'}T_\mu^{a'b'c'}. \tag{3.61}$$

Because the transformation matrix $H$ is a spacetime-dependent object, a vectorial connection needs to be included to preserve the gauge invariance of the Lagrangian. Similarly, an axial vector combination of exponential fields can be defined. Under

the Haag Theorem, these axial vectors are equivalent to the pseudo-Goldstone boson fields:

$$V_\mu = \frac{1}{2}(\xi\partial_\mu\xi^\dagger + \xi^\dagger\partial_\mu\xi), \tag{3.62}$$

$$V_\mu \to HV_\mu H^\dagger - (\partial_\mu H)H^\dagger, \tag{3.63}$$

$$A_\mu = \frac{i}{2}(\xi\partial_\mu\xi^\dagger - \xi^\dagger\partial_\mu\xi), \tag{3.64}$$

$$A_\mu \to HA_\mu H^\dagger. \tag{3.65}$$

Thus the covariant derivative can now be included for both octet and decuplet fields. As before, the decuplet requires a separate connection to act on each index:

$$\mathcal{D}_\mu B_v = \partial_\mu B_v + [V_\mu, B_v], \tag{3.66}$$

$$\mathcal{D}_\mu T_v^{\alpha abc} = \partial_\mu T_v^{\alpha abc} + V_{\mu a}^d T_v^{\alpha dbc} + V_{\mu b}^d T_v^{\alpha adc} + V_{\mu c}^d T_v^{\alpha abd}. \tag{3.67}$$

The most general lowest-order Lagrangian for the baryon octet and decuplet fields, including transition vertices, can be now written by identifying the relevant SU(3) invariants [JM91a, JM91b, Jen92, LS96, WL05, WLTY07]:

$$\begin{aligned}
\mathcal{L}_{\text{oct\&dec}}^{(1)} = {}& i\,\text{Tr}\,[\bar{B}_v(v\cdot\mathcal{D})B_v] + 2D\,\text{Tr}\,[\bar{B}_v S_v^\mu\{A_\mu, B_v\}] + 2F\,\text{Tr}\,[\bar{B}_v S_v^\mu[A_\mu, B_v]] \\
& - i\bar{T}_v^\mu(v\cdot\mathcal{D})T_{v\mu} + \mathcal{C}(\bar{T}_v^\mu A_\mu B_v + \bar{B}_v A_\mu T_v^\mu) \\
& + 2\mathcal{H}\bar{T}_v^\mu S_{v\alpha}A^\alpha T_{v\mu} + \Delta\bar{T}_v^\mu T_{v\mu}. \tag{3.68}
\end{aligned}$$

The so-called $D$-style and $F$-style couplings for the octet occur simply as linear combinations of the most general first-order invariants of flavour SU(3) symmetry. The reversed sign of the kinetic term of the decuplet simply encodes the spacelike nature of its positive energy spinors ($\mathcal{U}^2 < 0$), and the Rarita-Schwinger field propagators contain a polarization projector that sums over these spinors [JM91a]:

$$\mathcal{P}_v = \sum_{i=1}^{4} \mathcal{U}_i^\mu \bar{\mathcal{U}}_i^\nu = (v^\mu v^\nu - g^{\mu\nu}) - \frac{4}{3}S_v^\mu S_v^\nu. \tag{3.69}$$

When considering the mass renormalization of the nucleon in Chapters 4 and 5, contributions from the second-order octet Lagrangian $\mathcal{L}_{\text{oct}}^{(2)}$ are required, which correspond to an $NN\pi\pi$ vertex. This gives rise to a tadpole contribution. In full $SU(3)$ form, the vertices required from $\mathcal{L}_{\text{oct}}^{(2)}$ are [WL05]:

$$\mathcal{L}_{\text{tad}}^{(2)} = 2\sigma_M \operatorname{Tr}[\mathcal{M}_+]\operatorname{Tr}[\bar{B}B] + 2D_M \operatorname{Tr}[\bar{B}\{\mathcal{M}_+, B\}] + 2F_M \operatorname{Tr}[\bar{B}[\mathcal{M}_+, B]],\quad (3.70)$$

where $\mathcal{M}_+ \equiv \frac{1}{2}(\xi^\dagger \mathcal{M}\xi^\dagger + \xi\mathcal{M}\xi)$ is the Hermitian mass source constructed from the quark mass $\mathcal{M}$ [GSS88, WL05].

Consider now the lowest-order Lagrangian for the nucleon-pion interaction by simplifying Equation (3.68) to involve only the nucleon doublet field $\Psi = (p, n)^{\text{T}}$ and the $SU(2)$ pion triplet (see Appendix A.4). This is a useful approach when kaon loop contributions are neglected. The axial coupling constant below is simply defined as $\mathring{g}_A = D + F$ [SS05]:

$$\mathcal{L}_{\pi N}^{(1)} = \bar{\Psi}\left(\slashed{\partial} - \mathring{M}_N + \frac{\mathring{g}_A}{2\mathring{f}_\pi}\gamma^\mu\gamma_5\vec{\tau}\cdot\partial_\mu\vec{\pi}\right)\Psi.\quad (3.71)$$

The tadpole Lagrangian now takes the form:

$$\mathcal{L}_{\pi N}^{(2),\text{tad}} = c_2 \operatorname{Tr}[\mathcal{M}_+]\bar{\Psi}\Psi,\quad (3.72)$$

where the coeffcient is a combination of the LECs $\sigma_m$, $D_M$ and $F_M$, labelled $c_2$ in anticipation of the analysis presented in Chapter 4.

A local, chirally symmetric form of Equation (3.71) can be recovered simply with the replacement:

$$\partial_\mu \to \nabla_\mu = (\partial_\mu + \Gamma_\mu - \frac{i}{2}(l_\mu + r_\mu)),\quad (3.73)$$

$$\Gamma_\mu = \frac{1}{2}(\xi^\dagger(\partial_\mu - ir_\mu)\xi + \xi(\partial_\mu - il_\mu)\xi^\dagger),\quad (3.74)$$

and also by replacing the product $\vec{\tau}\cdot\partial_\mu\vec{\pi}$ with a more general object: the Hermitian axial combination $u_\mu \equiv i\{\xi^\dagger(\partial_\mu - ir_\mu)\xi - \xi(\partial_\mu - il_\mu)\xi^\dagger\}$. The values of $\mathring{M}_N$, $\mathring{g}_A$ and

$\overset{\circ}{f}_\pi$ are taken to be the nucleon mass, the axial coupling strength and the pion decay constant, respectively, in the chiral limit. The Goldberger-Treiman Relation relates the nucleon-pion interaction strength to the axial coupling $g_A$ [GT58], and can be obtained by comparing the matrix elements $\langle p|\pi(x)|n\rangle$ and $\langle p|\partial_\mu A^\mu(x)|n\rangle$ using the relation between the pion field and the axial current in Equation (3.23) as per PCAC [Col85]:

$$g_{\pi NN} \approx g_A \frac{M_N}{f_\pi}. \tag{3.75}$$

This equation becomes exact in the chiral limit $g_A(m_\pi^2 \to 0) = \overset{\circ}{g}_A$.

### 3.2.3   Electromagnetic Contributions

The baryon form factors comprise a parameterization for the matrix element obtained from the isovector quark current $J_\mu \equiv \bar{\psi} Q \gamma_\mu \psi$, where $Q$ is the SU(3) quark charge matrix $Q \equiv \mathrm{diag}(2/3, -1/3, -1/3)$. To evaluate this matrix element, one must calculate the fully-amputated vertex for a baryon-photon interaction, wedged between the usual in- and out-going fermion spinors $u^s(p)$ and $\bar{u}^{s'}(p')$:

$$\langle B(p')|J_\mu|B(p)\rangle = \bar{u}^{s'}(p') \left\{ \gamma_\mu F_1(Q^2) + \frac{i\sigma_{\mu\nu}q^\nu}{2M_B} F_2(Q^2) \right\} u^s(p), \tag{3.76}$$

for the tensor quantity $\sigma_{\mu\nu} \equiv \frac{i}{4}\{\gamma_\mu, \gamma_\nu\}$. $Q^2$ is a positive momentum transfer $Q^2 = -(p'-p)^2$, and $F_1$ and $F_2$ are called the Dirac and Pauli form factors, respectively. The Sachs electromagnetic form factors $G_{E,M}$ are the linear combinations:

$$G_E(Q^2) = F_1(Q^2) - \frac{Q^2}{4M_B^2} F_2(Q^2), \tag{3.77}$$

$$G_M(Q^2) = F_1(Q^2) + F_2(Q^2). \tag{3.78}$$

Thus, in the non-relativistic, heavy-baryon formulation:

$$\langle B(p')|J_\mu|B(p)\rangle = \bar{u}^{s'}(p') \left\{ v_\mu G_E(Q^2) + \frac{i\varepsilon_{\mu\nu\rho\sigma} v^\rho S_v^\beta q^\nu}{M_B} G_M(Q^2) \right\} u^s(p). \tag{3.79}$$

By considering the behaviour of the Sachs form factors at zero momentum transfer, one can construct moments and charge radii. Two such important examples that will be considered are the magnetic moment, and the electric charge radius of the isovector nucleon. Recall from Section 2.1.3 that the isovector nucleon is simply the combination $p - n$, which transforms as a vector in isospin space, chosen so that diagrams containing indirect couplings will cancel, and the computation will be less intensive. The magnetic moment $\mu_n^v$ is simply the value of $G_M^v$ at $Q^2 = 0$:

$$\mu_n^v = G_M^v(Q^2 = 0) \tag{3.80}$$

$$= 1 + \kappa_n^v. \tag{3.81}$$

The first term is simply the value of the Dirac form factor of the proton at $Q^2 = 0$, and the second term $\kappa_n^v$ is the anomalous magnetic moment originating from the finite-size behaviour of the hadron interactions of the effective quantum field theory: the hadron cloud, which surrounds the nucleon.

The electric charge radius is obtained by taking a derivative with respect to $Q^2$ in the limit that $Q^2$ equals zero:

$$\langle r^2 \rangle_E^v = \lim_{Q^2 \to 0} -6 \frac{\partial G_E(Q^2)}{\partial Q^2}. \tag{3.82}$$

For octet baryons, the magnetic moments obey the Coleman-Glashow SU(3) relations, related to the following Lagrangian of two independent terms [JLMS93, WLTY07, WLTY09a, WLTY09b]:

$$\mathcal{L}_{\text{oct}}^{\text{e-m}} = \frac{e}{4m_N} \left( \mu_D \operatorname{Tr} \bar{B}_v \sigma^{\mu\nu} \{F_{\mu\nu}^+, B_v\} + \mu_F \operatorname{Tr} \bar{B}_v \sigma^{\mu\nu} [F_{\mu\nu}^+, B_v] \right). \tag{3.83}$$

For an electromagnetic gauge field $\mathscr{A}_\mu$ with field strength tensor $F_{\mu\nu} \equiv \partial_{[\mu} \mathscr{A}_{\nu]}$, the quantity $F_{\mu\nu}^+$ has been chosen such that it is invariant under local chiral symmetry transformations:

$$F_{\mu\nu}^+ \equiv \frac{1}{2} (\xi^\dagger F_{\mu\nu} Q \xi + \xi F_{\mu\nu} Q \xi^\dagger). \tag{3.84}$$

In the case of decuplet baryons, there is only a single invariant term that can be

obtained from the group product $\mathbf{\bar{10}} \otimes \mathbf{10} \otimes \mathbf{8}$ that is proportional to their electric charge tensor $q_{ijk}$ [JLMS93]:

$$\mathcal{L}_{\text{dec}}^{\text{e}-\text{m}} = i\frac{e}{m_N}\mu_C\, q_{ijk}\, \bar{T}_{\text{v},ikl}^{\mu}\, T_{\text{v},jkl}^{\nu}\, F_{\mu\nu}^{+}. \tag{3.85}$$

The transition Lagrangian can be written out likewise:

$$\mathcal{L}_{\text{trans}}^{\text{e}-\text{m}} = i\frac{e}{2m_N}\mu_T F_{\mu\nu}\left(\varepsilon_{ijk}\, Q_l^i\, B_{\text{v}m}^j\, S_{\text{v}}^\mu\, T_{\text{v}}^{\nu,klm} + \varepsilon^{ijk}\, Q_i^l\, \bar{T}_{\text{v},klm}^\mu\, S_{\text{v}}^\nu\, B_{\text{v}j}^m\right). \tag{3.86}$$

These electromagnetic Lagrangians are obtained simply by collecting the photon-baryon terms from the electromagnetic covariant derivative. This new covariant derivative can be expressed by updating Equation (3.66) so that the electromagnetic field is included in both the vector connection $V_\mu$ from Equation (3.62) and the axial combination $A_\mu$ from Equation (3.64):

$$V_\mu \to V_\mu + \frac{1}{2}ie\mathscr{A}_\mu(\xi^\dagger Q\xi + \xi Q\xi^\dagger), \tag{3.87}$$

$$A_\mu \to A_\mu - \frac{1}{2}e\mathscr{A}_\mu(\xi Q\xi^\dagger - \xi^\dagger Q\xi). \tag{3.88}$$

The covariant derivative for the pseudo-Goldstone Lagrangian can be updated in a similar fashion:

$$\nabla_\mu U \to \nabla_\mu U + ie\mathscr{A}_\mu[Q, U]. \tag{3.89}$$

## 3.3  Regularization and Renormalization

### 3.3.1  Historical Overview

The calculation and interpretation of amplitudes from a quantum field theory proved more subtle than other theories due to their divergent behaviour. Despite success in predicting hitherto unexplained phenomena, many quantities calculated using the relevant quantum field theory become infinite, though the known experimental value is finite. Consideration of the Lamb Shift in the electron energy levels in hydrogen

atoms (1947) prompted the first real insight into this problem. It was conceived that if a quantity were altered infinitely by quantum corrections so that the final result was finite, the initial 'bare' quantity should never have been expected to be finite. That is, the bare quantity becomes renormalized. For example, the bare core of an electron has certain properties, such as electric charge, which become altered by an infinite amount due to vacuum polarizations. This polarization cloud surrounding the unphysical, bare electron core contains all possible diagrams of electron-positron pair-production from virtual (off-shell) photons, which serve to screen the electron core's infinite charge, so that the observed, long-range charge is $-1.6 \times 10^{-19}$ Coulomb, or $-e$ (in units of the charge of the proton). This 'running' of the electron's charge to large values under deep probing from hard momenta in Bhabha scattering was confirmed in 1997 by the TOPAZ Collaboration at TRISTAN [A$^+$05]. The virtual particles of a quantum field theory are simply consequences of the Green's Functions of the equations of motion. The Fourier transform of a particle propagator integrates the whole momentum spectrum, with a pole on the mass shell $k^2 = m^2$ (up to factors of $c$ and $\hbar$). Heisenberg's Uncertainty Principle for energy and time, $(\Delta E)(\Delta t) \geq \hbar$, allows the extra energy of pair-production, and other processes, for sufficiently small time. As a corollary, the virtual interactions take place over a spacelike time interval.

### 3.3.2   The Power-Counting Regime

The Lagrangians of χPT are constructed with the intention that they can be expanded in a series of some expansion scale, such as small momenta or masses. Although, ideally, the series is convergent for a sufficiently small expansion scale, it need not necessarily be convergent, and instead will often take the form of an asymptotic (or Poincaré) series. Nevertheless, in a realistic calculation, which involves calculating the expansion series only up to some finite order, it is desirable to be able to ensure that the uncertainty in the truncation is small. Thus, a knowledge of the applicable region of the expansion is as crucial as knowledge of the terms of the expansion series themselves. The range of values of the expansion scale for which a chiral expansion is convergent is known as the power-counting regime (PCR), and the ex-

pansion series is generally known as the chiral expansion.

The PCR is the region where the quark masses are small, and higher-order terms in the chiral expansion are negligible beyond the order calculated. Within the PCR, the truncation of the chiral expansion is reliable to some prescribed precision. A chief focus of this thesis is to establish a formal approach to determining the PCR of a truncated chiral expansion quantitatively. The chiral expansion will be examined, and the individual low-energy coefficients of the chiral expansion will be analyzed. The approach involves the examination of these low-energy coefficients as they undergo the process of renormalization. This approach provides a determination of the PCR for a truncated expansion in $\chi$EFT.

First, it is essential to discuss methods of regularization in the chiral loop integrals, so that the renormalization can take place. In order to renormalize a quantity, one must find a way to make the divergent amplitudes tractable, using a process called regularization. This involves solving an integral over propagators in such a way as to isolate the divergent piece, ready for handling with a suitable renormalization scheme. There is a wide variety of regularization schemes available. Pauli-Villars regularization (1949) involves the introduction of fictitious, 'auxiliary' particles, associated with some mass scale, into a Lagrangian with a quadratic interaction. The extra formal terms in the Lagragian vanish as the mass scale is taken to infinity, and then a subtraction can take place. However, because Pauli-Villars is not a gauge-covariant scheme, it is not applicable directly to Yang-Mills theory. In Slavnov's regularization scheme (1971) of higher covariant derivatives, once again, additional terms are added to the Lagrangian, but these do not render all amplitudes finite, thereby requiring a Pauli-Villars or other scheme to be used for divergent fermion-loop Feynman diagrams. In this thesis, a finite-range regularization scheme is used, which has powerful benefits in establishing the PCR, as will become apparent in Chapter 4.

### 3.3.3   Dimensional Regularization

Dimensional regularization (DR) (1972) is an important procedure whereby loop integrals are analytically continued to generalized fractional dimensions and shown to converge [tHV72]. The infinitesimal four-volume box $\mathrm{d}^4 k$ is replaced with $\mathrm{d}^{4-\varepsilon} k$, and the limit as $\varepsilon \to 0^+$ is then taken. For example, the integral over a single (Euclidean) pion propagator is easy solved in spherical polar coordinates, evaluating the angular part explicitly[2]:

$$\int \frac{\mathrm{d}^4 k}{(2\pi)^4} \frac{1}{k^2 + m_\pi^2} \to \lim_{\varepsilon \to 0^+} \int_0^\infty \frac{\mathrm{d}k}{(2\pi)^{4-\varepsilon}} \frac{k^{3-\varepsilon}}{k^2 + m_\pi^2} \frac{2\pi^{2-\varepsilon/2}}{\Gamma(2-\varepsilon/2)} \,. \qquad (3.90)$$

Thus the minimal subtraction scheme result is recovered correctly.

Since there is no explicit scale-dependence in the interaction, this minimal subtraction scheme makes DR suitable for use with elementary fields, where the absence of new degrees of freedom at higher energies is assumed. This is a powerful technique by which the divergent term(s) of a loop integral can be obtained, and then handled using a renormalization scheme.

Nevertheless, in the case of effective field theories, there exists an energy scale beyond which the effective fields are no longer the relevant degrees of freedom, and so DR is not ideally suited. Selecting a hard energy scale in the renormalization group equation, changes the relevant degrees of freedom in the Lagrangian. At high energy scales, the high de Broglie frequency would resolve the internal structure of the hadrons, which would be the quarks (and beyond, if such higher degrees of freedom exist). However, quarks are integrated out of the low-energy $\chi$EFT Lagrangian by construction. When one calculates quantum amplitudes over this high energy domain, there is no guarantee that one can efficiently subtract the model-dependent, ultraviolet physics with a finite number of counter-terms, as is required for successful renormalization, unless the perturbative expansion is convergent. Indeed this problem of beginning with rapidly varying loop contributions, which must then be removed with a finite number of counter-terms, can easily be overcome. The

---

[2]The Gamma function on $\mathbb{C}$ is defined as $\Gamma(z) = \int_0^\infty \mathrm{d}s\, e^{-s} s^{z-1}$.

hard momentum contributions to the chiral loop integrals can be suppressed via the introduction of a finite-range regulator.

### 3.3.4   Finite-Range Regularization

One alternative to DR is finite-range regularization (FRR), in which one introduces a functional form $u(k;\Lambda)$, known as a finite-range regulator, which controls the divergent integral at high momentum values. In this case, the integral over a single pion propagator would be modified as follows:

$$\int \frac{\mathrm{d}^4 k}{(2\pi)^4} \frac{1}{k^2 + m_\pi^2} \to \int \frac{\mathrm{d}^4 k}{(2\pi)^4} \frac{u^2(k;\Lambda)}{k^2 + m_\pi^2}.  \tag{3.91}$$

FRR involves the choice of a finite-valued momentum cutoff $\Lambda$. Allowing hard, internal momenta to flow through a loop integral yields unphysical results, in the form of a divergence. The high de Broglie frequency would resolve the internal structure of the hadrons, which would be the quarks (and beyond, if such higher degrees of freedom exist). Therefore, a finite value of $\Lambda$ is suitable for an effective field theory, where quarks are integrated out of the Lagrangian by construction. The choice of parameter $\Lambda$ determines how fast the integral will now converge, and the regulator function should satisfy $u|_{k=0} = 1$ and $u|_{k\to\infty} = 0$. The exact functional form chosen for the regulator should be independent of the result of calculation, as long as the perturbative expansion is convergent, that is, one works within the PCR.

FRR has already been shown to be a powerful technique in solving the chiral extrapolation problem and identifying the PCR. The infinite series is resummed so that leading-order terms are large and the series converges. A variety of choices of functional forms for the regulator have been demonstrated to agree with each other, and with DR, in extrapolating lattice QCD results for the mass of the nucleon to physical quark masses [LTY05]. Thus, the results of calculations using FRR are consistent with DR within the PCR.

Consider the example of a one-pion loop contribution for a nucleon, denoted $\Sigma_N$, with constant coefficient $\chi_N$. (This type of calculation is considered in more detail

in Chapter 4.) The chiral expansion for the mass of the nucleon in this simple case, with one pion loop only, takes the form:

$$M_N = \{a_0 + a_2 m_\pi^2 + a_4 m_\pi^4 + O(m_\pi^6)\} + \Sigma_N, \tag{3.92}$$

working to chiral order $O(m_\pi^4)$. The chiral expansion comprises a polynomial expansion in $m_\pi^2$ and the contribution from the one-pion loop. Each of the coefficients $a_0$, $a_2$ and $a_4$ is renormalized by the contributions from the loop integral, at each order. The result of the integral using DR is equivalent to a massless renormalization scheme, with no explicit momentum cutoff:

$$\Sigma_N = \frac{2\chi_N}{\pi} \int_0^\infty dk \frac{k^4}{k^2 + m_\pi^2} \tag{3.93}$$

$$= \frac{2\chi_N}{\pi} \int_0^\infty dk \frac{(k^2 + m_\pi^2)(k^2 - m_\pi^2) + m_\pi^4}{k^2 + m_\pi^2} \tag{3.94}$$

$$= \frac{2\chi_N}{\pi} \left( \int_0^\infty dk\, k^2 - m_\pi^2 \int_0^\infty dk \right) + \chi_N m_\pi^3. \tag{3.95}$$

In a massless renormalization scheme, there is no explicit momentum cutoff, so each of the coefficients $a_i$ undergoes an infinite renormalization or none at all:

$$c_0 = a_0 + \frac{2\chi_N}{\pi} \int_0^\infty dk\, k^2, \tag{3.96}$$

$$c_2 = a_2 - \frac{2\chi_N}{\pi} \int_0^\infty dk, \tag{3.97}$$

$$c_4 = a_4 + 0, \text{ etc.} \tag{3.98}$$

By contrast, in a FRR scheme, a momentum cutoff $\Lambda$ is introduced, and the chiral expansion is resummed. Using a sharp momentum cutoff $\Lambda$:

$$\Sigma_N(\Lambda) = \frac{2\chi_N}{\pi} \int_0^\Lambda dk \frac{k^4}{k^2 + m_\pi^2} \tag{3.99}$$

$$= \frac{2\chi_N}{\pi} \left( \frac{\Lambda^3}{3} - \Lambda m_\pi^2 + m_\pi^3 \arctan\left[\frac{\Lambda}{m_\pi}\right] \right) \tag{3.100}$$

$$= \frac{2\chi_N}{\pi} \frac{\Lambda^3}{3} - \frac{2\chi_N}{\pi} \Lambda m_\pi^2 + \chi_N m_\pi^3 - \frac{2\chi_N}{\pi} \frac{1}{\Lambda} m_\pi^4 + O(m_\pi^6). \tag{3.101}$$

The result obtained from DR can be recovered in an FRR scheme by taking the regularization scale parameter $\Lambda$ to infinity:

$$c_0 = a_0 + \frac{2\chi_N}{3}\Lambda^3 , \tag{3.102}$$

$$c_2 = a_2 - \frac{2\chi_N}{\pi}\Lambda , \tag{3.103}$$

$$c_4 = a_4 - \frac{2\chi_N}{\pi}\frac{1}{\Lambda} , \text{ etc.} \tag{3.104}$$

Thus, DR applied outside the PCR could be considered equivalent to a model with an arguably injudicious choice of cutoff scheme. The polynomial expansion of hadron mass is not expected to converge, and indeed it does not, using DR $\chi$PT, as mentioned by Young, *et al.* [YLT03]. Outside PCR, the expansion breaks down since the chiral expansion is truncated without an attempt to estimate the higher-order contributions [LTY05, LTY06].

In addition, because FRR involves the resummation of the higher-order terms of the chiral expansion, it affords an opportunity to perform a calculation beyond the PCR. Using FRR, one must select a value for the ultraviolet regularization scale $\Lambda$. The choice in the value of $\Lambda$ is irrelevant within the PCR, where the results of extrapolations are scheme-independent (so long as $\Lambda$ is not chosen to be too small, as explained in Section 4.2.1). Nevertheless, the principal exercise of this thesis will be to handle any scheme-dependence occuring in a $\chi$EFT calculation outside the PCR. By quantifying the scheme-dependence one arrives at a rigorous procedure for using FRR beyond the PCR.

In Chapter 4, a variety of finite-range regulators are used and compared. For example, the Heaviside Step Function $u^2(k;\Lambda) = \theta(\Lambda - k)$ is an acceptable choice; however, it is unfavorable for finite-volume considerations because discrete lattice momenta are either fully included in the integral or not included at all. This results in inconvenient finite-volume artefacts. In the investigation of the nucleon mass, the family of smoothly attenuating dipole regulators will be considered. The general
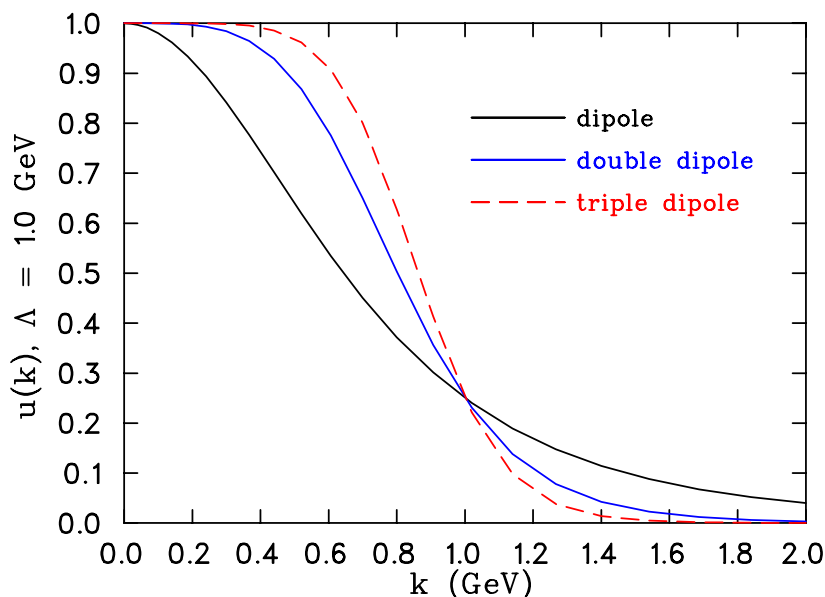
Figure 3.1: Behaviour of three dipole-like regulators as a function of momentum $k$, for a regulator parameter $\Lambda = 1.0$ GeV.

multiple-dipole function of order $n$ takes the following form, for a cutoff scale of $\Lambda$:

$$u_n(k;\Lambda) = \left(1 + \frac{k^{2n}}{\Lambda^{2n}}\right)^{-2}. \tag{3.105}$$

The standard dipole is recovered for $n = 1$. The cases $n = 2, 3$ are the 'double-' and 'triple-dipole' regulators, respectively. The behaviour of each of these three attenuators is shown in Figure 3.1. These functional forms allow one to interpolate between the dipole regulator and the step function (which corresponds to $n \to \infty$). These $n-$tuple-dipole regulators generate extra non-analytic terms.

It has been suggested in the literature that the only FRR scheme consistent with chiral symmetry uses the step function regulator [BHM04]. Djukanovic *et al.* [DSGS05] have demonstrated that more general functional forms can be generated by proposing a scheme in which the regulator function is interpreted as a modification to the propagators of the theory, obtained from a new chiral symmetry-preserving Lagrangian. Higher derivative coupling terms are built into the Lagrangian to produce a regulator from the Feynman Rules in a symmetry-preserving manner. Alternatively, one can choose the regulator judiciously such that any extra scheme-

dependent non-analytic terms are removed to any chosen order. The regulators used in the present investigation follow the latter approach. For example, the $n-$tuple dipole regulators generate extra non-analytic terms in the chiral expansion of Equation (4.2) in Chapter 4 at higher chiral orders. An explicit example of this is shown for the quenched $\rho$ meson mass in Section 6.1.2, once the renormalization scheme has been introduced.

# Chapter 4

# The Intrinsic Scale of the Nucleon

*"There lies the originality of our approach:* to deduce common sense from the quantum premises, including its limits− that is, to demonstrate also under which conditions common sense is valid, and what is its margin for error...

*[W]e no longer explain reality from our mental representation of it, taken for granted without question: but it is this representation,... that we want to* explain*[.]"*
(Omnès, R. 2002. *Quantum Philosophy: Understanding and Interpreting Contemporary Science* p.165) [Omn02]

## 4.1   Renormalization Issues for the Nucleon Mass

In chiral effective field theory ($\chi$EFT), the nucleon mass may be written as an ordered, chiral expansion in the quark mass. The Gell-Mann−Oakes−Renner Relation from Equation (3.43) entails the proportionality $m_q \propto m_\pi^2$. By considering the renormalization of the nucleon mass $\overset{\circ}{M}_N \to M_N$ from the Lagrangian in Equation (3.71), the chiral expansion will generally include a polynomial in $m_\pi^2$ and non-analytic terms obtained from the chiral loop integrals. In addition, to establish a model-independent framework in $\chi$PT, the expansion must display the properties of a convergent series for the terms considered. Recall that within the power-counting regime (PCR) the higher-order terms of the expansion may be regarded as sufficiently small for the truncation of the chiral expansion to be reliable to a prescribed

precision. However, truncated expansions are typically applied to a wide range of quark (or pion) masses, with little regard to a rigorous determination of the PCR. In the case of the nucleon mass, evidence suggests that the PCR is small: limited to $m_\pi \lesssim 200$ MeV at 1% accuracy at the chiral order $O(m_\pi^4 \log m_\pi)$ [Bea04a] [LTY05]. This estimate of the PCR of $\chi$PT was identified by comparing the results of infrared regularization, dimensional regularization (DR) and a variety of finite-range regulators in analyzing lattice quantum chromodynamics (lattice QCD) simulation results. The different regularization schemes constitute different ways of summing higher-order terms in the chiral expansion. Thus, the PCR is manifest when the pion mass dependence of the nucleon mass is independent of the renormalization scheme. In addition, the asymptotic nature of the chiral expansion places the focus on the first few terms of the expansion.

A survey of the literature for the baryon sector of $\chi$EFT illustrates the rarity of calculations beyond one-loop [MB99, MB06, SDGS07], and there are currently no two-loop calculations that incorporate the effects of placing a baryon in a finite volume. With only a few terms of the expansion known for certain, knowledge of the PCR of $\chi$EFT is as important as knowledge of the expansion itself. Though scheme-dependent, it is worthwhile to note that, using a dipole regulator with $\Lambda = 0.8$ GeV, the coefficient of the induced $m_\pi^5$ term compares favorably with the infinite-volume two-loop calculation [MB99, LTY04, LTY05, MB06, SDGS07].

### 4.1.1   Chiral Expansion of the Nucleon Mass

The nucleon mass expansion formula can be expressed in a form that collects the non-analytic behaviour into the loop integral contributions:

$$
M_N = \{a_0^\Lambda + a_2^\Lambda m_\pi^2 + a_4^\Lambda m_\pi^4 + O(m_\pi^6)\} + \Sigma_N(m_\pi^2, \Lambda) + \Sigma_\Delta(m_\pi^2, \Lambda)
$$
$$
+ \Sigma_{tad}(m_\pi^2, \Lambda) \tag{4.1}
$$
$$
= c_0 + c_2 m_\pi^2 + \chi_N m_\pi^3 + c_4 m_\pi^4 + \left(-\frac{3}{4\pi\Delta}\chi_\Delta + \chi_t\right) m_\pi^4 \log\frac{m_\pi}{\mu} + O(m_\pi^3). \tag{4.2}
$$
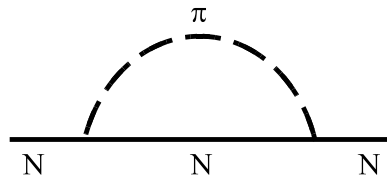
**Figure 4.1:** The pion loop contribution to the self-energy of the nucleon, providing the leading non-analytic contribution to the nucleon mass. All charge conserving transitions are implicit.
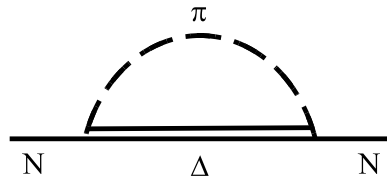


**Figure 4.2:** The pion loop contribution to the self-energy of the nucleon, allowing a transition to a nearby and strongly-coupled decuplet baryon.
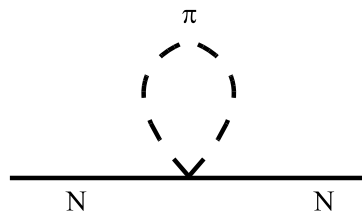


**Figure 4.3:** The $O(m_q)$ tadpole contribution to the nucleon self energy.

The superscript $\Lambda$ denotes the scale-dependence of the $a_i^\Lambda$ coefficients. The analytic terms in $m_\pi^2$ can be written as a polynomial with renormalized coefficients $c_i$. The non-analytic contributions arise from the self energy integrals ($\Sigma$), which correspond to the diagrams in Figures 4.1 through 4.3.

It is essential to note that the degrees of freedom present in the residual series coefficients $a_i^\Lambda$ are sufficient to eliminate any dependence on the regularization scale parameter $\Lambda$, to the order of the chiral expansion calculated: in this case $O(m_\pi^4 \log m_\pi)$. Any differences observed in results obtained at the same chiral order, but with different regularization schemes, are a direct result of considering data that lie outside the PCR (provided that the scale $\Lambda$ is not chosen so small that it introduces an unphysical low-energy scale).

## 4.1.2   Chiral Loop Integrals

Each of the loop integral contributions to the nucleon mass can be simplified to a convenient form by taking the non-relativistic heavy-baryon limit, and performing the pole integration for $k_0$. The integrals may be expanded out to a particular chiral order, in this case order $O(m_\pi^4 \log m_\pi)$, to obtain an analytic polynomial with coefficients $b_i^\Lambda$, and the leading-order non-analytic term. Using a finite-range regulator $u(k;\Lambda)$:

$$\Sigma_N(m_\pi^2;\Lambda) = \frac{\chi_N}{2\pi^2} \int d^3k \frac{k^2 u^2(k;\Lambda)}{k^2 + m_\pi^2} \tag{4.3}$$

$$= b_0^{\Lambda,N} + b_2^{\Lambda,N} m_\pi^2 + \chi_N m_\pi^3 + b_4^{\Lambda,N} m_\pi^4 + O(m_\pi^5), \tag{4.4}$$

$$\Sigma_\Delta(m_\pi^2;\Lambda) = \frac{\chi_\Delta}{2\pi^2} \int d^3k \frac{k^2 u^2(k;\Lambda)}{\omega(k)(\Delta + \omega(k))} \tag{4.5}$$

$$= b_0^{\Lambda,\Delta} + b_2^{\Lambda,\Delta} m_\pi^2 + b_4^{\Lambda,\Delta} m_\pi^4 - \frac{3}{4\pi\Delta} \chi_\Delta m_\pi^4 \log \frac{m_\pi}{\mu} + O(m_\pi^5), \tag{4.6}$$

$$\Sigma_{tad}(m_\pi^2;\Lambda) = c_2 m_\pi^2 \left( \frac{\chi_t}{4\pi} \int d^3k \frac{2u^2(k;\Lambda)}{\omega(k)} \right) \tag{4.7}$$

$$= c_2 m_\pi^2 \left( b_2^{\Lambda,t} + b_4^{\Lambda,t} m_\pi^2 + \chi_t m_\pi^2 \log \frac{m_\pi}{\mu} + O(m_\pi^5) \right), \tag{4.8}$$

where $\mu$ is an implicit mass scale from the logarithm, $\omega(k) = \sqrt{k^2 + m_\pi^2}$ and $\Delta$ is the nucleon-delta baryon mass-splitting, treated as a perturbation in the approximate flavour symmetry. The mass of the $\Delta$ baryon is chosen to be the centre of its Breit-Wigner resonance.

The $b_i^\Lambda$ coefficients renormalize the residual coefficients of the chiral expansion of Equation (4.1), to obtain the scale-independent coefficients $c_i$. Though both the $a_i^\Lambda$ coefficients and the $b_i^\Lambda$ coefficients are scale-dependent, adding them together at each order results in a scale-independent coefficient. These are the renormalized

coefficients $c_i$. Explicitly:

$$c_0 = a_0^\Lambda + b_0^{\Lambda,N} + b_0^{\Lambda,\Delta}, \tag{4.9}$$

$$c_2 = a_2^\Lambda + b_2^{\Lambda,N} + b_2^{\Lambda,\Delta} + b_2^{\Lambda,t'}, \tag{4.10}$$

$$c_4 = a_4^\Lambda + b_4^{\Lambda,N} + b_4^{\Lambda,\Delta} + b_4^{\Lambda,t'}, \text{ etc.} \tag{4.11}$$

This is simply a slight generalization from the worked example in Section 3.3.4. Dimensional analysis reveals that the coefficients $b_i^\Lambda$ are proportional to $\Lambda^{(3-i)}$. Thus it can be realized that as the cutoff scale $\Lambda$ tends to infinity, the result from DR, as described in Section 3.3.3, is recovered. At any finite $\Lambda$, a partial resummation of higher-order terms is introduced. Previous studies indicate that extrapolation results show very little sensitivity to the precise functional form of the regulator [LTY04].

A modification is now made to the integrals of Equations (4.3) through (4.8), by subtracting $b_i^\Lambda$ terms from their Taylor expansion, thus absorbing them into the corresponding low-energy coefficients $c_i$. This achieves the renormalization to a chosen chiral order. In this case, only the low-energy coefficients $c_0$ and $c_2$ will be analyzed. The amplitudes for each process are thus altered:

$$\tilde{\Sigma}_N(m_\pi^2;\Lambda) = \frac{\chi_N}{2\pi^2} \int d^3k \frac{k^2 u^2(k;\Lambda)}{k^2 + m_\pi^2} - b_0^{\Lambda,N} - b_2^{\Lambda,N} m_\pi^2 \tag{4.12}$$

$$= \chi_N m_\pi^3 + b_4^{\Lambda,N} m_\pi^4 + O(m_\pi^5), \tag{4.13}$$

$$\tilde{\Sigma}_\Delta(m_\pi^2;\Lambda) = \frac{\chi_\Delta}{2\pi^2} \int d^3k \frac{k^2 u^2(k;\Lambda)}{\omega(k)(\Delta + \omega(k))}$$
$$- b_0^{\Lambda,\Delta} - b_2^{\Lambda,\Delta} m_\pi^2 \tag{4.14}$$

$$= b_4^{\Lambda,\Delta} m_\pi^4 - \frac{3}{4\pi\Delta}\chi_\Delta m_\pi^4 \log\frac{m_\pi}{\mu} + O(m_\pi^5), \tag{4.15}$$

$$\tilde{\Sigma}_{tad}(m_\pi^2;\Lambda) = c_2 m_\pi^2 \left( \frac{\chi_t}{4\pi} \int d^3k \frac{2u^2(k;\Lambda)}{\omega(k)} - b_2^{\Lambda,t} \right) \tag{4.16}$$

$$= c_2 m_\pi^2 \left( b_4^{\Lambda,t} m_\pi^2 + \chi_t m_\pi^2 \log \frac{m_\pi}{\mu} + O(m_\pi^5) \right) \tag{4.17}$$

$$= c_2 m_\pi^2 \tilde{\sigma}_{tad}(m_\pi^2;\Lambda). \tag{4.18}$$

Note that the coefficient of the tadpole amplitude contains the renormalized low-energy coefficient $c_2$. This is because the same coefficient $c_2$ from the chiral expansion occurs in the tadpole Lagrangian in Equation (3.72). The tilde ($\tilde{\ }$) denotes that the integrals are written out in renormalized form to chiral order $O(m_\pi^2)$. As the $b_i^\Lambda$ coefficients are regulator and scale-dependent, the subtraction reshuffles this dependence into higher-order terms. The coefficients $a_0^\Lambda$ and $a_2^\Lambda$ of the analytic terms in the chiral expansion in Equation (4.2) automatically become the scale-independent renormalized coefficients $c_0$ and $c_2$.

With the renormalized integrals specified, the finite-range regularization (FRR) modified version of the chiral expansion in Equation (4.2) takes the form:

$$M_N = c_0 + c_2 m_\pi^2 (1 + \tilde{\sigma}_{tad}(m_\pi^2,\Lambda)) + a_4^\Lambda m_\pi^4 + \tilde{\Sigma}_N(m_\pi^2,\Lambda) + \tilde{\Sigma}_\Delta(m_\pi^2,\Lambda). \tag{4.19}$$

The $a_4^\Lambda$ term is left in unrenormalized form for simplicity. Indeed, the coefficient $b_4^\Lambda$ can be evaluated by expanding out corresponding loop integrals, such as in Reference [YLT03]. However, the focus here is on the behaviour of $c_0$ and $c_2$.

### 4.1.3   The Sigma Term

In addition to the mass of the nucleon in the chiral limit $c_0$, the low-energy constant (LEC) $c_2$ corresponding to the tadpole vertex is of interest phenomenologically because, by inspection of Equation (3.72), it is a measure of the explicit chiral symmetry breaking of the relevant flavour symmetry group. That is, a sigma term can be defined for the light quarks up and down, and the explicit breaking of the group $SU(2)_V \otimes SU(2)_A$ may be investigated. In order to obtain a value for the sigma term relating to the heavier strange quark, $\chi$EFT has been used to study the explicit break-

ing of the baryon octet representation of SU(3) [Gas81, NK87, BM97, YT10b].

It can be seen that the term $c_2 m_q$, and higher-order terms in the nucleon mass expansion formula of Equation (4.2), will disappear if the chiral symmetry breaking quark mass is zero. To investigate this, one can consider how the QCD Hamiltonian behaves under commutation with the three-component axial charge operator of flavour SU(2). If the symmetry were unbroken, all quantities $Q_A^i |0\rangle$ would vanish, so the commutator $[Q_A^i, \mathcal{H}_{QCD}]$ would also vanish. In the more general case, consider two applications of the commutator, which yield the symmetry breaking mass term $\mathcal{H}_{sb}$ from the total Hamiltonian. This defines the pion-nucleon sigma term [CD71, LTW00, WLT00, HMRW06, YT10b]:

$$\sigma_{\pi N} = \frac{1}{3} \langle N | [Q_A^i, [Q_A^i, \mathcal{H}_{QCD}]] | N \rangle \tag{4.20}$$

$$= \langle N | (m_u \bar{u}u + m_d \bar{d}d) | N \rangle = \langle N | \mathcal{H}_{sb} | N \rangle . \tag{4.21}$$

Under the simplification of mass degeneracy between quark fields (which is approximately true under flavour SU(2)), one can apply the Feynman$-$Hellmann Theorem [Fey39] and recover the important result for small $m_\pi^2$:

$$\sigma_{\pi N} = m_q \frac{\partial M_N}{\partial m_q} = c_2 m_\pi^2 + O(m_\pi^{5/2}) . \tag{4.22}$$

That is, the value of the sigma term is dominated by the leading-order term with coefficient $c_2$. The violation of this axial symmetry is therefore important for understanding the behaviour of hadrons, because a non-zero sigma term affects the structure of the interaction between hadrons and the meson cloud which surrounds them, and provides a small, but not statistically insignificant contribution to the total mass of the hadron.

The standard result for the sigma term using SU(2) $\chi$PT, incorporating meson loop corrections, is: $\Sigma_{\pi N} = 35 \pm 5$ MeV [Gas81]. By analyzing data from $\pi p$ and $\pi\pi$ scattering experiments [Höh83], an early analysis by Gasser suggests a value of $\Sigma_{\pi N} = 45 \pm 8$ MeV [GLS91]. The currently accepted value of the sigma term, due to the work of Koch, is larger than the theoretical value: $\Sigma_{\pi N} = 64 \pm 8$ MeV [KP80,

Koc82]. A more recent analysis of the experimental data by Pavan, incorporating a partial wave and dispersion relation analysis, suggests an even higher value of $\Sigma_{\pi N} = 79 \pm 7$ MeV [PSWA02]. In contrast, calculations from two-flavour dynamical quark lattice QCD comparatively underestimate the value of the sigma term. In a study by Güsken, it was found that $\Sigma_{\pi N} = 18 \pm 5$ MeV, by direct calculation of the scalar matrix element in Equation (4.21) [G$^+$99]. This apparently low value for the sigma term was found to be a consequence of its sensitivity to chiral extrapolation, and large pion masses (above 500 MeV) were used in the extrapolation [LTW00, YT10b].

### 4.1.4   Scheme-Independent Coefficients

The chiral coefficients $\chi_N$, $\chi_\Delta$ and $\chi_t$ for each integral are defined in terms of the pion decay constant, which is taken to be $f_\pi = 92.4$ MeV, and the axial coupling parameters $D$, $F$ and $\mathcal{C}$ which couple the baryons to the pion field, as shown in the Lagrangian $\mathcal{L}^{(1)}_{\text{oct\&dec}}$ of Equation (3.68). The coeffcient $c_2$, which occurs in the tadpole loop integral of Equations (4.16) through (4.18), is a combination of the LECs $\sigma_m$, $D_M$ and $F_M$, which occur in the tadpole Lagrangian of Equation (3.70). Though $c_2$ is treated as a fit parameter, the phenomenological values for the $D$, $F$ and $\mathcal{C}$ couplings are used, applying the SU(6) flavour-symmetry relations [Jen92, Leb95] to yield $\mathcal{C} = -2D$, $F = \frac{2}{3}D$ and the value $D = 0.76$:

$$\chi_N = -\frac{3}{32\pi f_\pi^2}(D+F)^2,\tag{4.23}$$

$$\chi_\Delta = -\frac{3}{32\pi f_\pi^2}\frac{8}{9}\mathcal{C}^2,\tag{4.24}$$

$$\chi_t = -\frac{3}{16\pi^2 f_\pi^2}.\tag{4.25}$$

These coefficients are constant and remain unaffected by renormalization scale or finite-volume effects. Ultimately, one may try to determine these directly from lattice simulation results. Nevertheless, because of the limited number of lattice simulation results currently available, this analysis will focus on the determination of $c_0$, $c_2$ and

the nucleon mass $M_N$.

## 4.1.5   Finite-Volume Effects

In lattice QCD, the introduction of finite-volume effects become significant for small box sizes. The expansion parameter $1/L$ contributing to finite-volume effects should be of the same order of magnitude as the momenta for the perturbation scheme to remain valid. If $L$ is small, the exponential factor $e^{-m_\pi L}$ no longer suppresses the finite-volume corrections [BNS10]. As a general rule, the characteristic dimensionless quantity $m_\pi L$ specifies the $\varepsilon$-regime through the condition $m_\pi L \leq 1$ [Han90, HL91, HL90]. This is a breakdown region in $\chi$PT, since divergences in the leading-order pion contributions cannot be approximated by standard perturbative techniques [BNS10].

Since the results of lattice simulations reflect the presence of discrete momentum values associated with the finite volume of the lattices, the formalism of $\chi$EFT must also take into account these finite-volume effects. $\chi$EFT is ideally suited for examining finite-volume effects, because of its accurate characterization of the dominant infrared physics. In order to accommodate the effect of the finite volume, the continuous loop integrals occurring in the meson loop calculations in an infinite volume are transformed into a sum over discrete momentum values. The difference between a loop sum and its corresponding loop integral is defined to be the finite-volume correction, which should vanish for all integrals as $m_\pi L$ becomes large [GL88, Bea04b]. While Equation (4.19) is useful in describing the pion mass evolution of the nucleon mass, for the consideration of lattice QCD results, one also needs to incorporate corrections to allow for the finite-volume nature of the numerical simulations. As the pion is the lightest degree of freedom in the system, it is the leading-order pion loop effects that are most sensitive to the periodic boundary conditions. The corrections can be determined by considering the transformation of each loop integral in Equations (4.12), (4.14) and (4.16) into a discrete sum for a given lattice size. The three-dimensional integrals can be replaced by summations over all possible momentum values [AAL+06]. It is useful to define the finite-volume correction to the

loop integral, by convention, by subtracting the integral from the sum quantity. This technique will be used to correct for finite-volume effects encountered in Chapters 4 through 7.

The finite-volume correction $\delta^{\mathrm{FVC}}$ can be written as the difference between the finite sum and the integral:

$$\delta_i^{\mathrm{FVC}}(m_\pi^2,\Lambda) = \frac{\chi_i}{2\pi^2}\left[\frac{(2\pi)^3}{L_x L_y L_z}\sum_{k_x,k_y,k_z} I_i(\vec{k},m_\pi^2,\Lambda) - \int \mathrm{d}^3k\, I_i(\vec{k},m_\pi^2,\Lambda)\right], \qquad (4.26)$$

where $i = N,\Delta$, and the integrands are denoted $I_i(\vec{k},m_\pi^2,\Lambda)$. The finite-volume corrections to the tadpole contribution are not considered in this investigation because of subtleties in their behaviour at large $m_\pi$. Details regarding the finite-volume behaviour of the tadpole amplitude are discussed in Appendix B.3, and a more general discussion of its convergence properties occurs in Section 8.2. By adding the relevant finite-volume correction to each loop contribution, the finite-volume nucleon mass can be parameterized:

$$M_N^V = c_0 + c_2 m_\pi^2(1+\tilde{\sigma}_{tad}) + a_4^\Lambda m_\pi^4 + (\tilde{\Sigma}_N + \delta_N^{\mathrm{FVC}}) + (\tilde{\Sigma}_\Delta + \delta_\Delta^{\mathrm{FVC}}). \qquad (4.27)$$

It is also shown that the finite-volume corrections are independent of the regularization scale $\Lambda$ in this domain. In Figures 4.4 and 4.6, the scale-dependence of the finite-volume corrections is shown for a dipole regulator (from Equation (3.105) in Chapter 3) and a 2.9 fm box (the same box size used for the PACS-CS data [A$^+$09]). It is of note that choosing $\Lambda$ too small suppresses the very infrared physics that one is trying to describe. Thus, caution should be exercised in choosing a suitable value of $\Lambda$. Figures 4.5 and 4.7 show the behaviour of the finite-volume correction for a 4.0 fm box, and the corrections are much smaller, as expected.

For large $\Lambda$, the finite-volume corrections, displayed in Figures 4.4 through 4.7, saturate to a fixed value. Provided that $\Lambda \gtrsim 0.8$ GeV, the estimated finite-volume corrections are stable for light pion masses. In order to preserve the scale-independence of the finite-volume corrections, their asymptotic result will be used. This approach has been demonstrated to be successful in previous studies [AK$^+$04]. Numeri-
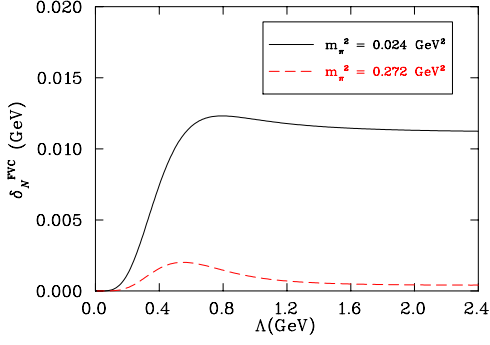
Figure 4.4: Behaviour of the finite-volume corrections $\delta_N^{\mathrm{FVC}}$ vs. $\Lambda$ on a 2.9 fm box using a dipole regulator. Results for two different values of $m_\pi^2$ are shown.
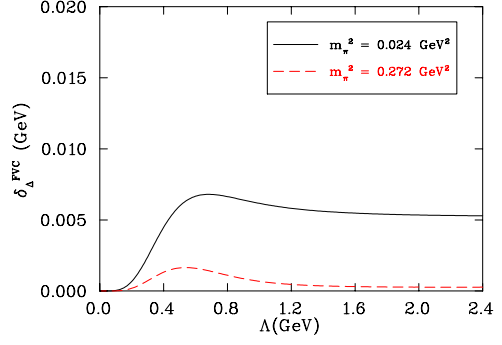


Figure 4.6: Behaviour of finite-volume corrections $\delta_\Delta^{\mathrm{FVC}}$ vs. $\Lambda$ on a 2.9 fm box using a dipole regulator. Results for two different values of $m_\pi^2$ are shown.
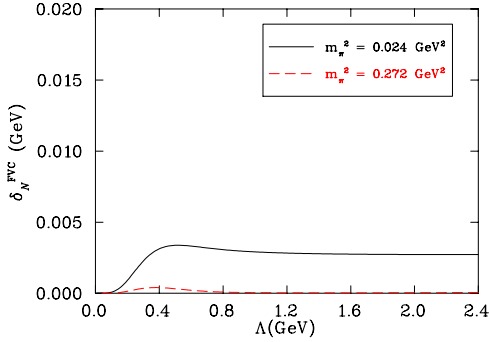


Figure 4.5: Behaviour of finite-volume corrections $\delta_N^{\mathrm{FVC}}$ vs. $\Lambda$ on a 4.0 fm box using a dipole regulator. Results for two different values of $m_\pi^2$ are shown.
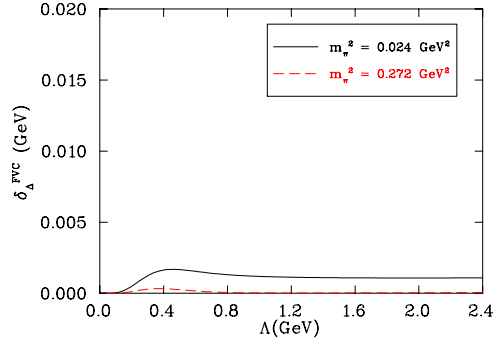


Figure 4.7: Behaviour of finite-volume corrections $\delta_\Delta^{\mathrm{FVC}}$ vs. $\Lambda$ on a 4.0 fm box using a dipole regulator. Results for two different values of $m_\pi^2$ are shown.

cally, this is achieved by evaluating the finite-volume corrections with a parameter, $\Lambda' = 2.0\,\mathrm{GeV}$, $\delta_i^{\mathrm{FVC}} = \delta_i^{\mathrm{FVC}}(\Lambda')$. It should be noted that this is equivalent to the more algebraic approach outlined by Beane [Bea04b].

## 4.2    The Intrinsic Scale: An Example by Construction

This $\chi$EFT extrapolation scheme to order $O(m_\pi^4 \log m_\pi)$ will be used in conjunction with lattice QCD data from JLQCD [O$^+$08], PACS-CS [A$^+$09] and CP-PACS

[AK$^+$02] to predict the nucleon mass for any value of $m_\pi^2$. The full set of data from each of these collaborations is listed in Appendix C, Tables C.1 through C.3. The JLQCD data were generated using overlap fermions in two-flavor QCD, but the lattice box size for each data point is $\sim 1.9$ fm, smaller than the other two data sets. The PACS-CS data were generated using non-perturbatively $O(a)$-improved Wilson quark action at a lattice box size of $\sim 2.9$ fm, but the data set only contains five data points and a large statistical error in the smallest $m_\pi^2$ point. The CP-PACS data were generated using a mean field improved clover quark action on lattice box sizes for each data point varying from $\sim 2.2$ fm to $\sim 2.8$ fm.

The lattice data used in this analysis will be used to extrapolate $M_N$ to the physical point by taking into account the relevant curvature from the loop integrals in Equations (4.13), (4.15) and (4.17). As an example, a regularization scale of $\Lambda = 1.0$ GeV was chosen for Figures 4.8 through 4.10, where the finite-volume corrected effective field theory appears concordant with previous QCDSF-UKQCD results [AK$^+$04]. An extrapolation or interpolation is achieved by subtracting the finite-volume loop integral contributions from each data point and then fitting the result to obtain the coefficients $c_0$, $c_2$ and $a_4^\Lambda$ using Equation (4.19). The finite- or infinite-volume loop integrals are then added back at any desired value of $m_\pi^2$.

If the regularization scale is altered from the choice $\Lambda = 1.0$ GeV, the extrapolation curve also changes. This signifies a scheme-dependence in the result due to using lattice QCD data beyond the PCR. To demonstrate this, consider the infinite-volume extrapolation of the CP-PACS data, as shown in Figure 4.11. Figure 4.11 also shows that the curves overlap exactly when $m_\pi^2$ is large, where the lattice data reside, and they diverge as the chiral regime is approached.

Consider an insightful scenario, whereby a set of ideal 'pseudodata' with known low-energy coefficients is produced, using the formula from Equation (4.27). A particular regularization scale is selected and a dense and precise pseudodata set is generated, which smoothly connects with the lattice simulation results. In this case, the pseudodata are converted to infinite-volume results in order to ensure that the following analysis is not simply a consequence of finite-volume effects. If all the
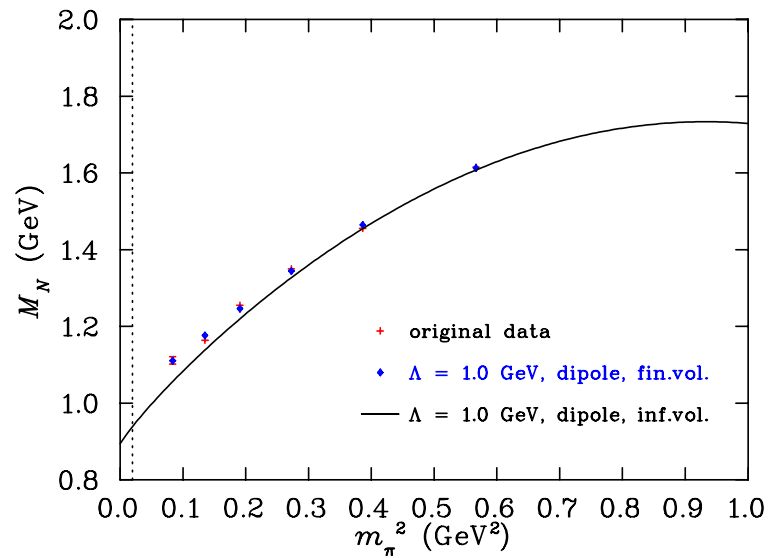
**Figure 4.8:** Example dipole extrapolation based on JLQCD data [O$^+$08], box size: 1.9 fm.
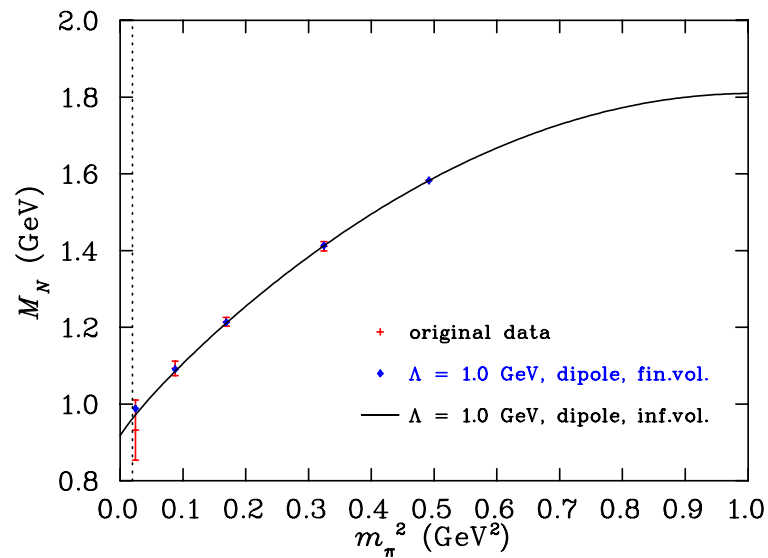


**Figure 4.9:** Example dipole extrapolation based on PACS-CS data [A$^+$09], box size: 2.9 fm.
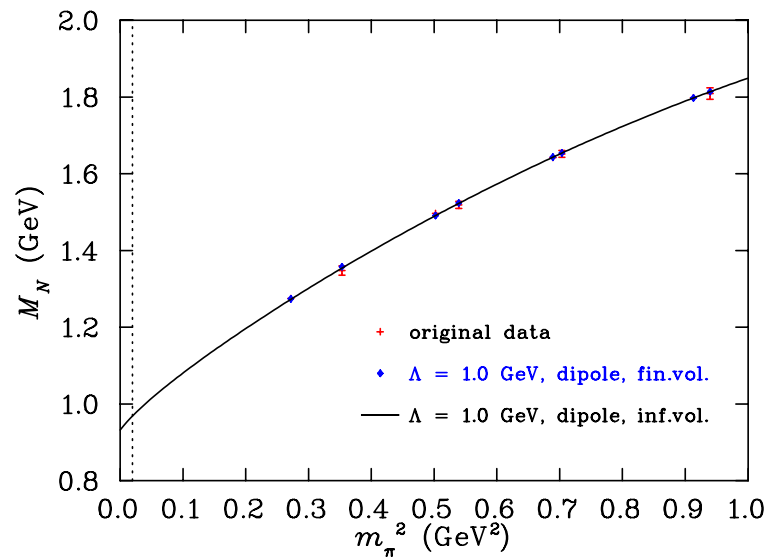


**Figure 4.10:** Example dipole extrapolation based on CP-PACS data [AK$^+$02], lattice sizes: $2.3 - 2.8$ fm.
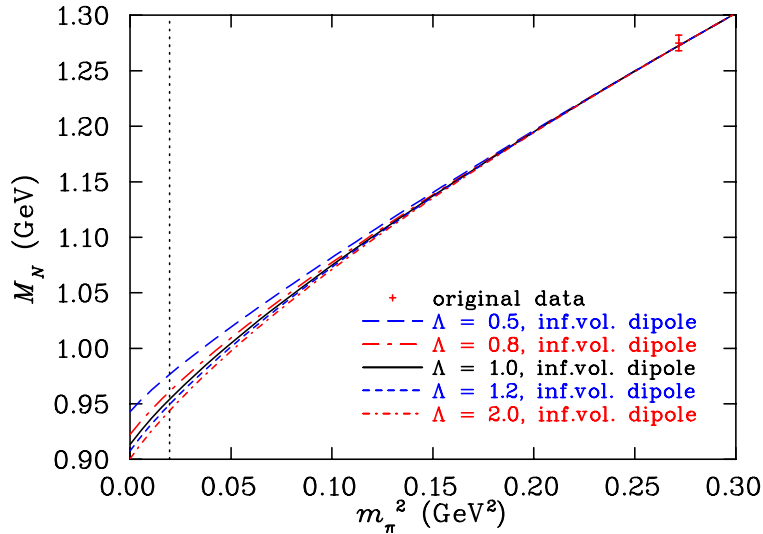
**Figure 4.11:** Close zoom of the regulator-dependence for dipole extrapolation based on CP-PACS data. Only the data point corresponding to the smallest $m_\pi^2$ value is shown at this scale.

data considered lie within the PCR then the choice of regularization scale is irrelevant, and the finite-range regularized chiral expansion is mathematically equivalent to scale-invariant renormalization schemes, including DR. This scenario will form the basis of the investigation of the PCR, and ultimately, will lead to determining the existence of an intrinsic scale hidden within the lattice QCD simulation results.

The pseudodata are produced by performing an extrapolation such as shown in Figures 4.8 through 4.10. The difference is that 100 infinite-volume extrapolation points are produced close to the chiral regime. The exercise is to treat these pseudodata as if they were lattice QCD data. Clearly, a regularization scheme must be chosen in generating the pseudodata. In this case, a dipole regulator was chosen and pseudodata were created at $\Lambda_c = 1.0$ GeV.

The regularization-dependence of the extrapolation is characterized by the scale-dependence of the coefficients $c_i$. These coefficients are obtained from fitting the pseudodata. Consider how $c_0$ and $c_2$ behave when analyzed with a variety of regularization scales in Figures 4.12 and 4.13. By using infinite-volume pseudodata, one eliminates the concern that the variation in $c_i$ with respect to $\Lambda$ is merely a finite-volume artefact.

Three pseudodata sets are compared, each with different upper bounds on the
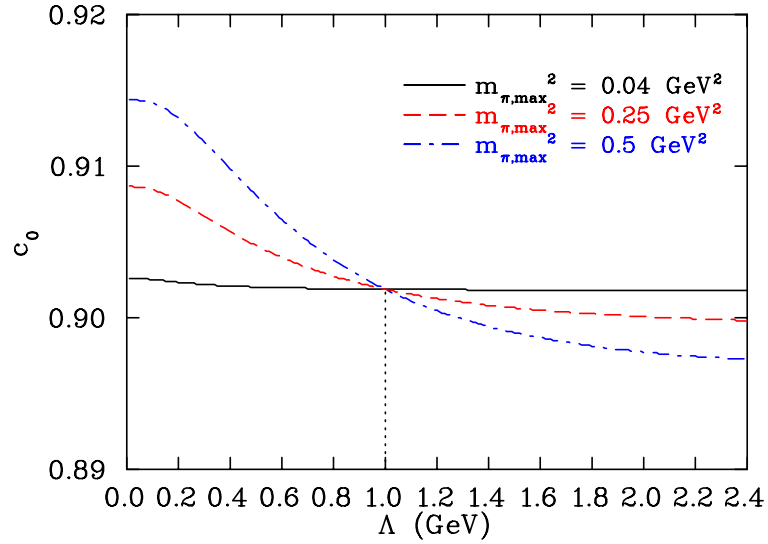
**Figure 4.12:**   Behaviour of $c_0$ vs. regularization scale $\Lambda$, based on infinite-volume pseudodata created with a dipole regulator at $\Lambda_c = 1.0$ GeV (based on lightest four data points from PACS-CS). Each curve uses pseudodata with a different upper value of pion mass $m^2_{\pi,\mathrm{max}}$.
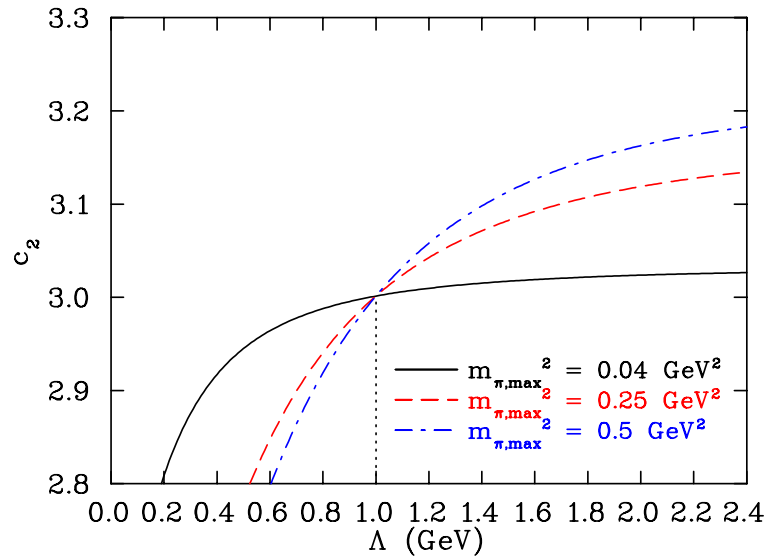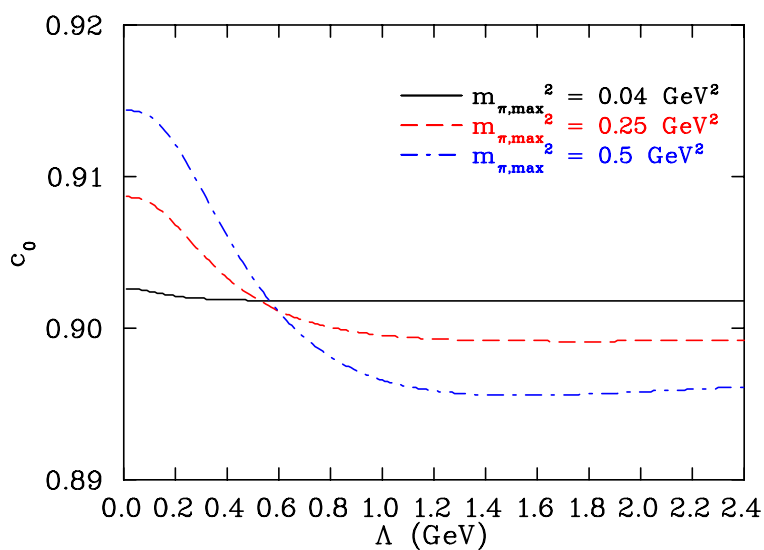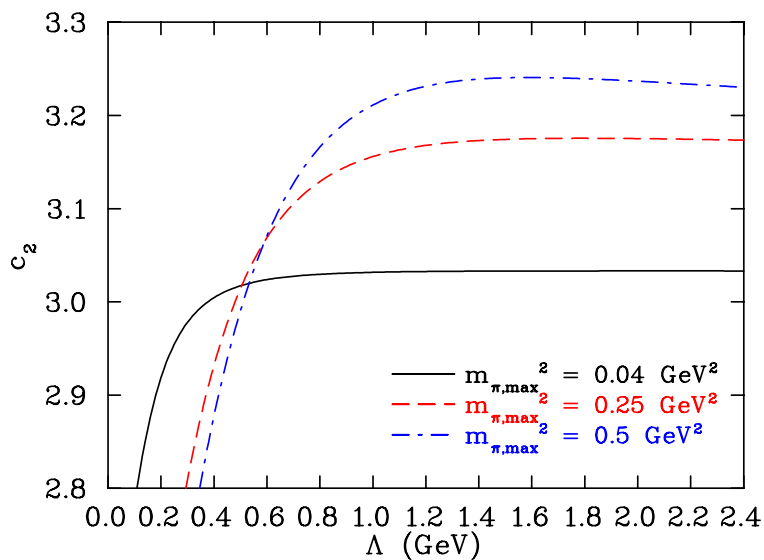


**Figure 4.13:**   Behaviour of $c_2$ vs. $\Lambda$, based on infinite-volume pseudodata created with a dipole regulator at $\Lambda_c = 1.0$ GeV (based on lightest four data points from PACS-CS).

range of $m_\pi^2$ considered in the fit. An increasing regulator-dependence in $c_0$ and $c_2$ is seen as the data extend outside the PCR. In Figures 4.12 and 4.13, the behaviour of the fit parameters $c_0$ and $c_2$, respectively, are shown as functions of the regularization scale $\Lambda$ for different values of $m_{\pi,\mathrm{max}}^2$. A steep line indicates a strong scheme-dependence in the result, and this occurs for data samples extending far outside the PCR. Scheme-independence will appear as a horizontal line, as is apparent for $m_{\pi,\mathrm{max}}^2 < 0.04\,\mathrm{GeV}^2$, in Figures 4.12 and 4.13. This indicates that the pseudodata lie within the PCR.

Note that in both figures all three curves (corresponding to different values of $m_{\pi,\mathrm{max}}^2$) arrive at stable values for $c_0$ and $c_2$ on the right-hand side of the plot, corresponding to large $\Lambda$. To read off the values of $c_0$ and $c_2$ for large $\Lambda$ is tempting, but this does not yield the correct values of $c_0$ and $c_2$, which are known by construction. The correct values of $c_0$ and $c_2$ are recovered at $\Lambda = 1.0\,\mathrm{GeV}$.

The analysis of the pseudodata in Figures 4.12 and 4.13 shows that even as the value of $m_{\pi,\mathrm{max}}^2$ is changed, the correct value of $c_0$ is recovered at exactly $\Lambda = \Lambda_\mathrm{c}$, where the curves intersect. The same value of $\Lambda$ for the intersection point is obtained by analyzing $c_2$. This suggests that when considering lattice QCD results extending outside the PCR, there may be an optimal finite-range cutoff. Physically, such a cutoff would be associated with an intrinsic scale reflecting the finite size of the source of the pion dressings. Mathematically, this optimal cutoff is reflected by an independence of the fit parameters on $m_{\pi,\mathrm{max}}^2$.

By analyzing the pseudodata with a different regulator, for example, a triple-dipole regulator, Figures 4.14 and 4.15 show that the scale of the intersection is no longer a clear point, but a cluster centred about 0.5 to 0.6 GeV. The triple-dipole will of course predict a different optimal scale, since the shape of the regulator is different from that of the dipole used to create the pseudodata. The essential point of this exercise is that clustering of curve intersections identifies a preferred renormalization scale that allows one to recover the correct low-energy coefficients. In this case, the crossing of the dash and dot-dash curves (from fitting) clearly identifies $\Lambda_\mathrm{trip}^\mathrm{scale} = 0.6$ GeV as a preferred regularization scale, which reflects the intrinsic scale used to

| param. | input | $\Lambda_{\text{trip}}^{\text{scale}} = 0.6$ $m_{\pi,\text{max}}^2 = 0.25$ | $\Lambda_{\text{trip}}^{\text{scale}} = 0.6$ $m_{\pi,\text{max}}^2 = 0.5$ | $\Lambda_{\text{trip}} = 2.4$ $m_{\pi,\text{max}}^2 = 0.25$ | $\Lambda_{\text{trip}} = 2.4$ $m_{\pi,\text{max}}^2 = 0.5$ |
|---|---|---|---|---|---|
| $c_0$ | 0.902 | 0.901 | 0.902 | 0.899 | 0.896 |
| $c_2$ | 3.00 | 3.07 | 3.07 | 3.17 | 3.23 |

Table 4.1: A comparison of the parameters $c_0$ (GeV) and $c_2$ (GeV$^{-1}$) at their input value (pseudodata created with a dipole at $\Lambda_c = 1.0$ GeV) with the values when analysed with a triple-dipole regulator. Different values of $\Lambda_{\text{trip}}$ (GeV) and $m_{\pi,\text{max}}^2$ (GeV$^2$) are chosen to demonstrate the scheme-dependence of $c_0$ and $c_2$ for data extending outside the PCR. Note: the values of $c_0$ and $c_2$ are calculated from an ideal model and thus they are exact; there are no statistical uncertainties.

create the data. Table 4.1 compares the values for $c_0$ and $c_2$ recovered in this analysis for two different regularization scales: the preferred value $\Lambda_{\text{trip}}^{\text{scale}} = 0.6$ GeV, and a large value $\Lambda_{\text{trip}} = 2.4$ GeV reflecting the asymptotic result recovered from DR. The input values of $c_0$ and $c_2$ used to create the pseudodata are also indicated.

## 4.2.1   Lower Bounds for the Regularization Scale

Figures 4.13 and 4.15 clearly indicate that the finite-range renormalization scheme breaks down if the FRR scale is too small. This is because $\Lambda$ must be large enough to include the chiral physics being studied. The exact value of a sensible lower bound in the FRR scale will depend on the functional form chosen as the regulator.

Figure 4.13 shows that the renormalization for $c_2$ breaks down for small values of $\Lambda$. FRR breaks down for a value of $\Lambda_{\text{dip}}$ much below 0.6 GeV, simply because the coefficients $b_i^{\Lambda}$ of the loop integral expansion in Equations (4.13), (4.15) and (4.17) are proportional to $\Lambda^{(3-i)}$. For higher-order terms with large $i$, the coefficients will become large when $\Lambda$ is small. In theory, these very large terms add up to zero, and so the limit $\Lambda \to 0$ amounts to neglecting the infrared physics of the hadron. In practice, the finite curvature and higher-order terms of the residual series are not large enough to cancel the small-$\Lambda$ behaviour of the $b_i^{\Lambda}$ coefficients, which dominate. This adversely affects the convergence properties of the chiral expansion. On the other hand, one obtains a residual series expansion with good convergence properties when $\Lambda$ reflects the intrinsic scale of the source of the pion dressings of the hadron

Figure 4.14:   Behaviour of $c_0$ vs. $\Lambda$, based on infinite-volume pseudodata created with a dipole regulator at $\Lambda_c = 1.0$ GeV but subsequently analyzed using a triple-dipole regulator.



Figure 4.15:   Behaviour of $c_2$ vs. $\Lambda$, based on infinite-volume pseudodata created with a dipole regulator at $\Lambda_c = 1.0$ GeV but subsequently analyzed using a triple-dipole regulator.

in question.

The pseudodata analysis provides a good indication of a lower bound for $\Lambda$ using a dipole regulator: $\Lambda_{\text{dip}} \gtrsim 0.6$ GeV. Similarly, Figure 4.15 suggests a lower bound for the triple-dipole regulator: $\Lambda_{\text{trip}} \gtrsim 0.3$ GeV. The same analysis can be repeated for the double-dipole regulator to obtain $\Lambda_{\text{doub}} \gtrsim 0.4$ GeV.

One can also estimate the lowest reasonable value of $\Lambda$ by considering arguments from phenomenology. Based on the physical values of the sigma commutator and the nucleon mass, a pion mass of $m_\pi \approx 0.5$ GeV is a suitable upper bound for the radius of convergence [BHLO02, YHL09, YT10a]. This follows from the estimate of the two-flavour pion-nucleon sigma term due to Gasser [GLS91]. Using the Gell-Mann$-$Oakes$-$Renner Relation $m_q \propto m_\pi^2$:

$$\Sigma_{\pi N} = m_\pi^2 \frac{\partial M_N}{\partial m_\pi^2} = c_2 m_\pi^2 + \chi_N m_\pi^3 + c_4 m_\pi^4 + O(m_\pi^5) \approx 45 \,\text{MeV} \,. \tag{4.28}$$

For good convergence, it is expected that the sigma term is dominated by the leading-order $c_2$ term. The second and third terms in the expansion are as large as the leading-order $c_2$ term for $m_\pi \approx 0.5$ GeV. Therefore, in order to maintain good convergence of the chiral expansion whilst ensuring the inclusion of important contributions to the chiral physics, one should choose a scale $\Lambda_{\text{sharp}} \sim 0.5$ GeV for a sharp cutoff (step function) regulator. To compare this estimate for the sharp cutoff to that of dipole-like regulators, one can calculate the regularization scale required such that $u_n^2(k;\Lambda) = 1/2$ when the momentum takes the energy scale of $\Lambda_{\text{sharp}}$. This results in a rough estimate for a sensible value for the dipole, double-dipole and triple-dipole regulators. These values are $\Lambda_{\text{dip}} \sim 1.1$ GeV, $\Lambda_{\text{doub}} \sim 0.76$ GeV and $\Lambda_{\text{trip}} \sim 0.66$ GeV, respectively.

In the forthcoming chapter, a range of regularization scales will be considered, and the intersections of the curves for the low-energy coefficients will be used to construct fits that include data sets that extend outside the PCR. This is done in order to identify the presence of an intrinsic scale for the pion source and an associated preferred regularization scale.

# Chapter 5

# Results for the Mass of the Nucleon

*"The datum is a classical property concerning only the instrument; it is the expression of a fact. The result concerns a property of the quantum world. The datum is an essential intermediary for reaching a result."* (Omnès, R. 2002. *Quantum Philosophy: Understanding and Interpreting Contemporary Science* p.209) [Omn02]

This quotation, and those introduced in Chapters 6 to 8, contain an argument that links data, results, theory and experience.

The aim of this chapter is to apply an analysis that allows a reliable extrapolation of the nucleon mass to the physical point by obtaining an optimal regularization scale, using lattice quantum chromodynamics (lattice QCD) simulation results. The identification of an optimal regularization scale, along with its associated systematic uncertainty, indicates the degree to which the lattice QCD simulation results extend beyond the power-counting regime (PCR). This quantifies and effectively handles the scheme-dependence of chiral extrapolations. Ultimately, the agreement among optimal regularization scales obtained from different simulation results indicates the existence of an intrinsic scale that characterizes the interaction between the pion cloud and the core of the nucleon. Such an agreement will be demonstrated through the results in this chapter, and Chapter 7. In Chapter 6, the procedure developed in this thesis for analyzing the renormalization flow of the low-energy coefficients, obtaining a possible intrinsic scale (or a range of acceptable regularization scales), and performing a robust chiral extrapolation will be tested.

In the previous Chapter, extrapolation of the lattice results was discussed in the context of finite-range regularized chiral effective field theory ($\chi$EFT). The scheme-dependence of the various extrapolations was analyzed. A method was developed for extracting an optimal finite-range regularization scale from ideal pseudodata. Since the pseudodata were generated at a known scale $\Lambda_c$, they contain an intrinsic scale by construction, and so it was demonstrated that an optimal finite-range regularization scale could be extracted from the pseudodata by analyzing the scale-dependence of the low-energy coefficients. This optimal scale was the same value as the intrinsic scale built into the pseudodata.

The pseudodata example leads the researcher to consider whether actual lattice QCD simulation results have an intrinsic cut-off scale embedded within them. That is, by analyzing lattice QCD data in the same way as the pseudodata, can a similar intersection point be obtained from the renormalization-scale flow of the low-energy coefficients? If so, it would indicate that the lattice data contain information regarding an optimal finite-range regularization scale, and thus provide evidence for the existence of an underlying intrinsic scale in the nucleon-pion interaction.

## 5.1    Evidence for an Intrinsic Scale in the Nucleon Mass

### 5.1.1    Renormalization Flow Analysis

Consider the mass of the nucleon as extrapolated from the results of lattice QCD simulations. The results for $c_0$ and $c_2$ as a function of the regularization scale $\Lambda$ are now presented for lattice QCD data from the collaborations: JLQCD, PACS-CS and CP-PACS. Initially, the chiral expansion, calculated to chiral order $O(m_\pi^3)$, should be used for fitting:

$$M_N = c_0 + c_2 m_\pi^2 (1 + \tilde{\sigma}_{tad}(m_\pi^2, \Lambda)) + \tilde{\Sigma}_N(m_\pi^2, \Lambda) + \tilde{\Sigma}_\Delta(m_\pi^2, \Lambda). \qquad (5.1)$$

Thus, the relevant fit parameters used in the extrapolation are $c_0$ and $c_2$ only. Results for the higher chiral order of $O(m_\pi^4 \log m_\pi)$ will be discussed in Section 5.1.3. The

resultant renormalization flows, using a dipole regulator, are shown in Figures 5.1 through 5.6; the results for the double-dipole case are shown in Figures 5.7 through 5.12; and the results for the triple-dipole are shown in Figures 5.13 through 5.18. On each plot of the renormalization flow in Figures 5.1 through 5.18 there are multiple curves, each corresponding to different values of the upper bound of the fit window, $m^2_{\pi,\max}$. A few example points are selected in Figures 5.1 through 5.18 to indicate the general size of the statistical error bars.

It should be noted that none of the curves in Figures 5.1 through 5.18 is flat to within 1% accuracy. All of the fits have lattice data included beyond the PCR. Clearly, there is a well-defined intersection point in each plot. Also, the value of $\Lambda$ at which the intersection point occurs is the same, even for different data sets, and for different $c_i$. The tight groupings of the curve crossings lend credence to the notion of an intrinsic scale that can be interpreted as a finite size of the source of the pion dressings of the nucleon. This is a central result of the analysis.

Using the method described in Chapter 4, the intersection point of the renormalization flow curves for different values of $m^2_{\pi,\max}$ is estimated from Figures 5.1 through 5.18. As an initial estimate, by inspection, a mean value for the optimal regularization scale of $\bar{\Lambda}^{\text{scale}}_{\text{dip}} \approx 1.3$ GeV was obtained for the dipole, a value of $\bar{\Lambda}^{\text{scale}}_{\text{doub}} \approx 1.0$ GeV was obtained for the double dipole, and a value of $\bar{\Lambda}^{\text{scale}}_{\text{trip}} \approx 0.9$ GeV was obtained for the triple-dipole. These values differ because the regulators have different shapes, as evident in Figure 3.1, and thus different values of $\Lambda^{\text{scale}}$ are required to create a similar suppression of large loop momenta. In order to determine an estimate of the systematic uncertainty in an extrapolation due to the choice of regularization scale $\Lambda^{\text{scale}}$, one should use a robust method for estimating the systematic uncertainty of $\Lambda^{\text{scale}}$ itself. In the following section, a chi-square-style analysis will be introduced to fulfill this requirement.

## 5.1.2  Analysis of Systematic Uncertainties

The optimal regularization scale $\Lambda^{\text{scale}}$ can be obtained from the renormalization flow curves using a chi-square-style analysis. In addition, the analysis will allow the
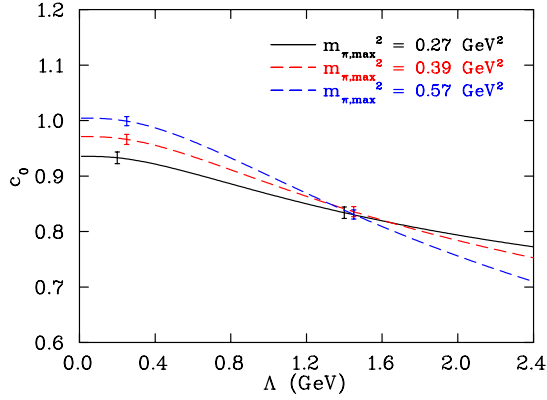
Figure 5.1:    Behaviour of $c_0$ vs. $\Lambda$, based on JLQCD data. The chiral expansion is taken to order $O(m_\pi^3)$ and a dipole regulator is used. A few points are selected to indicate the general size of the statistical error bars.
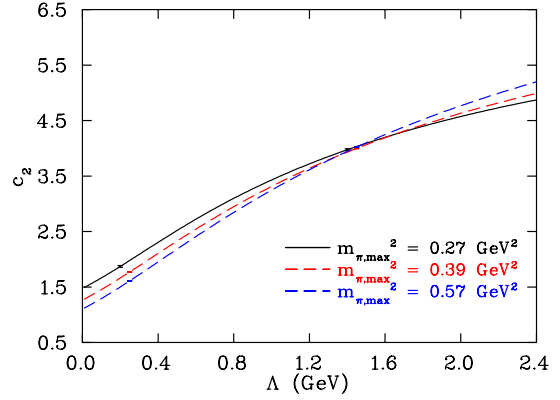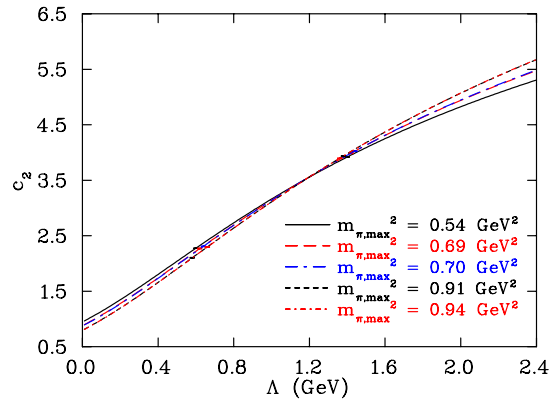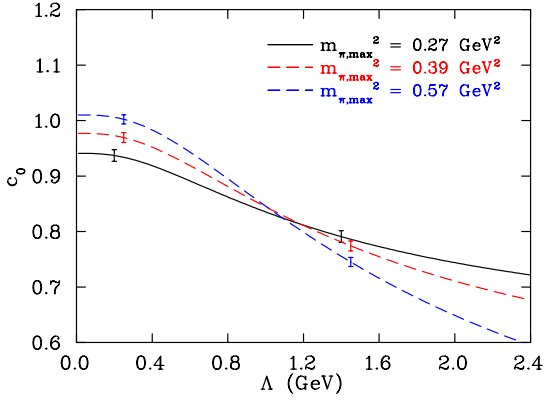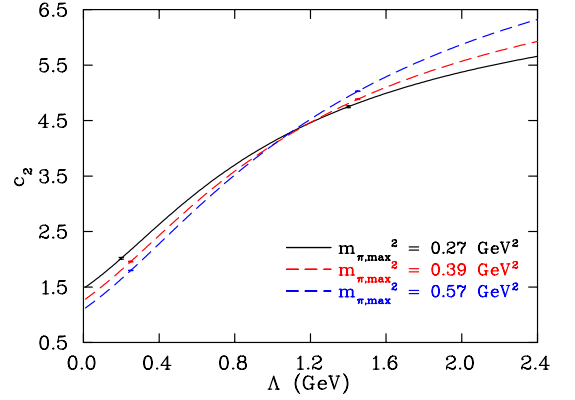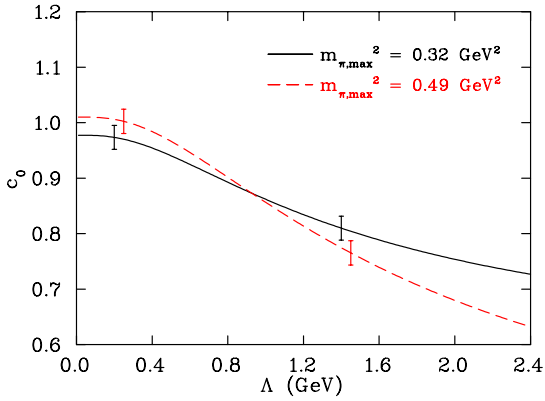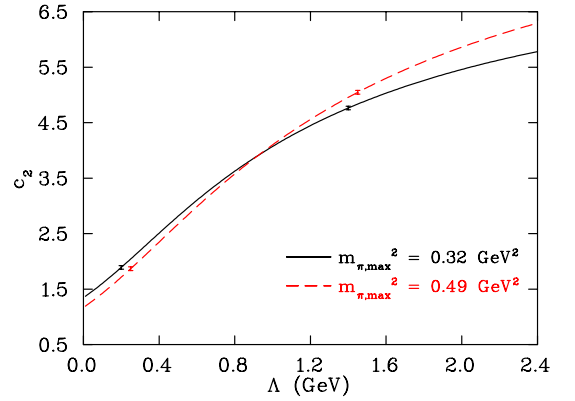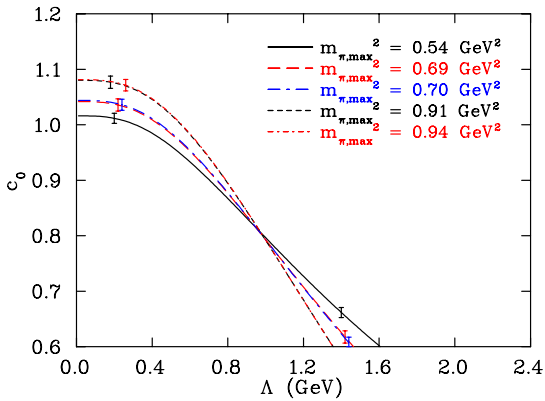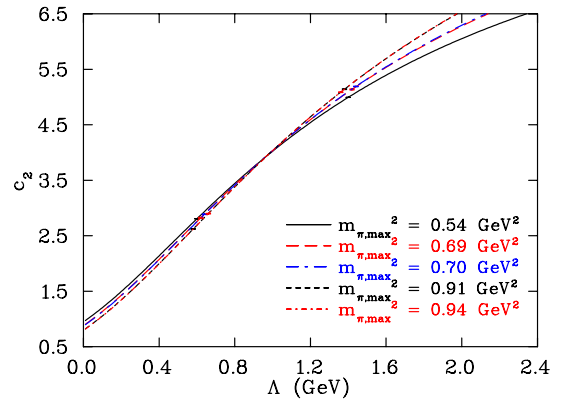


Figure 5.4:    Behaviour of $c_2$ vs. $\Lambda$, based on JLQCD data. The chiral expansion is taken to order $O(m_\pi^3)$ and a dipole regulator is used. A few points are selected to indicate the general size of the statistical error bars.
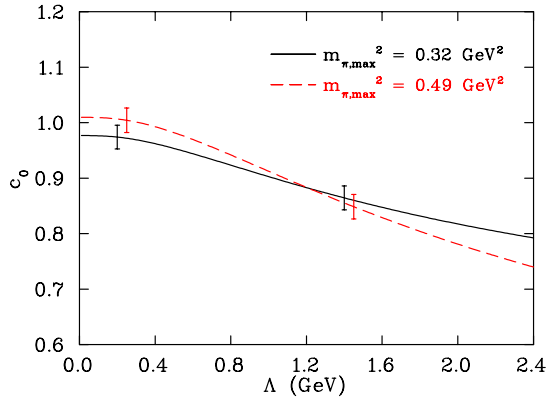


Figure 5.2:    Behaviour of $c_0$ vs. $\Lambda$, based on PACS-CS data. The chiral expansion is taken to order $O(m_\pi^3)$ and a dipole regulator is used. A few points are selected to indicate the general size of the statistical error bars.
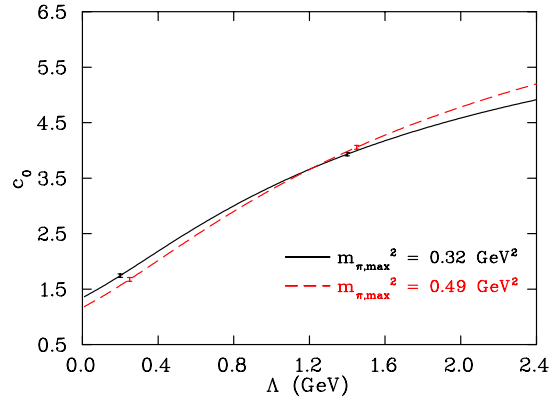


Figure 5.5:    Behaviour of $c_2$ vs. $\Lambda$, based on PACS-CS data. The chiral expansion is taken to order $O(m_\pi^3)$ and a dipole regulator is used. A few points are selected to indicate the general size of the statistical error bars.
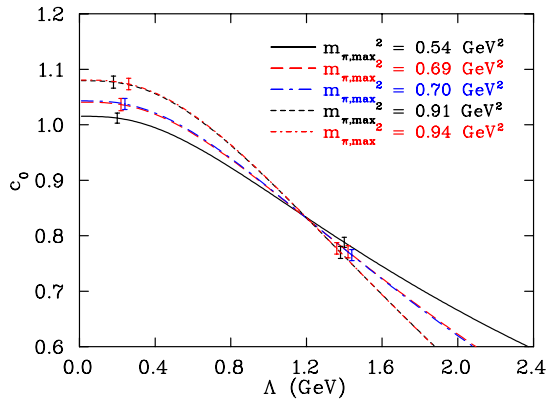


Figure 5.3:    Behaviour of $c_0$ vs. $\Lambda$, based on CP-PACS data. The chiral expansion is taken to order $O(m_\pi^3)$ and a dipole regulator is used. A few points are selected to indicate the general size of the statistical error bars.
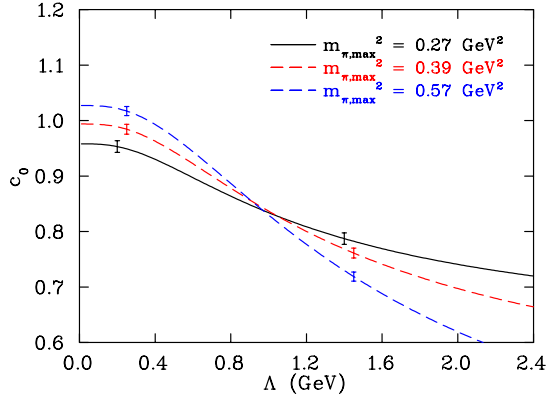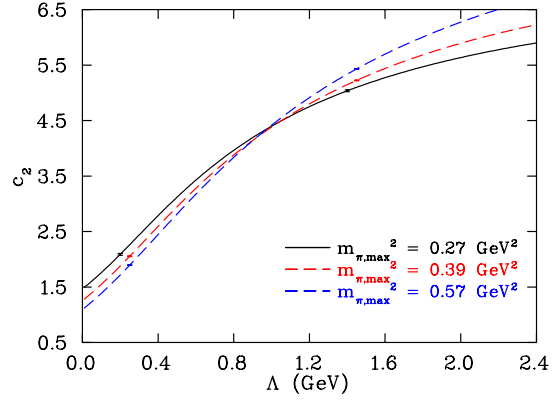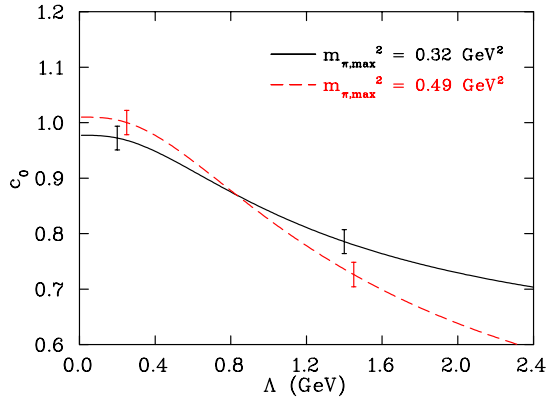


Figure 5.6:    Behaviour of $c_2$ vs. $\Lambda$, based on CP-PACS data. The chiral expansion is taken to order $O(m_\pi^3)$ and a dipole regulator is used. A few points are selected to indicate the general size of the statistical error bars.
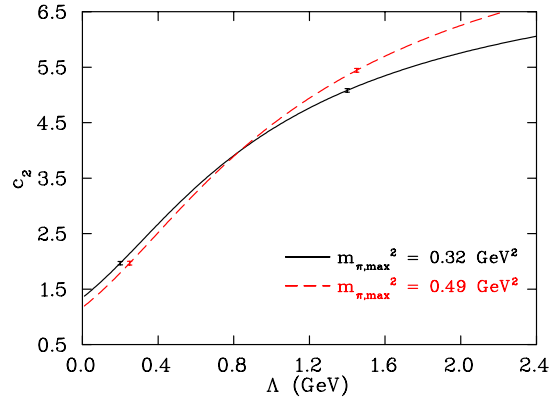
Figure 5.7:   Behaviour of $c_0$ vs. $\Lambda$, based on JLQCD data. The chiral expansion is taken to order $O(m_\pi^3)$ and a double-dipole regulator is used. A few points are selected to indicate the general size of the statistical error bars.



Figure 5.10:   Behaviour of $c_2$ vs. $\Lambda$, based on JLQCD data. The chiral expansion is taken to order $O(m_\pi^3)$ and a double-dipole regulator is used. A few points are selected to indicate the general size of the statistical error bars.
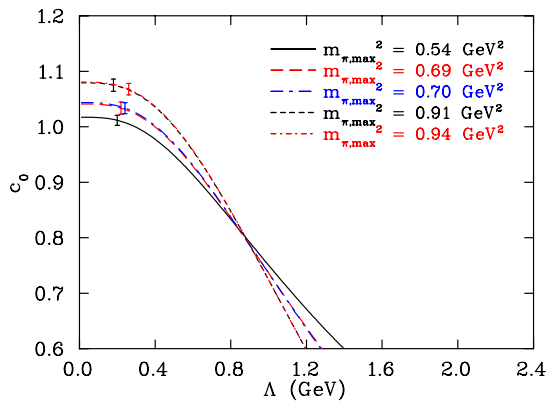


Figure 5.8:   Behaviour of $c_0$ vs. $\Lambda$, based on PACS-CS data. The chiral expansion is taken to order $O(m_\pi^3)$ and a double-dipole regulator is used. A few points are selected to indicate the general size of the statistical error bars.
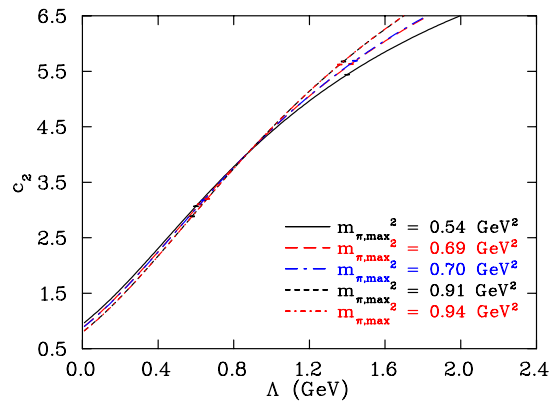


Figure 5.11:   Behaviour of $c_2$ vs. $\Lambda$, based on PACS-CS data. The chiral expansion is taken to order $O(m_\pi^3)$ and a double-dipole regulator is used. A few points are selected to indicate the general size of the statistical error bars.



Figure 5.9:   Behaviour of $c_0$ vs. $\Lambda$, based on CP-PACS data. The chiral expansion is taken to order $O(m_\pi^3)$ and a double-dipole regulator is used. A few points are selected to indicate the general size of the statistical error bars.



Figure 5.12:   Behaviour of $c_2$ vs. $\Lambda$, based on CP-PACS data. The chiral expansion is taken to order $O(m_\pi^3)$ and a double-dipole regulator is used. A few points are selected to indicate the general size of the statistical error bars.

Figure 5.13:   Behaviour of $c_0$ vs. $\Lambda$, based on JLQCD data. The chiral expansion is taken to order $O(m_\pi^3)$ and a triple-dipole regulator is used. A few points are selected to indicate the general size of the statistical error bars.



Figure 5.16:   Behaviour of $c_2$ vs. $\Lambda$, based on JLQCD data. The chiral expansion is taken to order $O(m_\pi^3)$ and a triple-dipole regulator is used. A few points are selected to indicate the general size of the statistical error bars.



Figure 5.14:   Behaviour of $c_0$ vs. $\Lambda$, based on PACS-CS data. The chiral expansion is taken to order $O(m_\pi^3)$ and a triple-dipole regulator is used. A few points are selected to indicate the general size of the statistical error bars.



Figure 5.17:   Behaviour of $c_2$ vs. $\Lambda$, based on PACS-CS data. The chiral expansion is taken to order $O(m_\pi^3)$ and a triple-dipole regulator is used. A few points are selected to indicate the general size of the statistical error bars.



Figure 5.15:   Behaviour of $c_0$ vs. $\Lambda$, based on CP-PACS data. The chiral expansion is taken to order $O(m_\pi^3)$ and a triple-dipole regulator is used. A few points are selected to indicate the general size of the statistical error bars.



Figure 5.18:   Behaviour of $c_2$ vs. $\Lambda$, based on CP-PACS data. The chiral expansion is taken to order $O(m_\pi^3)$ and a triple-dipole regulator is used. A few points are selected to indicate the general size of the statistical error bars.

extraction of an estimate of the variance for $\Lambda^{\text{scale}}$. The function $\chi^2_{dof}$ defined below allows easy identification of the intersection points in the renormalization flow plots, and a range associated with this central regularization scale. This function simply measures the degree to which the renormalization flow curves match.

The first step is to plot $\chi^2_{dof}$ against a variety of regularization scales. The value of $\bar{c}$ is given by the weighted mean formula, evaluated separately for each renormalized coefficient $c$ (with error $\delta c$) and regularization scale $\Lambda$:

$$\bar{c}(\Lambda) = \frac{\sum_{i=1}^{n} c(i;\Lambda)/(\delta c(i;\Lambda))^2}{\sum_{j=1}^{n} 1/(\delta c(j;\Lambda))^2} . \tag{5.2}$$

The following $\chi^2_{dof}$ treats relevant degrees of freedom as the extracted chiral coefficients with differing values of $m^2_{\pi,\text{max}}$:

$$\chi^2_{dof} = \frac{1}{n-1} \sum_{i=1}^{n} \frac{(c(i;\Lambda) - \bar{c}(\Lambda))^2}{(\delta c(i;\Lambda))^2}, \tag{5.3}$$

that is, $i$ corresponds to fits with differing values of $m^2_{\pi,\text{max}}$.

The $\chi^2_{dof}$ can be calculated as a function of the regularization scale $\Lambda$ for each of the renormalization plots of Figures 5.1 through 5.18. This will indicate the spread of the extrapolated values at each value of $\Lambda$. In the case of the PACS-CS data, the minimum of the $\chi^2_{dof}$ curve will be at the intersection point of the two curves. In the case of the JLQCD and CP-PACS data, with more than two curves, there is an interaction region on each plot, over a narrow window of $\Lambda$. The minima of $\chi^2_{dof}$ will indicate the value of $\Lambda$ that obtains the best agreement among the renormalization flow curves. This central value of $\Lambda$ will be taken to be the optimal regularization scale. The upper and lower bounds of $\Lambda$ obey the condition $\chi^2_{dof} < \chi^2_{dof,min} + 1/(dof)$. For each of the low-energy coefficients $c_0$ and $c_2$, the $\chi^2_{dof}$ curves for a dipole regulator are shown in Figures 5.19 through 5.24, the $\chi^2_{dof}$ curves for the double-dipole case are shown in Figures 5.25 through 5.30 and the $\chi^2_{dof}$ curves for the triple-dipole are shown in Figures 5.31 through 5.36. These plots indicate that there exists a statistically significant optimal regularization scale at this chiral order, for these data sets.
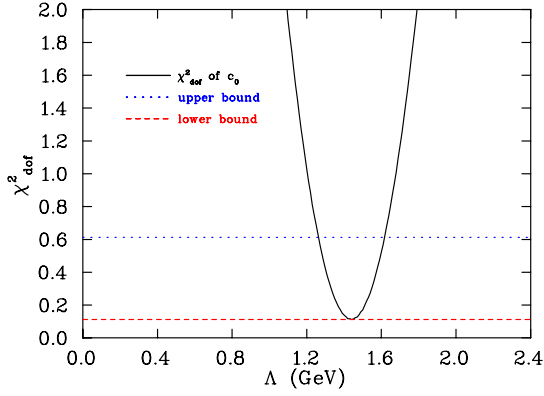
Figure 5.19:   Behaviour of $\chi^2_{dof}$ for $c_0$ vs. $\Lambda$, based on JLQCD data. The chiral expansion is taken to order $O(m^3_\pi)$ and a dipole regulator is used.
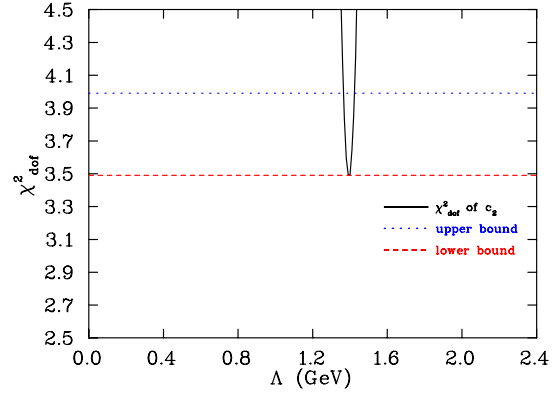


Figure 5.22:   Behaviour of $\chi^2_{dof}$ for $c_2$ vs. $\Lambda$, based on JLQCD data. The chiral expansion is taken to order $O(m^3_\pi)$ and a dipole regulator is used.
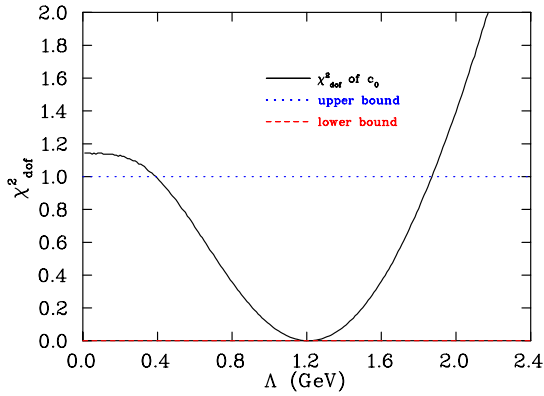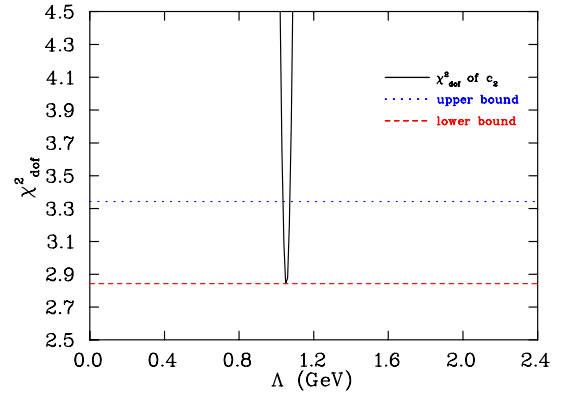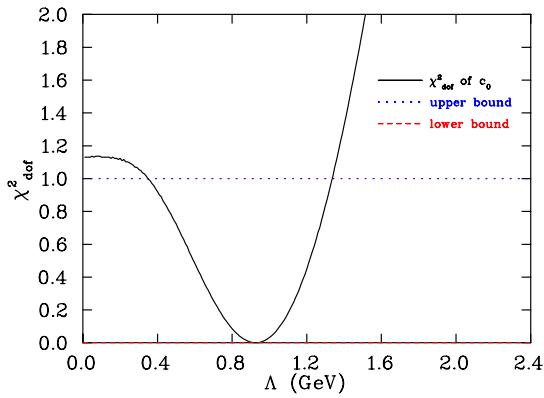


Figure 5.20:   Behaviour of $\chi^2_{dof}$ for $c_0$ vs. $\Lambda$, based on PACS-CS data. The chiral expansion is taken to order $O(m^3_\pi)$ and a dipole regulator is used.
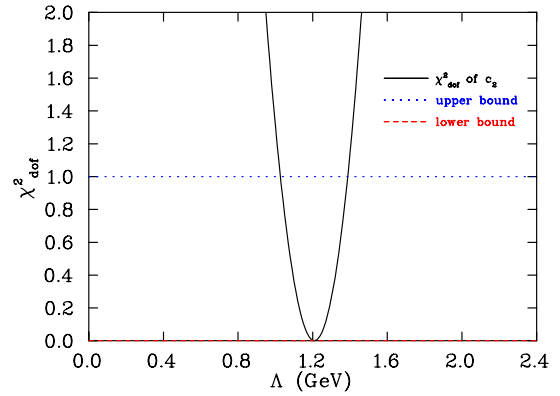


Figure 5.23:   Behaviour of $\chi^2_{dof}$ for $c_2$ vs. $\Lambda$, based on PACS-CS data. The chiral expansion is taken to order $O(m^3_\pi)$ and a dipole regulator is used.
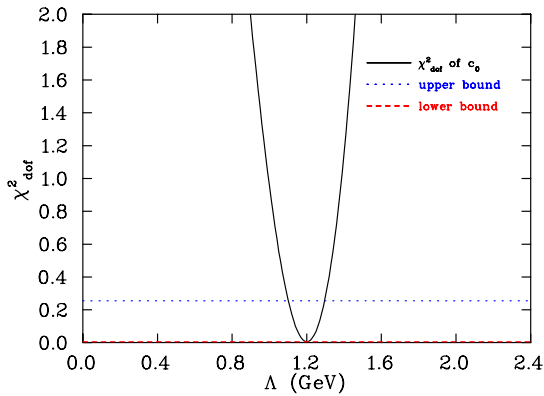


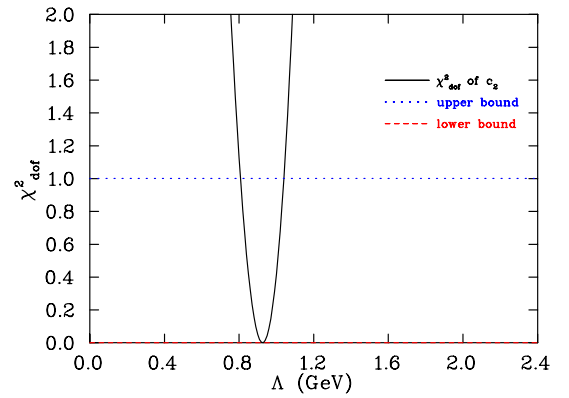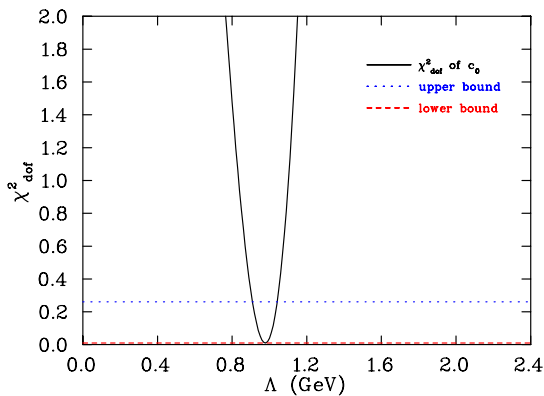Figure 5.21:   Behaviour of $\chi^2_{dof}$ for $c_0$ vs. $\Lambda$, based on CP-PACS data. The chiral expansion is taken to order $O(m^3_\pi)$ and a dipole regulator is used.
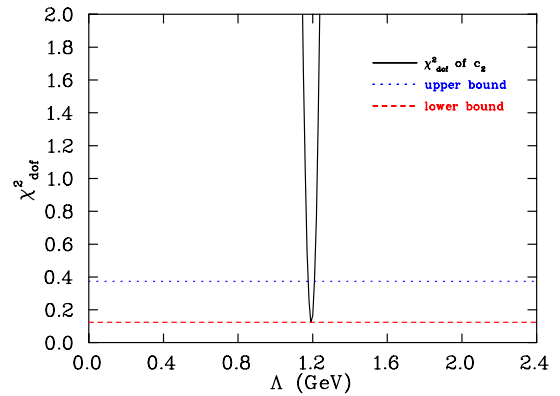


Figure 5.24:   Behaviour of $\chi^2_{dof}$ for $c_2$ vs. $\Lambda$, based on CP-PACS data. The chiral expansion is taken to order $O(m^3_\pi)$ and a dipole regulator is used.
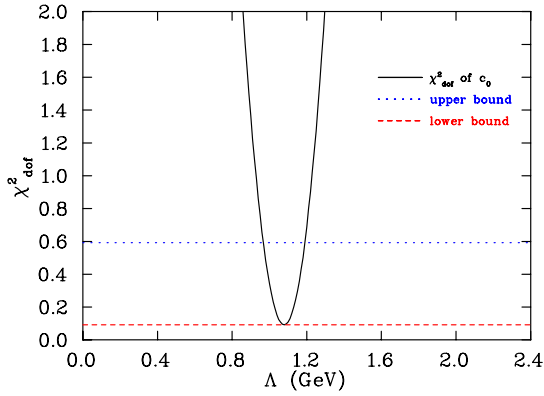
Figure 5.25:  Behaviour of $\chi^2_{dof}$ for $c_0$ vs. $\Lambda$, based on JLQCD data.  The chiral expansion is taken to order $O(m_\pi^3)$ and a double-dipole regulator is used.
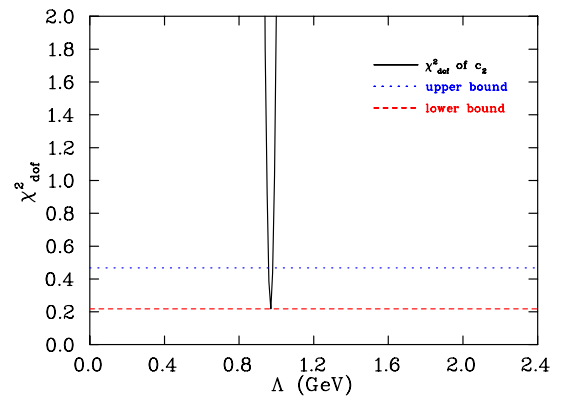


Figure 5.28:  Behaviour of $\chi^2_{dof}$ for $c_2$ vs. $\Lambda$, based on JLQCD data.  The chiral expansion is taken to order $O(m_\pi^3)$ and a double-dipole regulator is used.



Figure 5.26:  Behaviour of $\chi^2_{dof}$ for $c_0$ vs. $\Lambda$, based on PACS-CS data.  The chiral expansion is taken to order $O(m_\pi^3)$ and a double-dipole regulator is used.



Figure 5.29:  Behaviour of $\chi^2_{dof}$ for $c_2$ vs. $\Lambda$, based on PACS-CS data.  The chiral expansion is taken to order $O(m_\pi^3)$ and a double-dipole regulator is used.



Figure 5.27:  Behaviour of $\chi^2_{dof}$ for $c_0$ vs. $\Lambda$, based on CP-PACS data.  The chiral expansion is taken to order $O(m_\pi^3)$ and a double-dipole regulator is used.
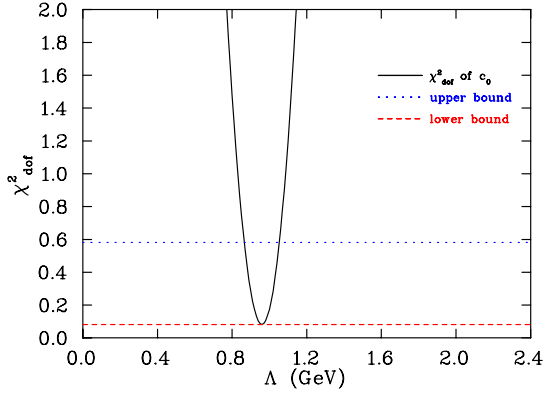


Figure 5.30:  Behaviour of $\chi^2_{dof}$ for $c_2$ vs. $\Lambda$, based on CP-PACS data.  The chiral expansion is taken to order $O(m_\pi^3)$ and a double-dipole regulator is used.

Figure 5.31:   Behaviour of $\chi^2_{dof}$ for $c_0$ vs. $\Lambda$, based on JLQCD data.  The chiral expansion is taken to order $O(m_\pi^3)$ and a triple-dipole regulator is used.
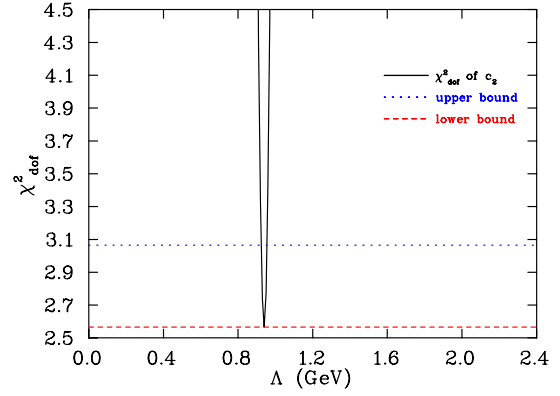


Figure 5.34:   Behaviour of $\chi^2_{dof}$ for $c_2$ vs. $\Lambda$, based on JLQCD data.  The chiral expansion is taken to order $O(m_\pi^3)$ and a triple-dipole regulator is used.
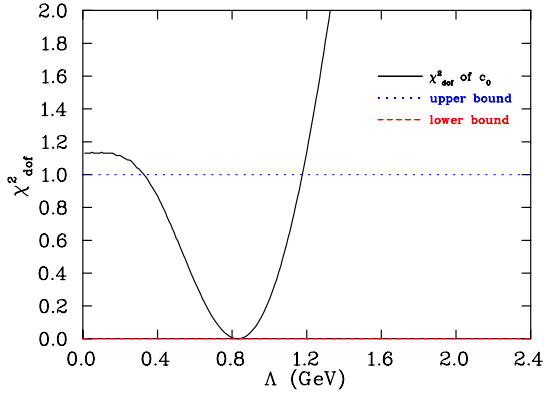


Figure 5.32:   Behaviour of $\chi^2_{dof}$ for $c_0$ vs. $\Lambda$, based on PACS-CS data.  The chiral expansion is taken to order $O(m_\pi^3)$ and a triple-dipole regulator is used.
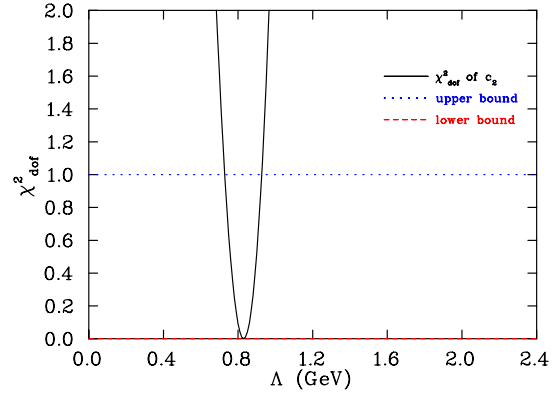


Figure 5.35:   Behaviour of $\chi^2_{dof}$ for $c_2$ vs. $\Lambda$, based on PACS-CS data.  The chiral expansion is taken to order $O(m_\pi^3)$ and a triple-dipole regulator is used.
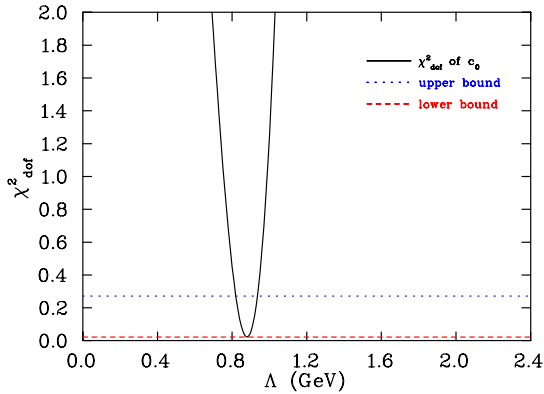


Figure 5.33:   Behaviour of $\chi^2_{dof}$ for $c_0$ vs. $\Lambda$, based on CP-PACS data.  The chiral expansion is taken to order $O(m_\pi^3)$ and a triple-dipole regulator is used.



Figure 5.36:   Behaviour of $\chi^2_{dof}$ for $c_2$ vs. $\Lambda$, based on CP-PACS data.  The chiral expansion is taken to order $O(m_\pi^3)$ and a triple-dipole regulator is used.
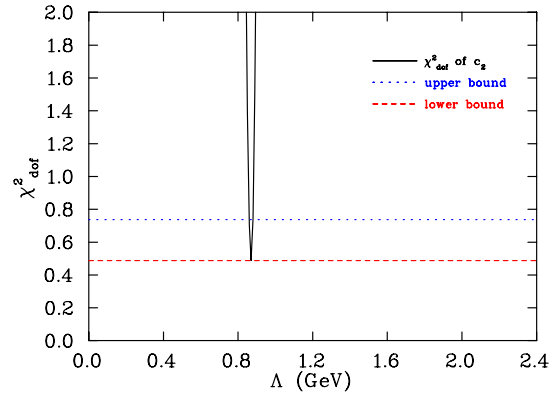
Furthermore, for each data set and regulator functional form, there is an agreement between the $c_0$ and $c_2$ analyses as to the value of this optimal scale. This provides evidence of the existence of an intrinsic scale embedded in that lattice data.

### 5.1.3   Effects at Higher Chiral Order

Consider the determination of $c_0$ and $c_2$ as a function of the regularization scale $\Lambda$, for a higher chiral order $O(m_\pi^4 \log m_\pi)$. As an example, the results for PACS-CS and CP-PACS data are shown in Figures 5.37 through 5.40. In this case, no clear intersection points in the renormalization curves can be found, and so one is unable to specify an optimal regularization scale. This certainly should be the case when working with data entirely within the PCR, because all renormalization procedures would be equivalent (to a prescribed level of accuracy) and so there could be no optimal scale. It has been demonstrated, however, that the data sets used in this study extend beyond the PCR. This is further verified by considering the evident scale-dependence of $c_0$ and $c_2$ in Figures 5.37 through 5.40. The fact that $c_0$ and $c_2$ change over the range of $\Lambda$ values indicates that the data are not inside the PCR where the renormalization must be scale-independent. Furthermore, since no preferred scale is revealed, any choice of $\Lambda$ appears equivalent at this order. While it is encouraging that the scheme-dependence has been weakened by working to higher order, it must be recognized that there is a systematic error associated with the choice of $\Lambda$. In the case of the CP-PACS results shown in Figures 5.38 and 5.40, it can be seen that the statistical errors are substantially smaller than the systematic error associated with a characteristic range, $\Lambda_{\text{lower}} < \Lambda < \infty$, where $\Lambda_{\text{lower}}$ is the lowest reasonable value of $\Lambda$, taken to be 0.6, 0.4 and 0.3 GeV for the dipole, double-dipole and triple-dipole regulator, respectively, as discussed in Section 4.2.1.

Since it is difficult to identify the optimal regularization scale at this chiral order, the results for chiral order $O(m_\pi^3)$ will be chosen to demonstrate the process of handling the existence of an optimal regularization scale in lattice QCD data. Values of $\Lambda^{\text{scale}}$ for different data sets and regulators, using chiral order $O(m_\pi^3)$, are given in Table 5.1. This table simply summarizes the central values from Figures 5.19
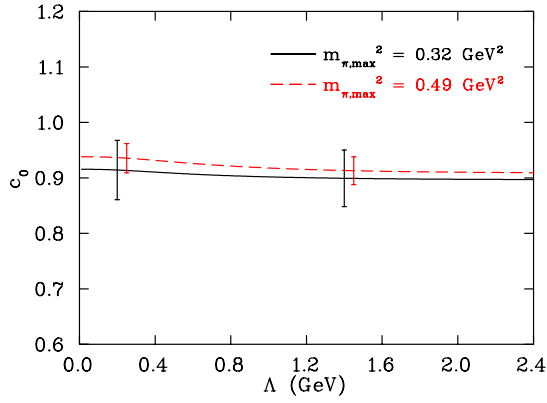
Figure 5.37:  Behaviour of $c_0$ vs. $\Lambda$, based on PACS-CS data. The chiral expansion is taken to order $O(m_\pi^4)$ and a dipole regulator is used. A few points are selected to indicate the general size of the statistical error bars.



Figure 5.39:  Behaviour of $c_2$ vs. $\Lambda$, based on PACS-CS data. The chiral expansion is taken to order $O(m_\pi^4)$ and a dipole regulator is used. A few points are selected to indicate the general size of the statistical error bars.
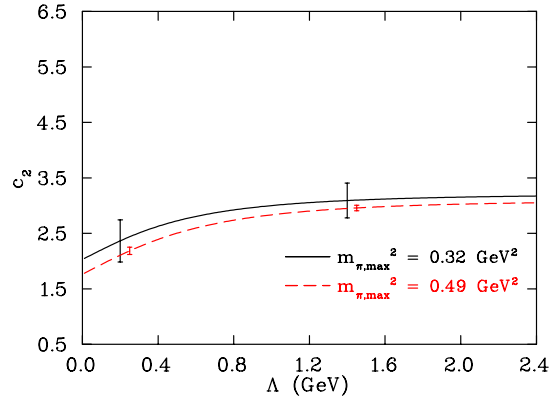


Figure 5.38:  Behaviour of $c_0$ vs. $\Lambda$, based on CP-PACS data. The chiral expansion is taken to order $O(m_\pi^4)$ and a dipole regulator is used. A few points are selected to indicate the general size of the statistical error bars.
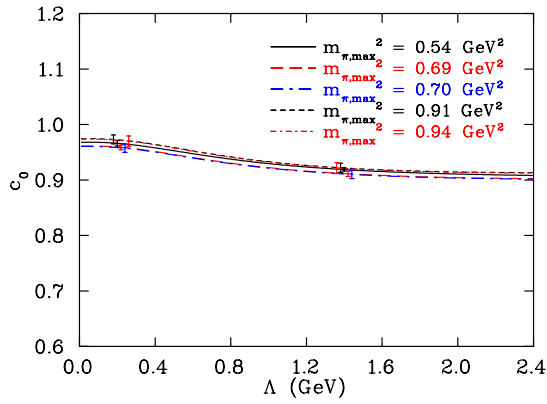


Figure 5.40:  Behaviour of $c_2$ vs. $\Lambda$, based on CP-PACS data. The chiral expansion is taken to order $O(m_\pi^4)$ and a dipole regulator is used. A few points are selected to indicate the general size of the statistical error bars.
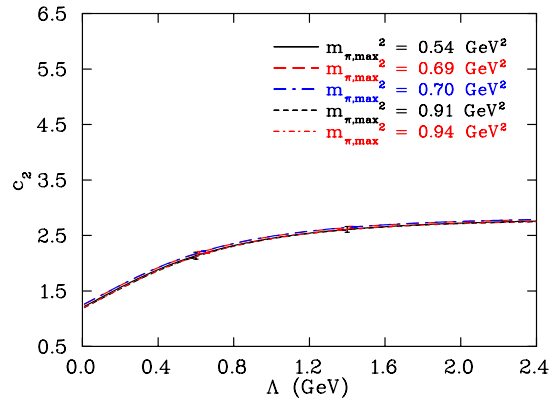
Table 5.1: Central values of $\Lambda$ in GeV, taken from the $\chi^2_{dof}$ analysis for $c_0$ and $c_2$, based on JLQCD, PACS-CS and CP-PACS data.

|  | regulator form | | |
| --- | --- | --- | --- |
| optimal scale | dipole | double | triple |
| $\Lambda^{\text{scale}}_{c_0,\text{JLQCD}}$ | $1.44^{+0.18}_{-0.18}$ | $1.08^{+0.11}_{-0.11}$ | $0.96^{+0.09}_{-0.09}$ |
| $\Lambda^{\text{scale}}_{c_2,\text{JLQCD}}$ | $1.40^{+0.02}_{-0.03}$ | $1.05^{+0.02}_{-0.01}$ | $0.94^{+0.01}_{-0.02}$ |
| $\Lambda^{\text{scale}}_{c_0,\text{PACS}-\text{CS}}$ | $1.21^{+0.66}_{-0.82}$ | $0.93^{+0.41}_{-0.58}$ | $0.83^{+0.35}_{-0.50}$ |
| $\Lambda^{\text{scale}}_{c_2,\text{PACS}-\text{CS}}$ | $1.21^{+0.18}_{-0.18}$ | $0.93^{+0.11}_{-0.12}$ | $0.83^{+0.10}_{-0.10}$ |
| $\Lambda^{\text{scale}}_{c_0,\text{CP}-\text{PACS}}$ | $1.20^{+0.10}_{-0.10}$ | $0.98^{+0.06}_{-0.07}$ | $0.88^{+0.06}_{-0.06}$ |
| $\Lambda^{\text{scale}}_{c_2,\text{CP}-\text{PACS}}$ | $1.19^{+0.02}_{-0.01}$ | $0.97^{+0.01}_{-0.01}$ | $0.87^{+0.01}_{-0.01}$ |

through 5.36. Such excellent agreement between the $c_0$ and $c_2$ analyses is remarkable, and indicative of the existence of an intrinsic scale in the data. There is also consistency among independent data sets. It is important to realize that the value of $\Lambda^{\text{scale}}$ is always the order of $\sim 1$ GeV, not 10 GeV, nor 100 GeV; nor is it infinity. However, in calculating the systematic uncertainty in the observables $c_0$, $c_2$, and the nucleon mass at the physical point due to the optimal regularization scale at order $O(m_\pi^4 \log m_\pi)$, two methods are provided. Firstly, the upper and lower bounds from the $\chi^2_{dof}$ analysis at order $O(m_\pi^3)$ are used to constrain $\Lambda$, and taken to be an accurate estimate of the systematic uncertainty in the contributions of higher-order terms. Secondly, variation of the observables across the aforementioned characteristic range of scale values, $\Lambda_{\text{lower}} < \Lambda < \infty$ are used. The results from both of these methods are displayed in Table 5.2.

The final results for the calculation of the renormalized coefficients $c_0$, $c_2$ and the nucleon mass $M_N$ extrapolated to the physical point ($m_{\pi,\text{phys}} = 140$ MeV) are summarized in Table 5.3. In this table, the nucleon mass is calculated at the optimal scale $\Lambda^{\text{scale}}$, which is the average of $\Lambda^{\text{scale}}_{c_0}$ and $\Lambda^{\text{scale}}_{c_2}$ for each data set. The extrapolations are performed at lattice sizes relevant to each data set: $L^{\text{JLQCD}}_{\text{extrap}} = 1.9$ fm, $L^{\text{PACS}-\text{CS}}_{\text{extrap}} = 2.9$ fm and $L^{\text{CP}-\text{PACS}}_{\text{extrap}} = 2.8$ fm. The estimate of the statistical error is quoted in the first pair of parentheses, and the systematic error, obtained from the

Table 5.2: Results at $O(m_\pi^4 \log m_\pi)$ for the systematic error due to the optimal regularization scale, calculated using two methods, for the values of $c_0$ (GeV), $c_2$ (GeV$^{-1}$) and the nucleon mass $M_N$ (GeV) extrapolated to the physical point ($m_{\pi,\text{phys}} = 140$ MeV). The first number in each column is the systematic error due to the optimal regularization scale using the upper and lower bound from the $\chi_{dof}^2$ analysis at order $O(m_\pi^3)$. The second number is the systematic error due to the intrinsic scale across the whole range of $\Lambda$ values from the lowest reasonable value ($\Lambda = \Lambda_{\text{lower}}$) obtained from the pseudodata analysis, to the asymptotic value ($\Lambda = \infty$).

| sys. err. | regulator form | | | | | |
| --- | --- | --- | --- | --- | --- | --- |
| | dipole | | double | | triple | |
| $\delta^\Lambda c_0^{\text{JLQCD}}$ | 0.001 | 0.009 | 0.001 | 0.013 | 0.001 | 0.016 |
| $\delta^\Lambda c_0^{\text{PACS-CS}}$ | 0.005 | 0.006 | 0.005 | 0.010 | 0.006 | 0.012 |
| $\delta^\Lambda c_0^{\text{CP-PACS}}$ | 0.002 | 0.024 | 0.002 | 0.037 | 0.002 | 0.045 |
| $\delta^\Lambda c_2^{\text{JLQCD}}$ | 0.02 | 0.31 | 0.03 | 0.38 | 0.01 | 0.48 |
| $\delta^\Lambda c_2^{\text{PACS-CS}}$ | 0.18 | 0.25 | 0.16 | 0.33 | 0.14 | 0.43 |
| $\delta^\Lambda c_2^{\text{CP-PACS}}$ | 0.02 | 0.40 | 0.02 | 0.58 | 0.02 | 0.73 |
| $\delta^\Lambda M_{N,\text{phys}}^{\text{JLQCD}}$ | 0.0004 | 0.0051 | 0.0003 | 0.0073 | 0.0003 | 0.0090 |
| $\delta^\Lambda M_{N,\text{phys}}^{\text{PACS-CS}}$ | 0.0022 | 0.0030 | 0.0025 | 0.0046 | 0.0025 | 0.0058 |
| $\delta^\Lambda M_{N,\text{phys}}^{\text{CP-PACS}}$ | 0.0012 | 0.0175 | 0.0013 | 0.0270 | 0.0014 | 0.0326 |

number of $m_\pi^2$ values used, is quoted in the second pair of parentheses. Two different weighted means are calculated. One incorporates the systematic error in the optimal regularization scale using the upper and lower bound from the $\chi_{dof}^2$ analysis at order $O(m_\pi^3)$. The other incorporates the systematic error due to the optimal regularization scale across the whole range of $\Lambda$ values, from the lowest reasonable value ($\Lambda = \Lambda_{\text{lower}}$) obtained from the pseudodata analysis, to the asymptotic value ($\Lambda = \infty$). The weighted means also include an estimate of the systematic error in the choice of regularization scale. All errors are added in quadrature. The lightest four data points from each of JLQCD, PACS-CS and CP-PACS lattice QCD data are used, and the nucleon mass is calculated at the scale determined by the data.

Table 5.3: Results at $O(m_\pi^4 \log m_\pi)$ for the values of $c_0$ (GeV), $c_2$ (GeV$^{-1}$) and the nucleon mass $M_N$ (GeV) extrapolated to the physical point ($m_{\pi,\text{phys}} = 140$ MeV). WM is the weighted mean of each row. The nucleon mass is calculated at the optimal scale $\Lambda^{\text{scale}}$, which is the average of $\Lambda^{\text{scale}}_{c_0}$ and $\Lambda^{\text{scale}}_{c_2}$ for each data set. The extrapolations are performed at lattice sizes relevant to each data set: $L^{\text{JLQCD}}_{\text{extrap}} = 1.9$ fm, $L^{\text{PACS}-\text{CS}}_{\text{extrap}} = 2.9$ fm and $L^{\text{CP}-\text{PACS}}_{\text{extrap}} = 2.8$ fm. The estimate of the statistical error is quoted in the first pair of parentheses, and the systematic error, obtained from the number of $m_\pi^2$ values used, is quoted in the second pair of parentheses. Two separate weighted means are calculated for each row. WM(1) incorporates the systematic error in the intrinsic scale using the upper and lower bound from the $\chi^2_{dof}$ analysis at order $O(m_\pi^3)$. The WM(2) incorporates the systematic error due to the intrinsic scale across the whole range of $\Lambda$ values, from the lowest reasonable value ($\Lambda = \Lambda_{\text{lower}}$) obtained from the pseudodata analysis, to the asymptotic value ($\Lambda = \infty$). The weighted means also include an estimate of the systematic error in the choice of the regulator functional form. All errors are added in quadrature. Note that any order $O(a)$ errors have not been incorporated into the total error analysis.

| | | regulator form | | | |
| parameter | dipole | double | triple | WM(1) | WM(2) |
|---|---|---|---|---|---|
| $c_0^{\text{JLQCD}}$ | 0.873(18)(16) | 0.875(17)(16) | 0.891(17)(16) | 0.880(29) | 0.879(32) |
| $c_0^{\text{PACS}-\text{CS}}$ | 0.900(51)(15) | 0.899(51)(14) | 0.898(51)(14) | 0.899(53) | 0.899(55) |
| $c_0^{\text{CP}-\text{PACS}}$ | 0.924(3)(8) | 0.914(3)(7) | 0.918(3)(7) | 0.918(13) | 0.920(37) |
| $c_2^{\text{JLQCD}}$ | 3.09(9)(11) | 3.18(9)(12) | 3.20(9)(11) | 3.16(18) | 3.14(43) |
| $c_2^{\text{PACS}-\text{CS}}$ | 3.06(32)(15) | 3.15(31)(14) | 3.17(31)(14) | 3.13(39) | 3.12(49) |
| $c_2^{\text{CP}-\text{PACS}}$ | 2.54(5)(4) | 2.70(5)(2) | 2.71(5)(3) | 2.66(18) | 2.61(60) |
| $M_{N,\text{phys}}^{\text{JLQCD}}$ | 1.02(2)(9) | 1.02(2)(9) | 1.02(2)(9) | 1.02(9) | 1.02(9) |
| $M_{N,\text{phys}}^{\text{PACS}-\text{CS}}$ | 0.967(45)(43) | 0.966(45)(43) | 0.966(45)(43) | 0.966(62) | 0.966(62) |
| $M_{N,\text{phys}}^{\text{CP}-\text{PACS}}$ | 0.982(2)(40) | 0.975(2)(43) | 0.978(2)(42) | 0.979(43) | 0.979(50) |

## 5.2   Summary and Specific Issues for the Nucleon Mass

Since the chiral expansion is only convergent within the PCR, a renormalization scheme such as finite-range regularization should be used for current lattice QCD results, which typically extend beyond the PCR. It was found that renormalization scheme-dependence occurs when lattice QCD data extending outside the PCR are used in the extrapolation. This has provided a new quantitative test for determining whether lattice QCD data lie within the PCR.

The optimal regularization scale $\Lambda^{\text{scale}}$ was selected as the scale at which the

renormalized coefficients are independent of the upper bound of the fit domain, $m^2_{\pi,\text{max}}$. This also means that the renormalized coefficients must not be identified with their asymptotic values at large $\Lambda$. It is also apparent that extremely low values of $\Lambda$ cause a breakdown of the finite-range renormalization. The cut-off scale associated with an ultraviolet regulator must be large enough for the loop integral contributions to be finite, so that the chiral physics is not suppressed.

The mean value of the optimal regularization scale for both the $c_0$ and $c_2$ analyses across each data set is $\bar{\Lambda}^{\text{scale}}_{\text{dip}} \approx 1.3$ GeV for the dipole form, $\bar{\Lambda}^{\text{scale}}_{\text{doub}} \approx 1.0$ GeV for the double-dipole form and $\bar{\Lambda}^{\text{scale}}_{\text{trip}} \approx 0.9$ GeV for the triple-dipole form. Each functional form naturally leads to a different value of optimal regularization scale due to its different shape of attenuation, as shown in Figure 3.1. The value of $\bar{\Lambda}^{\text{scale}}_{\text{dip}}$ is of particular interest in this investigation. In Chapter 7, the magnetic moment and the electric charge radius of the nucleon are analyzed with the same procedure, and using a dipole regulator. If an optimal regularization scale can be obtained for these electromagnetic properties of the nucleon, a comparison can be made with the optimal regularization scale from the analysis of the nucleon mass, to determine whether there exists an intrinsic scale in the nucleon. If the optimal regulators in each case are consistent with each other, this suggests the existence of a well-defined intrinsic energy scale in the nucleon-pion interaction. Nevertheless, a robust method for accomplishing a chiral extrapolation with a reliable and systematic estimate in the uncertainty has been provided.

In the next chapter, the procedure developed for obtaining an optimal regularization scale and performing a reliable chiral extrapolation is tested, by analyzing the quenched $\rho$ meson mass: an observable for which there does not exist an experimental value. This serves to demonstrate the ability of the extrapolation scheme to make predictions without prior bias.

# Chapter 6

# Results for the Mass of the Quenched ρ Meson

*"A rigorous theory must begin by specifying the attributes that make a given experimental device into a measuring instrument."* (Omnès, R. 2002. *Quantum Philosophy: Understanding and Interpreting Contemporary Science* p.209) [Omn02]

The quenched ρ meson mass offers a unique test case for the identification of an intrinsic scale, and subsequent extrapolation scheme. It serves to demonstrate the ability of the procedure to make predictions with reduced phenomenological bias, and also to highlight the difference between quenched and full quantum chromodynamics (QCD) in making extrapolations of an observable. By using the method developed in Chapter 4, an extrapolation is performed using quenched lattice QCD data that extend outside the power-counting regime (PCR).

In chiral effective field theory (χEFT), the diagrammatic formulation can be used to identify the major contributions to the ρ meson mass in quenched QCD (QQCD) [CR98, AAL$^+$06]. The leading-order diagrams are the double and single η′ hairpin diagrams as shown in Figures 6.1 and 6.4, respectively. The constant coefficients of these loop integrals are endowed with an uncertainty to encompass the possible effects of smaller contributions to order $O(m_\pi^4)$. Interactions with the flavour-singlet η′ are the most important contributions to the ρ meson mass in QQCD. This is an artefact of the quenched approximation, where the η′ also behaves as a pseudo-
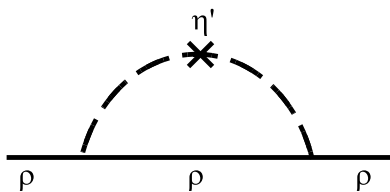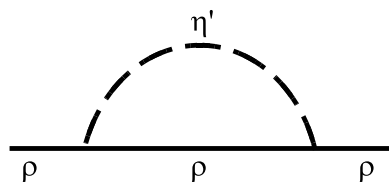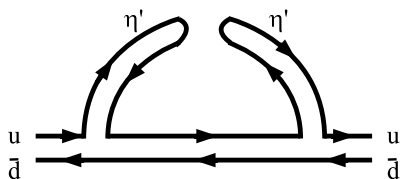
83

Figure 6.1: Double hairpin η′ diagram.



Figure 6.4: Single hairpin η′ diagram.



Figure 6.2: Double hairpin quark flow diagram.
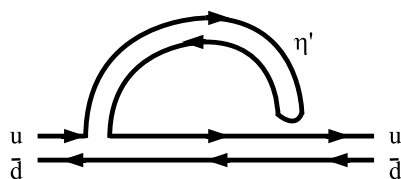


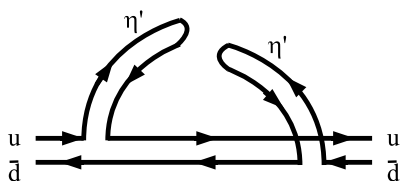Figure 6.5: Single hairpin quark flow diagram.



Figure 6.3:   Alternative double hairpin quark flow diagram.

Goldstone boson, having a mass that is degenerate with the pion. The dressing of the ρ meson by the η′ field is illustrated in Figures 6.2 through 6.5. Since the hairpin vertex must be a flavour-singlet, the mesons that can contribute are the η′ meson, and the ω meson. The contributions from the ω meson are insignificant due to OZI suppression and the small ρ-ω mass splitting. However, in QQCD, the η′ loop behaves much as a pion loop, yet with a slightly modified propagator.

In full QCD however, this would not be the case. The η′ masses are large compared to the pion, and the propagators of the η′ meson are suppressed due to their large denominators. If the η′ propagator in full QCD is expanded out, the terms can be summed as a geometric series and expressed in closed form, as a function of some massive coupling constant $M_0$ between the disconnected quark loops and pion

momentum $k$, as argued in Allton [AAL$^+$05]:

$$\frac{1}{k^2+m_\pi^2} - \frac{M_0^2}{(k^2+m_\pi^2)^2} \times$$
$$\left[1 - \frac{M_0^2}{k^2+m_\pi^2} + \left(\frac{M_0^2}{k^2+m_\pi^2}\right)^2 - \cdots\right] \tag{6.1}$$

$$= \frac{1}{k^2+m_\pi^2} - \frac{M_0^2}{(k^2+m_\pi^2)^2}\left[1 + \left(\frac{M_0^2}{k^2+m_\pi^2}\right)\right]^{-1} \tag{6.2}$$

$$= \frac{1}{k^2+m_\pi^2+M_0^2} \equiv \frac{1}{k^2+m_{\eta'}^2}. \tag{6.3}$$

However in QQCD, the first two terms of Equation (6.1) form the whole $\eta'$ propagator, since they alone correspond to the absence of disconnected loops, as shown in Figure 6.6.
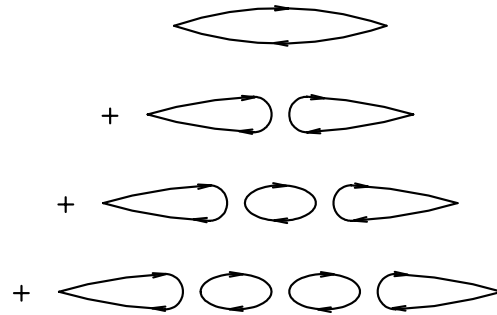


Figure 6.6: Diagrammatic representation of $\eta'$ propagator terms.

# 6.1    Renormalization of the Quenched ρ Meson Mass

## 6.1.1    Chiral Expansion of the Quenched ρ Meson Mass

The ρ meson mass extrapolation formula in QQCD can be expressed in a form that contains an analytic polynomial in $m_\pi^2$ plus the chiral loop integrals ($\Sigma^Q$):

$$m_{\rho,Q}^2 = a_0^\Lambda + a_2^\Lambda m_\pi^2 + a_4^\Lambda m_\pi^4 + \Sigma_{\eta'\eta'}^Q(m_\pi^2,\Lambda) + \Sigma_{\eta'}^Q(m_\pi^2,\Lambda) + O(m_\pi^6). \tag{6.4}$$

The coefficients $a_i^\Lambda$ are the 'residual series' coefficients, which correspond to direct quark-mass insertions in the underlying Lagrangian of chiral perturbation theory (χPT). However, the non-analytic behaviour of the expansion arises from the chiral loop integrals. Upon renormalization of the divergent loop integrals, these will correspond with low-energy constants of the quenched effective field theory. The extraction of these parameters from lattice QCD results will follow the same course as provided in Chapter 4.

By convention, the non-analytic terms from the double and single hairpin integrals are $\chi_1 m_\pi$ and $\chi_3 m_\pi^3$, respectively. The coefficients $\chi_1$ and $\chi_3$ of each integral are scheme-independent constants that can be estimated from phenomenology. That is, they can be expressed purely in terms of known constants from experiment, such as the pion decay constant $f_\pi = 92.4$ MeV, and a variety of parameters obtained from the underlying effective Lagrangian, as described in Section 6.1.3. The low-order expansion of the loop contributions takes the following form:

$$\Sigma_{\eta'\eta'}^Q = b_0^{\eta'\eta'} + \chi_1 m_\pi + b_2^{\eta'\eta'} m_\pi^2 + \chi_3^{\eta'\eta'} m_\pi^3 + b_4^{\eta'\eta'} m_\pi^4 + O(m_\pi^6), \tag{6.5}$$

$$\Sigma_{\eta'}^Q = b_0^{\eta'} + b_2^{\eta'} m_\pi^2 + \chi_3^{\eta'} m_\pi^3 + b_4^{\eta'} m_\pi^4 + O(m_\pi^6). \tag{6.6}$$

The coefficient $\chi_3$ is obtained by adding the contributions from both integrals, $\chi_3 = \chi_3^{\eta'\eta'} + \chi_3^{\eta'}$. As before, each integral has a solution in the form of a polynomial expansion analytic in $m_\pi^2$ plus non-analytic terms, of which the leading-order term is of greatest interest. In order to achieve an extrapolation based on an optimal finite-range regularization (FRR) scale, once again the scale-dependence of the low-energy

expansion must be removed through renormalization. The renormalization program of FRR combines the scheme-dependent $b_i$ coefficients from the chiral loops with the scheme-dependent $a_i$ coefficients from the residual series at each chiral order $i$. The result is a scheme-independent coefficient $c_i$:

$$c_0 = a_0^\Lambda + b_0^{\eta'\eta'} + b_0^{\eta'}, \tag{6.7}$$

$$c_2 = a_2^\Lambda + b_2^{\eta'\eta'} + b_2^{\eta'}, \tag{6.8}$$

$$c_4 = a_4^\Lambda + b_4^{\eta'\eta'} + b_4^{\eta'}, \text{ etc.} \tag{6.9}$$

That is, the underlying $a_i^\Lambda$ coefficients undergo a renormalization from the chiral loop integrals. The renormalized coefficients $c_i$ are an important part of the extrapolation technique. In this chapter, a stable and robust determination of the parameters $c_0$, $c_2$ and $c_4$ forms the core of the method for determining an optimal scale $\Lambda^{\text{scale}}$ of the mass of the ρ meson.

## 6.1.2   Chiral Loop Integrals

The loop integrals can again be expressed conveniently by taking the non-relativistic limit and performing the pole integration for $k_0$. Renormalization is achieved by subtracting the relevant terms in the Taylor expansion of the loop integrals, and absorbing them into the corresponding low-energy coefficients, $c_i$:

$$\tilde{\Sigma}_{\eta'\eta'}^Q(m_\pi^2;\Lambda) = \frac{-\chi_{\eta'\eta'}}{3\pi^2}\int d^3k \frac{(M_0^2 k^2 + \frac{5}{2}A_0 k^4)u^2(k;\Lambda)}{(k^2 + m_\pi^2)^2}$$
$$- b_0^{\eta'\eta'} - b_2^{\eta'\eta'}m_\pi^2 - b_4^{\eta'\eta'}m_\pi^4, \tag{6.10}$$

$$\tilde{\Sigma}_{\eta'}^Q(m_\pi^2;\Lambda) = \frac{\chi_{\eta'}}{2\pi^2}\int d^3k \frac{k^2 u^2(k;\Lambda)}{k^2 + m_\pi^2} - b_0^{\eta'} - b_2^{\eta'}m_\pi^2$$
$$- b_4^{\eta'}m_\pi^4. \tag{6.11}$$

The tilde ( ˜ ) denotes that the integrals are written out in renormalized form to chiral order $O(m_\pi^4)$. The coefficients $\chi_{\eta'\eta'}$ and $\chi_{\eta'}$ are related to the coefficients of the

leading-order non-analytic terms by the following:

$$\chi_1 = M_0^2 \chi_{\eta'\eta'}, \tag{6.12}$$

$$\chi_3 = \chi_3^{\eta'\eta'} + \chi_3^{\eta'} = A_0 \chi_{\eta'\eta'} + \chi_{\eta'}. \tag{6.13}$$

In choosing the form of regulator, one must be cautious to avoid any extra scheme-dependent, non-analytic terms that might occur at working chiral order. For example, consider pseudodata created from the lattice QCD simulations from the Kentucky Group, using a dipole regulator created using the scale: $\Lambda_c = 0.8$ GeV. The renormalization flow curves are shown in Figures 6.7 through 6.9. The dipole regulator induces non-analytic terms proportional to $m_\pi$ and $m_\pi^3$ in the loop integral expansion formulae. By writing out the regulator-dependence explicitly in the coefficients $\tilde{b}_i$, the following equations are obtained:

$$\Sigma_{\eta'\eta'}^{Q,\mathrm{dip}}(k;\Lambda) = \Lambda \tilde{b}_0^{\eta'\eta'} + \chi_1 m_\pi + \frac{\tilde{b}_2^{\eta'\eta'}}{\Lambda} m_\pi^2 + \frac{\tilde{b}_3^{\eta'\eta'}}{\Lambda^2} m_\pi^3 + \frac{\tilde{b}_4^{\eta'\eta'}}{\Lambda^3} m_\pi^4 + \frac{\tilde{b}_5^{\eta'\eta'}}{\Lambda^4} m_\pi^5 + O(m_\pi^6), \tag{6.14}$$

$$\Sigma_{\eta'}^{Q,\mathrm{dip}}(k;\Lambda) = \Lambda^3 \tilde{b}_0^{\eta'} + \Lambda \tilde{b}_2^{\eta'} m_\pi^2 + \chi_3 m_\pi^3 + \frac{\tilde{b}_4^{\eta'}}{\Lambda} m_\pi^4 + \frac{\tilde{b}_5^{\eta'}}{\Lambda^2} m_\pi^5 + O(m_\pi^6). \tag{6.15}$$

Clearly, the renormalization flow is compromised by the extra non-analytic terms appearing at such a close chiral order to the fit parameters. Though it is possible to provide additional fit parameters $a_3^\Lambda$ and $a_5^\Lambda$ to contain the contribution from these terms, there are often not enough available lattice simulation results to constrain all coefficients. Instead, a more effective approach is to choose a regulator functional form such that the extra non-analytic terms do not appear in the chiral expansion. By selecting an multiple-dipole regulator corresponding to a choice of $n > 2$ in Equation (3.105) in Chapter 3, the suppression of additional non-analytic terms below the working chiral order $O(m_\pi^4)$ is assured. If one also decides to remove extra $m_\pi^5$ terms, a triple-dipole is sufficient to remove additional non-analytic terms below chiral order $O(m_\pi^6)$. The renormalization flow curves for pseudodata created with a double-dipole are shown in Figures 6.10 through 6.12. The renormalization flow
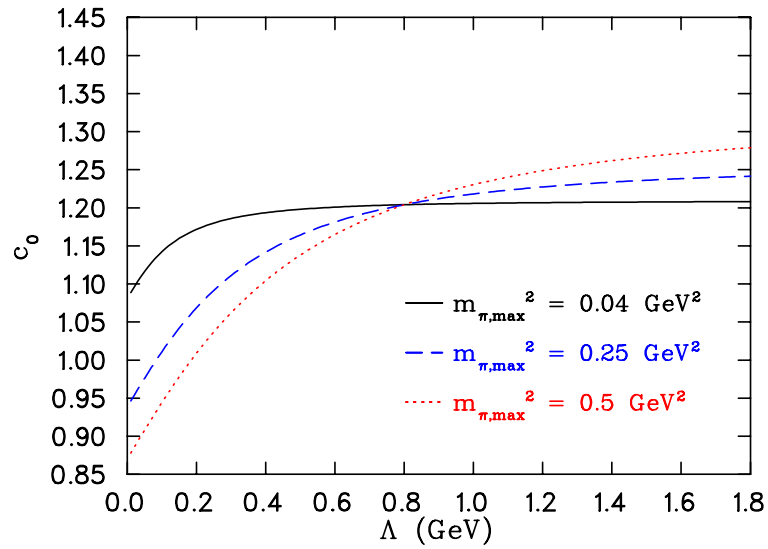
Figure 6.7:   Behaviour of $c_0$ vs. $\Lambda$ based on infinite-volume pseudodata created with a dipole regulator at $\Lambda_c = 0.8$ GeV (based on Kentucky Group data).  Each curve uses pseudodata with a different upper value of pion mass $m_{\pi,\text{max}}^2$.
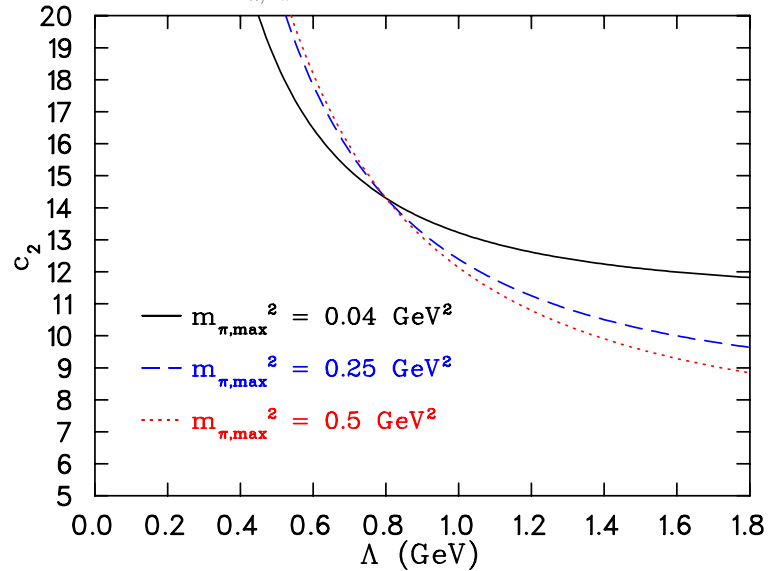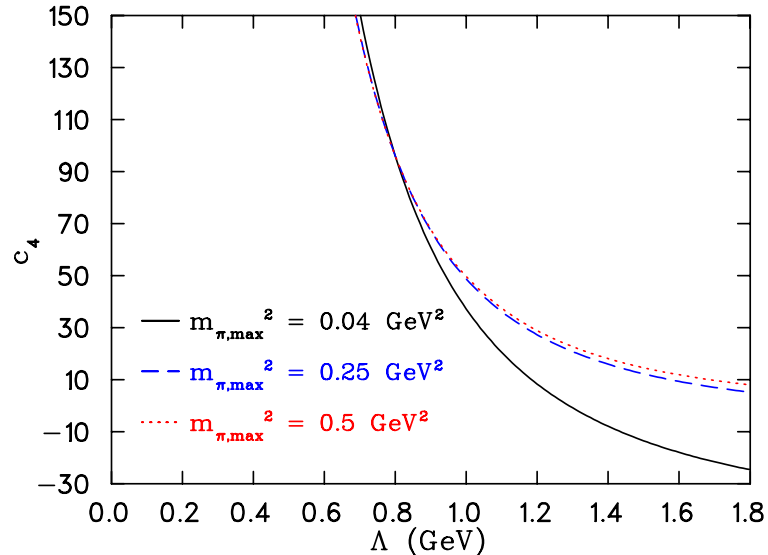


Figure 6.8:   Behaviour of $c_2$ vs. $\Lambda$ based on infinite-volume pseudodata created with a dipole regulator at $\Lambda_c = 0.8$ GeV (based on Kentucky Group data).



Figure 6.9:   Behaviour of $c_4$ vs. $\Lambda$ based on infinite-volume pseudodata created with a dipole regulator at $\Lambda_c = 0.8$ GeV (based on Kentucky Group data).
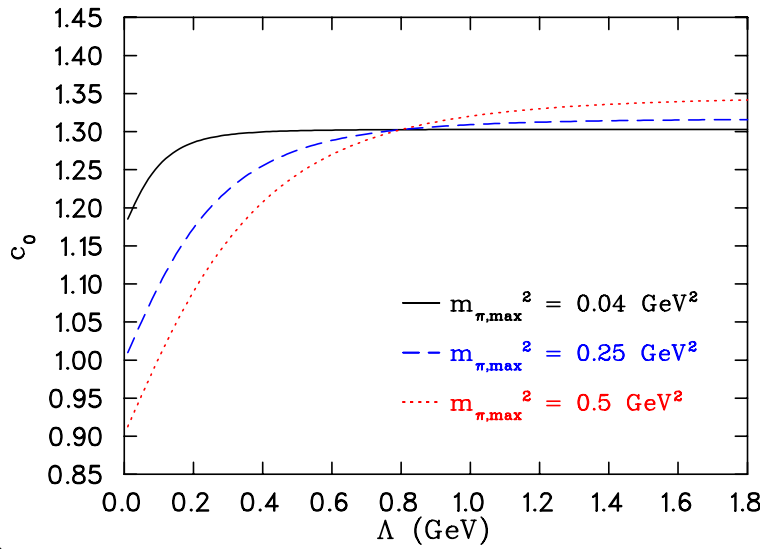
**Figure 6.10:**   Behaviour of $c_0$ vs. $\Lambda$ based on infinite-volume pseudodata created with a double-dipole regulator at $\Lambda_c = 0.8$ GeV (based on Kentucky Group data). Each curve uses pseudodata with a different upper value of pion mass $m_{\pi,max}^2$.
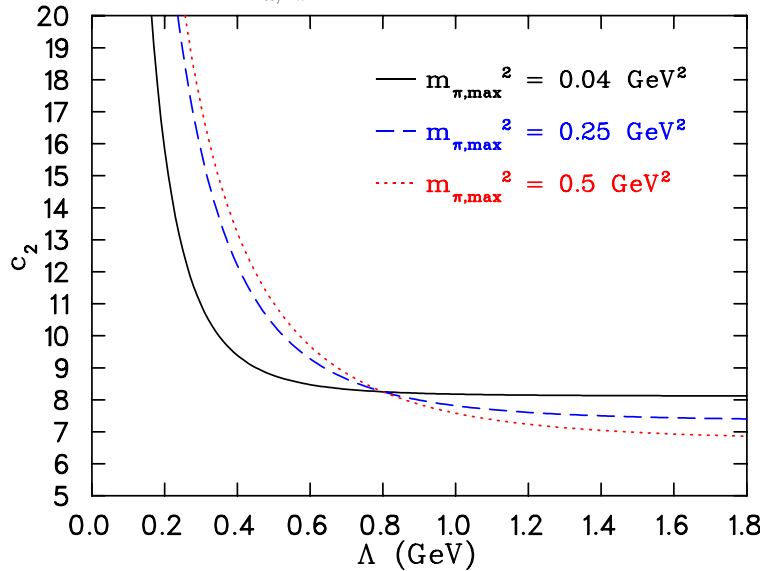


**Figure 6.11:**   Behaviour of $c_2$ vs. $\Lambda$ based on infinite-volume pseudodata created with a double-dipole regulator at $\Lambda_c = 0.8$ GeV (based on Kentucky Group data).



**Figure 6.12:**   Behaviour of $c_4$ vs. $\Lambda$ based on infinite-volume pseudodata created with a double-dipole regulator at $\Lambda_c = 0.8$ GeV (based on Kentucky Group data).
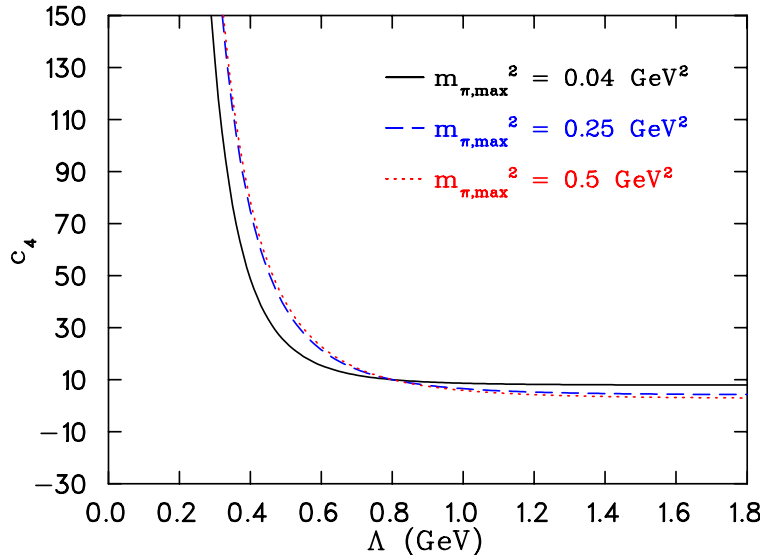
curves for pseudodata created with a triple-dipole regulator are shown in Figures
6.13 through 6.15. In both cases, the pseudodata are created using the scale: $\Lambda_c = 0.8$
GeV.

With the loop integrals specified, Equation (6.4) can be rewritten in terms of the
renormalized coefficients $c_i$:

$$m_{\rho,Q}^2 = c_0 + c_2 m_\pi^2 + c_4 m_\pi^4 + \tilde{\Sigma}_{\eta'\eta'}^Q(m_\pi^2;\Lambda) + \tilde{\Sigma}_{\eta'}^Q(m_\pi^2;\Lambda) + O(m_\pi^6) \tag{6.16}$$

$$= c_0 + \chi_1 m_\pi + c_2 m_\pi^2 + \chi_3 m_\pi^3 + c_4 m_\pi^4 + O(m_\pi^6) . \tag{6.17}$$

Equation (6.16) is the extrapolation formula for $m_{\rho,Q}^2$ at infinite lattice volume. The
fit coefficients are $c_0$, $c_2$ and $c_4$; and $m_{\rho,Q}$ is obtained by taking the square root of
either Equation (6.16) or (6.17).

## 6.1.3   Scheme-Independent Coefficients

The convention used for defining the values of $\chi_1$, $\chi_3$ and the various coupling con-
stants that occur in each, follows Booth [BCF97]. For the possible different values
that coupling constants can take, the definitions from Chow & Rey [CR98], Armour
*et.al.* [AAL$^+$06] and Sharpe [Sha97] are used. The types of vertices available are
displayed in Figure 6.16, where the couplings $g_2$ and $g_4$ occur explicitly in the two
diagrams considered here. Booth suggests naturalness for $g_2 \sim 1$, and that $g_4 \sim 1/N_c$
[BCF97]. These quenched coupling constants can be connected to the experimental
value of $g_{\omega\rho\pi}$ as per Lublinsky [Lub97] by the relation:

$$g_2 = \frac{1}{2} g_{\omega\rho\pi} f_\pi , \tag{6.18}$$

where $g_{\omega\rho\pi} = 14 \pm 2$ GeV$^{-1}$ and the pion decay constant is again taken to be $f_\pi =$
92.4 MeV. Thus $g_2$ is chosen to be $0.65 \pm 0.09$ GeV and $g_4$ is chosen to be $g_2/3$. The
coupling between the separate legs of the double hairpin diagram are approximated
by the massive constant $M_0^2 \propto m_{\eta'}^2$. The next-order correction to $M_0$ in momentum $k$
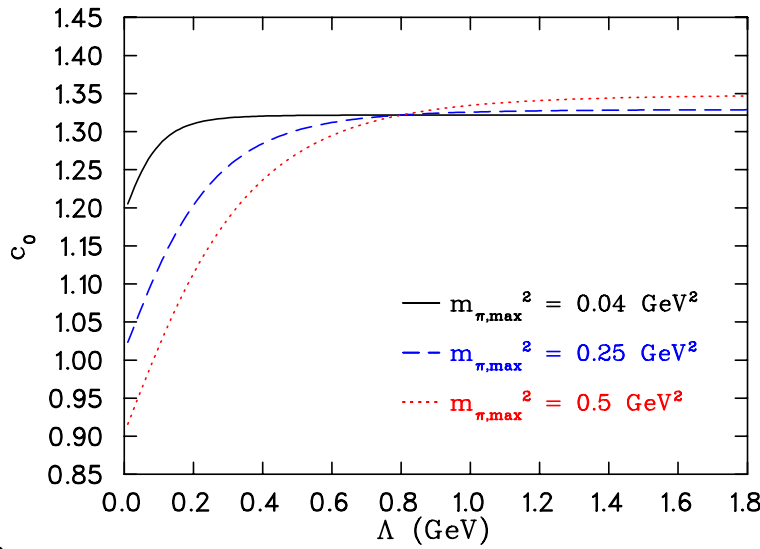defines the coupling to be $-M_0^2 + A_0 k^2$. These constants can be connected to the full

Figure 6.13:   Behaviour of $c_0$ vs. $\Lambda$ based on infinite-volume pseudodata created with a triple-dipole regulator at $\Lambda_c = 0.8$ GeV (based on Kentucky Group data). Each curve uses pseudodata with a different upper value of pion mass $m^2_{\pi,\mathrm{max}}$.
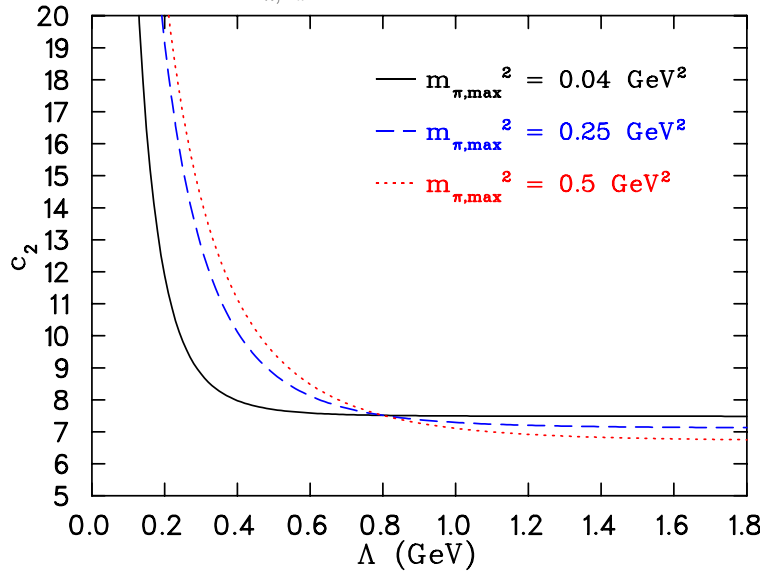


Figure 6.14:   Behaviour of $c_2$ vs. $\Lambda$ based on infinite-volume pseudodata created with a triple-dipole regulator at $\Lambda_c = 0.8$ GeV (based on Kentucky Group data).



Figure 6.15:   Behaviour of $c_4$ vs. $\Lambda$ based on infinite-volume pseudodata created with a triple-dipole regulator at $\Lambda_c = 0.8$ GeV (based on Kentucky Group data).

> NOTE:
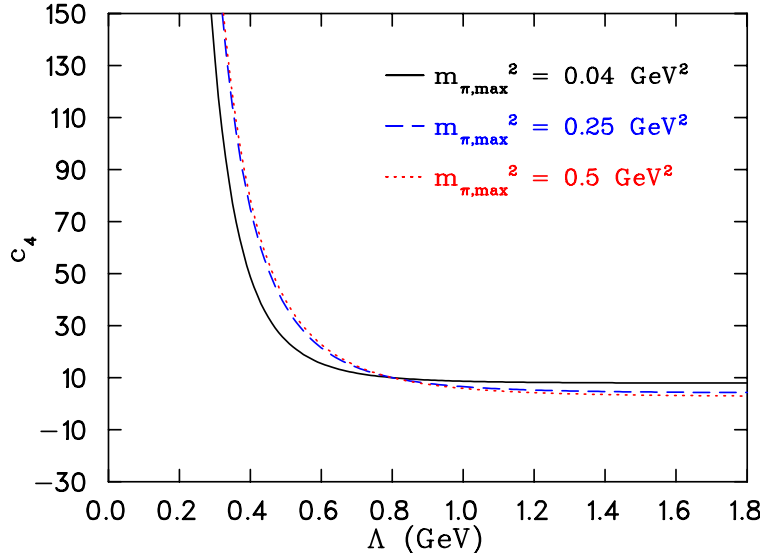> This figure is included on page 93 of the print copy of
> the thesis held in the University of Adelaide Library.

Figure 6.16: Coupling types following convention introduced by Booth [BCF97].

QCD $\eta'$ meson mass $m_{\eta'}$ by considering the geometric series of terms as illustrated earlier, in Figure 6.6. As a result, $M_0^2$ is taken to be $0.6 \pm 0.2$ GeV$^2$ and $A_0$ is taken to be $0 \pm 0.2$. The central values of each quantity are used in the final analysis.

The coefficients $\chi_{\eta'\eta'}$ and $\chi_{\eta'}$ can be specified in terms of the relevant coupling constants:

$$\chi_{\eta'\eta'} = -2\,\overset{\circ}{m}_\rho\, \frac{g_2^2}{4\pi f_\pi^2}\,,$$
$$\chi_{\eta'} = -2\,\overset{\circ}{m}_\rho\, \frac{g_2 g_4}{6\pi f_\pi^2}\,, \tag{6.19}$$

where the couplings are defined relative to $\overset{\circ}{m}_\rho$, representing the ρ meson mass in the chiral limit, which is taken to be 770 MeV.

The finite-volume version of Equation (6.16) can thus be expressed:

$$m_{\rho,Q}^2 = c_0 + c_2 m_\pi^2 + c_4 m_\pi^4 + (\tilde{\Sigma}_{\eta'\eta'}^Q(m_\pi^2;\Lambda) + \delta_{\eta'\eta'}^{\text{FVC}}(m_\pi^2;\Lambda'))$$
$$+ (\tilde{\Sigma}_{\eta'}^Q(m_\pi^2;\Lambda) + \delta_{\eta'}^{\text{FVC}}(m_\pi^2;\Lambda')) + O(m_\pi^6)\,. \tag{6.20}$$

## 6.2    Extrapolating the Quenched ρ Meson Mass

### 6.2.1    Renormalization Flow Analysis

The data displayed in Figure 6.17 are split into two parts. All the data points to the left of the solid vertical line are unused in the extrapolation and kept in reserve. This is so that the extrapolation can be checked against these known data points. The data points to the right of the solid vertical line are used for extrapolation. The full set of data is also listed in Appendix C, Table C.4. Note that in QQCD, the simulation results are correlated. The correlations have been taken into account in all fits and extrapolations.

In order to produce an extrapolation to each test value of $m_\pi^2$, an FRR scale $\Lambda$ must be selected. As an example, one can choose a triple-dipole regulator at $\Lambda = 1.0$ GeV. By using Equation (6.20), finite- and infinite-volume extrapolations are shown in Figure 6.18. The values of $m_\pi^2$ selected for the finite-volume extrapolations exactly correspond with the missing low-energy data points set aside earlier. The physical point $m_\pi^2 = 0.0196$ GeV$^2$ is included as well.

Now the regularization scale-dependence of low-energy coefficients $c_0$, $c_2$ and $c_4$ is investigated for various upper limits of range of pion masses. The renormalization of these low-energy coefficients is considered across a range of $\Lambda$ values. Each renormalization flow curve corresponds to a different value of maximum pion mass, $m_{\pi,\text{max}}^2$. Thus the behaviour of the renormalization of the low-energy coefficients can be examined as the lattice data set is extended further outside the PCR. Figures 6.19 through 6.21 show the renormalization flow curves for each of $c_0$, $c_2$ and $c_4$. Each data point plotted has an associated error bar, but for the sake of clarity only a few points are selected to indicate the general size of the statistical error bars. Using the procedure described in Chapter 4, the optimal regularization scale is identified by the value of the regularization scale that minimizes the discrepancies among the renormalization flow curves. This indicates the scale at which the renormalization of each $c_i$ is least sensitive to truncation of the data. Physically, this value of $\Lambda$ can be associated with an intrinsic scale related to the size of the source of the pion cloud.
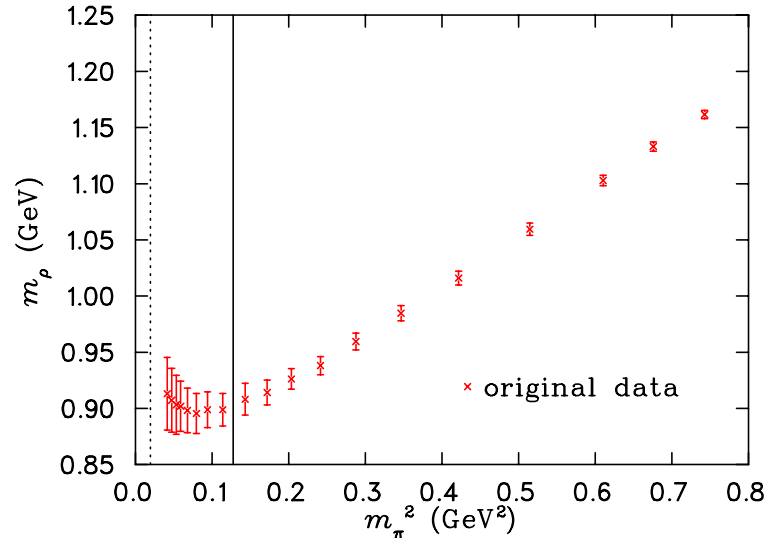
**Figure 6.17:** Quenched lattice QCD data for the ρ meson mass provided by the Kentucky Group. The dashed vertical line indicates the physical pion mass and the solid vertical line shows how the data set is split into two parts.
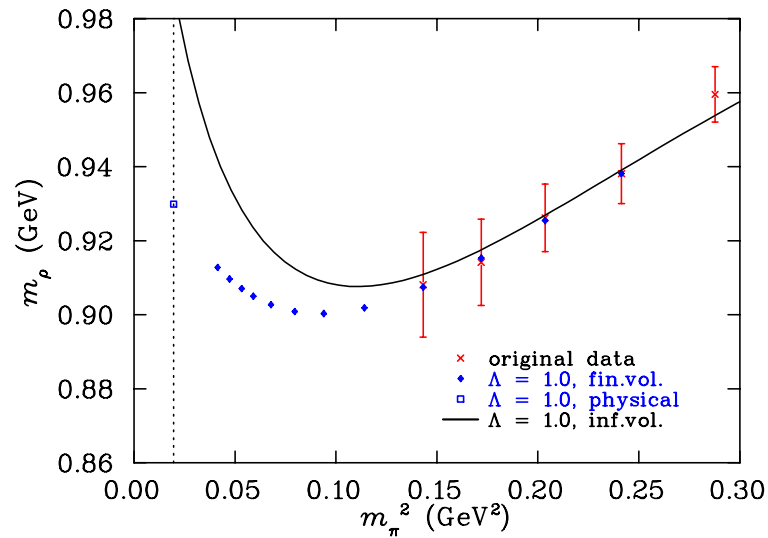


**Figure 6.18:** A test extrapolation based on the four original data points shown. Both the finite- and infinite-volume results are shown for a triple-dipole regulator at $\Lambda = 1.0$ GeV. The dashed vertical line indicates the physical pion mass.
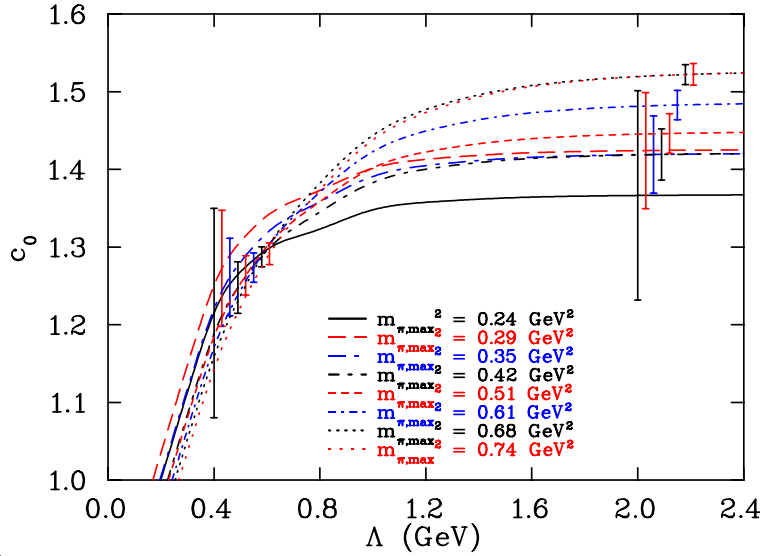
**Figure 6.19:** Behaviour of $c_0$ vs. $\Lambda$ based on Kentucky Group data. A triple-dipole regulator is used. A few points are selected to indicate the general size of the statistical error bars.



**Figure 6.20:** Behaviour of $c_2$ vs. $\Lambda$ based on Kentucky Group data. A triple-dipole regulator is used. A few points are selected to indicate the general size of the statistical error bars.



**Figure 6.21:** Behaviour of $c_4$ vs. $\Lambda$ based on Kentucky Group data. A triple-dipole regulator is used. A few points are selected to indicate the general size of the statistical error bars.
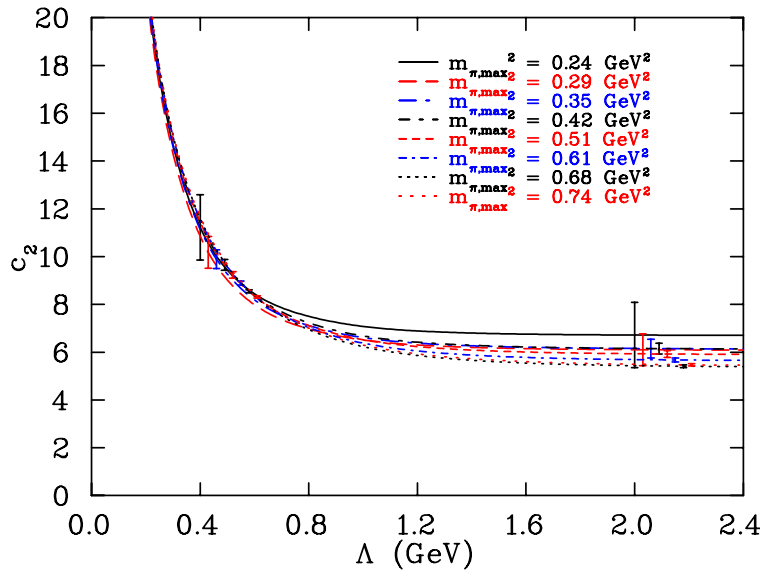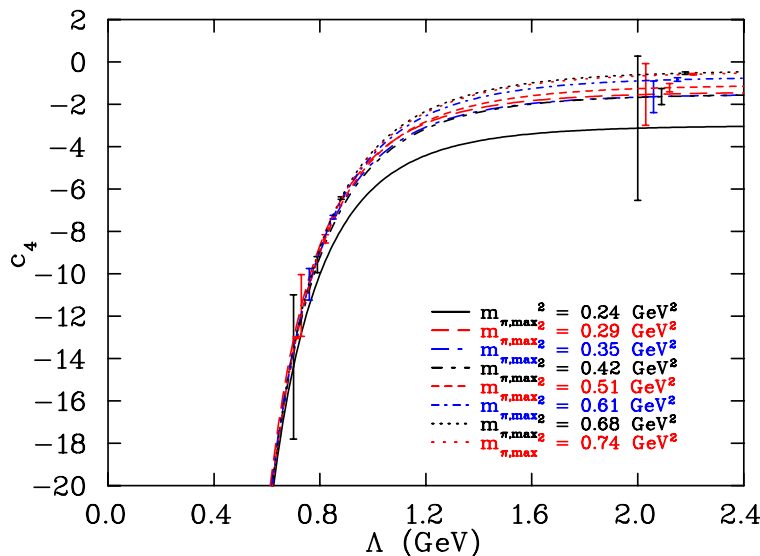
By examining Figures 6.19 through 6.21, increasing $m_{\pi,\mathrm{max}}^2$ leads to greater scale-dependence in the renormalization, since the data sample lies further from the PCR. Since the effective field theory is calculated to a finite chiral order, complete scale-independence across all possible $\Lambda$ values will not occur in practice. An asymptotic value is usually observed in the renormalization flow as $\Lambda$ becomes large, indicating that the higher-order terms of the chiral expansion are effectively zero. However, these asymptotic values of the coefficients are poor estimates of their correct values, as previously demonstrated in the pseudodata analysis in Chapter 4. Instead, the best estimates of the low-energy coefficients lie in the identification of the intersection point of the renormalization flow of these coefficients. It is also of note that, for small values of $\Lambda$, the FRR scheme breaks down, as observed for the nucleon mass in Section 4.2.1. The regularization scale must be at least large enough to include the chiral physics being studied.

## 6.2.2    Intrinsic Scale and Systematic Uncertainties

The optimal regularization scale $\Lambda^{\mathrm{scale}}$ can be obtained from the renormalization flow curves using a chi-square-style analysis. In addition, the analysis will allow the extraction of a variance for $\Lambda^{\mathrm{scale}}$. Knowing how the data are correlated, the systematic errors from the coupling constants and $\Lambda^{\mathrm{scale}}$ will be combined to obtain an error estimate for each extrapolation point. Of particular interest are the values of $m_{\rho,Q}$ at those values of $m_\pi^2$ that are explored in the lattice simulations, but are excluded in the chiral extrapolation. The function $\chi_{dof}^2$ is constructed in the same way as Equations (5.2) and (5.3).

The $\chi_{dof}^2$ plots using a triple-dipole regulator are shown in Figures 6.22 through 6.24. The optimal regularization scale $\Lambda^{\mathrm{scale}}$ is taken to be the central value $\Lambda^{\mathrm{central}}$ of each plot. The upper and lower bounds of $\Lambda$ obey the condition $\chi_{dof}^2 < \chi_{dof,min}^2 + 1/(dof)$. The results for the optimal regularization scales obtained from analyzing each low-energy coefficient, and their associated upper and lower bounds, are shown in Table 6.1. It is remarkable that each low-energy coefficient leads to the same optimal value of $\Lambda$, i.e. $\Lambda_{\mathrm{central}} = 0.67$ GeV. By averaging the results among $c_0$, $c_2$,
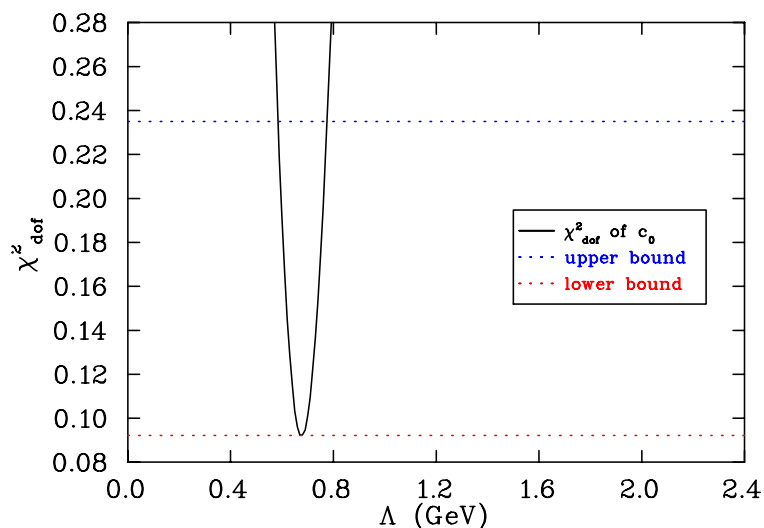
Figure 6.22: $\chi^2_{dof}$ for $c_0$ versus $\Lambda$, corresponding to the renormalization flow curves displayed in Figure 6.19 based on Kentucky Group data. A triple-dipole regulator is used.



Figure 6.23: $\chi^2_{dof}$ for $c_2$ versus $\Lambda$, corresponding to the renormalization flow curves displayed in Figure 6.20 based on Kentucky Group data. A triple-dipole regulator is used.



Figure 6.24: (color online). $\chi^2_{dof}$ for $c_4$ versus $\Lambda$, corresponding to the renormalization flow curves displayed in Figure 6.21 based on Kentucky Group data. A triple-dipole regulator is used.
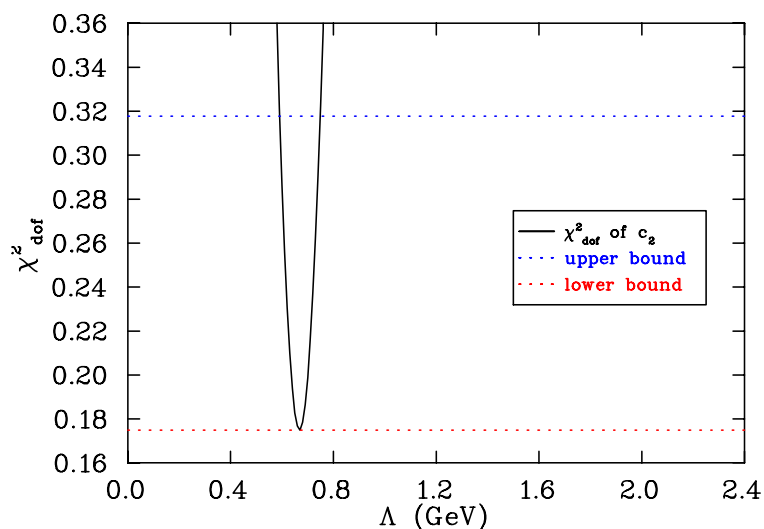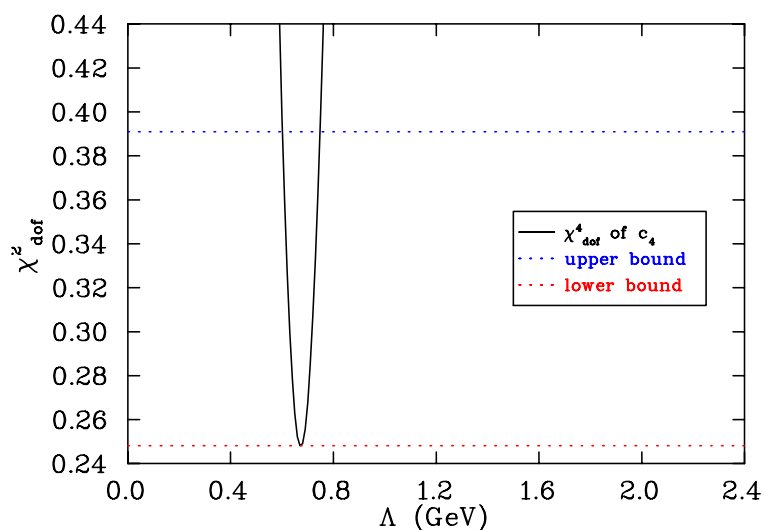
Table 6.1: Values of the central, upper and lower regularization scales, in GeV, obtained from the $\chi^2_{dof}$ analysis of $c_0$, $c_2$ and $c_4$, displayed in Figures 6.22 through 6.24.

| scale (GeV) | $c_0$ (Fig.6.22) | $c_2$ (Fig.6.23) | $c_4$ (Fig.6.24) |
|---|---|---|---|
| $\Lambda_{\text{central}}$ | 0.67 | 0.67 | 0.67 |
| $\Lambda_{\text{upper}}$ | 0.78 | 0.75 | 0.75 |
| $\Lambda_{\text{lower}}$ | 0.58 | 0.59 | 0.60 |

and $c_4$, the optimal regularization scale $\Lambda_{\text{scale}}$ for the quenched ρ meson mass can be calculated for this data set: $\Lambda_{\text{scale}} = 0.67^{+0.09}_{-0.08}$ GeV.

The result of the final extrapolation, using the estimate of the optimal regularization scale $\Lambda_{\text{scale}} = 0.67^{+0.09}_{-0.08}$ GeV, and using the initial data set to predict the low-energy data points, is shown in Figure 6.25. The extrapolation to the physical point obtained for this quenched data set is: $m^{\text{ext}}_{\rho,Q}(m^2_{\pi,\text{phys}}) = 0.925^{+0.053}_{-0.049}$ GeV, an uncertainty of less than 6%.

Each extrapolation point displays two error bars. The inner error bar corresponds to the systematic uncertainty in the parameters only, and the outer error bar corresponds to the systematic and statistical uncertainties of each point added in quadrature. Also, the infinite-volume extrapolation curve is displayed in order to illustrate the effect of finite-volume corrections to the loop integrals.

In Figure 6.26, the extrapolation predictions are compared against the actual simulation results, which were not included in the fit. Both the extrapolations and the simulation results display the same non-analytic curvature near the physical point. Figure 6.27 shows the data plotted with error bars correlated relative to the lightest data point in the original set, $m^2_\pi = 0.143$ GeV$^2$. To highlight the importance of this application of an extended χEFT, a simple linear fit is included in Figure 6.27. By ignoring low-energy chiral physics, the linear fit is statistically incorrect at the physical point. All of the missing original data points are consistent with the extrapolations' systematic uncertainties. After statistical correlations are subtracted, the extrapolated points correspond to an error bar almost half the size of that of the lattice data points. In order to match this precision at low energies, the time required
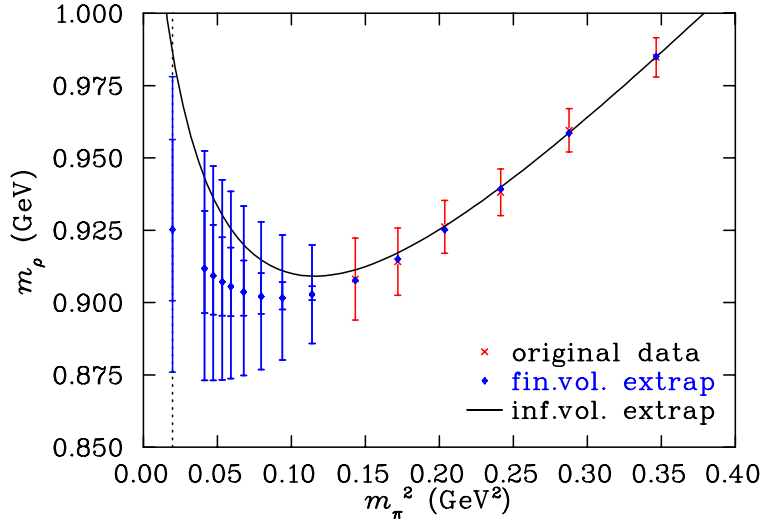
**Figure 6.25:** Extrapolation at $\Lambda_{\text{scale}} = 0.67^{+0.09}_{-0.08}$ GeV based on Kentucky Group data, and using the optimal number of data points, corresponding to $\hat{m}^2_{\pi,\text{max}} = 0.35$ GeV$^2$. The inner error bar on the extrapolation points represents purely the systematic error from parameters. The outer error bar represents the systematic and statistical error estimates added in quadrature.



**Figure 6.26:** Comparison of chiral extrapolation predictions (blue diamond) with Kentucky Group data (red cross). Extrapolation is performed at $\Lambda_{\text{scale}} = 0.67^{+0.09}_{-0.08}$ GeV, and using the optimal number of data points, corresponding to $\hat{m}^2_{\pi,\text{max}} = 0.35$ GeV$^2$. The inner error bar on the extrapolation points represents purely the systematic error from parameters. The outer error bar represents the systematic and statistical error estimates added in quadrature.
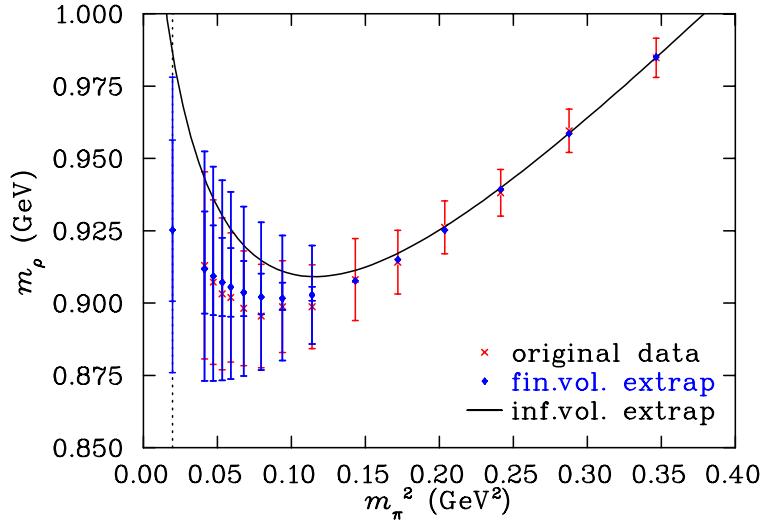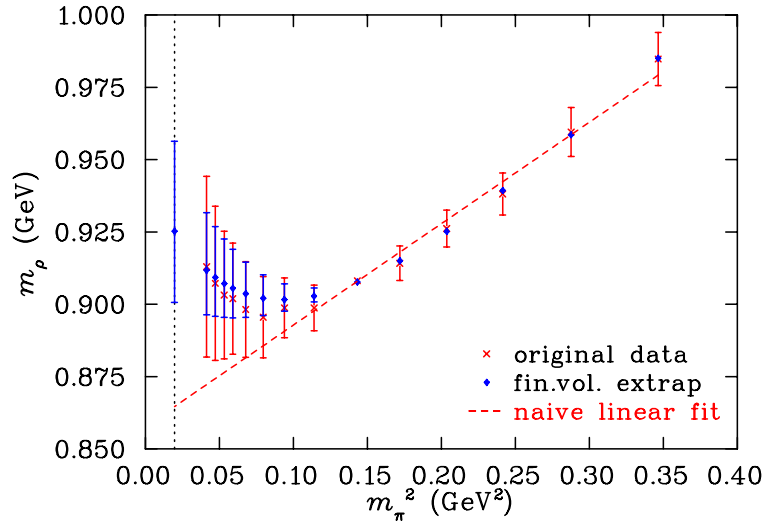
**Figure 6.27:** Comparison of chiral extrapolation predictions (blue diamond) with Kentucky Group data (red cross), with errors correlated relative to the point at $m_\pi^2 = 0.143$ GeV$^2$. Extrapolation is performed at $\Lambda_{\text{scale}} = 0.67^{+0.09}_{-0.08}$ GeV, and using the optimal number of data points, corresponding to $\hat{m}_{\pi,\text{max}}^2 = 0.35$ GeV$^2$. The error bar on the extrapolation points represents the systematic error only. A simple linear fit, on the optimal pion mass region, is included for comparison.

in lattice simulations would increase by approximately four times.

In order to check if scheme-independence is recovered using data within the PCR, the low-energy data that were initially excluded from analysis can now be treated in the same way. That is, renormalization flow curves can be constructed as a function of $\Lambda$ for sequentially increasing $m_{\pi,\text{max}}^2$. The results are shown in Figures 6.28 through 6.30. Clearly, the renormalization flow curves for each plot corresponding to $c_0$, $c_2$ and $c_4$ are flatter than those of the initial analysis, indicating a reduction in the regularization scale-dependence due to the use of data closer to the PCR. One is not able to extract an optimal regularization scale from these plots, as shown in the behaviour of $\chi_{dof}^2$, displayed in Figures 6.31 through 6.33. However, each $\chi_{dof}^2$ curve provides a lower bound for the regularization scale, where FRR breaks down [HLY10], as discussed in Section 6.2.1. These lower bounds are: $\Lambda_{\text{lower}}^{c_0} = 0.39$ GeV, $\Lambda_{\text{lower}}^{c_2} = 0.52$ GeV and $\Lambda_{\text{lower}}^{c_4} = 0.59$ GeV.

The statistical error bars of the low-energy coefficients corresponding to a small number of data points in Figures 6.28 through 6.30 are large, and a statistical difference among the curves does not appear until $m_{\pi,\text{max}}^2 \approx 0.11$ GeV$^2$. Thus the identi-

Figure 6.28: Behaviour of $c_0$ vs. $\Lambda$ for the initially excluded low-energy data. A triple-dipole regulator is used. A few points are selected to indicate the general size of the statistical error bars.



Figure 6.29: Behaviour of $c_2$ vs. $\Lambda$ for the initially excluded low-energy data. A triple-dipole regulator is used. A few points are selected to indicate the general size of the statistical error bars.
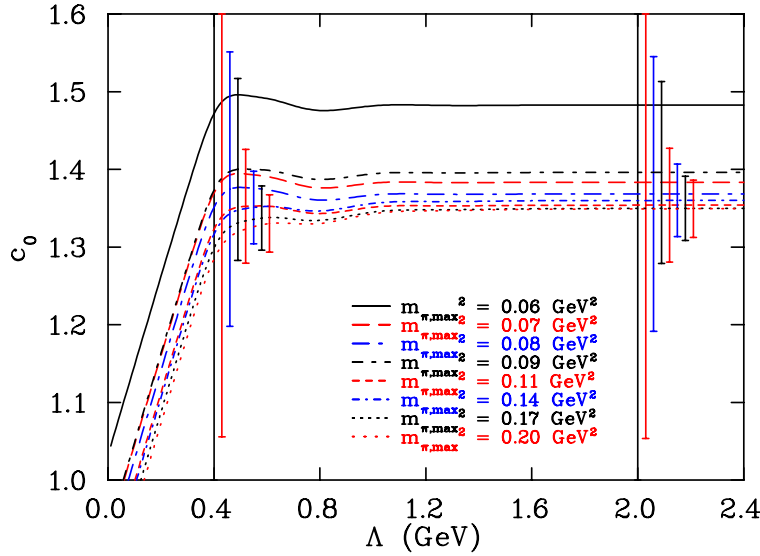


Figure 6.30: Behaviour of $c_4$ vs. $\Lambda$ for the initially excluded low-energy data. A triple-dipole regulator is used. A few points are selected to indicate the general size of the statistical error bars.
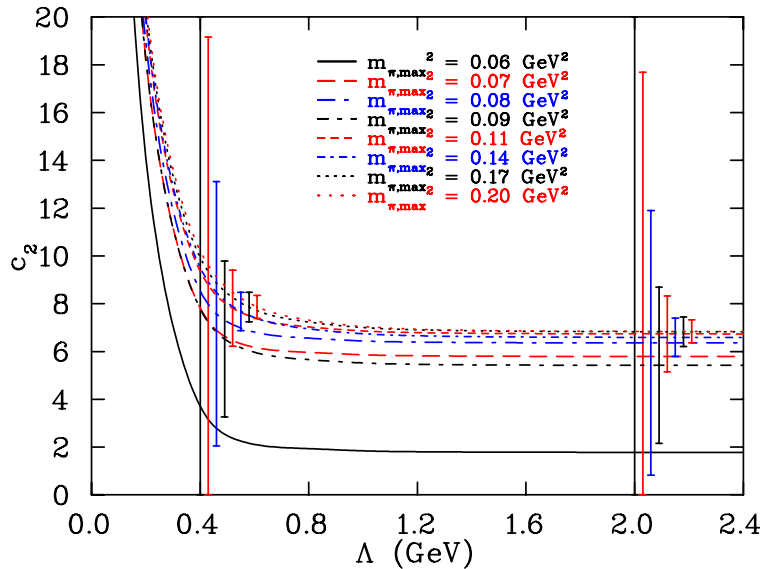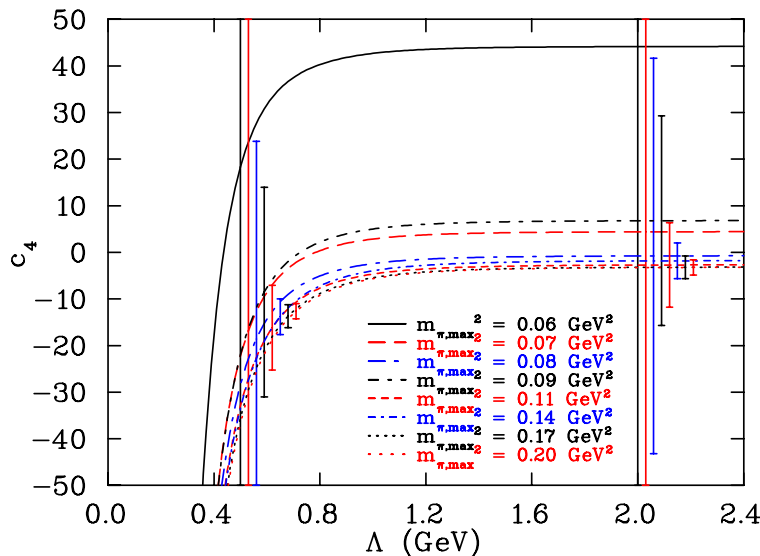
fication of an optimal regularization scale will be aided by incorporating data corresponding to even larger values of $m^2_{\pi,\text{max}}$. By considering *all* of the available data, the behaviour of $\chi^2_{dof}$, as displayed in Figures 6.34 through 6.36, resolve precise optimal regularization scales: $\Lambda^{c0}_{\text{central}} = 0.72$ GeV, $\Lambda^{c2}_{\text{central}} = 0.71$ GeV and $\Lambda^{c4}_{\text{central}} = 0.71$ GeV. The systematic errors obtained from each $\chi^2_{dof}$ curve seem arbitrarily constrained as a consequence of including more data points, which extend well outside the chiral regime, and possibly outside the applicable region of FRR techniques. This issue is addressed in the ensuing section.

### 6.2.3   Optimal Pion Mass Region and Systematic Uncertainties

In this section, a robust method for determining an optimal range of pion masses is presented. This range corresponds to an optimal number of simulation results to be used for fitting. First, consider the extrapolation of the quenched ρ meson mass, which can now be completed. The statistical uncertainties in the values of $c_0$, $c_2$, $c_4$ are dependent on $m^2_{\pi,\text{max}}$. As a consequence, the uncertainty in the extrapolated ρ meson mass $m^{\text{ext}}_{\rho}$ must also be dependent on $m^2_{\pi,\text{max}}$. Since the estimate of the statistical uncertainty in an extrapolated point will tend to decrease as more data are included in the fit, one might naïvely choose to use the largest $m^2_{\pi,\text{max}}$ value possible in the data set. However, at some large value of $m^2_{\pi,\text{max}}$, FRR χEFT will not provide a valid model for obtaining a suitable fit. At this upper bound of applicability for FRR χEFT, the uncertainty in an extrapolated point is dominated by the systematic error in the underlying parameters. This is due to a greater scheme-dependence in extrapolations using data extending outside the PCR, meaning that the extrapolations are more sensitive to changes in the parameters of the loop integrals. Thus there is a balance point $m^2_{\pi,\text{max}} = \hat{m}^2_{\pi,\text{max}}$, where the statistical and systematic uncertainties (added in quadrature) in an extrapolation are minimized.

   In order to obtain this value $\hat{m}^2_{\pi,\text{max}}$, consider the behaviour of the extrapolation of the ρ meson mass to the physical point $m^{\text{ext}}_{\rho,Q}(m^2_{\pi,\text{phys}})$, as a function of $m^2_{\pi,\text{max}}$. Treating the parameters $g_2$, $g_4$, $M^2_0$, $A_0$ and $\Lambda^{\text{scale}}$ as independent, their systematic uncertainties from these sources are added in quadrature. In addition, the systematic

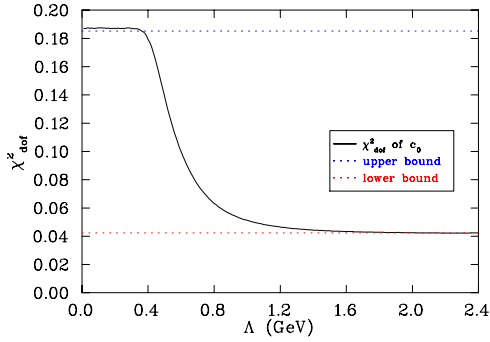Figure 6.31: $\chi^2_{dof}$, for $c_0$ versus $\Lambda$, corresponding to the renormalization flow curves displayed in Figure 6.28. A lower bound for the regularization scale is found: $\Lambda^{c_0}_{\text{lower}} = 0.39$ GeV.



Figure 6.34: $\chi^2_{dof}$, for $c_0$ versus $\Lambda$, corresponding to all available data, including the low-energy set.



Figure 6.32: $\chi^2_{dof}$, for $c_2$ versus $\Lambda$, corresponding to the renormalization flow curves displayed in Figure 6.29. A lower bound for the regularization scale is found: $\Lambda^{c_2}_{\text{lower}} = 0.52$ GeV.



Figure 6.35: $\chi^2_{dof}$, for $c_2$ versus $\Lambda$, corresponding to all available data, including the low-energy set.



Figure 6.33: $\chi^2_{dof}$, for $c_4$ versus $\Lambda$, corresponding to the renormalization flow curves displayed in Figure 6.30. A lower bound for the regularization scale is found: $\Lambda^{c_4}_{\text{lower}} = 0.59$ GeV.
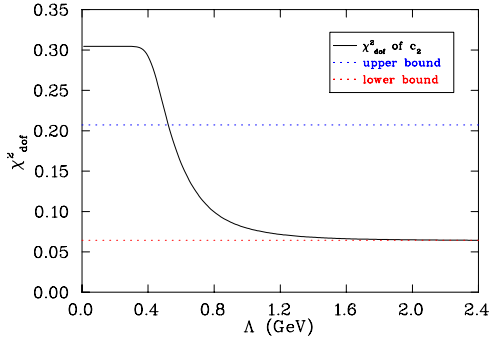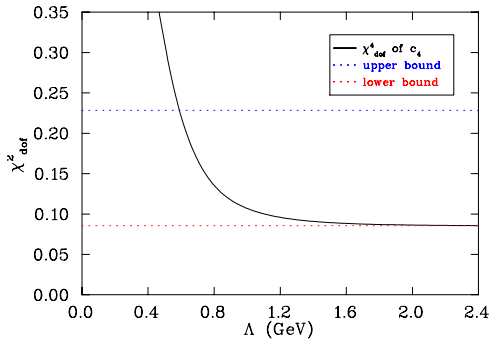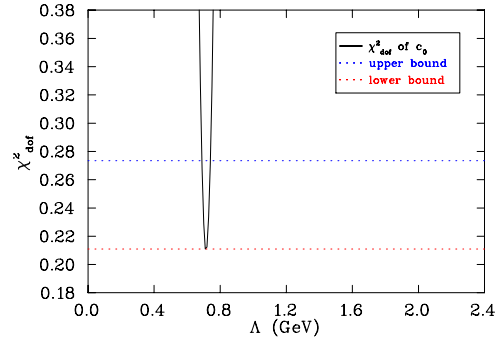


Figure 6.36: $\chi^2_{dof}$, for $c_4$ versus $\Lambda$, corresponding to all available data, including the low-energy set.
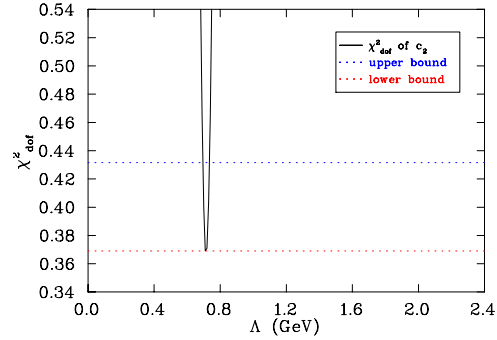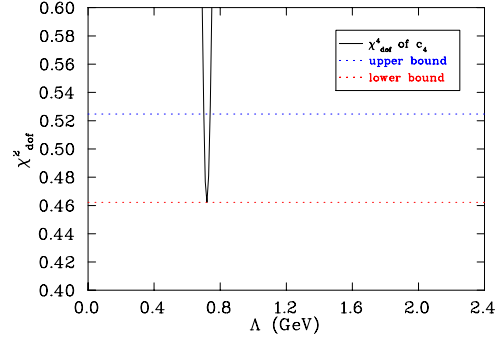
uncertainty due to the choice of the regulator functional form is roughly estimated by comparing the results using the double-dipole and the step function. These functional forms are the two most different forms of the various regulators considered, since the dipole was excluded due to the extra non-analytic contributions it introduces. The results for the initial and complete data sets are shown in Figures 6.37 and 6.38, respectively. Figure 6.37 indicates an optimal value $\hat{m}^2_{\pi,\max} = 0.35 \text{ GeV}^2$, which will be used in the final extrapolations, in order to check the results of this method with the low-energy data. By using only the data contained in the optimal pion mass region, constrained by $\hat{m}^2_{\pi,\max}$, an estimate of the optimal regularization scale may be calculated with a more generous corresponding systematic uncertainty. The value $\Lambda^{\text{scale}} = 0.64 \text{ GeV}$ is the average of $\Lambda^{\text{scale}}_{c_0}$, $\Lambda^{\text{scale}}_{c_2}$ and $\Lambda^{\text{scale}}_{c_4}$ using this method. The $\chi^2_{dof}$ analysis does not provide an upper or lower bound at this value of $\hat{m}^2_{\pi,\max}$. These two estimates of the optimal regularization scale are consistent with each other. Both shall be used and compared in the final analysis. Figure 6.38 indicates an optimal value $\hat{m}^2_{\pi,\max} = 0.20 \text{ GeV}^2$ for the complete data set. A higher density of data in the low-energy region serves to decrease the statistical error estimate of extrapolations to the low-energy region. The corresponding value of $\Lambda^{\text{scale}}$ is unconstrained in this case, since the data lie close to the PCR.

The values of $c_0$, $c_2$ and $c_4$ for both the original data set and the complete data set are shown in Table 6.2, with statistical error estimate quoted first, and systematic uncertainty due to the parameters $g_2$, $g_4$, $M_0^2$, $A_0$, $\Lambda^{\text{scale}}$ and the regulator functional form quoted second. In the case of the original data set, the value of $c_4$ is not well determined, due to the small number of data points used. In the case of the complete data set, the results are dominated by statistical uncertainty, and this also results in an almost unconstrained value of $c_4$. The coefficients of the complete set are less well-determined due to the fact that $\hat{m}^2_{\pi,\max} = 0.20 \text{ GeV}^2$, leaving only low-energy results with large statistical uncertainties for fitting.

The result using the estimate of the optimal regularization scale $\Lambda^{\text{scale}} = 0.64$ GeV, with the systematic uncertainty calculated by varying $\Lambda$ across all suitable values, and using the initial data set, is shown in Figure 6.39. The extrapolation to
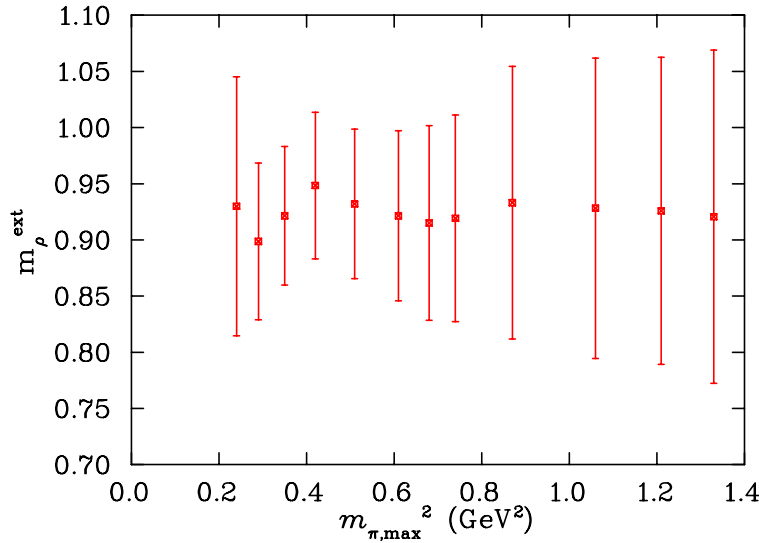
**Figure 6.37:**  Behaviour of the extrapolation of the quenched ρ meson mass to the physical point $m_{\rho,Q}^{\text{ext}}(m_{\pi,\text{phys}}^2)$ vs. $m_{\pi,\text{max}}^2$ using the initial data set, which excludes the lowest mass data points. In each case, $c_0$ is obtained using the scale $\Lambda_{\text{central}}$ (for a triple-dipole regulator) as obtained from the $\chi_{dof}^2$ analysis. The error bars include the statistical and systematic uncertainties in $c_0$ added in quadrature. The optimal value $\hat{m}_{\pi,\text{max}}^2 = 0.35$ GeV$^2$.
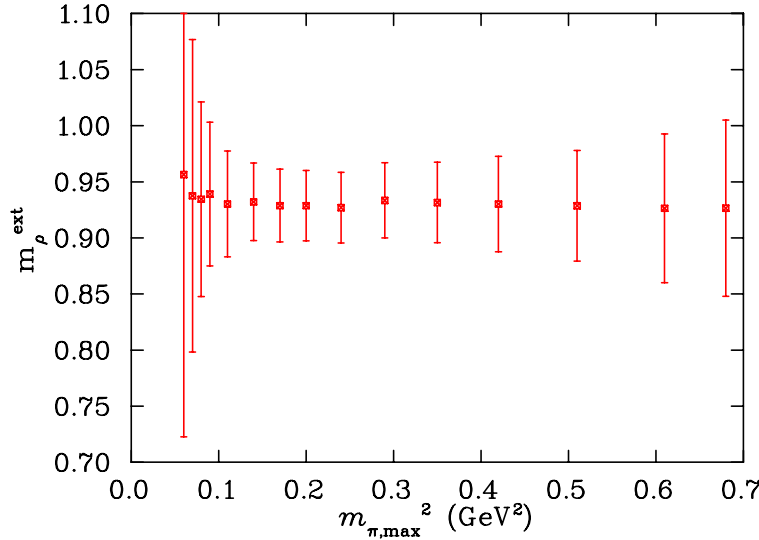


**Figure 6.38:**  Behaviour of the extrapolation of the quenched ρ meson mass to the physical point $m_{\rho,Q}^{\text{ext}}(m_{\pi,\text{phys}}^2)$ vs. $m_{\pi,\text{max}}^2$ using the complete data set, which includes the lowest mass data points. In each case, $c_0$ is obtained using the scale $\Lambda_{\text{central}}$ (for a triple-dipole regulator) as obtained from the $\chi_{dof}^2$ analysis. The error bars include the statistical and systematic uncertainties in $c_0$ added in quadrature. The optimal value $\hat{m}_{\pi,\text{max}}^2 = 0.20$ GeV$^2$.

Table 6.2: The values of $c_0$, $c_2$ and $c_4$ as obtained from both the original data set and the complete set, which includes the low-energy data. In each case, the coefficients are evaluated using the scale $\Lambda_{\text{central}}$ (for a triple-dipole regulator) as obtained from the $\chi^2_{dof}$ analysis. The value of $m^2_{\pi,\text{max}}$ used is that which yields the smallest error bar in adding statistical and systematic uncertainties in quadrature. For the initial data set, $\hat{m}^2_{\pi,\text{max}} = 0.35$ GeV$^2$. For the complete data set, $\hat{m}^2_{\pi,\text{max}} = 0.20$ GeV$^2$. The statistical uncertainty is quoted in the first pair of parentheses, and the systematic uncertainty is quoted in the second pair of parentheses. For the original data set, $c_4$ is not well determined, with only a small number of data. For the complete data set, large statistical uncertainties result in an almost unconstrained value of $c_4$. The coefficients of the complete set are less well-determined due to the fact that $\hat{m}^2_{\pi,\text{max}} = 0.20$ GeV$^2$, leaving only low-energy results with large statistical uncertainties for fitting.

|              | $c_0(\text{GeV}^2)$ | $c_2$ | $c_4(\text{GeV}^{-2})$ |
|--------------|---------------------|-------|------------------------|
| original set | 1.31(5)(17)         | 7.9(4)(26) | $-16.2(8)(382)$   |
| complete set | 1.35(4)(241)        | 6.8(5)(31) | $-3.3(17)(361)$   |

the physical point obtained for this quenched data set is: $m^{\text{ext}}_{\rho,Q}(m^2_{\pi,\text{phys}}) = 0.922^{+0.065}_{-0.060}$ GeV, an uncertainty of approximately 7%. Figure 6.40 shows the data plotted with error bars correlated relative to the lightest data point in the original set, $m^2_\pi = 0.143$ GeV$^2$, using $\Lambda_{\text{scale}} = 0.64$ GeV, and varying $\Lambda$ across its full range of values. This naturally increases the estimate of the systematic uncertainty of the extrapolations, but also serves to demonstrate how closely the results from lattice QCD and χEFT match.

## 6.3   Summary and Specific Issues for the Quenched ρ Meson

A technique for isolating an optimal regularization scale was investigated in QQCD through an examination of the quenched ρ meson mass. The result is a successful extrapolation based on an extended χEFT procedure. By using quenched lattice QCD results that extended beyond the PCR, an optimal regularization scale was obtained from the renormalization flow of the low-energy coefficients $c_0$, $c_2$ and $c_4$. The optimal scale is found to be $\Lambda^{\text{scale}} = 0.67^{+0.09}_{-0.08}$ GeV. An optimal value of the maximum pion mass used for fitting was also calculated, and was found to be
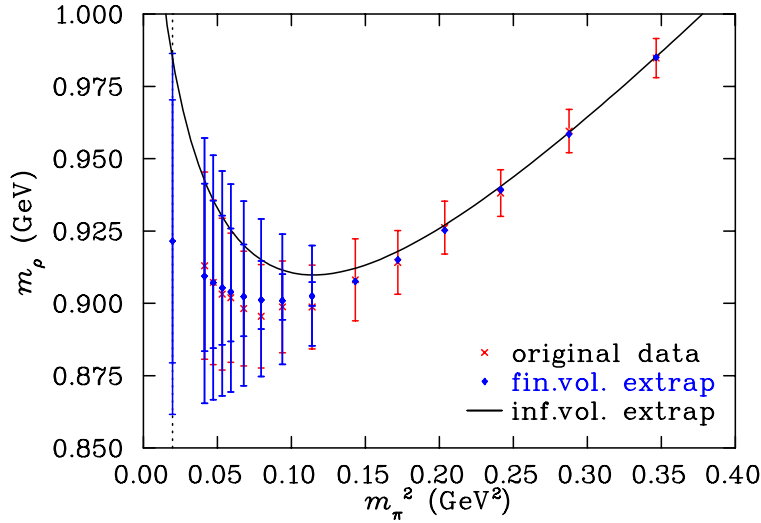
**Figure 6.39:**  Comparison of chiral extrapolation predictions (blue diamond) with Kentucky Group data (red cross). Extrapolation is performed at $\Lambda_{\text{scale}} = 0.64$ GeV, varied across the whole range of $\Lambda$ values, and using the optimal number of data points, corresponding to $\hat{m}^2_{\pi,\text{max}} = 0.35$ GeV$^2$. The inner error bar on the extrapolation points represents purely the systematic error from parameters. The outer error bar represents the systematic and statistical error estimates added in quadrature.
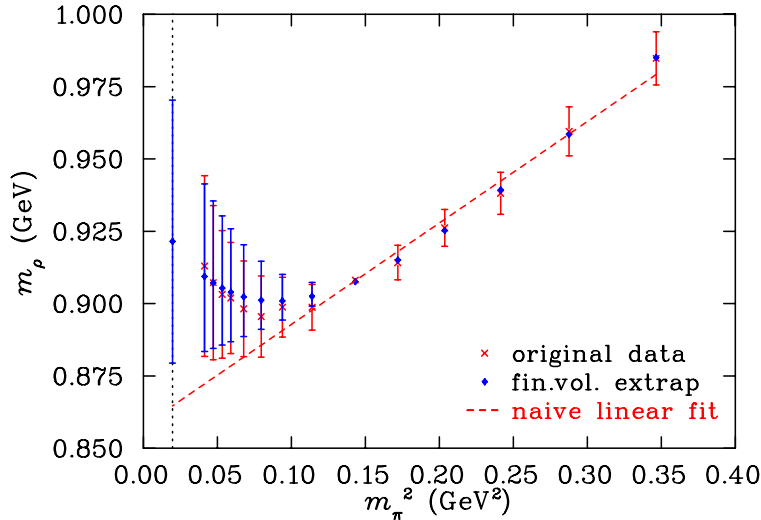


**Figure 6.40:**  Comparison of chiral extrapolation predictions (blue diamond) with Kentucky Group data (red cross), with errors correlated relative to the point at $m^2_\pi = 0.143$ GeV$^2$. Extrapolation is performed at $\Lambda_{\text{scale}} = 0.64$ GeV, varied across the whole range of $\Lambda$ values, and using the optimal number of data points, corresponding to $\hat{m}^2_{\pi,\text{max}} = 0.35$ GeV$^2$. The error bar on the extrapolation points represents the systematic error only. A simple linear fit, on the optimal pion mass region, is included for comparison.

$\hat{m}_{\pi,\text{max}}^2 = 0.35$ GeV$^2$.  By using only the data contained in the optimal pion mass region, constrained by $\hat{m}_{\pi,\text{max}}^2$, a value $\Lambda^{\text{scale}} = 0.64$ GeV is estimated for the optimal regularization scale, with a wider systematic uncertainty corresponding to the entire range of values of $\Lambda$.  These two estimates of the optimal regularization scale are consistent with each other.

The mass of the ρ meson was calculated in the low-energy region.  At the physical point, the result of the extrapolation, using $\Lambda^{\text{scale}} = 0.67^{+0.09}_{-0.08}$ GeV, is: $m_{\rho,Q}^{\text{ext}}(m_{\pi,\text{phys}}^2) = 0.925^{+0.053}_{-0.049}$ GeV. The result of the extrapolation, using $\Lambda^{\text{scale}} = 0.64$ GeV, with the systematic uncertainty calculated by varying $\Lambda$ across all suitable values, is: $m_{\rho,Q}^{\text{ext}}(m_{\pi,\text{phys}}^2) = 0.922^{+0.065}_{-0.060}$ GeV. The extrapolation also correctly predicts the low-energy curvature that was observed when the low-energy lattice simulation results were revealed.

Since there exists no experimental value for the mass of a particle in the quenched approximation, this analysis demonstrates the ability of the technique to make predictions without phenomenologically motivated bias. The results clearly indicate a successful procedure for using lattice QCD data outside the PCR to extrapolate an observable to the chiral regime.

# Chapter 7

# Electromagnetic Properties of the Nucleon

*"[W]e can establish the key to our conclusion:* the datum and the result are logically equivalent.*"* (Omnès, R. 2002. *Quantum Philosophy: Understanding and Interpreting Contemporary Science* p.209) [Omn02]

In this chapter, the focus is turned to the magnetic moment and the electric charge radius of the nucleon. The magnetic moment is often studied for the physical significance of its anomalous component, obtained from the Pauli form factor $F_2$ (defined in Equation (3.76)). Since electrically charged pions with non-zero angular momentum dress the nucleon, they contribute non-trivially to its magnetic moment, altering the value from its semi-classical Dirac value. Likewise, the electric charge radius, or more precisely, the gradient of the Sachs electric form factor $G_E$ in the soft-photon limit, provides a phenomenological test of quantum chromodynamics (QCD) theory. The leading-order low-energy contributions from virtual processes provide non-analytic behaviour in the chiral expansion. Chiral extrapolations for an infinite-volume box agree with experiment at the physical point, as will be evident later in this chapter. It is of interest in this investigation to determine if an optimal regularization scale may also be extracted from lattice QCD results for these two observables. If so, it would provide compelling evidence for the existence of an intrinsic scale for the source of the pion cloud of the nucleon.

In lattice QCD, the isovector combination of the nucleon is often calculated, as described in Section 2.1.3. Feynman diagrams including any photons coupling to sea-quark loops cancel in the case of the isovector, and the distinction between VQCD and full QCD vanishes. This is fortunate, since the calculation of the disconnected loops is computationally expensive. As a result, preliminary lattice QCD isovector results for two-flavor $O(a)$-improved Wilson quark action from the QCDSF Collaboration are analyzed.

The magnetic moment and the electric charge radius can each be written as chiral expansions, ordered in $m_\pi^2$, due to the Gell-Mann$-$Oakes$-$Renner Relation from Equation (3.43) in Chapter 3. Each expansion comprises a polynomial residual series, and loop integrals that contribute to non-analytic chiral behaviour. The diagrams that correspond to the leading-order loop integrals are shown in Figures 7.1 through 7.3.

# 7.1   Renormalization of the Magnetic Moment

## 7.1.1   Chiral Expansion of the Magnetic Moment

Recalling the definition of the magnetic moment of the isovector nucleon in Equation (3.80), the chiral expansion is as follows:

$$\mu_n^{\text{isov}} = a_0^\Lambda + a_2^\Lambda m_\pi^2 + \mathcal{T}_N^\mu(m_\pi^2;\Lambda) + \mathcal{T}_\Delta^\mu(m_\pi^2;\Lambda) + O(m_\pi^4),  \tag{7.1}$$

for loop integrals denoted ($\mathcal{T}$) to differentiate them from the self energies. In this instance, only two free parameters are chosen, since the non-analytic contributions are included only to chiral order $O(m_\pi^2 \log m_\pi)$. For a process with zero mass-splitting, such as that shown in the diagram in Figure 7.1, the leading-order non-analytic term is proportional to $m_\pi$; a lower chiral order than the leading-order term in the nucleon mass expansion. As a result, greater chiral curvature is expected, and the automatic renormalization process introduced in Chapter 4 will be constructed only to order $O(m_\pi^0)$, that is, for the chiral coefficient $c_0$. The fully renormalized chiral expansion
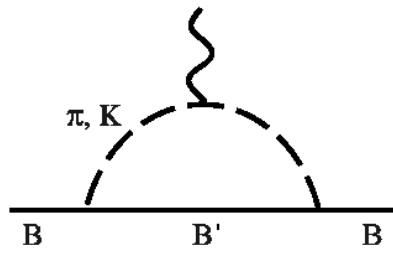
Figure 7.1: The pion/kaon loop contribution (with photon attachment) to the magnetic moment and the electric charge radius of an octet baryon $B$, allowing a transition to a baryon $B'$. All charge conserving transitions are implicit.
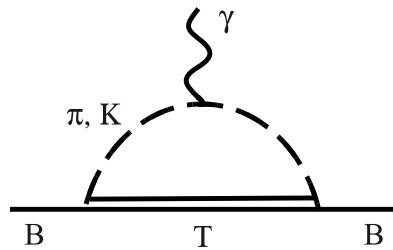


Figure 7.2: The pion/kaon loop contribution (with photon attachment) to the magnetic moment and the electric charge radius of an octet baryon $B$, allowing a transition to a nearby and strongly-coupled decuplet baryon $T$.
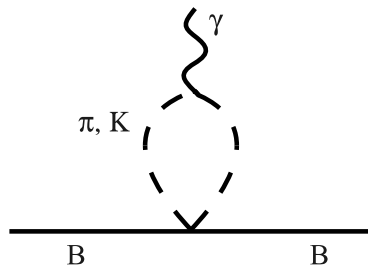


Figure 7.3: The tadpole contribution at $O(m_q)$ (with photon attachment) to the electric charge radius of an octet baryon $B$.

may be written to leading non-analytic order $O(m_\pi)$ as:

$$\mu_n^{\text{isov}} = c_0 + \chi_N^\mu m_\pi + O(m_\pi^2)\,, \tag{7.2}$$

where $\mu$ is an implicit mass scale. Note also that the diagram in Figure 7.3 does not contribute to the magnetic moment of the nucleon since, in this case, the photon couples to spinless pseudo-Goldstone bosons that have no orbital angular momentum.

## 7.1.2   Chiral Loop Integrals

Each loop integral has a solution in the form of a polynomial expansion analytic in $m_\pi^2$ plus non-analytic terms, of which the leading-order term is of particular interest:

$$\mathcal{T}_N^\mu(m_\pi^2;\Lambda) = b_0^{\mu,\Lambda,N} + \chi_N^\mu m_\pi + b_2^{\mu,\Lambda,N} m_\pi^2 + O(m_\pi^3), \tag{7.3}$$

$$\mathcal{T}_\Delta^\mu(m_\pi^2;\Lambda) = b_0^{\mu,\Lambda,\Delta} + b_2^{\mu,\Lambda,\Delta} m_\pi^2 + \chi_\Delta^\mu m_\pi^2 \log m_\pi/\mu + O(m_\pi^3), \tag{7.4}$$

where $\mu$ is a mass scale associated with the logarithm.

The corresponding loop integrals can be expressed in a convenient form by taking the non-relativistic heavy-baryon limit, and performing the pole integration for $k_0$. The integral corresponding to the diagram in Figure 7.1 takes the form [WLTY07, WLTY09a]:

$$\tilde{\mathcal{T}}_N^\mu(m_\pi^2;\Lambda) = \frac{-\chi_N^\mu}{\pi^2}\int d^3k \frac{(\hat{q}\times\vec{k})^2 u^2(k;\Lambda)}{(k^2+m_\pi^2)^2} - b_0^{\mu,\Lambda,N} \tag{7.5}$$

$$= \frac{-\chi_N^\mu}{\pi^2}\int d^3k \frac{k_\perp^2 u^2(k;\Lambda)}{(k^2+m_\pi^2)^2} - b_0^{\mu,\Lambda,N} \tag{7.6}$$

$$= \frac{-\chi_N^\mu}{3\pi^2}\int d^3k \frac{k^2 u^2(k;\Lambda)}{(k^2+m_\pi^2)^2} - b_0^{\mu,\Lambda,N}, \tag{7.7}$$

where $\hat{q}$ is the direction of the external momentum introduced by an incoming photon. The argument for this substitution of the perpendicular part $k_\perp$ is expounded in Appendix B.1.1. The function $u(k;\Lambda)$ is the regulator, with associated momentum cut-off scale $\Lambda$. In this case, a dipole regulator will be used (corresponding to a choice of $n = 1$ in Equation (3.105) in Chapter 3). Since the working-order $O(m_\pi^2 \log m_\pi)$ of the calculation is less than in the case of the nucleon mass analysis, there is a reduced possibility of extra scale-dependent non-analytic terms frustrating the chiral fit. Thus, ensuring that these scale-dependent non-analytic terms are removed from the chiral expansion is not so vital, and a dipole form is an acceptable choice of regulator. The integral corresponding to the diagram in Figure 7.2 takes

the form:

$$\tilde{\mathcal{T}}_\Delta^\mu(m_\pi^2;\Lambda) = \frac{-\chi_\Delta^\mu}{\pi^2} \int d^3k \frac{k_\perp^2 (2\omega(k)+\Delta)u^2(k;\Lambda)}{2\omega^3(k)[\omega(k)+\Delta]^2} - b_0^{\mu,\Lambda,\Delta} \tag{7.8}$$

$$= \frac{-\chi_\Delta^\mu}{3\pi^2} \int d^3k \frac{k^2 (2\omega(k)+\Delta)u^2(k;\Lambda)}{2\omega^3(k)[\omega(k)+\Delta]^2} - b_0^{\mu,\Lambda,\Delta}, \tag{7.9}$$

where $\omega(k) = \sqrt{k^2+m_\pi^2}$ and $\Delta$ is the mass-splitting. The chiral coefficients $\chi_N^\mu$ and $\chi_\Delta^\mu$ are constants in terms of the chiral Lagrangian of Equation (3.68) in Chapter 3:

$$\chi_N^{\mu,p} = -\frac{M_N}{8\pi f_\pi^2}(D+F)^2 = -\chi_N^{\mu,n}, \tag{7.10}$$

$$\chi_\Delta^{\mu,p} = -\frac{M_N}{8\pi f_\pi^2}\frac{2C^2}{9} = -\chi_\Delta^{\mu,n}. \tag{7.11}$$

On the finite-volume lattice, each momentum component is quantized in units of $2\pi/L$, that is, $k_i = n_i 2\pi/L$ for integers $n_i$. Finite-volume corrections $\delta^{\mu,\mathrm{FVC}}$ are written as the difference between the finite sum and the corresponding integral. It is known that the finite-volume corrections saturate to a fixed result for large values of regularization scale [HLY10]. As before, this is achieved in practice by evaluating the finite-volume corrections with fixed regularization scale: $\Lambda' = 2.0$ GeV. The finite-volume version of Equation (7.1) can thus be expressed as:

$$\mu_n = c_0 + a_2^\Lambda m_\pi^2 + (\tilde{\mathcal{T}}_N^\mu(m_\pi^2;\Lambda) + \delta_N^{\mu,\mathrm{FVC}}(m_\pi^2;\Lambda'))$$

$$+ (\tilde{\mathcal{T}}_\Delta(m_\pi^2;\Lambda) + \delta_\Delta^{\mu,\mathrm{FVC}}(m_\pi^2;\Lambda')) + O(m_\pi^4). \tag{7.12}$$

## 7.2  Evidence for an Intrinsic Scale in the Magnetic Moment

The analysis of the magnetic moment of the nucleon provides an excellent check for the identification of an intrinsic scale in the nucleon-pion interaction. Using chiral effective field theory ($\chi$EFT), it has been demonstrated in Chapter 5 that lattice QCD results for the nucleon mass have an energy scale embedded within them. This prop-

erty is a consequence of the small size of the power-counting regime (PCR), where the expansion formulae of chiral perturbation theory ($\chi$PT) hold formally. Since a selection of lattice QCD results reasonable for fitting an extrapolation invariably extend outside the restrictive PCR [LTY05], the validity of a formal scheme for extrapolation, and for identifying the leading-order terms in the chiral expansion, is compromised. Fortunately, a finite-range regularization (FRR) scheme, in conjunction with $\chi$EFT as described in Chapter 4, provides a robust method for achieving an extrapolation to physical quark masses, and identifying an intrinsic scale embedded within lattice QCD results.

Recall that the method proceeds by analyzing the behaviour of the renormalization of one or more low-energy coefficients of the chiral expansion as a function of the FRR scale. Ideally, that is, with lattice QCD results constrained entirely within the PCR, the renormalized coefficients should be independent of regularization scale. However, in practice, a scale-dependence is observed; particularly for data sets including data points corresponding to large quark masses. By truncating the lattice QCD results at different values of $m^2_{\pi,\text{max}}$, an optimal FRR scale can be identified. This optimal scale is the value of $\Lambda$ at which the low-energy coefficient under analysis is least sensitive to the truncation of the lattice data. If the optimal scale is consistent among the analyses of magnetic moment and the nucleon mass in Chapter 5, it provides evidence for an intrinsic scale in the nucleon.

The preliminary QCDSF results for the magnetic moment at a variety of $m^2_\pi$ values are displayed in Figure 7.4. The experimental value is also marked. The set of data is listed in Appendix C, Table C.5. The lattice sizes of each data point vary from 1.43 to 3.04 fm using $N_f = 2$ and $O(a)$-improved Wilson quark action. A simple linear fit is included in this plot, which does not take into account the chiral loop integrals, nor the finite-volume corrections to the data. Therefore, it is not surprising that the linear fit fails to reach the experimental value of the magnetic moment at the physical pion mass. Since the lattice QCD results extend outside the PCR, the result of an extrapolation that includes the chiral loop integrals will be scale-dependent. However, the scale-dependence may be ameliorated using the
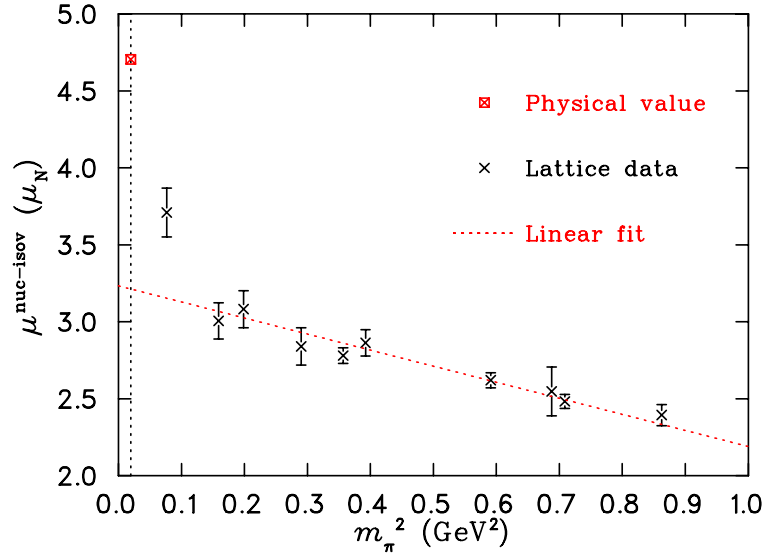
**Figure 7.4:** Preliminary lattice QCD data for $\mu_n^{\text{isov}}$ from QCDSF, with the physical value from experiment as marked.

procedure, which obtains both an optimal regularization scale and an estimate of its systematic uncertainty, constrained by the lattice results.

## 7.2.1  Renormalization Flow Analysis

In order to obtain the optimal regularization scale, the low-energy coefficient $c_0$ from Equation (7.12) will be calculated across a range of values of regularization scale $\Lambda$. Thus the renormalization flow can be constructed. Multiple renormalization flow curves may be obtained by constraining the fit window by a maximum, $m_{\pi,\text{max}}^2$, and sequentially adding data points to extend further outside the PCR. The renormalization flow curves for a dipole regulator are plotted on the same set of axes in Figure 7.5. Note that each data point plotted has an associated error bar, but for the sake of clarity only a few points are selected to indicate the general size of the statistical error bars. As more data are included in the fit, a greater degree of scale-dependence is observed. There is a reasonably well-defined value of $\Lambda$ at which the renormalization of $c_0$ is least sensitive to the truncation of the data: $\Lambda^{\text{scale}} \approx 1.1$ GeV. This indicates the optimal regularization scale embedded within the lattice QCD results themselves.
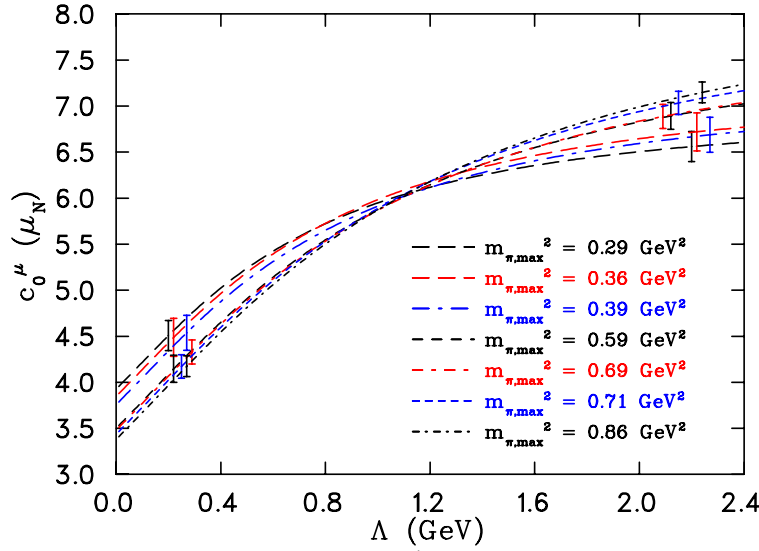
Figure 7.5:   The renormalization flow of $c_0$ for $\mu_n^{\text{isov}}$ obtained using a dipole regulator, based on lattice QCD data from QCDSF.
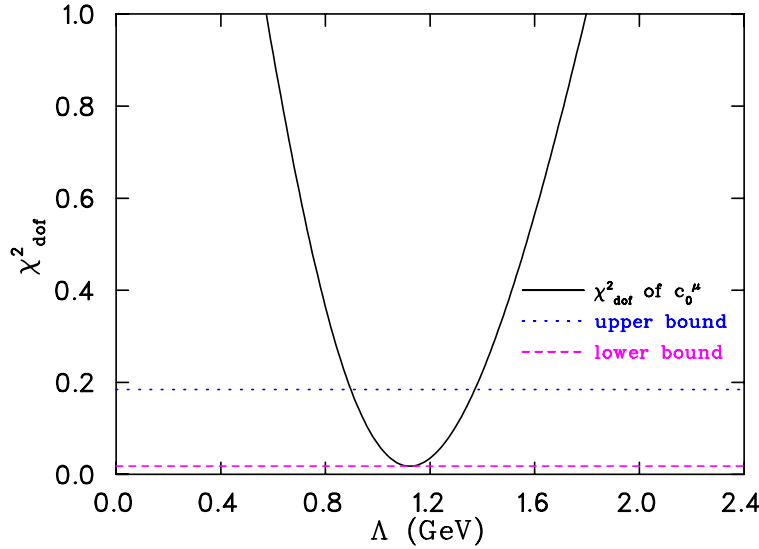


Figure 7.6:   $\chi_{dof}^2$ for the renormalization flow of $c_0$ for $\mu_n^{\text{isov}}$ obtained using a dipole regulator, based on lattice QCD data from QCDSF.

## 7.2.2   Analysis of Systematic Uncertainties

The optimal regularization scale for a dipole form can be more precisely extracted from Figure 7.5 using the chi-square-style analysis. Such an analysis will also provide a measure of the systematic uncertainty in the optimal regularization scale. By plotting $\chi_{dof}^2$ against the regularization scale $\Lambda$, where $dof$ equals the number of curves $n$ minus one for the fit parameter $c_0$, a measure of the spread of the renor-

malization flow curves can be calculated, and the intersection point obtained. The $\chi^2_{dof}$ plot corresponding to Figure 7.5 is shown in Figure 7.6. The optimal regularization scale $\Lambda^{\text{scale}}$ is taken to be the central value $\Lambda^{\text{central}}$ of the plot, and the upper and lower bounds obey the condition $\chi^2_{dof} < \chi^2_{dof,min} + 1/(dof)$. Thus the optimal regularization scale for a dipole regulator is: $\Lambda^{\text{scale}} = 1.13^{+0.22}_{-0.20}$ GeV. This value is consistent with the optimal regularization scale obtained for the nucleon mass using a dipole form, based on lattice QCD results in Chapter 5. Recall that the mean value for the optimal regularization scale from the nucleon mass analysis is: $\bar{\Lambda}^{\text{scale}}_{\text{dip}} \approx 1.3$ GeV. This provides evidence that the optimal regularization scale is associated with an intrinsic scale characterizing the size of the nucleon, as probed by the pion.

### 7.2.3   Chiral Extrapolation Results

Using the optimal regularization scale, extrapolations or interpolations can be made to any quark mass. Consider the behaviour of the magnetic moment as a function of the quark mass as shown in Figure 7.7 (in physical units). Here, the finite-volume expansion of Equation (7.12) is constrained by the lattice results from several different volumes. Extrapolation curves are then plotted for infinite volume and a variety of finite volumes at which current lattice QCD results are produced. For each curve, only the values for which $m_\pi L > 3$ are plotted, provisionally, to avoid undesired effects of the $\varepsilon$-regime. The infinite-volume extrapolation to the physical point is within 2% of the experimentally derived value: $\mu^{\text{isov}}_n = 4.6798\mu_N$. The finite-volume extrapolations are useful for estimating the result of a lattice QCD calculation at certain box sizes. This can provide a benchmark for estimating the outcome of a lattice QCD simulation at larger and untested box sizes. Note that even a relatively standard 3 fm lattice box length will differ significantly from the experimental value at the physical point. Since the data points in Figure 7.7 are at differing finite volumes, the infinite-volume corrected data are also displayed in Figure 7.8.
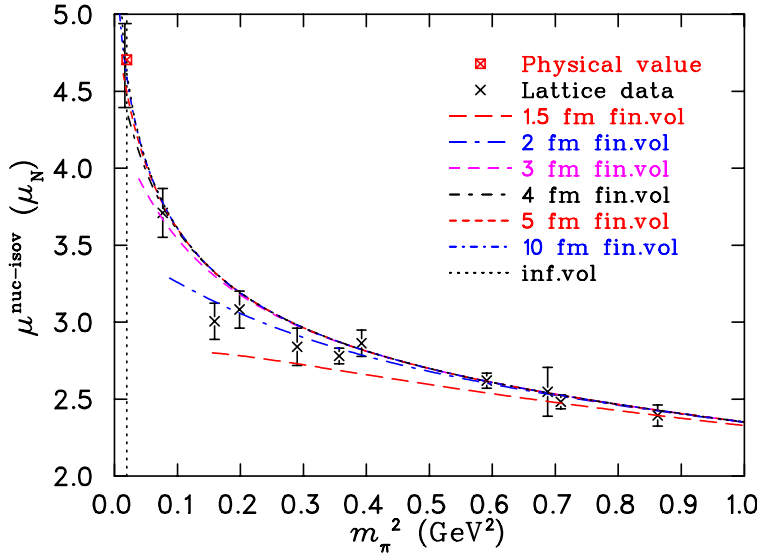
**Figure 7.7:** Extrapolations of $\mu_n^{\text{isov}}$ at different finite volumes and infinite volume, using a dipole regulator, based on lattice QCD data from QCDSF, lattice sizes: $1.43 - 3.04$ fm. The provisional constraint $m_\pi L > 3$ is used. The physical value from experiment is marked. An estimate in the uncertainty in the extrapolation due to $\Lambda^{\text{scale}}$ has been calculated from Figure 7.6, and is indicated at the physical value of $m_\pi^2$. The curve corresponding to a lattice size of 10 fm is almost indistinguishable from the infinite-volume curve.
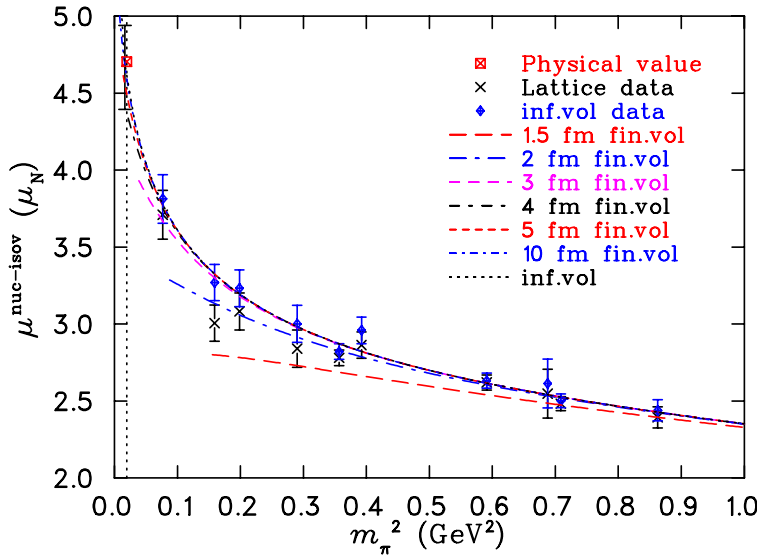


**Figure 7.8:** Extrapolations of $\mu_n^{\text{isov}}$ at different finite volumes and infinite volume, using a dipole regulator, based on lattice QCD data from QCDSF, lattice sizes: $1.43 - 3.04$ fm. The provisional constraint $m_\pi L > 3$ is used. The infinite-volume corrected data points are shown. The physical value from experiment is marked. An estimate in the uncertainty in the extrapolation due to $\Lambda^{\text{scale}}$ has been calculated from Figure 7.6, and is indicated at the physical value of $m_\pi^2$. The curve corresponding to a lattice size of 10 fm is almost indistinguishable from the infinite-volume curve.

# 7.3    Finite-Volume Considerations for the Electric Charge Radius

Reliable extrapolations take into account finite-volume effects, as well as leading-order chiral loop corrections. In many cases, calculating the finite-volume corrections to loop integrals poses no essential problems. Examples of χEFT analyses accounting for finite-volume effects can be found in References [Bea04b, HLY10].

However, the treatment of the electric charge radius is more challenging. Once form factors have been extracted from the lattice simulation, they are typically converted directly into charge radii, The essential difficulty lies in the definition of the charge 'radius' at finite volume. In order to define the radius, a derivative in the momentum transfer $Q^2 = \vec{q}^2 - q_0^2$ (at $Q^2 = 0$) must be applied to the electric form factor. This approach breaks down on the lattice, where only discrete momentum values are allowed.

In this chapter, a method is outlined for handling finite-volume corrections to a given lattice simulation result. It will be discovered that the finite-volume corrections to the loop integrals must be applied before the conversion from form factor to charge radius. By applying the finite-volume corrections directly to the electric form factor, and ensuring that the procedure preserves the electric charge normalization, an extrapolation in $Q^2$ may be used to construct an infinite-volume charge radius. The infinite-volume charge radius can be defined as normal. A finite-volume charge radius may also be defined, as long as an allowed value of $Q^2$ is used in the conversion from infinite to finite volume.

The first challenge involves the definition of the electric charge radius in terms of this derivative in Equation (3.82). Since only certain, discrete values of momenta are allowed on the lattice, the derivative may only be constructed from these allowed momenta when calculating finite-volume corrections. This crucial observation becomes apparent when a comparison is made between the loop integrals evaluated at allowed, and unallowed, values of momentum transfer, respectively. The comparison is shown in Figures 7.9 and 7.10, for momentum $q = (2\pi n/L)$, on the lattice. Here,

Figure 7.9: Finite-volume correction for the loop integral contributing to $G_E$, with $q = q_{min}$. The choice of $q/2 = q_{min}/2$ is not an allowed value on the lattice. The momentum translated and untranslated behaviour of the finite-volume correction are inconsistent with each other.



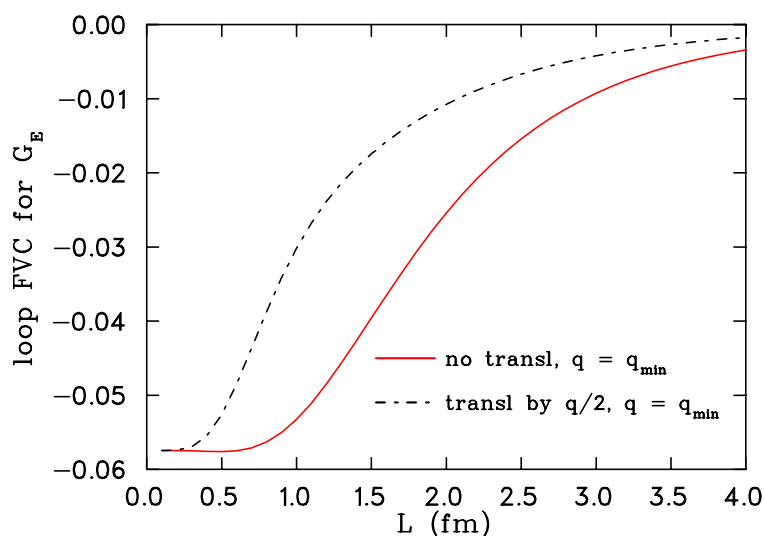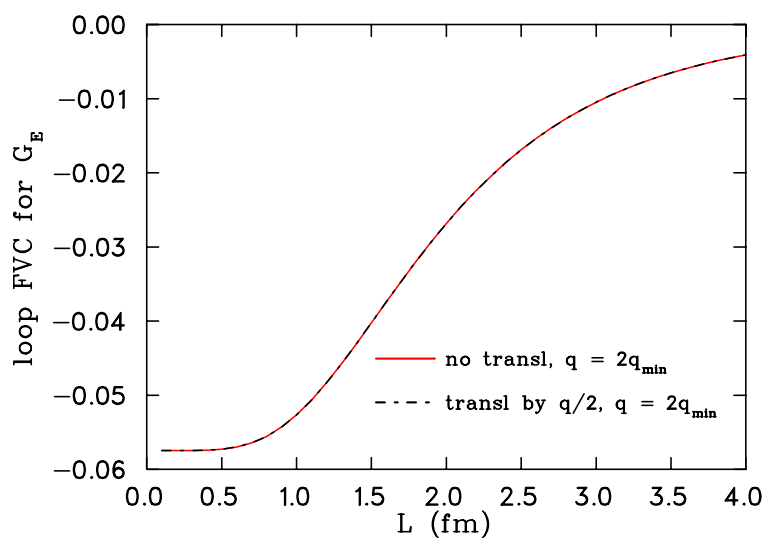Figure 7.10: Finite-volume correction for the loop integral contributing to $G_E$, with $q = 2q_{min}$. The choice of $q/2 = q_{min}$ is an allowed value on the lattice. Therefore, the momentum translated and untranslated behaviour of the finite-volume correction is identical.

$n$ is an integer. Note that, if there is a momentum-translation in the loop integrals, $k \to k - q/2$, the choice of $q = q_{\min} = (2\pi/L)$ (for box length $L$), means that $q/2$ is no longer an allowed value on the lattice, and these finite-volume corrections will be inconsistent with the untranslated result. Under such a momentum-translation, external momenta of $q/2$ flow through the loop integral, and one should choose at least a value of $q = 2q_{\min}$ to define a consistent discrete derivative for use in the definition of the charge radius in Equation (3.82). However, choosing a momentum transfer of $q = q_{\min}$ for a moderate lattice size of 3 fm leads to a relatively large value: $Q^2 \approx 700$ MeV$^2$. In defining the charge radius, the necessary extrapolation to $Q^2 = 0$ will be made more reliable by choosing a value of $Q^2$ to be as small as possible. This situation differs from the infinite-volume calculation of loop integrals, where true momentum-translation invariance is restored, and a continuous derivative may be used as normal.

## 7.3.1   Chiral Loop Integrals

Though loop integrals in the continuum limit are invariant under momentum translations $k \to k + cq$, $c \in \mathbb{Z}$ (for internal loop momentum $k$), a finite-volume loop sum must not include any values of $q$ less than $q_{\min} = (2\pi/L)$. Therefore, to obtain a suitable charge radius one chooses a definition of the loop integrals such that no factors of $\vec{q}/2$ appear. In fact, as long as no fractions of $\vec{q}$ appear in the integrand, the finite-volume version will converge correctly to the infinite-volume version as the box length is taken to infinity, for $q = (2\pi n/L)$, $n \in \mathbb{Z}$:

$$\mathcal{T}_N^E(Q^2) = \frac{\chi_N^E}{3\pi} \int \mathrm{d}^3 k \, \frac{(k^2 - \vec{k} \cdot \vec{q}) \, u(\vec{k}; \Lambda) \, u(\vec{k} - \vec{q}; \Lambda)}{\omega_{\vec{k}} \omega_{\vec{k}-\vec{q}} (\omega_{\vec{k}} + \omega_{\vec{k}-\vec{q}})}, \tag{7.13}$$

$$\mathcal{T}_\Delta^E(Q^2) = \frac{\chi_\Delta^E}{3\pi} \int \mathrm{d}^3 k \, \frac{(k^2 - \vec{k} \cdot \vec{q}) \, u(\vec{k}; \Lambda) \, u(\vec{k} - \vec{q}; \Lambda)}{(\omega_{\vec{k}} + \Delta)(\omega_{\vec{k}-\vec{q}} + \Delta)(\omega_{\vec{k}} + \omega_{\vec{k}-\vec{q}})}, \tag{7.14}$$

$$\mathcal{T}_{\mathrm{tad}}^E(Q^2) = \frac{\chi_t^E}{\pi} \int \mathrm{d}^3 k \, \frac{u^2(\vec{k}; \Lambda)}{\omega_{\vec{k}} + \omega_{\vec{k}-\vec{q}}}, \tag{7.15}$$

where $\omega_{\vec{k}} = \sqrt{\vec{k}^2 - m_\pi^2}$, and $\Delta$ is the mass-splitting. The chiral coefficients $\chi_N^E$ and $\chi_\Delta^E$ and $\chi_t^E$ are summarized by Wang [WLTY09a]:

$$\chi_N^{E,p} = \frac{5}{16\pi^2 f_\pi^2}(D+F)^2 = -\chi_N^{E,n}, \tag{7.16}$$

$$\chi_\Delta^{E,p} = -\frac{5}{16\pi^2 f_\pi^2}\frac{4C^2}{9} = -\chi_\Delta^{E,n}, \tag{7.17}$$

$$\chi_t^{E,p} = -\frac{1}{16\pi^2 f_\pi^2} = -\chi_t^{E,n}. \tag{7.18}$$

The integrals which contribute to the electric charge radius, denoted $(T^E)$, are exactly analogous to the integrals $(\mathcal{T}^E)$ defined in Equations (7.13) through (7.15), that correspond to the electric form factor $G_E$. To obtain the integrals that contribute to the charge radius, one simply takes the derivative with respect to momentum transfer $Q^2$ at vanishingly small values of $Q^2$. This is allowed in the infinite-volume limit:

$$T^E = \lim_{Q^2 \to 0} -6\frac{\partial \mathcal{T}^E(Q^2)}{\partial Q^2}. \tag{7.19}$$

Note that the ensuing procedure for calculating the finite-volume corrected electric charge radius uses only the infinite-volume versions of the chiral loop integrals. Fitting methods need only be applied at infinite volume. Thus, the external momentum derivative in Equation (7.19) need not be discretized, but may remain a continuous derivative.

To achieve a chiral extrapolation, it is convenient to subtract the coefficients $b_0^\Lambda$ from the respective loop integrals that contribute to the electric charge radius:

$$\tilde{T}_N^E = T_N^E - b_0^{\Lambda,N}, \tag{7.20}$$

$$\tilde{T}_\Delta^E = T_\Delta^E - b_0^{\Lambda,\Delta}, \tag{7.21}$$

$$\tilde{T}_{\mathrm{tad}}^E = T_{\mathrm{tad}}^E - b_0^{\Lambda,t}. \tag{7.22}$$

This removes the regularization scale-dependence from the lowest-order fit parameter of the chiral expansion. This technique provides an advantage in easily extracting the low-energy coefficient $c_0$ from the chiral expansion, described in Section 7.3.2.

As emphasized already, Figures 7.9 and 7.10 show that the finite-volume corrections to the loop integrals cannot be applied directly to the charge radius itself. The momentum discretization ruins the circular symmetry in $q$ except at the values coinciding with lattice momentum values $(2\pi n/L)$, $n \in \mathbb{Z}$. The finite-volume corrections should be applied to the electric form factor $G_E(Q^2)$ instead. A momentum convention in the loop integral is chosen such that $q$ may be chosen to be $q_{\min} = (2\pi n/L)$. The procedure for achieving the correct finite-volume corrections is outlined below.

First, the lattice finite-volume charge radius $\langle r^2 \rangle_E^L$ must be converted into a finite-volume form factor $G_E^L(Q^2)$, using $q = q_{\min} = (2\pi/L)$. This is achieved through use of an extrapolation in $Q^2$. As an example, a dipole Ansatz yields the following formula:

$$G_E^L(Q_{\min}^2) = \left( 1 + \frac{Q_{\min}^2 \langle r^2 \rangle_E^L}{12} \right)^{-2}, \qquad (7.23)$$

where $Q_{\min}^2 = \vec{q}_{\min}^2 - (E_N - M_N)^2$. In many cases, this simply reverses the steps used to convert lattice results to charge radii. In this investigation, the electric form factor was fortunately obtained directly from the preliminary lattice QCD data from QCDSF. The next step is to transform the finite-volume form factor $G_E^L(Q_{\min}^2)$ to an infinite-volume form factor $G_E^\infty(Q_{\min}^2)$, so that the infinite-volume charge radius can be calculated. This is achieved by subtracting the electric charge symmetry-preserving finite-volume correction, defined by:

$$\Delta_L(Q_{\min}^2, 0) = \delta_L \left[ \mathcal{T}^E(Q_{\min}^2) - \mathcal{T}^E(0) \right]. \qquad (7.24)$$

The second term of Equation (7.24) ensures that both infinite- and finite-volume form factors are correctly normalized, that is, $G_E^{L,\infty}(0) = 1$. Thus, the infinite-volume electric form factor can be calculated using the equation:

$$G_E^\infty(Q_{\min}^2) = G_E^L(Q_{\min}^2) - \Delta_L(Q_{\min}^2, 0). \qquad (7.25)$$

### 7.3.2   Chiral Expansion of the Electric Charge Radius

The infinite-volume charge radius $\langle r^2 \rangle_E^\infty$ can be recovered from the form factor by using the extrapolation in $Q^2$. Once the infinite-volume charge radius has been obtained, a chiral extrapolation can be performed if needed. The chiral loop integrals corresponding to the charge radius are those defined by Equation (7.19). Using the dipole Ansatz:

$$\langle r^2 \rangle_E^\infty = \frac{12}{Q_{\min}^2} \left( \sqrt{\frac{1}{G_E^\infty(Q_{\min}^2)}} - 1 \right). \tag{7.26}$$

This infinite-volume radius, calculated at multiple values of $m_\pi^2$, can be used for fitting and obtaining coefficients from the chiral expansion:

$$\langle r^2 \rangle_E^\infty = \{c_0^{(\mu)} + a_2^\Lambda m_\pi^2\} + \tilde{T}_N^E(m_\pi^2; \Lambda) + \tilde{T}_\Delta^E(m_\pi^2; \Lambda) + \tilde{T}_{\text{tad}}^E(m_\pi^2; \Lambda) + O(m_\pi^4), \tag{7.27}$$

where the expansion has been renormalized in anticipation of the analysis of the renormalization flow of the coefficient $c_0$. This expansion contains an analytic polynomial in $m_\pi^2$ plus the leading-order chiral loop integrals, from which non-analytic behaviour arises.

By evaluating the loop integrals, the fully renormalized chiral expansion can be written in terms of a polynomial in $m_\pi^2$ and non-analytic terms. To leading non-analytic order $O(\log m_\pi)$:

$$\langle r^2 \rangle_E^\infty = c_0^{(\mu)} + (\chi_N^E + \chi_t^E) \log \frac{m_\pi}{\mu} + O(m_\pi^2). \tag{7.28}$$

Since the chiral expansion of Equation (7.28) contains a logarithm, the value of $c_0$ can only be extracted relative to some mass scale $\mu$, which is chosen to be 1 GeV.

Finally, the finite-volume charge radius can be evaluated by adding the finite-volume correction to the form factor at any box length $\tilde{L}$, and corresponding momentum transfer on the lattice, $\tilde{Q}_{\min}^2$:

$$G_E^{\tilde{L}}(\tilde{Q}_{\min}^2) = G_E^\infty(\tilde{Q}_{\min}^2) + \Delta_{\tilde{L}}(\tilde{Q}_{\min}^2, 0). \tag{7.29}$$

The finite-volume charge radii are obtained from the chosen extrapolation formula at box size $\tilde{L}$. An electric charge radius may be calculated at any desired value of box length, based on lattice QCD simulation results. Thus, the finite-volume behaviour of the charge radius may be analyzed.

## 7.4   Evidence for an Intrinsic Scale in the Electric Charge Radius

The preliminary QCDSF results for the electric charge radius of the nucleon are displayed, with the experimental value marked, in Figure 7.11. The set of data is also listed in Appendix C, Table C.6. The lattice sizes of each data point vary from 1.92 to 3.25 fm using $N_f = 2$ and $O(a)$-improved Wilson quark action. A simple linear fit is included in this plot, which does not take into account the non-analytic behaviour of the chiral loop integrals, nor the finite-volume corrections to the data. Just as for the case of the magnetic moment, the linear fit does not reach the experimental value of the electric charge radius at the physical pion mass. Since the lattice QCD results extend outside the PCR, the result of an extrapolation will be scale-dependent. However, this scale-dependence can be handled by obtaining an optimal regularization scale using the aforementioned procedure.

### 7.4.1   Renormalization Flow Analysis

In order to obtain an optimal regularization scale, the low-energy coefficient $c_0^{(\mu)}$ from Equation (7.27) will be calculated across a range of regularization scale values. Multiple renormalization flow curves may be obtained by constraining the fit window by a maximum, $m_{\pi,\max}^2$, and sequentially adding data points to extend further outside the PCR. The renormalization flow curves for a dipole regulator are plotted on the same set of axes in Figure 7.12. Note that each data point plotted has an associated error bar, but for the sake of clarity only a few points are selected to indi-
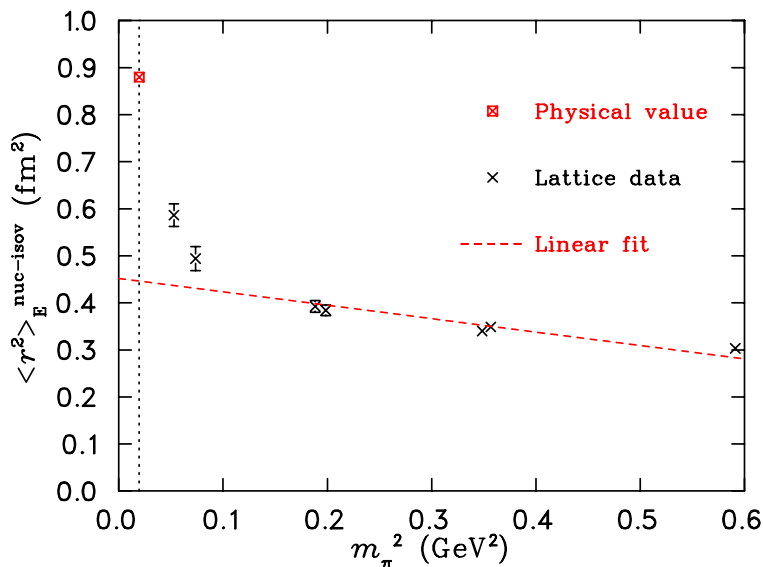
**Figure 7.11:**  Preliminary lattice QCD data for $\langle r^2 \rangle_E^{\text{isov}}$ from QCDSF, with physical value from experiment as marked.
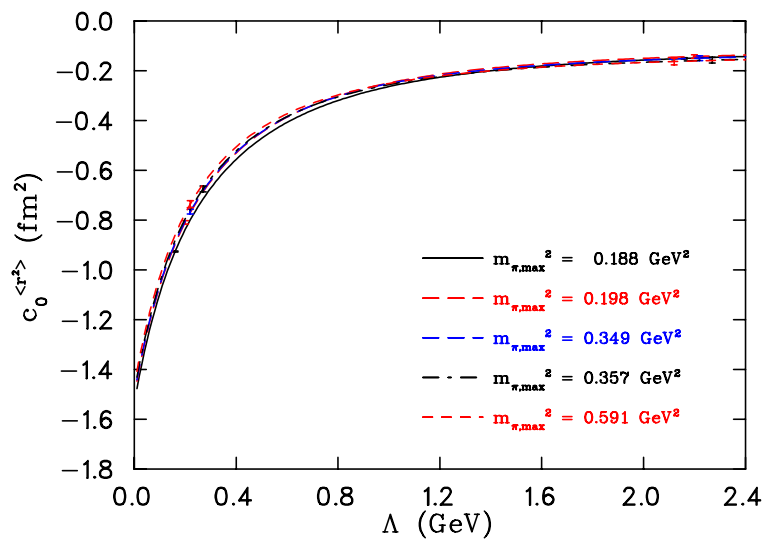


**Figure 7.12:**  The renormalization flow of $c_0$ for $\langle r^2 \rangle_E^{\text{isov}}$ obtained using a dipole regulator, based on preliminary lattice QCD data from QCDSF. $c_0$ is calculated relative to the energy scale $\mu = 1$ GeV.

cate the general size of the statistical error bars. Note that, unlike the analysis of the nucleon mass and the magnetic moment, there is no distinct intersection point in the renormalization flow curves. In addition, the regularization scale-dependence of the coefficient $c_0^{(\mu)}$ is very slight, as long as the regularization scale is not too small, as discussed in Section 4.2.1. This lack of scale-dependence is a natural consequence of the logarithm in the chiral expansion of Equation (7.28), which is slowly-varying with respect to the regularization scale.

## 7.4.2    Analysis of Systematic Uncertainties

An optimal regularization scale for a dipole form can nevertheless be extracted from Figure 7.12 using the chi-square-style analysis. The analysis also provides a measure of the systematic uncertainty in the optimal scale. By plotting $\chi^2_{dof}$ against the regularization scale $\Lambda$, where $dof$ equals the number of curves $n$ minus one, a measure of the spread of the renormalization flow curves can be calculated, and the intersection point obtained. The function $\chi^2_{dof}$ is constructed in the same way as Equations (5.2) and (5.3). The $\chi^2_{dof}$ plot corresponding to Figure 7.12 is shown in Figure 7.13. Thus the optimal dipole regularization scale for a dipole regulator is: $\Lambda^{\text{scale}} = 1.67^{+0.66}_{-0.33}$ GeV. This value, though larger than optimal dipole regularization scale values obtained from the previous analyses of the nucleon mass and the magnetic moment, is nevertheless consistent, with one-standard-deviation agreement. Thus, strong evidence is found that the optimal regularization scale indicates the existence of an intrinsic scale, which characterizes the nucleon-pion interaction.

## 7.4.3    Chiral Extrapolation Results

Using the optimal regularization scale, a reliable chiral extrapolation can be performed, with the systematic uncertainty in the optimal regularization scale taken into account. Consider the behaviour of the electric charge radius as a function of the quark mass as shown in Figure 7.14 (in physical units). Extrapolation curves are plotted for infinite-volume, and a variety of finite-volumes at which current lattice QCD results are produced. For each curve, only the values for which $m_\pi L > 3$
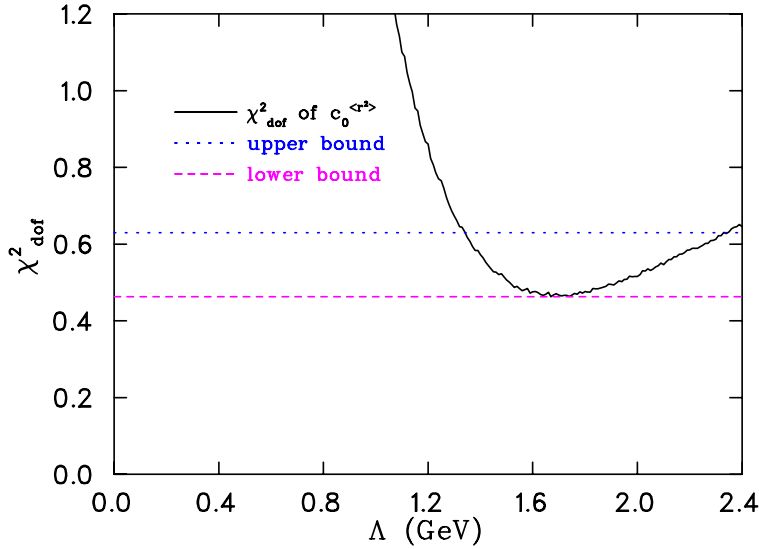
Figure 7.13: $\chi^2_{dof}$ for the renormalization flow of $c_0$ for $\langle r^2 \rangle^{\text{isov}}_E$ obtained using a dipole regulator, based on preliminary lattice QCD data from QCDSF. $c_0$ is calculated relative to the energy scale $\mu = 1$ GeV.

are plotted, provisionally, to avoid undesired effects of the $\varepsilon$-regime. The infinite-volume extrapolation to the physical point differs from the experimentally derived value: $\langle r^2 \rangle^{\text{isov}}_E = 0.88$ fm$^2$, by merely 0.5%. The finite-volume extrapolations are also useful for estimating the result of a lattice QCD calculation at certain box sizes. This can also provide a benchmark for estimating the outcome of a lattice QCD simulation at larger and untested box sizes. Note that the result of an extrapolation to the physical point, using an optimistic 4 fm lattice box length, will differ significantly from the experimental value. Since the data points in Figure 7.14 are at differing finite volumes, the infinite-volume corrected data points are displayed in Figure 7.15.

To highlight the insensitivity of the extrapolation to the regularization scale $\Lambda^{\text{scale}}$, an estimate of the systematic uncertainty in the extrapolation to the physical point solely due to $\Lambda^{\text{scale}}$ is displayed in Figure 7.16. The size of the error bar at the physical point is comparable to that due to statistical uncertainty, as shown in Figure 7.17. This indicates that, in the case of the electric charge radius, the identification of an intrinsic scale is borderline, due to the dominance of the logarithm in the chiral expansion, and its slowly varying property in the large $m_\pi$ regime. Therefore, chiral extrapolations of the electric charge radius are more robust, in the sense that the scale-dependence in the result is suppressed, and the identification of an intrinsic

scale is not so vital as in the case of the nucleon mass or magnetic moment.

## 7.5    Summary and Specific Issues for the Electromagnetic Properties of the Nucleon

It was discovered that finite-volume corrections for charge radii are ill-defined on the lattice. The use of continuous derivatives in constructing the electric charge radius leads to inconsistent results for the finite-volume corrections. It was discovered that the finite-volume corrections must be applied to the electric form factors rather than to the charge radii directly. Therefore, a procedure was developed to apply finite-volume corrections to the electric form factor, strictly involving momenta available on the lattice. The resultant finite-volume corrected form factor may then be converted into a charge radius using an extrapolation in momentum transfer $Q^2$.

The technique for obtaining an optimal regularization scale from lattice QCD data has been investigated in the context of the magnetic moment and the electric charge radius of the isovector nucleon. By using recent, preliminary lattice QCD results from QCDSF, an optimal regularization scale for a dipole regulator was obtained. This was achieved, in each case, by analyzing the renormalization flow of the low-energy coefficient $c_0$ of the relevant chiral expansion with respect to the scale $\Lambda$, whilst extending the data step-wise beyond the PCR. A regularization scale was discovered, for both the magnetic moment and the electric charge radius, for which the renormalization of each $c_0$ is least sensitive to the truncation of the lattice QCD data. The values of the optimal regularization scale were consistent with each other, as well as with the results from the nucleon mass analysis. Thus an intrinsic scale has been uncovered, which characterizes the size of the nucleon, as probed by the pion.

Using the value of the intrinsic scale, the extrapolation of the magnetic moment and the electric charge radius to the physical pion mass and the infinite-volume limit is consistent with experiment. The finite-volume extrapolations provide a benchmark for estimating the outcome of a lattice QCD simulation at realistic or currently

**Figure 7.14:**   Extrapolations of $\langle r^2 \rangle_E^{\text{isov}}$ at different finite volumes and infinite volume, using a dipole regulator, based on preliminary lattice QCD data from QCDSF, lattice sizes: $1.92 - 3.25$ fm. The provisional constraint $m_\pi L > 3$ is used.  The physical value from experiment is marked.  The curve corresponding to a lattice size of 10 fm is almost indistinguishable from the infinite-volume curve.



**Figure 7.15:**   Extrapolations of $\langle r^2 \rangle_E^{\text{isov}}$ at different finite volumes and infinite volume, using a dipole regulator, based on preliminary lattice QCD data from QCDSF, lattice sizes: $1.92 - 3.25$ fm. The provisional constraint $m_\pi L > 3$ is used.  The infinite-volume corrected data points are shown. The physical value from experiment is marked.  The curve corresponding to a lattice size of 10 fm is almost indistinguishable from the infinite-volume curve.
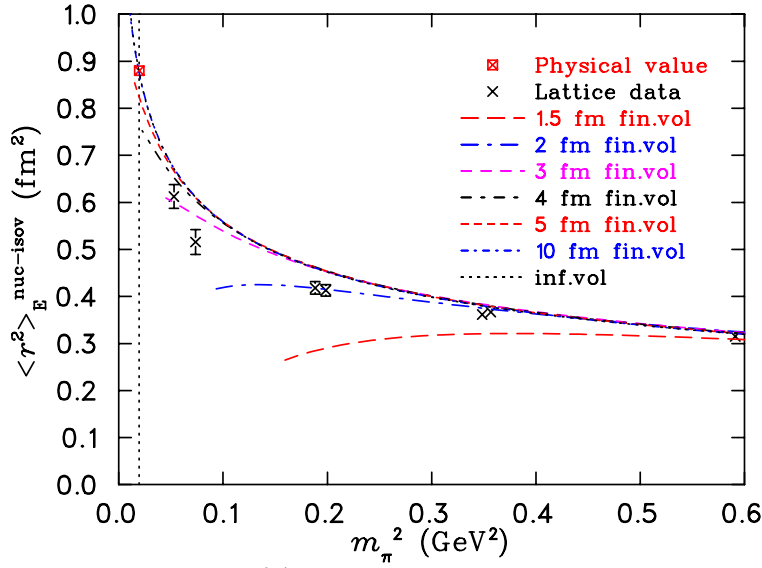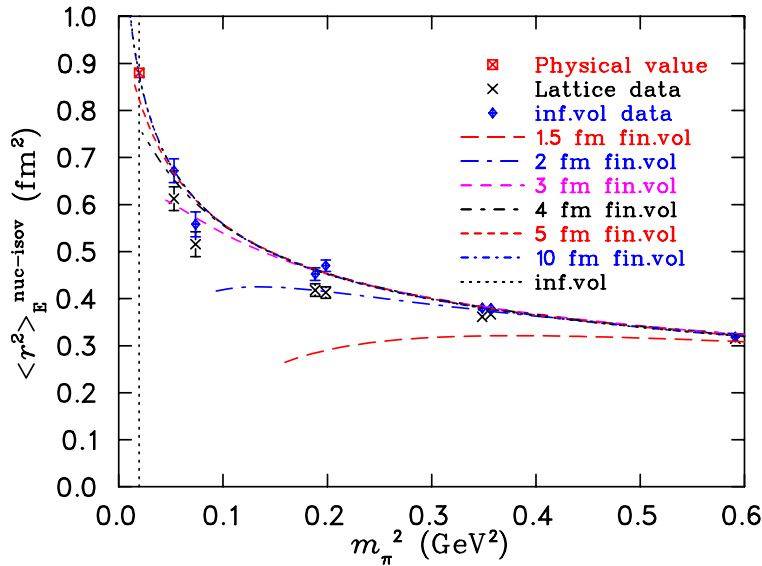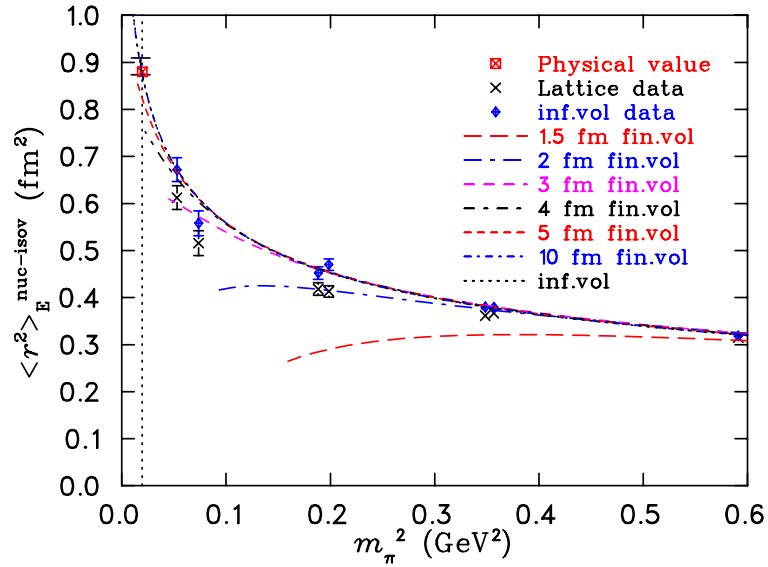
**Figure 7.16:**  Extrapolations of $\langle r^2 \rangle_E^{\text{isov}}$ at different finite volumes and infinite volume, using a dipole regulator, based on preliminary lattice QCD data from QCDSF, lattice sizes: $1.92 - 3.25$ fm. The provisional constraint $m_\pi L > 3$ is used. The infinite-volume corrected data points are shown. The physical value from experiment is marked. An estimate in the uncertainty in the extrapolation, due to $\Lambda^{\text{scale}}$, has been calculated from Figure 7.13, and is indicated at the physical value of $m_\pi^2$. The curve corresponding to a lattice size of 10 fm is almost indistinguishable from the infinite-volume curve.



**Figure 7.17:**  Extrapolations of $\langle r^2 \rangle_E^{\text{isov}}$ at different finite volumes and infinite volume, using a dipole regulator, based on preliminary lattice QCD data from QCDSF, lattice sizes: $1.92 - 3.25$ fm. The provisional constraint $m_\pi L > 3$ is used. The physical value from experiment is marked. An estimate of the statistical uncertainty in the extrapolation is marked at the physical value of $m_\pi^2$. The curve corresponding to a lattice size of 10 fm is almost indistinguishable from the infinite-volume curve.
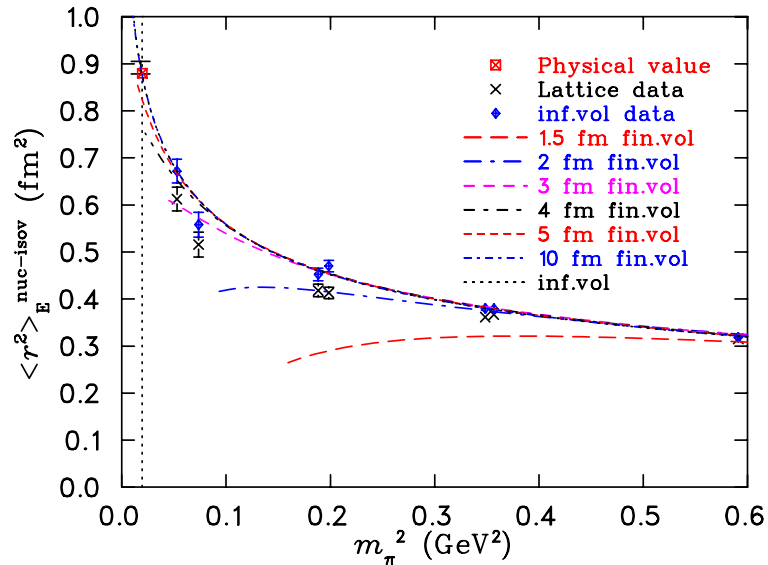
optimistic lattice box sizes.

The results clearly demonstrate a successful procedure for using lattice QCD data to extrapolate an observable to the low-energy region of QCD.

# Chapter 8

# Conclusion

*"Recall that in our theoretical construction those probabilities appeared simply as a logical, or linguistic, tool. It is only at this stage that they finally acquire the empirical significance they were lacking, and that chance enters the theoretical framework."* (Omnès, R. 2002. *Quantum Philosophy: Understanding and Interpreting Contemporary Science* p.209) [Omn02]

## 8.1 Evaluation and Summary Analysis

Chiral effective field theory ($\chi$EFT) offers unique insights into the low-energy behaviour of hadrons. By using $\chi$EFT in conjunction with lattice quantum chromodynamics (lattice QCD) results, a deeper understanding of the underlying chiral interactions may be derived. In particular, the mathematical behaviour of the chiral expansion of an observable, within a power-counting scheme (PCR), was investigated. This led to the development of a method for identifying the PCR, where the renormalization of the low-energy coefficients of the chiral expansion are independent of the regularization scale. Novel methods for identifying a preferred renormalization scheme allowed the extrapolation of an observable to the chiral regime, and to infinite-volume lattice box sizes, without introducing a regularization scale in an *ad hoc* fashion.

In this thesis, a procedure was established whereby an optimal regularization

135

scale could be obtained from lattice QCD data. By constructing some ideal pseudo-data using a known functional form, and based on actual lattice simulation results, the behaviour of the low-energy coefficients, with respect to the regularization scale, indicated an optimal value for the scale. By considering pseudodata sets that extended increasingly beyond the PCR, there was a value of regularization scale at which the renormalization was least sensitive to this extension. This optimal scale is the value at which the correct values of the low-energy coefficients are recovered.

Actual lattice simulation results for the nucleon mass, magnetic moment and electric charge radius were also analyzed using the same procedure. In each case, the analysis led to a consistent value of optimal regularization scale. In cases where multiple low-energy coefficients were analyzed, the optimal scale realized from each matched exactly: a non-trivial result.

The analysis of lattice simulation results for the mass of the quenched $\rho$ meson was used to test the robustness of the method. A reliable technique for determining an optimal regularization scale, and performing infinite-volume and chiral extrapolations, was established.

Comparing the optimal scales obtained from the nucleon mass, magnetic moment and electric charge radius analyses, a consistent optimal regularization scale was found. This indicates the existence of an intrinsic energy scale that characterizes the nucleon-pion interaction: the size of the nucleon as probed by the pion.

In the analysis of the nucleon mass, as described in Chapter 5, it was demonstrated that a preferred regularization scheme exists only for data sets extending outside the PCR. However, it is not always possible to identify this scale. The scale-dependence of an observable can be weakened by working to a higher chiral order. The aforementioned procedure was used to calculate the nucleon mass at the physical point, the low-energy coefficients $c_0$ and $c_2$, and their associated statistical and systematic errors. Several different functional forms of regulator were considered, and lattice QCD data from JLQCD, PACS-CS and CP-PACS were used in the analyses. By working to chiral order $O(m_\pi^3)$, an optimal cut-off scale $\Lambda^{\text{scale}}$ for each set of lattice QCD data was obtained, and an estimate of the systematic error in the choice

of renormalization scheme was calculated, using a chi-square-style analysis. A mean value for the optimal regularization scale of $\bar{\Lambda}_{\text{dip}}^{\text{scale}} \approx 1.3$ GeV was obtained for the dipole, $\bar{\Lambda}_{\text{doub}}^{\text{scale}} \approx 1.0$ GeV for the double-dipole and $\bar{\Lambda}_{\text{trip}}^{\text{scale}} \approx 0.9$ GeV for the triple-dipole. An analysis of the lowest suitable value for a regularization scale allowed the identification of a breakdown region of finite-range regularization (FRR). The existence of a breakdown region indicates that the ultraviolet regularization scale is low enough to remove or suppress the low-energy chiral behaviour being analyzed.

The robustness of the procedure for determining an optimal regularization scale and performing chiral extrapolations was tested in Chapter 6. In order to establish the predictive power of the procedure, the quenched ρ meson mass was considered. Because an experimental value of this observable does not exist, its calculation served to demonstrate the ability of the procedure to make predictions without prior bias. Using lattice simulation results from the Kentucky Group, the procedure was tested, and the interesting low-energy simulation results were *predicted correctly*. By restricting the procedure to use only higher energy simulation data points, the low-energy coefficients $c_0$, $c_2$ and $c_4$ were considered and an optimal regularization scale was identified: $\Lambda_{\rho,\text{trip}}^{\text{scale}} = 0.67_{-0.08}^{+0.09}$ GeV. An optimal value of the maximum pion mass used for fitting was also calculated, and was found to be $\hat{m}_{\pi,\text{max}}^2 = 0.35$ GeV$^2$. By using only the data contained in the optimal pion mass region, constrained by $\hat{m}_{\pi,\text{max}}^2$, a value $\Lambda_{\rho,\text{trip}}^{\text{scale}} = 0.64$ GeV is estimated for the optimal regularization scale, with a wider systematic uncertainty corresponding to the entire range of suitable values of $\Lambda$. These two estimates of the optimal regularization scale are consistent with each other.

Upon revealing the omitted low-energy data, the extrapolations were compared to the simulation results at each value of pion mass. The correct chiral curvature was reproduced by the extrapolations, indicating the non-analytic chiral behaviour of the loop integrals. The results of extrapolations using χEFT, and the results of lattice QCD simulations were demonstrated to be consistent. The extrapolation to the physical point obtained for this quenched data set, using $\Lambda_{\rho,\text{trip}}^{\text{scale}} = 0.67_{-0.08}^{+0.09}$ GeV, is: $m_{\rho,Q}^{\text{ext}}(m_{\pi,\text{phys}}^2) = 0.925_{-0.049}^{+0.053}$ GeV, an uncertainty of less than 6%. The result of the

extrapolation, using $\Lambda^{\text{scale}}_{\rho,\text{trip}} = 0.64$ GeV, with the systematic uncertainty calculated by varying $\Lambda$ across all suitable values, is: $m^{\text{ext}}_{\rho,Q}(m^2_{\pi,\text{phys}}) = 0.922^{+0.065}_{-0.060}$ GeV, an uncertainty of only 7%.

In the case of the electromagnetic properties of the nucleon, preliminary results from QCDSF were used. The magnetic moment of the isovector nucleon was analyzed for a dipole regulator. A well-defined optimal regularization scale was obtained: $\Lambda^{\text{scale}}_{\mu,\text{dip}} = 1.13^{+0.22}_{-0.20}$ GeV, for chiral order $O(m^2_\pi \log m_\pi)$, and a successful extrapolation to the physical pion mass and infinite-volume was achieved, and compared to the experimental value. The infinite-volume extrapolation to the physical point was within 2% of the experimentally derived value.

When considering charge radii, there are subtleties in performing finite-volume corrections. In defining the charge radius, the finite-volume corrections must be applied before an extrapolation to $Q^2 = 0$ is taken. Thus the finite-volume corrections must be applied to the form factors directly. Using this method, the electric charge radius of the isovector nucleon was analyzed for a dipole regulator. Assuming the regularization scale is not within the breakdown region of FRR, the scale-dependence of the low-energy coefficient $c^\mu_0$ (up to some scale $\mu$ of the chiral logarithm) is weak. The leading-order non-analytic behaviour of the logarithm in the chiral expansion is slowly varying with respect to the regularization scale. Nevertheless, an optimal regularization scale was obtained: $\Lambda^{\text{scale}}_{E,\text{dip}} = 1.67^{+0.66}_{-0.33}$ GeV, working to chiral order $O(m^2_\pi \log m_\pi)$. A successful extrapolation to the physical pion mass and infinite-volume was achieved, and compared to the experimental value. The infinite-volume extrapolation was merely 0.5% different from the experimentally derived value.

Figure 8.1 collates the values of the intrinsic scale for a dipole regulator obtained from each of the three sets of lattice results from the nucleon mass analysis, the magnetic moment analysis and the electric charge radius analysis. In summary, a method for determining the existence of a well defined intrinsic scale has been discovered. It has also been illustrated how its value can be determined from lattice QCD results.
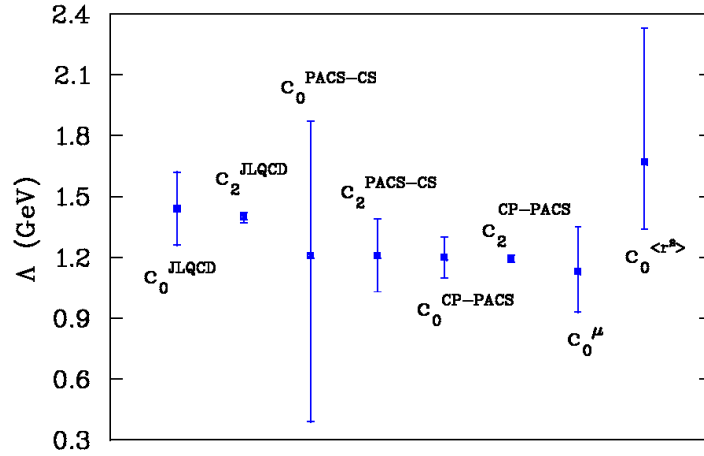
Figure 8.1: Collated values for the intrinsic scale obtained from each data set for the nucleon mass, magnetic moment and electric charge radius, by analyzing a variety of low-energy coefficients. Each point, with its associated systematic error bar, is labelled by the low-energy coefficient analyzed. The results from the analyses of the nucleon mass are further denoted by the collaboration whose lattice results are used. $c_0^\mu$ and $c_0^{\langle r^2 \rangle}$ denote the intrinsic scale obtained from the analysis of the low-energy coefficient $c_0$ corresponding to the magnetic moment, and the electric charge radius expansions, respectively. A dipole regulator is used.

## 8.2  Future Studies and Further Developments

The research presented in this thesis encourages several avenues for further investigation. In the heavy-baryon formulation of chiral perturbation theory ($\chi$PT), presented first for the renormalization of the mass of the nucleon in Chapter 4, the finite-volume corrections to the tadpole contribution are not evaluated. This is due to a technical subtlety associated with the large $m_\pi$ behaviour of the finite-volume correction, due to the $m_\pi^2$ coefficient occurring in Equations (4.16) through (4.18). The tadpole finite-volume corrections diverge as $m_\pi^4$. Since it is known that the finite-volume corrections must converge [Bea04b], and lattice QCD simulations do not exhibit any divergence associated with large $m_\pi$ on a finite volume, higher-order terms, for example, those occurring at order $O(m_\pi^4)$, must act to reduce the estimated value of the finite-volume correction.

In the analysis of the renormalization flow of the nucleon mass, it was discovered that the scale dependence was weakened by working to a sufficiently high chiral order. It was also found, however, that the residual scale-dependence persisted as a significant component of the systematic uncertainty. For efficient propagation of this

uncertainty, an interesting future direction would be to consider Bayesian methods of marginalization over the scale-dependence [SP09].

More generally, this research provides a strong basis for the investigation of baryon resonances by analysing lattice QCD simulations. Resonances of the nucleon, such as the Roper Resonance, are not well understood in terms of effective field theory. The structure and behaviour of the resonances lend themselves to a fruitful future area of research. Indeed, it is not possible to link the finite-volume results of lattice QCD to experiment without understanding their relation to the multiparticle states that dress the resonances. FRR $\chi$EFT is particularly well-suited to exploring this important area of research.

## 8.3   Codetta

*"[T]he collective efforts of numerous physicists have revealed some of nature's best-kept secrets. And once revealed, these explanatory gems have opened vistas on a world we thought we knew, but whose splendor we had not even come close to imagining."* (Greene, B. 1999. *The Elegant Universe* p.386) [Gre99]

The dynamics of quantum chromodynamics provide a rich framework for the investigation of the properties of hadrons. In particular, low-energy effective field theory allows one to glean insights into the physical behaviour of subatomic particles and the structure of matter. By incorporating the fundamental symmetries of quantum chromodynamics into the action, chiral perturbation theory provides a robust method for the calculation of hadronic observables within the power-counting regime. In this thesis, finite-range regularized chiral effective field theory was used to develop a procedure for performing calculations beyond the power-counting regime, and handling any subsequent finite-range regularization scale-dependence. Using chiral effective field theory in conjunction with the non-perturbative approach of lattice quantum chromodynamics, chiral extrapolations; finite-volume effects; the consequences of dynamical chiral symmetry breaking on subatomic behaviour; the importance of strangeness; vacuum polarizations; and many other phenomena yield

fruitful understanding into the inner workings of the universe.

**Concluding Statement**

Chiral effective field theory allows the identification of an intrinsic energy scale in the nucleon-pion interaction from lattice simulation results. An optimal finite-range regularization scale, obtained from analyzing the renormalization flow of the low-energy coefficients of the chiral expansion, allows successful extrapolations to be made to the chiral regime and to the infinite-volume limit. There is strong evidence to suggest that the optimal scale characterizes the intrinsic energy scale of the interaction between the pion and the nucleon.

The datum, the results and the rigorous theory integrate to form a strong argument. Chiral effective field theory extended beyond the power counting-regime allows the identification of an intrinsic energy scale, and leads to a robust method for chiral and infinite-volume extrapolations. This is the original contribution of this thesis.

*"We have thus achieved the point where the theory may finally be compared with experience, and the road leading from formalism to concrete reality is at last complete."* (Omnès, R. 2002. *Quantum Philosophy: Understanding and Interpreting Contemporary Science* p.209) [Omn02]

# Appendix A

# Conventions

## A.1   Dirac and Pauli Spin Matrices

The Pauli matrices are usually chosen as such:

$$\tau^1 = \begin{pmatrix} 0 & 1 \\ 1 & 0 \end{pmatrix} \tag{A.1}$$

$$\tau^2 = \begin{pmatrix} 0 & -i \\ i & 0 \end{pmatrix} \tag{A.2}$$

$$\tau^3 = \begin{pmatrix} 1 & 0 \\ 0 & -1 \end{pmatrix} \tag{A.3}$$

There are several conventions for the definition of the Dirac matrices (such as Weyl/Chiral or the Majorana Representation). Here is the Dirac Representation:

$$\gamma^0 = \begin{pmatrix} \mathbb{I} & 0 \\ 0 & -\mathbb{I} \end{pmatrix} \tag{A.4}$$

$$\gamma^i = \begin{pmatrix} 0 & \sigma^i \\ -\sigma^i & 0 \end{pmatrix} \tag{A.5}$$

$$\gamma_5 = \begin{pmatrix} 0 & \mathbb{I} \\ \mathbb{I} & 0 \end{pmatrix} = i\gamma^0\gamma^1\gamma^2\gamma^3. \tag{A.6}$$

All representations of these matrices satisfy the requirement of Clifford Algebra due to the conditions imposed in the derivation of the Dirac Equation [Pes95].

$$\{\gamma^\mu, \gamma^\nu\} = 2g^{\mu\nu}, \tag{A.7}$$

$$\{\gamma^\mu, \gamma_5\} = 0. \tag{A.8}$$

## A.2   $SU(3)$ Gell-Mann Matrices

The generators of the Lie Group $SU(3)$ satisfy the commutator relations:

$$[\lambda^a, \lambda^b] = if^{abc}\lambda^c. \tag{A.9}$$

This, combined with the relevant Jacobi Indentities for the generators, defines the structure constants [Pes95]:

$$f^{ade}f^{bcd} + f^{bde}f^{cad} + f^{cde}f^{abd}. \tag{A.10}$$

## A.3   Spinor Fields

The equal-time canonical anti-commutation relations for Dirac spinor fields are:

$$\{\psi(x), \bar{\psi}(y)\}_{x_0=y_0} = \hbar\delta^3(\vec{x} - \vec{y}), \tag{A.11}$$

$$\{\psi(x), \psi(y)\}_{x_0=y_0} = 0. \tag{A.12}$$

The fields take the form [Pes95]:

$$\psi(x) = \int \frac{\mathrm{d}^3p}{(2\pi)^3} \frac{1}{\sqrt{2\omega_{\vec{p}}}} \sum_s \left( a_{\vec{p}}^s u^s(p)e^{-ip\cdot x} + b_{\vec{p}}^{s\dagger} v^s(p)e^{ip\cdot x} \right), \tag{A.13}$$

and the canonical anti-commutation relations expressed in terms of the Pauli-Jordan function:

$$\{\psi(x), \bar{\psi}(y)\} = (i\slashed{\partial}_x + m)i\Delta(x - y; m). \tag{A.14}$$

The Grassmann algebra is defined by the anticommutation rule between Grassmann variables $\psi$ and a commutation rule with non-Grassmann numbers $c$:

$$\{\psi_i, \psi_j\} = 0 = [\psi_i, c].$$ (A.15)

For Berezin integration over fermion spinor fields $\psi$ and $\bar{\psi}$, the follow rules are adopted:

- $$\int d\psi_i \psi_j = \int d\bar{\psi}_i \bar{\psi}_j = c\,\delta_{ij},$$ (A.16)

- $$\int d\psi_i \frac{\partial f}{\partial \psi_j} = 0,$$ (A.17)

where the non-Grassmann constant $c$ is chosen, by convention, to be equal to 1 and the function $f$ is defined on the Grassmann algebra. As a consequence of Equation (A.17), the Berezin integral over unity vanishes:

$$\int d\psi = \int d\bar{\psi} = 0.$$ (A.18)

## A.4   Meson and Baryon Field Definitions

The SU(3) mixed-symmetric meson octet fields $\pi(x) = \pi^a(x)\lambda^a$ can be encoded in a traceless $3 \times 3$ matrix of the form:

$$\pi(x) = \sqrt{2} \begin{pmatrix} \frac{1}{\sqrt{2}}\pi^0 + \frac{1}{\sqrt{6}}\eta & \pi^+ & K^+ \\ \pi^- & -\frac{1}{\sqrt{2}}\pi^0 + \frac{1}{\sqrt{6}}\eta & K^0 \\ K^- & \bar{K}^0 & \frac{-2}{\sqrt{6}}\eta \end{pmatrix},$$ (A.19)

In SU(2) the pions form the triplet representation $(\pi^-, \pi^0, \pi^+)$ which can be written by summing over the Pauli spin matrices in Appendix (A.1):

$$\pi(x) = \tau^a \pi^a(x) = \begin{pmatrix} \pi^0 & \sqrt{2}\pi^+ \\ \sqrt{2} & -\pi^0 \end{pmatrix},$$ (A.20)

Using the convention for Clebsch-Gordan coefficients from Wang *et al.* [WLTY09a], the the mixed-symmetric baryon octet matrix has the form:

$$B(x) = \begin{pmatrix} \frac{1}{\sqrt{2}}\Sigma^0 + \frac{1}{\sqrt{6}}\Lambda & \Sigma^+ & p \\ \Sigma^- & -\frac{1}{\sqrt{2}}\Sigma^0 + \frac{1}{\sqrt{6}}\Lambda & n \\ \Xi^- & \Xi^0 & \frac{-2}{\sqrt{6}}\Lambda \end{pmatrix}, \tag{A.21}$$

The maximally symmetric decuplet tensor (suppressing Lorentz indices) has elements defined by:

$$T_{111} = \Delta^{++}, \; T_{112} = \frac{1}{\sqrt{3}}\Delta^+, \; T_{122} = \frac{1}{\sqrt{3}}\Delta^0, \; T_{222} = \Delta^-,$$

$$T_{113} = \frac{1}{\sqrt{3}}\Sigma^{*,+}, \quad T_{123} = \frac{1}{\sqrt{6}}\Sigma^{*,0}, \quad T_{223} = \frac{1}{\sqrt{3}}\Sigma^{*,-},$$

$$T_{133} = \frac{1}{\sqrt{3}}\Xi^{*,0}, \quad T_{233} = \frac{1}{\sqrt{3}}\Xi^{*,-}, \quad T_{333} = \Omega^-. \tag{A.22}$$

# Appendix B

# Integration Techniques

## B.1 Magnetic Quantities

### B.1.1 Angular Components of Magnetic Moment Loop Integrals

In anticipation of applying finite-volume corrections to chiral loop integrals by comparing them to their respective summations on the lattice, the time-component of the $\mathrm{d}^4k$ integral is evaluated using Cauchy's Integral Formula, and a $\mathrm{d}^3k$ integral remains for analysis, as in Chapters 4 through 6.

When calculating the magnetic moment in the heavy-baryon limit, without explicitly specifying a regularization scheme, the one-loop integral (corresponding to Figure 7.1) takes the following form:

$$\mathcal{T}_N^\mu = -\frac{\chi_N^\mu}{2\pi^2}\int \mathrm{d}^3k \frac{(\hat{q}\times\vec{k})^2}{(k^2+m_\pi^2)^2}\,. \tag{B.1}$$

It is useful to be able to simplify the angular part of the integral, formed by the cross product of external momentum direction $\hat{q}$ with the loop momentum $\vec{k}$, into a numerical coefficient. In order for this to be valid in calculating finite-volume corrections, the simplification must hold in both integral and sum forms of the loop

diagram. Evaluating the angular part of Equation (B.1) yields:

$$T_N^\mu = -\frac{\chi_N^\mu}{2\pi^2} \int_0^{2\pi} d\varphi \int_0^\infty dk \int_{-1}^{+1} dx \frac{k^4(1-x^2)}{(k^2+m_\pi^2)^2} \tag{B.2}$$

$$= -\frac{\chi_N^\mu}{\pi} \int_0^\infty dk \int_{-1}^1 dx \frac{k^4(1-x^2)}{(k^2+m_\pi^2)^2} \tag{B.3}$$

$$= -\frac{4\chi_N^\mu}{3\pi} \int_0^\infty dk \frac{k^4}{(k^2+m_\pi^2)^2} . \tag{B.4}$$

Now, this one-dimensional integral can be transformed into a three-dimensional integral simply by adding in a naïve solid angle component, using the identity: $\frac{1}{4\pi} \int d\Omega = 1$:

$$T_N^\mu = -\frac{4\chi_N^\mu}{3\pi} \frac{1}{4\pi} \int d\Omega \int_0^\infty dk \frac{k^4}{(k^2+m_\pi^2)^2} \tag{B.5}$$

$$= -\frac{\chi_N^\mu}{3\pi^2} \int d^3k \frac{k^2}{(k^2+m_\pi^2)^2} . \tag{B.6}$$

Comparing Equations (B.1) and (B.6) shows that the objective has been achieved for the integral case. For finite volume sums, the result may not hold in general, and so must be checked independently. Define the following sum for box length $L$:

$$T_{N,L}^\mu = -\frac{\chi_N^\mu}{2\pi^2} \left(\frac{2\pi}{L}\right)^3 \sum_{\vec{k}} \frac{(\hat{q} \times \vec{k})^2}{(k^2+m_\pi^2)^2} . \tag{B.7}$$

Because $k^2 \equiv \vec{k}^2$ is symmetrical in directions $\hat{k}_{x,y,z}$, it follows that:

$$\vec{k}^2 = k_x^2 + k_y^2 + k_z^2 = 3k_i^2 \quad (i = x,y,z), \tag{B.8}$$

$$\text{and since} \quad (\hat{q} \times \vec{k}) = k_\perp^2, \tag{B.9}$$

$$\text{it follows} \quad k_\perp^2 = 2k_i^2. \tag{B.10}$$

Thus:

$$\mathcal{T}_{N,L}^{\mu} = -\frac{\chi_N^{\mu}}{\pi^2} \left(\frac{2\pi}{L}\right)^3 \sum_{\vec{k}} \frac{k_i^2}{(k^2+m_\pi^2)^2} \tag{B.11}$$

$$= -\frac{\chi_N^{\mu}}{3\pi^2} \left(\frac{2\pi}{L}\right)^3 \sum_{\vec{k}} \frac{k^2}{(k^2+m_\pi^2)^2}, \tag{B.12}$$

which is the finite-volume equivalent of Equation (B.6).

## B.1.2   Combinatorial Simplification

The calculation of the three-dimensional finite sum can be made more efficient computationally, by transforming it to a one-dimensional sum in terms of the new variable $n^2 = k^2(2\pi/L)^2$. It does, however, require calculation of the number of configurations of the squares of $k_x$, $k_y$ and $k_z$ to obtain each value of $n^2$, denoted $C^{(3)}(n^2)$. Thus, for an integrand $I(\vec{k})$:

$$\left(\frac{2\pi}{L}\right)^3 \sum_{\vec{k}}^{k_{\text{max}}} I(\vec{k}) = \left(\frac{2\pi}{L}\right)^3 \sum_{n^2}^{n_{\text{max}}^2} C^{(3)} I(n^2), \tag{B.13}$$

where $n_{\text{max}}^2 = k_{\text{max}}^2(2\pi/L)^2$.

## B.1.3   Sachs Magnetic Form Factors at Finite $Q^2$

Consider calculations involving the leading-order pion loop contributions to the magnetic form factor $G_M(Q^2)$ at finite $Q^2$, (allowing non-zero mass splitting $\Delta$). The following integral can be made more easily calculable using spherical polar co-

ordinates (using $\omega(\vec{k}) = \sqrt{k^2 + m_\pi^2}$):

$$
\mathcal{T}_N^\mu(Q^2) = -\frac{\chi_N^\mu}{\pi^2} \int d^3k \Big[
$$
$$
\frac{k_y^2 \left[\omega(\vec{k}) + \omega(\vec{k}+\vec{q}) + \Delta\right]}{\omega(\vec{k})\left[\omega(\vec{k}) + \Delta\right]\omega(\vec{k}+\vec{q})\left[\omega(\vec{k}+\vec{q}) + \Delta\right]\left[\omega(\vec{k}) + \omega(\vec{k}+\vec{q})\right]} \Big]
$$
(B.14)
$$
= -\frac{\chi_N^\mu}{\pi^2} \int_0^{2\pi} d\varphi \int_0^\pi d\theta \int_0^\infty dk \Big[
$$
$$
\frac{k_y^2 k^2 \sin\theta \left[\omega(k) + \omega(k+q) + \Delta\right]}{\omega(k)\left[\omega(k) + \Delta\right]\omega(k+q)\left[\omega(k+q) + \Delta\right]\left[\omega(k) + \omega(k+q)\right]} \Big].
$$
(B.15)

The integral can be further altered to remove the infinite integral under the change of variables $k \to k/(1-k)$. For arbitrary function $f$:

$$
\int_0^\infty dk\, f(k) = \int_0^1 dk\, \frac{f(k/(1-k))}{(1-k)^2}.
$$
(B.16)

Thus, defining (for convenience) $p(k) \equiv k/(1-k)$, Equation (B.15) becomes:

$$
\mathcal{T}_N^\mu(Q^2) =
$$
$$
-\frac{\chi_N^\mu}{\pi^2} \int_0^{2\pi} d\varphi \int_{-1}^1 dx \int_0^1 dk \Big[
$$
$$
\frac{k_y^2\, p^2 \left[\omega(p) + \omega(p+q) + \Delta\right]}{\omega(p)\left[\omega(p) + \Delta\right]\omega(p+q)\left[\omega(p+q) + \Delta\right]\left[\omega(p) + \omega(p+q)\right](1-k)^2} \Big].
$$
(B.17)

## B.2   Electric Charge Radius Integral Expansions

For the infinite-volume electric charge radius, the chiral loop integrals must be calculated for use with the chiral expansion of Equation (7.27). Each loop integrand is expanded out for small $Q^2$, and the derivative in the limit of vanishing $Q^2$ is extracted. Using the notation of Chapter 7, and a dipole regulator, the one-loop contribution

takes the following form:

$$
T_N^E = \lim_{Q^2 \to 0} -6 \frac{\partial \mathcal{T}_N^E(Q^2)}{\partial Q^2}
$$

$$
= \frac{6\chi_N^E}{5\pi} \int d^3k \frac{\partial}{\partial q^2} \left[ \frac{(\vec{k}+\vec{q}/2)\cdot(\vec{k}-\vec{q}/2)\, u_{\mathrm{dip}}(\vec{k}+\vec{q}/2\,;\Lambda)\, u_{\mathrm{dip}}(\vec{k}-\vec{q}/2\,;\Lambda)}{\omega(\vec{k}+\vec{q}/2)\omega(\vec{k}-\vec{q}/2)[\omega(\vec{k}+\vec{q}/2)+\omega(\vec{k}-\vec{q}/2)]} \right]\Bigg|_{q^2=0}
$$
$$(B.18)$$

$$
= \frac{6\chi_N^E}{5\pi} \int d^3k \Big( \Lambda^8\{ -\omega^2(\vec{k})(\vec{k}^2+\Lambda^2)(13\vec{k}^4+2m_\pi^2\Lambda^2+5\vec{k}^2(2m_\pi^2+\Lambda^2))
$$
$$
+\vec{k}^4(21\vec{k}^4+16m_\pi^4+5\Lambda^4+2\vec{k}^2(16m_\pi^2+5\Lambda^2))\cos^2\theta\} \Big)\Big(16\omega^7(\vec{k})(\vec{k}^2+\Lambda^2)^6\Big)^{-1}.
$$
$$(B.19)$$

If a mass-splitting is included:

$$
T_\Delta^E = \frac{6\chi_\Delta^E}{5\pi} \int d^3k \frac{\partial}{\partial q^2} \left[ \frac{(\vec{k}+\vec{q}/2)\cdot(\vec{k}-\vec{q}/2)\, u_{\mathrm{dip}}(\vec{k}+\vec{q}/2\,;\Lambda)\, u_{\mathrm{dip}}(\vec{k}-\vec{q}/2\,;\Lambda)}{(\omega(\vec{k}+\vec{q}/2)+\Delta)(\omega(\vec{k}-\vec{q}/2)+\Delta)[\omega(\vec{k}+\vec{q}/2)+\omega(\vec{k}-\vec{q}/2)]} \right]\Bigg|_{q^2=0}
$$
$$(B.20)$$

$$
= \frac{6\chi_\Delta^E}{5\pi} \int d^3k \Big( \Lambda^8\{ -\omega(\vec{k})(\vec{k}^2+\Lambda^2)[13\vec{k}^6+2m_\pi^2(m_\pi^2+\Delta(2\omega(\vec{k})+\Delta))\Lambda^2
$$
$$
+\vec{k}^4(23m_\pi^2+24\omega(\vec{k})\Delta+11\Delta^2+5\Lambda^2)
$$
$$
+\vec{k}^2(10m_\pi^4+\Delta(8\omega(\vec{k})+3\Delta)\Lambda^2+m_\pi^2(20\omega(\vec{k})\Delta+10\Delta^2+7\Lambda^2))]
$$
$$
+\vec{k}^4[21\vec{k}^6+16m_\pi^6+16m_\pi^4\Delta(2\omega(\vec{k})+\Delta)+5m_\pi^2\Lambda^4+\Delta(4\omega(\vec{k})+\Delta)\Lambda^4
$$
$$
+\vec{k}^4(53m_\pi^2+36\omega(\vec{k})\Delta+17\Delta^2+10\Lambda^2)
$$
$$
+\vec{k}^2(48m_\pi^4+\Lambda^2(8\omega(\vec{k})\Delta+2\Delta^2+5\Lambda^2)+2m_\pi^2(32\omega(\vec{k})\Delta+16\Delta^2+5\Lambda^2))]\cos^2\theta\} \Big)
$$
$$
\times \Big(16\omega^5(\vec{k})(\omega(\vec{k})+\Delta)^4(\vec{k}^2+\Lambda^2)^6\Big)^{-1}.
$$
$$(B.21)$$

Similarly, the tadpole contribution takes the following form:

$$
T_{\mathrm{tad}}^E = \frac{6\chi_t^E}{\pi} \int d^3k \frac{\partial}{\partial q^2} \left[ \frac{u_{\mathrm{dip}}^2(\vec{k}\,;\Lambda)}{\omega(\vec{k}+\vec{q}/2)+\omega(\vec{k}-\vec{q}/2)} \right]\Bigg|_{q^2=0}
$$
$$(B.22)$$

$$
= \frac{6\chi_t^E}{\pi} \int d^3k \frac{\vec{k}^2\cos^2\theta-\omega^2(\vec{k})}{16\omega^5(\vec{k})} u_{\mathrm{dip}}^2(\vec{k}\,;\Lambda).
$$
$$(B.23)$$

## B.3    Finite Volume Corrections to Tadpole Amplitudes

Finite-volume corrections should vanish as $m_\pi^2$ becomes large, as observed in lattice quantum chromodynamics (lattice QCD) simupations. This has also been observed, in turn, for each of the finite-volume corrections involved in the extrapolation of the nucleon mass to fourth-order. However, the tadpole finite-volume correction, $\delta_{tad}^{\text{FVC}}$, is different in that it is multiplied by a factor of $m_\pi^2$, as evident in Equation (4.7). The product $c_2 m_\pi^2 \delta_{tad}^{\text{FVC}}$ is not convergent for large $m_\pi$. Figures B.1 and B.2 show the behaviour of the tadpole finite-volume correction for a 2.9 fm box and a 4.0 fm box, respectively.

The finite-volume estimate of $c_2$, denoted $c_2^V$, is not in general the same value as the infinite-volume $c_2$. Thus the finite-volume correction of the tadpole cannot be written as simply the difference between the finite volume sum and the infinite volume integral, but must distinguish between $c_2^V$ and $c_2$:

$$c_2 m_\pi^2 \delta_{tad}^{\text{FVC}} = c_2 m_\pi^2 \left( \frac{c_2^V}{c_2} \Sigma_{tad}^V - \Sigma_{tad} \right) . \tag{B.24}$$

Since $c_2$ is by definition the coefficient of the $m_\pi^2$ term in the nucleon mass expansion, the renormalization of the residual coefficient $a_2$ by the contributions from the integrals $\Sigma_N$, $\Sigma_\Delta$ and $\Sigma_{tad}$, defined in Equations (4.3) through (4.8), can be written as follows:

$$c_2 m_\pi^2 = (a_2 + b_2^N + b_2^\Delta + c_2 b_2^t) m_\pi^2 , \tag{B.25}$$

$$\Rightarrow c_2 = \frac{a_2^\Delta + b_2^N + b_2^\Delta}{1 - b_2^t} . \tag{B.26}$$

An analogous relation exists for the finite volume $c_2^V$:

$$c_2^V = \frac{a_2 + b_2^{V,N} + b_2^{V,\Delta}}{1 - b_2^{V,t}} . \tag{B.27}$$

By simultaneously solving for $a_2$ and $c_2^V$, the ratio $c_2^V / c_2$ can be calculated in principle, and the tadpole finite volume corrections are tractable. It should be noted
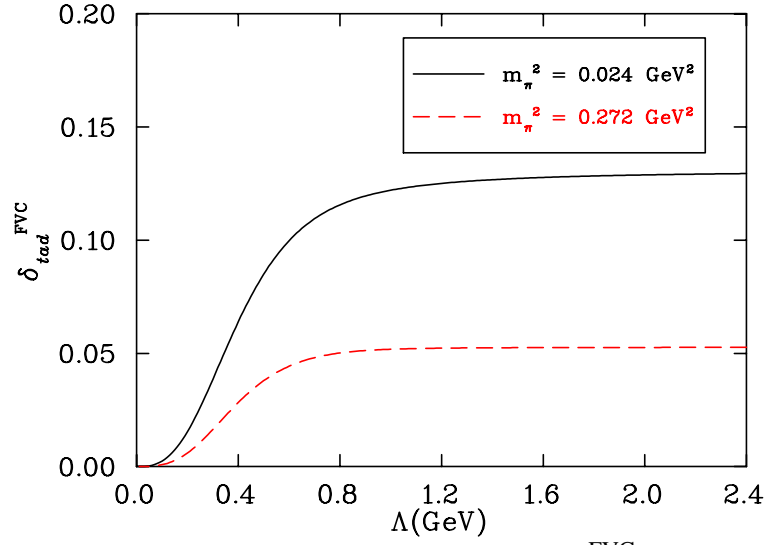
Figure B.1: Behaviour of the finite-volume corrections $\delta_{tad}^{FVC}$ vs. $\Lambda$ on a 2.9 fm box using a dipole regulator. Results for two different values of $m_\pi^2$ are shown.
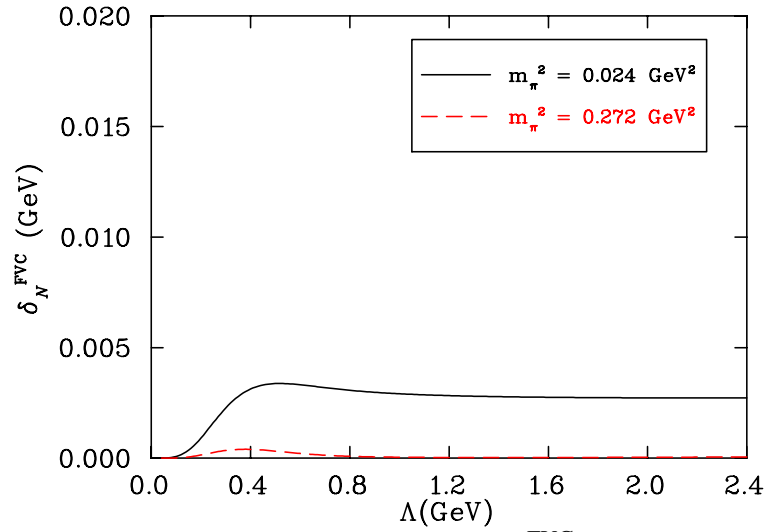


Figure B.2: Behaviour of finite-volume corrections $\delta_{tad}^{FVC}$ vs. $\Lambda$ on a 4.0 fm box using a dipole regulator. Results for two different values of $m_\pi^2$ are shown.

however, that this does not resolve the problem of divergent behaviour for large $m_\pi$.

# Appendix C

# Lattice Simulation Results

Table C.1: JLQCD [O$^+$08] lattice QCD simulation results for the nucleon mass $M_N$ at various pion mass squared values $m_\pi^2$. The lattice spacing is 0.118 fm and the spatial lattice length is 1.90 fm.

| $m_\pi^2$(GeV$^2$) | $M_N$(GeV) | $m_\pi L$ |
|---|---|---|
| 0.567 | 1.615(6) | 7.25 |
| 0.386 | 1.456(6) | 5.98 |
| 0.273 | 1.350(6) | 5.03 |
| 0.191 | 1.255(6) | 4.20 |
| 0.135 | 1.164(8) | 3.54 |
| 0.084 | 1.111(10) | 2.78 |

Table C.2: PACS-CS [A$^+$09] lattice QCD simulation results for the nucleon mass $M_N$ at various pion mass squared values $m_\pi^2$. The lattice spacing is 0.0907 fm and the spatial lattice length is 2.90 fm.

| $m_\pi^2$(GeV$^2$) | $M_N$(GeV) | $m_\pi L$ |
|---|---|---|
| 0.492 | 1.583(5) | 10.32 |
| 0.325 | 1.411(12) | 8.38 |
| 0.169 | 1.215(12) | 6.05 |
| 0.087 | 1.093(19) | 4.35 |
| 0.024 | 0.932(78) | 2.29 |

Table C.3: CP-PACS [AK$^+$02] lattice QCD simulation results for the nucleon mass $M_N$, the lattice spacing $a$ and the spatial lattice length $L$ at various pion mass squared values $m_\pi^2$.

| $m_\pi^2$(GeV$^2$) | $M_N$(GeV) | $a$(fm) | $L$(fm) | $m_\pi L$ |
|---|---|---|---|---|
| 0.940 | 1.809(15) | 0.102 | 2.45 | 12.03 |
| 0.913 | 1.798(4) | 0.130 | 3.12 | 15.11 |
| 0.704 | 1.652(9) | 0.099 | 2.38 | 10.10 |
| 0.689 | 1.643(5) | 0.123 | 2.95 | 12.42 |
| 0.539 | 1.519(9) | 0.095 | 2.28 | 8.49 |
| 0.502 | 1.497(6) | 0.118 | 2.83 | 10.17 |
| 0.353 | 1.348(12) | 0.092 | 2.21 | 6.65 |
| 0.272 | 1.275(7) | 0.111 | 2.66 | 7.04 |

Table C.4: Quenched lattice QCD data for the $\rho$ meson mass $m_\rho$ at various pion mass squared values $m_\pi^2$. The lattice size is $20^3 \times 32$, with a lattice spacing of 0.153 fm.

| $m_\pi^2(\text{GeV}^2)$ | $m_\rho(\text{GeV})$ | $m_\pi L$ |
|---|---|---|
| 3.150 | 2.001(1) | 27.53 |
| 2.187 | 1.700(2) | 22.94 |
| 1.742 | 1.548(2) | 20.47 |
| 1.329 | 1.399(2) | 17.88 |
| 1.212 | 1.354(2) | 17.08 |
| 1.062 | 1.294(2) | 15.98 |
| 0.867 | 1.214(3) | 14.44 |
| 0.743 | 1.162(4) | 13.37 |
| 0.676 | 1.133(4) | 12.75 |
| 0.610 | 1.103(5) | 12.12 |
| 0.515 | 1.060(5) | 11.13 |
| 0.422 | 1.016(6) | 10.07 |
| 0.347 | 0.985(7) | 9.13 |
| 0.288 | 0.960(8) | 8.32 |
| 0.241 | 0.938(8) | 7.62 |
| 0.204 | 0.926(9) | 7.00 |
| 0.172 | 0.914(11) | 6.43 |
| 0.143 | 0.908(14) | 5.87 |
| 0.114 | 0.899(15) | 5.24 |
| 0.094 | 0.899(16) | 4.75 |
| 0.080 | 0.896(18) | 4.38 |
| 0.068 | 0.898(20) | 4.04 |
| 0.059 | 0.902(22) | 3.77 |
| 0.053 | 0.903(26) | 3.58 |
| 0.047 | 0.907(28) | 3.37 |
| 0.041 | 0.913(32) | 3.15 |

Table C.5: Preliminary lattice QCD simulation results from QCDSF for the isovector nucleon magnetic moment $\mu_n^v$, the lattice spacing $a$ and the spatial lattice length $L$ at various pion mass squared values $m_\pi^2$.

| $m_\pi^2(\text{GeV}^2)$ | $\mu_n^v(\mu_N)$ | $a(\text{fm})$ | $L(\text{fm})$ | $m_\pi L$ |
|---|---|---|---|---|
| 0.863 | 2.394(69) | 0.089 | 1.43 | 6.73 |
| 0.709 | 2.483(45) | 0.073 | 1.76 | 7.50 |
| 0.688 | 2.548(159) | 0.091 | 1.45 | 6.11 |
| 0.591 | 2.621(49) | 0.084 | 2.01 | 7.85 |
| 0.392 | 2.863(86) | 0.070 | 1.67 | 5.30 |
| 0.357 | 2.781(51) | 0.084 | 2.03 | 6.13 |
| 0.290 | 2.840(121) | 0.070 | 1.67 | 4.57 |
| 0.198 | 3.082(120) | 0.081 | 1.96 | 4.42 |
| 0.159 | 3.006(118) | 0.077 | 1.84 | 3.72 |
| 0.077 | 3.711(158) | 0.076 | 3.04 | 4.26 |

Table C.6: Preliminary lattice QCD simulation results from QCDSF for the isovector nucleon electric charge radius $\langle r^2 \rangle_E$, the lattice spacing $a$ and the spatial lattice length $L$ at various pion mass squared values $m_\pi^2$.

| $m_\pi^2(\text{GeV}^2)$ | $\langle r^2 \rangle_E(\text{fm}^2)$ | $a(\text{fm})$ | $L(\text{fm})$ | $m_\pi L$ |
|---|---|---|---|---|
| 0.591 | 0.303(8) | 0.084 | 2.01 | 7.85 |
| 0.357 | 0.349(6) | 0.084 | 2.03 | 6.13 |
| 0.349 | 0.340(5) | 0.080 | 1.92 | 5.75 |
| 0.198 | 0.384(11) | 0.081 | 1.96 | 4.42 |
| 0.188 | 0.392(12) | 0.068 | 2.19 | 4.81 |
| 0.074 | 0.494(25) | 0.076 | 3.04 | 4.18 |
| 0.053 | 0.586(24) | 0.068 | 3.25 | 3.79 |

# Bibliography

[A⁺05]      P. Achard et al. Measurement of the running of the electromagnetic coupling at large momentum-transfer at LEP. *Phys.Lett.*, B623:26–36, 2005.

[A⁺09]      S. Aoki et al. 2+1 Flavor Lattice QCD toward the Physical Point. *Phys.Rev.*, D79:034503, 2009.

[AAL⁺05]    C. R. Allton, W. Armour, D. B. Leinweber, A. W. Thomas, and R. D. Young. Chiral and continuum extrapolation of partially-quenched lattice results. *Phys. Lett.*, B628:125–130, 2005.

[AAL⁺06]    W. Armour, C. R. Allton, D. B. Leinweber, A. W. Thomas, and R. D. Young. Unified chiral analysis of the vector meson spectrum from lattice qcd. *J. Phys.*, G32:971–992, 2006.

[AK⁺02]     A. Ali Khan et al. Light Hadron Spectroscopy with Two Flavors of Dynamical Quarks on the Lattice. *Phys. Rev.*, D65:054505, 2002.

[AK⁺04]     A. Ali Khan et al. The nucleon mass in N(f) = 2 lattice QCD: Finite size effects from chiral perturbation theory. *Nucl. Phys.*, B689:175–194, 2004.

[BCF97]     M. Booth, G. Chiladze, and A. F. Falk. Quenched chiral perturbation theory for vector mesons. *Phys. Rev.*, D55:3092–3100, 1997.

[Bea04a]    Silas R. Beane. In search of the chiral regime. *Nucl. Phys.*, B695:192–198, 2004.

[Bea04b]   Silas R. Beane.  Nucleon masses and magnetic moments in a finite volume. *Phys. Rev.*, D70:034507, 2004.

[Ber08]    Veronique Bernard. Chiral Perturbation Theory and Baryon Properties. *Prog. Part. Nucl. Phys.*, 60:82–160, 2008.

[BHLO02]   B. Borasoy, B. R. Holstein, R. Lewis, and P. P. A. Ouimet.  Long distance regularization in chiral perturbation theory with decuplet fields. *Phys. Rev.*, D66:094020, 2002.

[BHM04]    Veronique Bernard, Thomas R. Hemmert, and Ulf-G. Meissner. Cutoff schemes in chiral perturbation theory and the quark mass expansion of the nucleon mass. *Nucl. Phys.*, A732:149–170, 2004.

[BM97]     B. Borasoy and Ulf-G. Meissner.  Chiral expansion of baryon masses and sigma terms. *Annals Phys.*, 254:192–232, 1997.

[BNS10]    Oliver Bar, Silvia Necco, and Andrea Shindler.  The epsilon regime with twisted mass Wilson fermions. *JHEP*, 1004:053, 2010.

[Boh92]    D. Bohm. *Thought as a System*.  Routledge London and New York, 1992.

[Bor07]    Bugra Borasoy.  Introduction to Chiral Perturbation Theory.  pages 1–26, 2007.

[CD71]     T.P. Cheng and Roger F. Dashen.  Is SU(2) x SU(2) a better symmetry than SU(3)? *Phys.Rev.Lett.*, 26:594, 1971.

[CJJ$^+$74]   A. Chodos, R. L. Jaffe, K. Johnson, Charles B. Thorn, and V. F. Weisskopf.  A New Extended Model of Hadrons.  *Phys. Rev.*, D9:3471–3495, 1974.

[Col85]    S. Coleman. *Aspects of Symmetry, Selected Erice Lectures*. Cambridge University Press, 1985.

[CR98]     C. K. Chow and S. J. Rey. Quenched and partially quenched chiral per-
           turbation theory for vector and tensor mesons. *Nucl. Phys.*, B528:303–
           321, 1998.

[DGH96]    J. F. Donahue, E. Golowich, and B. R. Holstein. *Dynamics of the
           Standard Model (Cambridge Monographs on Particle Physics, Nu-
           clear Physics and Cosmology).* Cambridge University Press, New Ed
           Edition, 1996.

[Dir28a]   P.A.M. Dirac. The Quantum theory of electron. 2. *Proc.Roy.Soc.Lond.*,
           A118:351, 1928.

[Dir28b]   Paul A.M. Dirac. The Quantum theory of electron.
           *Proc.Roy.Soc.Lond.*, A117:610–624, 1928.

[DLL96]    S. J. Dong, J. F. Lagae, and K. F. Liu. $\pi n \sigma$ term , $\bar{s}s$ in nucleon, and
           scalar form factor — a lattice study. *Phys. Rev.*, D54:5496–5500, 1996.

[DSGS05]   D. Djukanovic, M. R. Schindler, J. Gegelia, and S. Scherer. Improving
           the ultraviolet behavior in baryon chiral perturbation theory. *Phys.
           Rev.*, D72:045002, 2005.

[Fey39]    R. P. Feynman. Forces in Molecules. *Phys. Rev.*, 56:340–343, 1939.

[FKOU95]   M. Fukugita, Y. Kuramashi, M. Okawa, and A. Ukawa. Pion - nucleon
           sigma term in lattice qcd. *Phys. Rev.*, D51:5319–5322, 1995.

[G$^+$99]  S. Gusken et al. The Pion nucleon sigma term with dynamical Wilson
           fermions. *Phys.Rev.*, D59:054504, 1999.

[Gas81]    J. Gasser. Hadron Masses and Sigma Commutator in the Light of Chi-
           ral Perturbation Theory. *Annals Phys.*, 136:62, 1981.

[Geo90]    Howard Georgi. AN EFFECTIVE FIELD THEORY FOR HEAVY
           QUARKS AT LOW- ENERGIES. *Phys. Lett.*, B240:447–450, 1990.

161

[GHK64]    G.S. Guralnik, C.R. Hagen, and T.W.B. Kibble. Global Conservation Laws and Massless Particles. *Phys.Rev.Lett.*, 13:585–587, 1964.

[GL88]     J. Gasser and H. Leutwyler. Spontaneously Broken Symmetries: Effective Lagrangians at Finite Volume. *Nucl.Phys.*, B307:763, 1988.

[GLS91]    J. Gasser, H. Leutwyler, and M.E. Sainio. Sigma term update. *Phys.Lett.*, B253:252–259, 1991.

[GM64]     Murray Gell-Mann. A Schematic Model of Baryons and Mesons. *Phys.Lett.*, 8:214–215, 1964.

[GML60]    Murray Gell-Mann and M Levy. The axial vector current in beta decay. *Nuovo Cim.*, 16:705, 1960.

[GMOR68]   Murray Gell-Mann, R. J. Oakes, and B. Renner. Behavior of current divergences under SU(3) x SU(3). *Phys. Rev.*, 175:2195–2199, 1968.

[GN74]     David J. Gross and Andre Neveu. Dynamical Symmetry Breaking in Asymptotically Free Field Theories. *Phys.Rev.*, D10:3235, 1974.

[Gre99]    B. Greene. *The Elegant Universe*. Jonathan Cape London, 1999.

[GSS88]    J. Gasser, M. E. Sainio, and A. Svarc. Nucleons with Chiral Loops. *Nucl. Phys.*, B307:779, 1988.

[GT58]     M. L. Goldberger and S. B. Treiman. Decay of the pi meson. *Phys. Rev.*, 110:1178–1184, 1958.

[Gue66]    M. Guenin. On the interaction picture. *Communications in Mathematical Physics*, 3:120–132, 1966.

[GW73a]    D.J. Gross and Frank Wilczek. Asymptotically Free Gauge Theories. 1. *Phys.Rev.*, D8:3633–3652, 1973.

[GW73b]    D.J. Gross and Frank Wilczek. Ultraviolet Behavior of Nonabelian Gauge Theories. *Phys.Rev.Lett.*, 30:1343–1346, 1973.

[GW74]     D.J. Gross and Frank Wilczek. ASYMPTOTICALLY FREE GAUGE THEORIES. 2. *Phys.Rev.*, D9:980–993, 1974.

[Haa58]    R. Haag. Quantum field theories with composite particles and asymptotic conditions. *Phys. Rev.*, 112:669–673, 1958.

[Han90]    F. C. Hansen. Finite-size effects in spontaneously broken su(n) su(n) theories. *Nuclear Physics B*, 345(2-3):685 – 708, 1990.

[HL90]     P. Hasenfratz and H. Leutwyler. Goldstone boson related finite size effects in field theory and critical phenomena with o(n) symmetry. *Nuclear Physics B*, 343(1):241 – 284, 1990.

[HL91]     F. C. Hansen and H. Leutwyler. Charge correlations and topological susceptibility in qcd. *Nuclear Physics B*, 350(1-2):201 – 227, 1991.

[HLY10]    J. M. M. Hall, D. B. Leinweber, and R. D. Young. Power Counting Regime of Chiral Effective Field Theory and Beyond. *Phys. Rev.*, D82:034010, 2010.

[HMRW06]   A. Holl, P. Maris, C. D. Roberts, and S. V. Wright. Schwinger functions and light-quark bound states, and sigma terms. *Nucl. Phys. Proc. Suppl.*, 161:87–94, 2006.

[Höh83]    G. Höhler. Pion nucleon scattering. *Landolt-Börnstein*, 9B2, ed. H. Schopper (Springer) Berlin, 1983.

[Jen92]    Elizabeth Ellen Jenkins. Baryon masses in chiral perturbation theory. *Nucl. Phys.*, B368:190–203, 1992.

[JLMS93]   Elizabeth Ellen Jenkins, Michael E. Luke, Aneesh V. Manohar, and Martin J. Savage. Chiral perturbation theory analysis of the baryon magnetic moments. *Phys. Lett.*, B302:482–490, 1993.

[JM91a]    Elizabeth Ellen Jenkins and Aneesh V. Manohar. Baryon chiral perturbation theory. 1991. Talk presented at the Workshop on Effective Field Theories of the Standard Model, Dobogoko, Hungary, Aug 1991.

163

[JM91b]     Elizabeth Ellen Jenkins and Aneesh V. Manohar.  Baryon chiral per-
            turbation theory using a heavy fermion Lagrangian.   *Phys. Lett.*,
            B255:558–562, 1991.

[Joh78]     K. Johnson.   A FIELD THEORY LAGRANGIAN FOR THE MIT
            BAG MODEL. *Phys. Lett.*, B78:259, 1978.

[Koc82]     R. Koch. *Z. Phys.*, C15:161, 1982.

[KP80]      R. Koch and E. Pietarinen. *Nucl. Phys.*, A336:331, 1980.

[Leb95]     Richard F. Lebed.   Determination of SU(6) Clebsch-Gordan coeffi-
            cients and baryon mass and electromagnetic moment relations. *Phys.
            Rev.*, D51:5039–5052, 1995.

[LS96]      James N. Labrenz and Stephen R. Sharpe.  Quenched chiral perturba-
            tion theory for baryons. *Phys. Rev.*, D54:4595–4608, 1996.

[LSSW96]    M. Luscher, S. Sint, R. Sommer, and P. Weisz.  Chiral symmetry and
            o(a) improvement in lattice qcd. *Nucl. Phys.*, B478:365–400, 1996.

[LTTW00]    Derek Bruce Leinweber, Anthony William Thomas, Kazuo Tsushima,
            and Stewart Victor Wright.  Baryon masses from lattice QCD: Beyond
            the perturbative chiral regime. *Phys. Rev.*, D61:074502, 2000.

[LTW00]     Derek Bruce Leinweber, Anthony William Thomas, and Stewart Victor
            Wright.  Lattice QCD calculations of the sigma commutator.  *Phys.
            Lett.*, B482:109–113, 2000.

[LTY04]     Derek Bruce Leinweber, Anthony William Thomas, and Ross Daniel
            Young. Physical nucleon properties from lattice QCD. *Phys. Rev. Lett.*,
            92:242002, 2004.

[LTY05]     D. B. Leinweber, A. W. Thomas, and R. D. Young.  Extrapolation of
            lattice qcd results beyond the power- counting regime. *Nucl. Phys.*,
            A755:59–70, 2005.

[LTY06] D. B. Leinweber, A. W. Thomas, and R. D. Young. Power counting regime of chiral extrapolation and beyond. *PoS*, LAT2005:048, 2006.

[Lub97] M. Lublinsky. g(omega rho pi) reexamined. *Phys. Rev.*, D55:249–254, 1997.

[MB99] Judith A. McGovern and Michael C. Birse. On the absence of fifth-order contributions to the nucleon mass in heavy-baryon chiral perturbation theory. *Phys. Lett.*, B446:300–305, 1999.

[MB06] Judith A. McGovern and Michael C. Birse. Convergence of the chiral expansion for the nucleon mass. *Phys. Rev.*, D74:097501, 2006.

[MG84] Aneesh Manohar and Howard Georgi. Chiral Quarks and the Nonrelativistic Quark Model. *Nucl. Phys.*, B234:189, 1984.

[MTT80] Gerald A. Miller, Anthony William Thomas, and S. Theberge. Pion - Nucleon Scattering in the Cloudy Bag Model. *Phys. Lett.*, B91:192, 1980.

[NK87] Ann E. Nelson and David B. Kaplan. Strange Condensate Realignment in Relativistic Heavy Ion Collisions. *Phys.Lett.*, B192:193, 1987.

[NN95] R. Narayanan and H. Neuberger. A construction of lattice chiral gauge theories. *Nucl. Phys.*, B443:305–385, 1995.

[O$^+$08] H. Ohki et al. Nucleon sigma term and strange quark content from lattice QCD with exact chiral symmetry. *Phys. Rev.*, D78:054502, 2008.

[Omn02] R. Omnès. *Quantum Philosophy: Understanding and Interpreting Contemporary Science*. Princeton University Press, 2002.

[Pes95] D. V. Peskin, M. E. Schroeder. *An Introduction to Quantum Field Theory*. Perseus Books Publishing L.L.C., 1995.

[Pol73] H.David Politzer. Reliable Perturbative Results for Strong Interactions? *Phys.Rev.Lett.*, 30:1346–1349, 1973.

[Pro96]     Serban Protopopescu. Observation of the Top Quark. *Nuovo Cim.*, A109:755–769, 1996.

[PSWA02]    M.M. Pavan, I.I. Strakovsky, R.L. Workman, and R.A. Arndt. The Pion nucleon Sigma term is definitely large: Results from a G.W.U. analysis of pi nucleon scattering data. *PiN Newslett.*, 16:110–115, 2002.

[RCR10]     H.L.L. Roberts, L. Chang, and C.D. Roberts. Impact of dynamical chiral symmetry breaking on meson structure and interactions. 2010.

[RS80]      M. Reed and B. Simon. *Methods of Modern Mathematical Physics, Vol 1: Functional Analysis*. Academic Press, 1980.

[RW94]      Craig D. Roberts and Anthony G. Williams. Dyson-Schwinger equations and their application to hadronic physics. *Prog.Part.Nucl.Phys.*, 33:477–575, 1994.

[SDGS07]    M. R. Schindler, D. Djukanovic, J. Gegelia, and S. Scherer. Chiral expansion of the nucleon mass to order O(q**6). *Phys. Lett.*, B649:390–393, 2007.

[Sha97]     Stephen R. Sharpe. Chiral perturbation theory and weak matrix elements. *Nucl. Phys. Proc. Suppl.*, 53:181–198, 1997.

[SP09]      Matthias R. Schindler and Daniel R. Phillips. Bayesian Methods for Parameter Estimation in Effective Field Theories. *Annals Phys.*, 324:682–708, 2009.

[SS05]      Stefan Scherer and Matthias R. Schindler. A Chiral perturbation theory primer. 2005.

[SW85]      B. Sheikholeslami and R. Wohlert. Improved continuum limit lattice action for qcd with wilson fermions. *Nucl. Phys.*, B259:572, 1985.

[tHV72]     G. 't Hooft and M. J. G. Veltman. Regularization and renormalization of gauge fields. *Nucl. Phys.*, B44:189–213, 1972.

[VW84]    C. Vafa and Edward Witten. Restrictions on Symmetry Breaking in Vector-Like Gauge Theories. *Nucl. Phys.*, B234:173, 1984.

[Wei95]    S. Weinberg. *The Quantum Theory of Fields*. Cambridge University Press, 1995.

[Wil74]    Kenneth G. Wilson. Confinement of Quarks. *Phys.Rev.*, D10:2445–2459, 1974.

[WL05]    Andre Walker-Loud. Octet baryon masses in partially quenched chiral perturbation theory. *Nucl. Phys.*, A747:476–507, 2005.

[WLT00]    Stewart Victor Wright, Derek Bruce Leinweber, and Anthony William Thomas. The sigma commutator from lattice QCD. *Nucl. Phys.*, A680:137–140, 2000.

[WLTY07]    P. Wang, Derek Bruce Leinweber, Anthony William Thomas, and Ross Daniel Young. Chiral extrapolation of nucleon magnetic form factors. *Phys. Rev.*, D75:073012, 2007.

[WLTY09a]    P. Wang, D.B. Leinweber, A.W. Thomas, and R.D. Young. Chiral extrapolation of octet-baryon charge radii. *Phys.Rev.*, D79:094001, 2009.

[WLTY09b]    P. Wang, D.B. Leinweber, A.W. Thomas, and R.D. Young. Strange magnetic form factor of the proton at Q**2 = 0.23- GeV**2. *Phys.Rev.*, C79:065202, 2009.

[Y$^+$06]    W. M. Yao et al. Review of particle physics. *J. Phys.*, G33:1–1232, 2006.

[YHL09]    Ross D. Young, Jonathan M. M. Hall, and Derek B. Leinweber. Towards selecting a finite-range regularization scale. 2009.

[YLT03]    R. D. Young, D. B. Leinweber, and A. W. Thomas. Convergence of chiral effective field theory. *Prog. Part. Nucl. Phys.*, 50:399–417, 2003.

[YT10a]    R.D. Young and A.W. Thomas. Octet baryon masses and sigma terms from an SU(3) chiral extrapolation. *Phys.Rev.*, D81:014503, 2010.

[YT10b]    Ross D. Young and Anthony W. Thomas. Recent results on nucleon sigma terms in lattice QCD. *Nucl.Phys.*, A844:266C–271C, 2010.

[Z$^+$02]   J. M. Zanotti et al. Hadron masses from novel fat-link fermion actions. *Phys. Rev.*, D65:074507, 2002.

# Power counting regime of chiral effective field theory and beyond

J. M. M. Hall,[1] D. B. Leinweber,[1] and R. D. Young[1,2]

[1]*Special Research Centre for the Subatomic Structure of Matter (CSSM), School of Chemistry & Physics,
University of Adelaide, SA 5005, Australia*
[2]*Argonne National Laboratory, 9700 South Cass Avenue, Argonne, Illinois 60439, USA*
(Received 12 March 2010; published 10 August 2010)

Chiral effective field theory ($\chi$EFT) complements numerical simulations of quantum chromodynamics (QCD) on a space-time lattice. It provides a model-independent formalism for connecting lattice simulation results at finite volume and a variety of quark masses to the physical world. The asymptotic nature of the chiral expansion places the focus on the first few terms of the expansion. Thus, knowledge of the power-counting regime (PCR) of $\chi$EFT, where higher-order terms of the expansion may be regarded as negligible, is as important as knowledge of the expansion itself. Through the consideration of a variety of renormalization schemes and associated parameters, techniques to identify the PCR where results are independent of the renormalization scheme are established. The nucleon mass is considered as a benchmark for illustrating this general approach. Because the PCR is small, the numerical simulation results are also examined to search for the possible presence of an intrinsic scale which may be used in a nonperturbative manner to describe lattice simulation results outside of the PCR. Positive results that improve on the current optimistic application of chiral perturbation theory ($\chi$PT) beyond the PCR are reported.

## I. INTRODUCTION

The low energy chiral effective field theory ($\chi$EFT) of quantum chromodynamics (QCD) provides a model-independent approach for understanding the consequences of dynamical chiral-symmetry breaking in the chiral properties of hadrons. Nonanalytic contributions in the quark mass are generated by the pseudo-Goldstone meson dressings of hadrons through meson-loop integrals. Chiral perturbation theory ($\chi$PT) provides a formal approach to counting the powers of low-energy momenta and quark masses such that an ordered expansion in powers of the quark mass $m_q \propto m_\pi^2$ is constructed. $\chi$PT indicates that, in general, the most singular nonanalytic contributions to hadron properties lie in the one-loop ''meson cloud'' of the hadron. For example, the leading nonanalytic behavior of a baryon mass is proportional to $m_q^{3/2}$ or $m_\pi^3$. More generally, baryon masses can be written as an ordered expansion in quark mass or $m_\pi^2$.

To establish a model-independent framework in $\chi$PT, the expansion must display the properties of a convergent series for the terms considered. There is a power-counting regime (PCR) where the quark mass is small, and higher-order terms in the expansion are negligible beyond the order calculated. Within the PCR, the truncation of the chiral expansion is reliable to a prescribed precision.

The asymptotic nature of the chiral expansion places the focus on the first few terms of the expansion. A survey of the literature for the baryon sector of $\chi$EFT illustrates the rarity of calculations beyond one-loop [1–3], and there are no two-loop calculations which incorporate the effects of placing a baryon in a finite volume. With only a few terms

of the expansion known for certain, knowledge of the PCR of $\chi$EFT is as important as knowledge of the expansion itself. It is within the PCR that higher-order terms of the expansion may be regarded as negligible.

Numerical simulations of QCD on a space-time lattice are complemented by $\chi$EFT through the provision of a model-independent formalism for connecting lattice simulation results to the physical world. Simulations at finite volume and a variety of quark masses are related to the infinite volume and physical quark masses through this formalism. However, the formalism is accurate only if one works within the PCR of the truncated expansion. Present practice in the field is best described as optimistic. Truncated expansions are regularly applied to a wide range of quark (or pion) masses with little regard to a rigorous determination of the PCR.

When considering nucleons, there is some evidence that the PCR may be quite small; constrained by $m_\pi \lesssim$ 200 MeV at 1% accuracy at the chiral order $\mathcal{O}(m_\pi^4 \log m_\pi)$ [4,5]. This estimate of the PCR of $\chi$PT was identified using specific finite-range regularization (FRR) techniques to analyze lattice QCD data. Using FRR, the regime is manifest when the quark-mass dependence of the nucleon mass is independent of the renormalization-scheme parameter.

A chief focus of this paper is to establish a rigorous approach to determining the PCR of a truncated chiral expansion quantitatively. Through the consideration of a variety of renormalization schemes and associated parameters, new techniques to identify the PCR are established. The PCR is the regime where results are scheme independent. The nucleon mass is considered as a benchmark for

illustrating this general approach. Here, the chiral expansion is examined, focusing on the individual low-energy coefficients of the chiral expansion. This approach provides a determination of the PCR for a truncated expansion in $\chi$EFT. As discussed in detail in the following section, the PCR is indeed small for the nucleon mass. Other observables are expected to show a similar if not smaller PCR. Thus most of today's lattice simulation results lie outside the PCR, and the truncated chiral expansions have been used to extrapolate from outside the PCR. The low-energy coefficients determined by applying the truncated expansion outside the PCR will take on unphysical values, as they accommodate important but otherwise missing contributions from nonnegligible higher-order terms.

While continued advances in numerical simulations of lattice QCD will be vital to some extent in resolving this problem, the physical value of the strange-quark mass presents a challenge that will not diminish with supercomputing advances. If one were to include the effects of kaons, vital to understanding strangeness in the nucleon, for example, then one must either calculate to significantly higher order in the expansion of $\chi$PT or develop new nonperturbative approaches which utilize the nonperturbative information expressed in the lattice simulation results. Since the former is likely to be compromised by the asymptotic nature of the expansion, attention is given to the latter approach.

Thus the second focus of this paper is to examine the numerical simulation results, to identify the possible presence of an intrinsic scale. This may then be used to address lattice simulation results outside of the PCR in a nonperturbative manner. Of course, the nonperturbative formalism must incorporate the exact perturbative results of $\chi$PT in the PCR. Positive results are reported that improve on the current optimistic application of $\chi$PT outside of the PCR.

The outline of the presentation is as follows. Section II reviews chiral effective field theory and the process of regularization and renormalization. The adoption of FRR provides a wide range of schemes and scales, which overlap with the more popular massless renormalization schemes as the finite-range regulator parameter is taken to infinity. Section III investigates FRR in the context of a particular model. By generating a set of pseudodata and analyzing it with a variety of renormalization schemes, a robust method for determining the PCR is obtained, along with an optimal renormalization scale to use beyond the PCR. Finally, Section IV includes the analysis of three sets of lattice results for the nucleon mass, utilizing the tools developed in the previous section. Conclusions are summarized in Sec. V.

## II. EFFECTIVE FIELD THEORY

This section begins by briefly reviewing the process of regularization and renormalization in finite-range regular-

ized chiral effective field theory, providing a range of renormalization schemes and scales. A central focus is to search for the dependence of physical results on the scheme and associated scales, as these will be an indication that one is applying the chiral expansion outside the PCR.

The focus is to establish techniques that provide a quantitative test of whether a given range of $m_\pi$ lies within the PCR. This is achieved through an examination of the flow of the low-energy coefficients as a function of the renormalization scheme parameter(s). A negligible dependence would confirm that the pion-mass range is within the PCR. On the other hand, the properties of the flow will be used to identify a preferred regularization scheme in a nonperturbative sense that best describes the results beyond the PCR.

### A. Renormalization in FRR $\chi$EFT

Using the standard Gell-Mann–Oakes–Renner relation connecting quark and pion masses, $m_q \propto m_\pi^2$ [6], the formal chiral expansion of the nucleon can be written as a polynomial expansion in $m_\pi^2$ plus the meson-loop integral contributions:

$$M_N = \{a_0 + a_2 m_\pi^2 + a_4 m_\pi^4 + \mathcal{O}(m_\pi^6)\} + \Sigma_N + \Sigma_\Delta + \Sigma_{\text{tad}}. \tag{1}$$

The pion cloud corrections are considered in the heavy-baryon limit, with loop integrals, $\Sigma_N$, $\Sigma_\Delta$, and $\Sigma_{\text{tad}}$, corresponding to Figs. 1–3, respectively. The coefficients $a_i$ of the analytic polynomial, contained in brackets { } in Eq. (1)
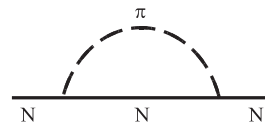


FIG. 1. The pion loop contribution to the self-energy of the nucleon, providing the leading nonanalytic contribution to the nucleon mass. All charge conserving transitions are implicit.
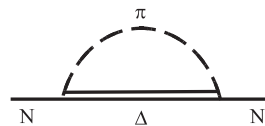


FIG. 2. The pion loop contribution to the self-energy of the nucleon allowing transitions to the nearby and strongly coupled decuplet baryons.
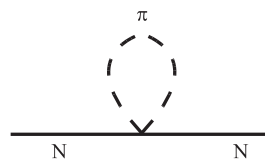


FIG. 3. Tadpole contributions to the nucleon self-energy.

, are related to the low energy constants of $\chi$PT. In this investigation, they will be determined by fitting to lattice QCD data. These coefficients will be referred to as the *residual series* coefficients. These bare coefficients undergo renormalization due to contributions from the loop integrals $\Sigma_N$, $\Sigma_\Delta$, and $\Sigma_{\text{tad}}$.

Under the most general considerations, each loop integral, when evaluated, produces an analytic polynomial in $m_\pi^2$ and nonanalytic terms:

$$\Sigma_N = b_0^N + b_2^N m_\pi^2 + \chi_N m_\pi^3 + b_4^N m_\pi^4 + \mathcal{O}(m_\pi^5), \quad (2)$$

$$\Sigma_\Delta = b_0^\Delta + b_2^\Delta m_\pi^2 + b_4^\Delta m_\pi^4 + \frac{3}{4\pi\Delta}\chi_\Delta m_\pi^4 \log\frac{m_\pi}{\mu} + \mathcal{O}(m_\pi^5), \quad (3)$$

$$\Sigma_{\text{tad}} = b_2^{t'} m_\pi^2 + b_4^{t'} m_\pi^4 + \chi_t' m_\pi^4 \log\frac{m_\pi}{\mu} + \mathcal{O}(m_\pi^5). \quad (4)$$

Here $\Delta$ is the delta-nucleon mass splitting in the chiral limit, taken to be 292 MeV. $\chi_N$, $\chi_\Delta$, and $\chi_t'$ denote the model-independent chiral coefficients of the terms that are nonanalytic in the quark mass. The $b_i$ coefficients are renormalization-scheme dependent as are the $a_i$ coefficients. It can be noted that the tadpole loop contribution $\Sigma_{\text{tad}}$ does not produce a $b_0^t$ term because it enters with a leading factor of $m_\pi^2$, as discussed in Sec. II B. The primes on the coefficients $b_2^{t'}$ and $\chi_t'$ here simply indicate that they will be used later in a slightly different form.

The process of renormalization in FRR $\chi$EFT proceeds by combining the renormalization-scheme-dependent coefficients to provide the physical low-energy coefficients, which are denoted as $c_i$. Thus, the nucleon mass expansion takes on the standard form:

$$M_N = c_0 + c_2 m_\pi^2 + \chi_N m_\pi^3 + c_4 m_\pi^4$$
$$+ \left(-\frac{3}{4\pi\Delta}\chi_\Delta + c_2\chi_t\right)m_\pi^4 \log\frac{m_\pi}{\mu} + \mathcal{O}(m_\pi^5). \quad (5)$$

By comparing Eqs. (1) through (5), the following renormalization procedure is obtained:

$$c_0 = a_0 + b_0^N + b_0^\Delta, \quad (6)$$

$$c_2 = a_2 + b_2^N + b_2^\Delta + b_2^{t'}, \quad (7)$$

$$c_4 = a_4 + b_4^N + b_4^\Delta + b_4^{t'}, \text{ etc.} \quad (8)$$

The coefficients $c_i$ are scheme-independent quantities, and this property will be demonstrated when determined within the PCR. The value of $c_0$ is the nucleon mass in the chiral limit ($m_\pi^2 = 0$), and $c_2$ is related to the so-called sigma term of explicit chiral-symmetry breaking [7–9]. The nonanalytic terms $m_\pi^3$ and $m_\pi^4 \log m_\pi/\mu$ have known coefficients denoted by $\chi_N$, $\chi_\Delta$, and $\chi_t$. The value of $c_4$ is scale dependent, such that the total $m_\pi^4$ term in Eq. (5), including

the logarithm, is independent of the scale $\mu$. It can be noted that the nucleon mass itself is completely independent of the choice of $\mu$. For the numerical analysis, $\mu$ is set equal to 1 GeV.

Of course, EFT loop calculations are commonly divergent without some regularization method. Since the effective field theory is only applicable for low energies, hard momenta contributions to loop calculations may be eliminated. However, the traditional schemes including dimensional regularization (DR) often do not involve an explicit scale dependence when evaluating loop diagrams. Without any momentum cutoff, the $b_i$ coefficients from each loop integral become either infinite or vanish, and the $c_i$ coefficients from Eq. (5) undergo an infinite renormalization or none at all:

$$c_0 = a_0 - \infty, \quad (9)$$

$$c_2 = a_2 + \infty, \quad (10)$$

$$c_4 = a_4 + 0, \text{ etc.} \quad (11)$$

Since the $c_i$ coefficients are finite after renormalization, the $a_i$ coefficients must have been infinite, with the opposite sign of the $b_i$ coefficients. As emphasized above, both the $a_i$ and $b_i$ coefficients are scheme dependent. The infinities are absorbed in constructing the $c_i$ coefficients and thus subtracted from the chiral expansion. This minimal subtraction scheme with no explicit scale dependence makes DR quite suitable for elementary fields, where the *absence* of new degrees of freedom at higher energies is assumed. However, for EFTs there is an energy scale beyond which the effective fields are no longer the relevant degrees of freedom. When one integrates loop contributions over this high-energy domain, there is no guarantee that one can efficiently subtract the model-dependent, ultraviolet physics with a finite number of counterterms (unless in the PCR). As a result, the chiral expansion typically only shows reliable convergence properties over a narrow range of pion mass.

Indeed this problem of beginning with rapidly varying loop contributions, which must then be removed with a finite number of counterterms, can easily be overcome. The hard momentum contributions to the meson-loop diagrams can be suppressed via the introduction of a regulator. As such, the coefficients of the residual expansion are likely to be smaller, and the utility of the expansion has the potential to apply to a broader range of quark or pion masses. The introduction of a regulator acts to resum the chiral expansion, with loop integrals having the general properties described in Eqs. (2) through (4).

The resummation of the chiral series through the introduction of a regulator (or similar variant) has been studied in various instances [5,10–18]. The method consists of inserting a regulator function $u(k^2)$ into the integrand of the meson-loop integrals. The regulator can take any form,

so long as it is normalized to 1, and approaches 0 sufficiently fast to ensure convergence of the loop. Unlike DR, this method involves an explicit momentum cutoff scale, $\Lambda$. The chiral expansion can now be written in terms of this cutoff scale:

$$M_N = \{a_0^\Lambda + a_2^\Lambda m_\pi^2 + a_4^\Lambda m_\pi^4 + \mathcal{O}(m_\pi^6)\} + \Sigma_N(m_\pi^2, \Lambda)$$
$$+ \Sigma_\Delta(m_\pi^2, \Lambda) + \Sigma_{\text{tad}}(m_\pi^2, \Lambda). \quad (12)$$

The superscript $\Lambda$ denotes the scheme dependence of the $a_i^\Lambda$ coefficients. The loop integrals are functions of the scale $\Lambda$ and also $m_\pi^2$.

Through the introduction of the regulator, the loop integrals are now low-energy contributions, significant for small $m_\pi^2$ and becoming negligible as $m_\pi^2$ becomes large. The scheme-dependent $a_i^\Lambda$ coefficients undergo a renormalization, as before, via their combination with the $b_i^\Lambda$ coefficients, whose scheme dependence is now explicit, reflecting the regularization of the loop integrals:

$$c_0 = a_0^\Lambda + b_0^{\Lambda,N} + b_0^{\Lambda,\Delta}, \quad (13)$$

$$c_2 = a_2^\Lambda + b_2^{\Lambda,N} + b_2^{\Lambda,\Delta} + b_2^{\Lambda,t'}, \quad (14)$$

$$c_4 = a_4^\Lambda + b_4^{\Lambda,N} + b_4^{\Lambda,\Delta} + b_4^{\Lambda,t'}, \text{ etc.} \quad (15)$$

Dimensional analysis reveals that the coefficients $b_i$ are proportional to $\Lambda^{(3-i)}$. Thus it can be realized that as the cutoff scale $\Lambda$ goes to infinity the FRR expansion reduces to that of Eq. (5) via Eqs. (9) through (11). At any finite $\Lambda$, a partial resummation of higher-order terms is introduced.

Previous studies indicate that extrapolation results show very little sensitivity to the precise functional form of the regulator [14]. In this investigation, the family of smoothly attenuating dipole regulators will be considered. The general $n$-tuple dipole function takes the following form, for a cutoff scale of $\Lambda$:

$$u_n(k^2) = \left(1 + \frac{k^{2n}}{\Lambda^{2n}}\right)^{-2}. \quad (16)$$

The standard dipole is recovered for $n = 1$. The cases $n = 2, 3$ are the "double-" and "triple-dipole" regulators, respectively. In the following, $u(k^2)$ is used to denote one of these regulators. This functional form allows one to interpolate between the dipole regulator and the step function (which corresponds to $n \to \infty$).

In a study by Bernard *et al.* [15], it was suggested that only a sharp cutoff FRR scheme is consistent with chiral symmetry. Djukanovic *et al.* [16] have demonstrated more general functional forms can be generated by proposing a scheme in which the regulator function is interpreted as a modification to the propagators of the theory, obtained from a new chiral-symmetry-preserving Lagrangian. Higher-derivative coupling terms are built into the Lagrangian in order to produce a regulator from the Feynman rules in a symmetry-preserving manner.

The regulators used in the present investigation are introduced in a less systematic fashion, such that chiral symmetry is not automatically preserved to the order calculated. The higher-derivative couplings of the regulator induces scheme-dependent nonanalytic terms. To maintain chiral symmetry, one must introduce the necessary vertex corrections.

Alternatively, one can choose the regulator judiciously such that any extra scheme-dependent nonanalytic terms are removed to any chosen order. For example, the $n$-tuple dipole regulators generate extra nonanalytic terms in the chiral expansion of Eq. (5) at higher chiral orders. For a dipole regulator, regulator-dependent nonanalytic terms occur at odd powers of $m_\pi$, beginning at $\mathcal{O}(m_\pi^5)$.[1] In the case of the double dipole, the nonanalytic terms begin at $\mathcal{O}(m_\pi^7)$, and for the triple dipole the nonanalytic terms begin only at $\mathcal{O}(m_\pi^9)$.

In a final observation, it is essential to note that the degrees of freedom present in the residual series coefficients, $a_i^\Lambda$, are sufficient to eliminate any dependence on the regulator parameter, $\Lambda$, to the order of the chiral expansion calculated: in this case $\mathcal{O}(m_\pi^4)$. By definition, higher-order terms in the FRR expansion are negligible in the PCR, and therefore FRR $\chi$EFT is mathematically equivalent to $\chi$PT in the PCR. Any differences observed in results obtained at the same chiral order but with different regularization schemes are a direct result of considering data that lie outside the PCR (provided that the regulator $\Lambda$ is not chosen too small such as to introduce an unphysical low-energy scale).

### B. Loop integrals and definitions

The leading order loop integral contributions to the nucleon mass, corresponding to the diagrams in Figs. 1–3 can be simplified to a convenient form by taking the heavy-baryon limit and performing the pole integration for $k_0$. Renormalization, as outlined above, is achieved by subtracting the relevant terms in the Taylor expansion of the loop integrals and absorbing them into the corresponding low-energy constants, $c_i$:

$$\tilde{\Sigma}_N = \chi_N \frac{1}{2\pi^2} \int d^3k \frac{k^2 u^2(k^2)}{\omega^2(k)} - b_0^{\Lambda,N} - b_2^{\Lambda,N} m_\pi^2 \quad (17)$$

$$= \chi_N m_\pi^3 + b_4^{\Lambda,N} m_\pi^4 + \mathcal{O}(m_\pi^5), \quad (18)$$

$$\tilde{\Sigma}_\Delta = \chi_\Delta \frac{1}{2\pi^2} \int d^3k \frac{k^2 u^2(k^2)}{\omega(k)(\Delta + \omega(k))} - b_0^{\Lambda,\Delta} - b_2^{\Lambda,\Delta} m_\pi^2 \quad (19)$$

---

[1]While scheme-dependent, it is significant to note that with a dipole regulator, $\Lambda = 0.8$ GeV, the coefficient of the induced $m_\pi^5$ term compares favorably with the two-loop calculation [1–3,5,14]

$$= b_4^{\Lambda,\Delta} m_\pi^4 - \frac{3}{4\pi\Delta} \chi_\Delta m_\pi^4 \log\frac{m_\pi}{\mu} + \mathcal{O}(m_\pi^5), \qquad (20)$$

$$\tilde{\Sigma}_{\text{tad}} = c_2 m_\pi^2 \left( \chi_t \frac{1}{4\pi} \int \mathrm{d}^3 k \frac{2u^2(k^2)}{\omega(k)} - b_2^{\Lambda,t} \right) \qquad (21)$$

$$= c_2 m_\pi^2 \left( b_4^{\Lambda,t} m_\pi^2 + \chi_t m_\pi^2 \log\frac{m_\pi}{\mu} + \mathcal{O}(m_\pi^5) \right) \qquad (22)$$

$$= c_2 m_\pi^2 \tilde{\sigma}_{\text{tad}}. \qquad (23)$$

These integrals are expressed in terms of the pion energy, $\omega(k) = \sqrt{k^2 + m_\pi^2}$. The tilde (̃) denotes that the integrals are written out in renormalized form to chiral order $\mathcal{O}(m_\pi^2)$. As the $b_i$ coefficients are regulator and scale dependent, this subtraction removes this dependence. The coefficients $a_0$ and $a_2$ of the analytic terms in the chiral expansion in Eq. (5) are now automatically the renormalized coefficients $c_0$ and $c_2$. This is because the $b_0$ and $b_2$ terms in Eqs. (13) and (14) are removed in the subtraction. Note also that the tadpole amplitude in Eqs. (22) and (23) contains the renormalized $c_2$ in its coefficient. The interaction vertex in this diagram arises from expanding out the pion field in the leading quark-mass insertion.

The constant coefficients $\chi_N$, $\chi_\Delta$, and $\chi_t$ for each integral are defined in terms of the pion decay constant, which is taken to be $f_\pi = 93$ MeV, and the axial coupling parameters $D$, $F$, and $\mathcal{C}$ which couple the baryons to the pion field. The phenomenological values for these couplings are used, applying the SU(6) flavor-symmetry relations [19,20] to yield $\mathcal{C} = -2D$, $F = \frac{2}{3}D$ and the value $D = 0.76$:

$$\chi_N = -\frac{3}{32\pi f_\pi^2}(D + F)^2, \qquad (24)$$

$$\chi_\Delta = -\frac{3}{32\pi f_\pi^2}\frac{8}{9}\mathcal{C}^2, \qquad (25)$$

$$\chi_t = -\frac{3}{16\pi^2 f_\pi^2}. \qquad (26)$$

With the renormalized integrals specified, the FRR modified version of the chiral expansion in Eq. (5) takes the form:

$$M_N = c_0 + c_2 m_\pi^2 (1 + \tilde{\sigma}_{\text{tad}}) + a_4^\Lambda m_\pi^4 + \tilde{\Sigma}_N + \tilde{\Sigma}_\Delta. \quad (27)$$

The $a_4^\Lambda$ term is left in unrenormalized form for simplicity. Indeed, the $b_4$ can be evaluated by expanding out corresponding loop integrals, such as in Ref. [12]. However, the focus here is on the behavior of $c_0$ and $c_2$.

Since the results of lattice simulations reflect the presence of discrete momentum values associated with the finite volume of the lattices, the formalism must also take into account these finite-volume effects. In order to accom-

modate the effect of the finite volume, the continuous loop integrals occurring in the meson-loop calculations in infinite volume are transformed into a sum over discrete momentum values. The difference between a loop sum and its corresponding loop integral is the finite-volume correction, which should vanish for all integrals as $m_\pi L$ becomes large [21].

While Eq. (27) is useful in describing the pion-mass evolution of the nucleon mass, for the consideration of lattice QCD results, one also needs to incorporate corrections to allow for the finite-volume nature of the numerical simulations. As the pion is the lightest degree of freedom in the system, it is the leading order pion loop effects that are most sensitive to the periodic boundary conditions. The corrections can be determined by considering the transformation of each loop integral in Eqs. (17), (19), and (21), into a discrete sum for lattice volume $V = L_x L_y L_z$ [22]:

$$\int \mathrm{d}^3 k \rightarrow \frac{(2\pi)^3}{L_x L_y L_z} \sum_{k_x, k_y, k_z}. \qquad (28)$$

Each momentum component is quantized in units of $2\pi/L$, that is $k_i = n_i 2\pi/L$ for integers $n_i$. The finite-volume correction $\delta^{\text{FVC}}$ can be written as the difference between the finite sum and the integral:

$$\delta_i^{\text{FVC}} = \frac{\chi_i}{2\pi^2}\left[ \frac{(2\pi)^3}{L_x L_y L_z} \sum_{k_x, k_y, k_z} I_i(\vec{k}, m_\pi^2, \Lambda) \right.$$
$$\left. - \int \mathrm{d}^3 k I_i(\vec{k}, m_\pi^2, \Lambda) \right], \qquad (29)$$

where $i = N$, $\Delta$, and the integrands are denoted $I_i(\vec{k}, m_\pi^2, \Lambda)$. By adding the relevant finite-volume correction (FVC) to each loop contribution, the finite-volume nucleon mass can be parameterized:

$$M_N^V = c_0 + c_2 m_\pi^2 (1 + \tilde{\sigma}_{\text{tad}}) + a_4^\Lambda m_\pi^4 + (\tilde{\Sigma}_N + \delta_N^{\text{FVC}})$$
$$+ (\tilde{\Sigma}_\Delta + \delta_\Delta^{\text{FVC}}). \qquad (30)$$

It is also anticipated that the FVC are independent of the regularization scale $\Lambda$ in this domain. In Figs. 4 and 5, the scale dependence of the finite-volume corrections is shown for a dipole regulator and a 2.9 fm box (the same box size used for the PACS-CS data [23]). It is notable that choosing $\Lambda$ too small suppresses the very infrared physics that one is trying to describe, and therefore it is sensible to be cautious by not selecting a $\Lambda$ that is too low. Figures 6 and 7 show the behavior of the FVC for a 4.0 fm box, and the corrections are much smaller as expected.

For large $\Lambda$ the results saturate to a fixed result. For the light pion masses, provided $\Lambda \gtrsim 0.8$ GeV, the estimated finite-volume corrections are stable. The asymptotic result is used, which has been demonstrated to be successful in previous studies [24]. Numerically, this is achieved by evaluating the finite-volume corrections with a parameter, $\Lambda' = 2.0$ GeV, $\delta_i^{\text{FVC}} = \delta_i^{\text{FVC}}(\Lambda')$. It should be noted that
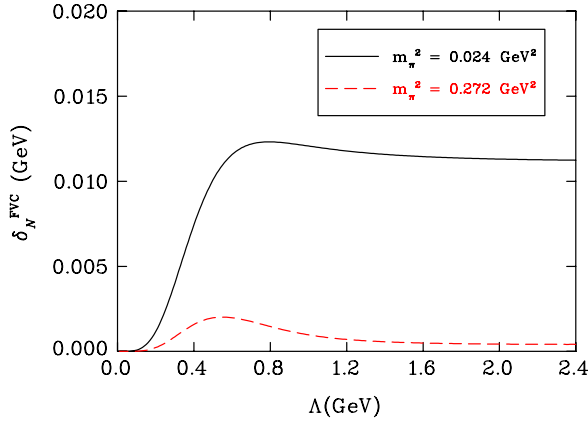
FIG. 4 (color online). Behavior of the finite-volume corrections $\delta_N^{\text{FVC}}$ vs $\Lambda$ on a 2.9 fm box using a dipole regulator. Results for two different values of $m_\pi^2$ are shown.
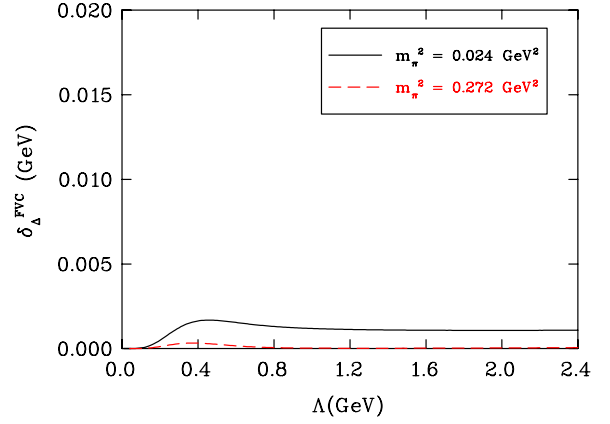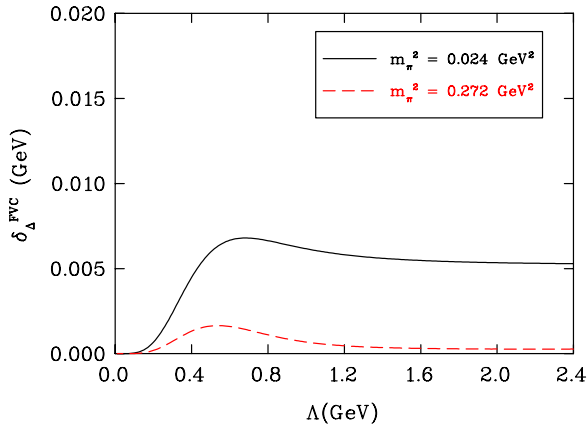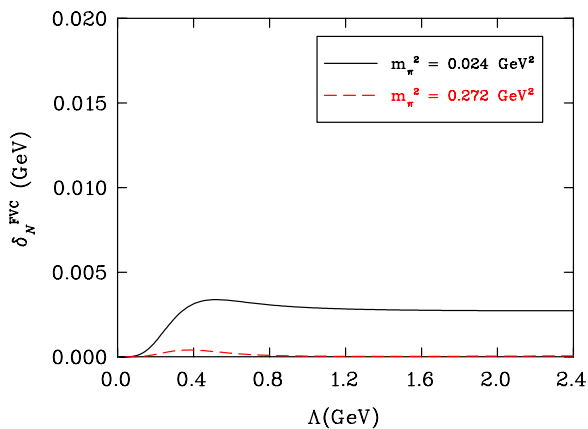


FIG. 5 (color online). Behavior of finite-volume corrections $\delta_\Delta^{\text{FVC}}$ vs $\Lambda$ on a 2.9 fm box using a dipole regulator. Results for two different values of $m_\pi^2$ are shown.



FIG. 6 (color online). Behavior of finite-volume corrections $\delta_N^{\text{FVC}}$ vs $\Lambda$ on a 4.0 fm box using a dipole regulator. Results for two different values of $m_\pi^2$ are shown.



FIG. 7 (color online). Behavior of finite-volume corrections $\delta_\Delta^{\text{FVC}}$ vs $\Lambda$ on a 4.0 fm box using a dipole regulator. Results for two different values of $m_\pi^2$ are shown.

this is equivalent to the more algebraic approach outlined in Ref. [21].

## III. INTRINSIC SCALE: PSEUDODATA

This $\chi$EFT extrapolation scheme to order $\mathcal{O}(m_\pi^4 \log m_\pi)$ will be used in conjunction with lattice QCD data from JLQCD [27], PACS-CS [23], and CP-PACS [28] collaborations to predict the nucleon mass for any value of $m_\pi^2$. The lattice data used in this analysis can be used to extrapolate $M_N$ to the physical point by taking into account the relevant curvature from the loop integrals in Eqs. (18), (20), and (22). As an example, a regulator value of $\Lambda = 1.0$ GeV was chosen for Figs. 8–10, where the finite-volume corrected EFT appears concordant with previous QCDSF-UKQCD collaboration results [24]. If the regulator is changed away from the choice $\Lambda = 1.0$ GeV, the extrapolation curve also changes. This signifies a scheme dependence in the result due to using lattice QCD data beyond the PCR.
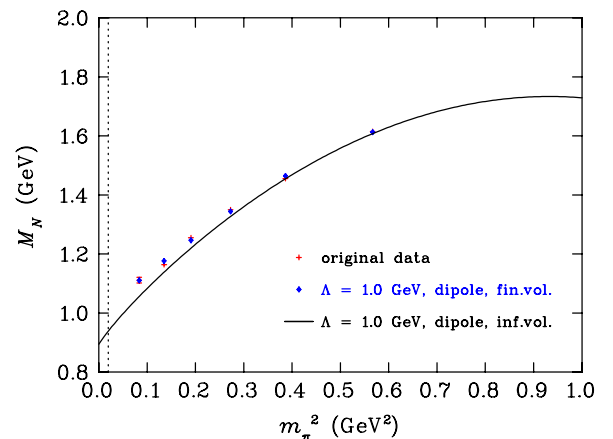


FIG. 8 (color online). Example dipole extrapolation based on JLQCD data [27], box size: 1.9 fm.
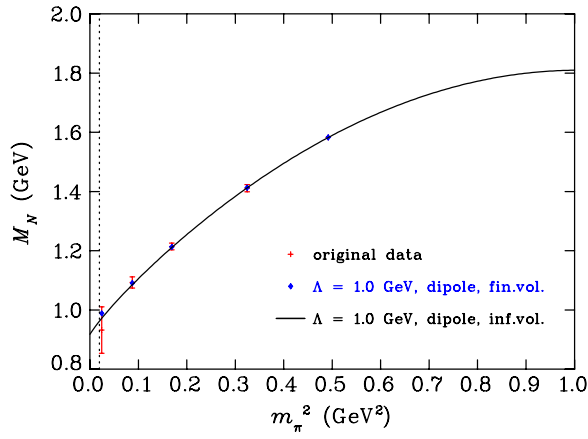
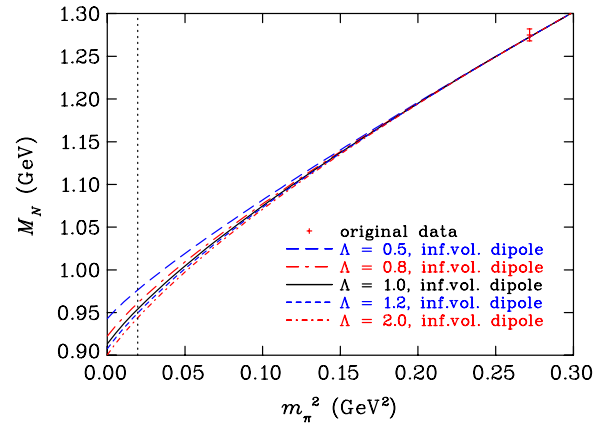FIG. 9 (color online).   Example dipole extrapolation based on PACS-CS data [23], box size: 2.9 fm.



FIG. 11 (color online).   Close zoom of the regulator dependence for dipole extrapolation based on CP-PACS data. Only the data point corresponding to the smallest $m_\pi^2$ value is shown at this scale.

To demonstrate this, consider the infinite volume extrapolation of the CP-PACS data. The extrapolation is achieved by subtracting the finite-volume loop integral contributions defined in Eqs. (17), (19), and (21) from each data point and then fitting the result to obtain the coefficients $c_0$, $c_2$, and $a_4^\Lambda$ as shown in Eq. (27). The infinite volume loop integrals are then added back at any desired value of $m_\pi^2$.

Figure 11 shows that the curves overlap exactly when $m_\pi^2$ is large, where the lattice data reside. They diverge as the chiral regime is approached. This section addresses this problem in detail.

A particular regularization scale is selected and a dense and precise data set is generated, which smoothly connects with state of the art lattice simulation results. If all the data considered lie within the PCR then the choice of regulator parameter is irrelevant, and the FRR chiral expansion is mathematically equivalent to scale-invariant renormalzation schemes including DR. However, the purpose here is to consider an insightful scenario, whereby a set of *ideal*

pseudodata with known low-energy coefficients is produced. This scenario will form the basis of the investigation of the PCR, and ultimately the possible existence of an intrinsic scale hidden within the actual lattice QCD data.

The pseudodata are produced by performing a finite-volume extrapolation such as that shown in Figs. 8–10. The difference is that 100 infinite volume extrapolation points are produced close to the chiral regime. The exercise is to pretend that it is actual lattice QCD data. Clearly, a regularization scheme must be chosen to produce the pseudodata. In this case, a dipole regulator was chosen and pseudodata were created at $\Lambda_c \equiv 1.0$ GeV.

The regularization dependence of the extrapolation is characterized by the scale dependence of the renormalized constants $c_i$. Consider how $c_0$ and $c_2$ behave when analyzed with a variety of regulator values in Figs. 12 and 13.



FIG. 10 (color online).   Example dipole extrapolation based on CP-PACS data [28], box size: 2.3–2.8 fm.
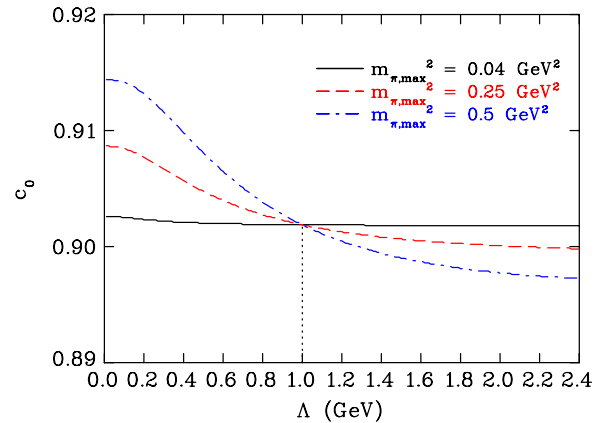


FIG. 12 (color online).   Behavior of $c_0$ vs regulator parameter $\Lambda$, based on infinite volume pseudodata created with a dipole regulator at $\Lambda_c = 1.0$ GeV (based on lightest four data points from PACS-CS). Each curve uses pseudodata with a different upper value of pion mass $m_{\pi,\text{max}}^2$.
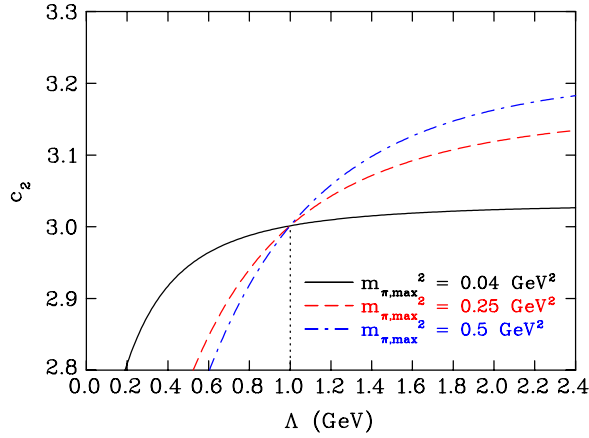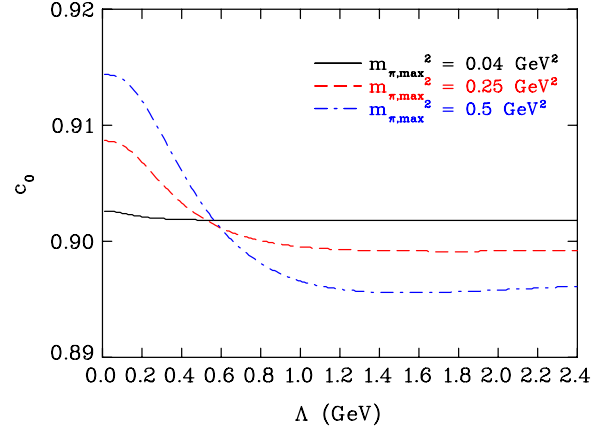
FIG. 13 (color online).   Behavior of $c_2$ vs $\Lambda$, based on infinite volume pseudodata created with a dipole regulator at $\Lambda_c = 1.0$ GeV (based on lightest four data points from PACS-CS). Each curve uses pseudodata with a different upper value of pion mass $m_{\pi,\text{max}}^2$.

By choosing to use pseudodata produced at infinite volume, one eliminates the concern that behavior of the low energy constants across a range of regulators and pion masses is a finite-volume artefact. The equivalents of Figs. 12 and 13 for finite-volume pseudodata exhibit the same features.

If three pseudodata sets are compared, each with different upper bounds on the range of $m_\pi^2$ considered in the fit, an increasing regulator dependence in $c_0$ and $c_2$ is seen further from the PCR. A steep line indicates a strong scheme dependence in the result, and naturally occurs for data samples extending far outside the PCR. Scheme independence will appear as a completely horizontal graph. The latter is what one expects for a value of $m_{\pi,\text{max}}^2 < 0.04$ GeV$^2$, as shown in Figs. 12 and 13. Note that, for each figure, all three curves (corresponding to different $m_{\pi,\text{max}}^2$) arrive at stable values for $c_0$ and $c_2$ on the right-hand side of the graph (large $\Lambda$). To read off the values of $c_0$ and $c_2$ for large $\Lambda$ is tempting but wrong. It is known that the correct values of $c_0$ and $c_2$ are recovered at $\Lambda = 1.0$ GeV, because at that value the pseudodata were created.

The analysis of the pseudodata in Figs. 12 and 13 shows that as the value of $m_{\pi,\text{max}}^2$ is changed, the correct value of $c_0$ is recovered at exactly $\Lambda = \Lambda_c$, where the curves intersect. This is also the intersection point for $c_2$ at $\Lambda = \Lambda_c$. This suggests that when considering lattice QCD results extending outside the PCR, there may be an optimal finite-range cutoff. Physically, such a cutoff would be associated with an intrinsic scale reflecting the finite size of the source of the pion dressings. Mathematically, this optimal cutoff is reflected by an independence of the fit parameters on $m_{\pi,\text{max}}^2$.

To illustrate the nontriviality of this scale of curve-intersection, the pseudodata were analyzed with a different regulator, e.g. a triple-dipole regulator. Figures 14 and 15



FIG. 14 (color online).   Behavior of $c_0$ vs $\Lambda$, based on infinite volume pseudodata created with a dipole regulator at $\Lambda_c = 1.0$ GeV but subsequently analyzed using a triple-dipole regulator.

show that the scale of the intersection is no longer a clear point but a cluster centered about 0.5 to 0.6 GeV. The triple dipole will of course predict a different ''best scale'', since the shape of the regulator is different from that of the dipole used to create the pseudodata. The essential point of this exercise is that clustering of curve intersections identifies a preferred renormalization scale that allows one to recover the correct low-energy coefficients. In this case, the crossing of the dashed and dotted-dashed curves (from fitting) clearly identifies $\Lambda_{\text{trip}}^{\text{scale}} = 0.6$ GeV as a preferred regulator, which reflects the intrinsic scale used to create the data. Table I compares the values for $c_0$ and $c_2$ recovered in this analysis for two different regulators: the preferred value $\Lambda_{\text{trip}}^{\text{scale}} = 0.6$ GeV, and a large value $\Lambda_{\text{trip}} = 2.4$ GeV reflecting the asymptotic result recovered
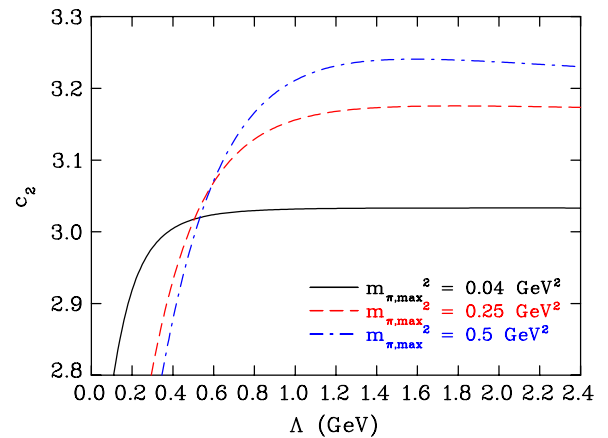


FIG. 15 (color online).   Behavior of $c_2$ vs $\Lambda$, based on infinite volume pseudodata created with a dipole regulator at $\Lambda_c = 1.0$ GeV but subsequently analyzed using a triple-dipole regulator.

TABLE I. A comparison of the parameters $c_0$ (GeV) and $c_2$ (GeV$^{-1}$) at their input value (pseudodata created with a dipole at $\Lambda_c = 1.0$ GeV) with the values when analyzed with a triple-dipole regulator. Different values of $\Lambda_{\text{trip}}$ (GeV) and $m_{\pi,\text{max}}^2$ (GeV$^2$) are chosen to demonstrate the scheme dependence of $c_0$ and $c_2$ for data extending outside the PCR.

| Parameter | Input | $\Lambda_{\text{trip}}^{\text{scale}} = 0.6$ $m_{\pi,\text{max}}^2 = 0.25$ | $\Lambda_{\text{trip}} = 2.4$ $m_{\pi,\text{max}}^2 = 0.25$ | $\Lambda_{\text{trip}} = 2.4$ $m_{\pi,\text{max}}^2 = 0.5$ |
|---|---|---|---|---|
| $c_0$ | 0.902 | 0.901 | 0.899 | 0.896 |
| $c_2$ | 3.00 | 3.07 | 3.17 | 3.23 |

from DR. The input values of $c_0$ and $c_2$ used to create the pseudodata are also indicated.

Note that the finite-range renormalization scheme breaks down if the finite-range regulator is too small. This is because $\Lambda$ must be large enough to include the chiral physics being studied. The exact value of a sensible lower bound in the finite-range regulator will depend on the functional form chosen as regulator. This is estimated for three dipolelike regulators in Sec. IV.

Figure 13 shows that the renormalization for $c_2$ breaks down for small values of the regulator $\Lambda$. FRR breaks down for a value of $\Lambda_{\text{dip}}$ much below 0.6 GeV, because the coefficients $b_i$ of the loop integral expansion in Eqs. (18), (20), and (22) are proportional to $\Lambda^{(3-i)}$. For high-order terms with large $i$, the coefficients will become large when $\Lambda$ is small. This will adversely affect the convergence properties of the chiral expansion. One obtains a residual series expansion with good convergence properties only when $\Lambda$ reflects the intrinsic scale of the source of the pion dressings of the hadron in question.

The pseudodata analysis provides a good indication of a lower bound for $\Lambda$ using a dipole regulator: $\Lambda_{\text{dip}} \gtrsim$ 0.6 GeV. Similarly, Fig. 6 suggests a lower bound for the triple-dipole regulator: $\Lambda_{\text{trip}} \gtrsim 0.3$ GeV. The same analysis can be repeated for the double-dipole regulator to obtain $\Lambda_{\text{doub}} \gtrsim 0.4$ GeV.

One may also constrain the lowest value that $\Lambda$ can take by considering phenomenological arguments. Based on the physical values of the sigma commutator and the nucleon mass, a pion mass of $m_\pi \approx 0.5$ GeV bounds the radius of convergence [13,25,26]. Therefore, in order to ensure the inclusion of important contributions to the chiral physics, one should choose an energy scale $\Lambda_{\text{sharp}} \sim 0.5$ GeV for a sharp cutoff (step function) regulator. To compare this estimate for the sharp cutoff to that of dipolelike regulators, one can calculate the regulator value required such that $u_n^2(k^2) = 1/2$ when the momentum takes the energy scale of $\Lambda_{\text{sharp}}$. This results in a rough estimate for a sensible value for the dipole, double dipole, and triple dipole. These values are $\Lambda_{\text{dip}} \sim 1.1$ GeV, $\Lambda_{\text{doub}} \sim 0.76$ GeV, and $\Lambda_{\text{trip}} \sim 0.66$ GeV, respectively. In any event, a wide range of regulator values will be considered, and the intersections of the curves for the low-energy coefficients will be used in

order to construct fits outside the PCR. This will be done in order to identify the presence of an intrinsic scale for the pion source and an associated preferred regularization scale.

## IV. INTRINSIC SCALE: LATTICE RESULTS

### A. Evidence for an intrinsic scale

In the example of the pseudodata, an optimal finite-range cutoff was obtained from the data themselves. Clearly, the pseudodata have an *intrinsic scale*: the renormalization scale $\Lambda_c$ at which they were created. This test example leads the researcher to wonder if actual lattice QCD data have an intrinsic cutoff scale embedded within them. That is, by analyzing lattice QCD data in the same way as the pseudodata, can a similar intersection point be obtained from the renormalization scale flow of $c_0$ and $c_2$? If so, this indicates that the lattice QCD data contain information regarding an optimal finite-range regularization scale, which can be calculated.

The results for the renormalization of $c_0$ and $c_2$ as a function of $\Lambda$ are now presented for JLQCD [27], PACS-CS [23], and CP-PACS [28] lattice QCD data. The JLQCD data use overlap fermions in two-flavor QCD, but the lattice box size for each data point is $\sim$1.9 fm, smaller than the other two data sets. The PACS-CS data use the nonperturbatively $\mathcal{O}(a)$-improved Wilson quark action at a lattice box size of $\sim$2.9 fm, but the data set only contains five data points and a large statistical error in the smallest $m_\pi^2$ point. The CP-PACS data use a mean field improved clover quark action on lattice box sizes for each data point varying from $\sim$2.2 fm to $\sim$2.8 fm.

The chiral expansion is first used to chiral order $\mathcal{O}(m_\pi^3)$. In this case, the fit parameters are $c_0$ and $c_2$ only. The results for a dipole regulator are shown in Figs. 16–21, the results for the double-dipole case are shown in Figs. 22–27,
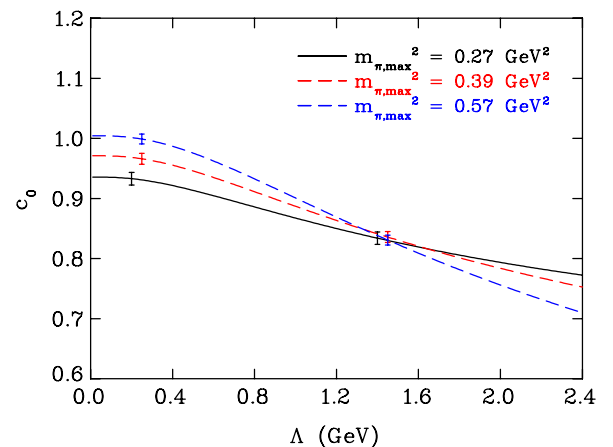


FIG. 16 (color online). Behavior of $c_0$ vs $\Lambda$, based on JLQCD data. The chiral expansion is taken to order $\mathcal{O}(m_\pi^3)$, and a dipole regulator is used. A few points are selected to indicate the general size of the statistical error bars.
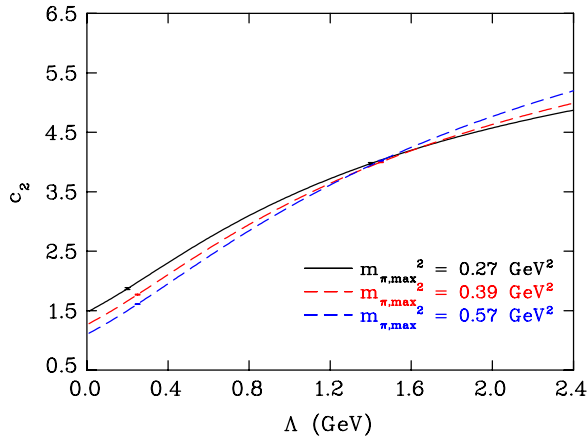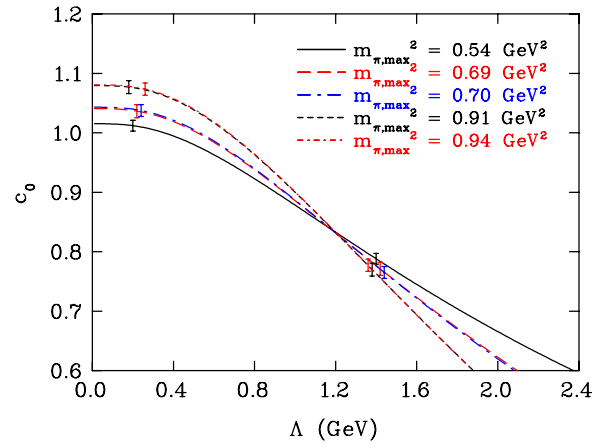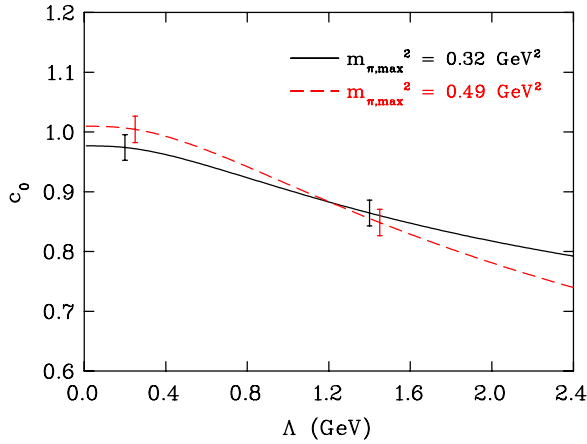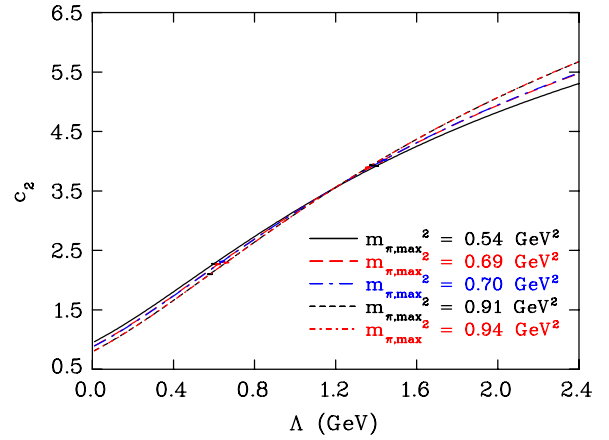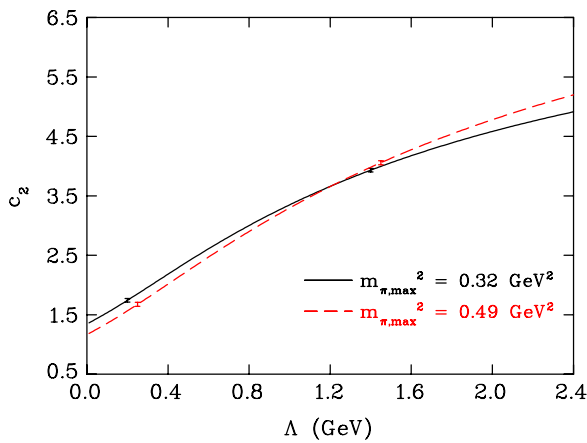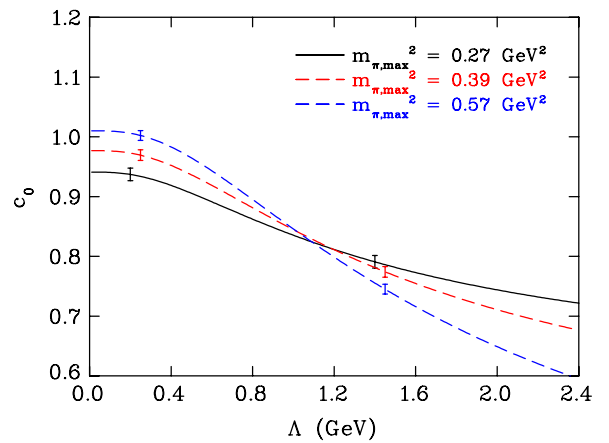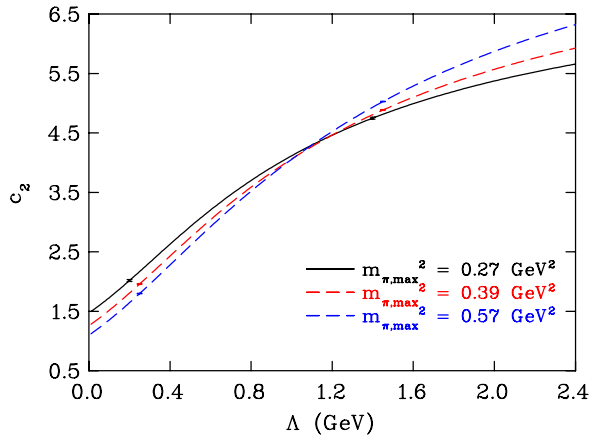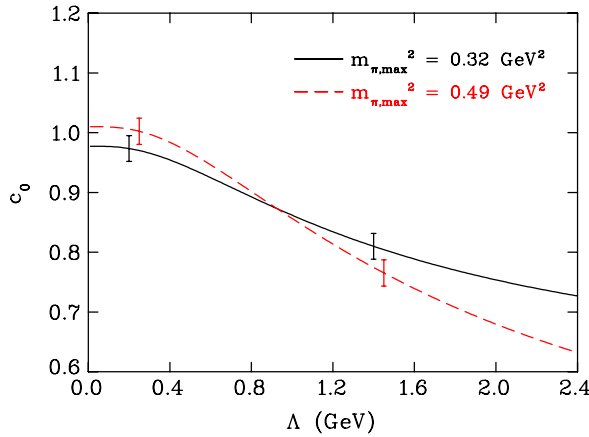
FIG. 17 (color online). Behavior of $c_2$ vs $\Lambda$, based on JLQCD data. The chiral expansion is taken to order $\mathcal{O}(m_\pi^3)$, and a dipole regulator is used. A few points are selected to indicate the general size of the statistical error bars.
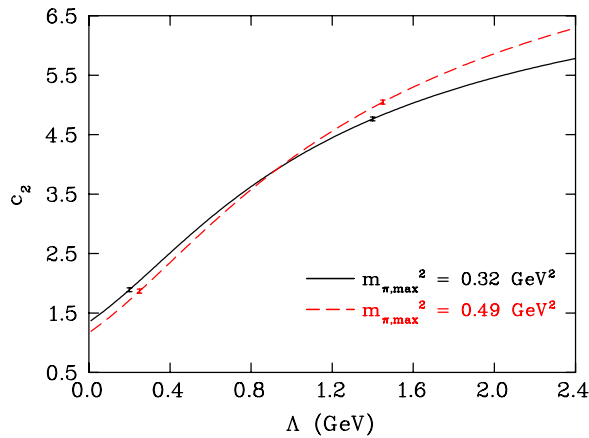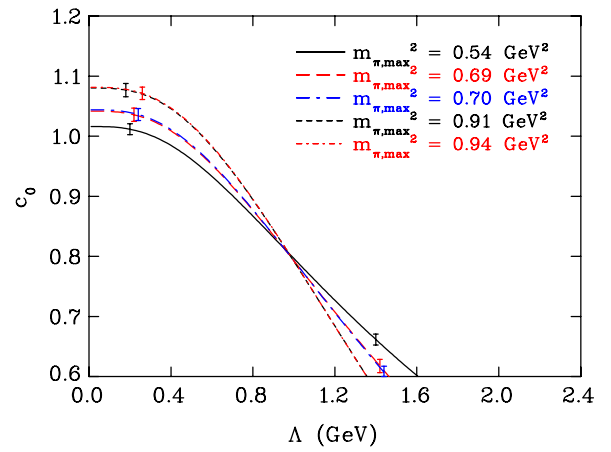


FIG. 18 (color online). Behavior of $c_0$ vs $\Lambda$, based on PACS-CS data. The chiral expansion is taken to order $\mathcal{O}(m_\pi^3)$, and a dipole regulator is used. A few points are selected to indicate the general size of the statistical error bars.



FIG. 19 (color online). Behavior of $c_2$ vs $\Lambda$, based on PACS-CS data. The chiral expansion is taken to order $\mathcal{O}(m_\pi^3)$, and a dipole regulator is used. A few points are selected to indicate the general size of the statistical error bars.



FIG. 20 (color online). Behavior of $c_0$ vs $\Lambda$, based on CP-PACS data. The chiral expansion is taken to order $\mathcal{O}(m_\pi^3)$, and a dipole regulator is used. A few points are selected to indicate the general size of the statistical error bars.



FIG. 21 (color online). Behavior of $c_2$ vs $\Lambda$, based on CP-PACS data. The chiral expansion is taken to order $\mathcal{O}(m_\pi^3)$, and a dipole regulator is used. A few points are selected to indicate the general size of the statistical error bars.



FIG. 22 (color online). Behavior of $c_0$ vs $\Lambda$, based on JLQCD data. The chiral expansion is taken to order $\mathcal{O}(m_\pi^3)$ and a double-dipole regulator is used. A few points are selected to indicate the general size of the statistical error bars.

FIG. 23 (color online). Behavior of $c_2$ vs $\Lambda$, based on JLQCD data. The chiral expansion is taken to order $\mathcal{O}(m_\pi^3)$ and a double-dipole regulator is used. A few points are selected to indicate the general size of the statistical error bars.



FIG. 24 (color online). Behavior of $c_0$ vs $\Lambda$, based on PACS-CS data. The chiral expansion is taken to order $\mathcal{O}(m_\pi^3)$ and a double-dipole regulator is used. A few points are selected to indicate the general size of the statistical error bars.



FIG. 25 (color online). Behavior of $c_2$ vs $\Lambda$, based on PACS-CS data. The chiral expansion is taken to order $\mathcal{O}(m_\pi^3)$ and a double-dipole regulator is used. A few points are selected to indicate the general size of the statistical error bars.



FIG. 26 (color online). Behavior of $c_0$ vs $\Lambda$, based on CP-PACS data. The chiral expansion is taken to order $\mathcal{O}(m_\pi^3)$ and a double-dipole regulator is used. A few points are selected to indicate the general size of the statistical error bars.

and the results for the triple dipole are shown in Figs. 28–33. To estimate the statistical error in the renormalized constants $\delta c$, a bootstrap technique of 200 configurations of nucleon mass data is used. The configurations differ by the statistical error in the data, with values generated by a Gaussian distribution. In each plot, the same configurations are used for a variety of values of $\Lambda$ considered. A few points are selected in Figs. 16–33 to indicate the general size of the statistical error bars.

It should be noted that none of these curves is flat to within 1% accuracy. All fits have included data beyond the commonly accepted PCR. Clearly, there is a well-defined intersection point in the renormalization flow curves. Also, the value of $\Lambda$ at which the intersection point occurs is the same even for different data sets, and for different $c_i$. The tight groupings of the curve crossings lend credence to the ansatz of an intrinsic scale associated with the finite size of
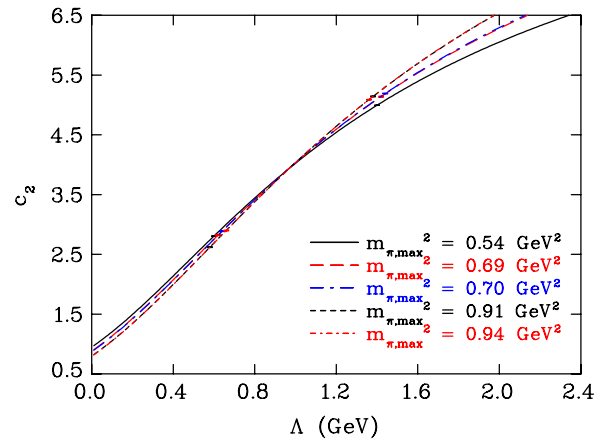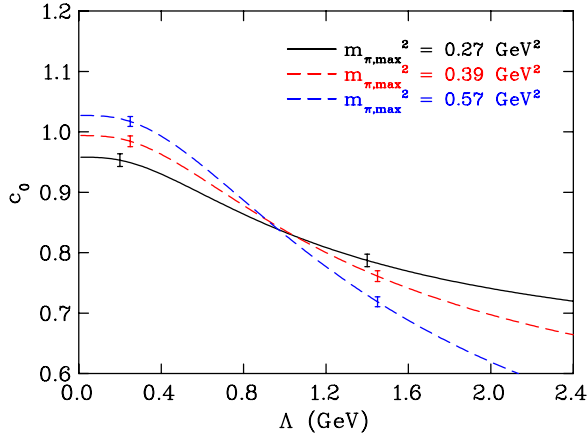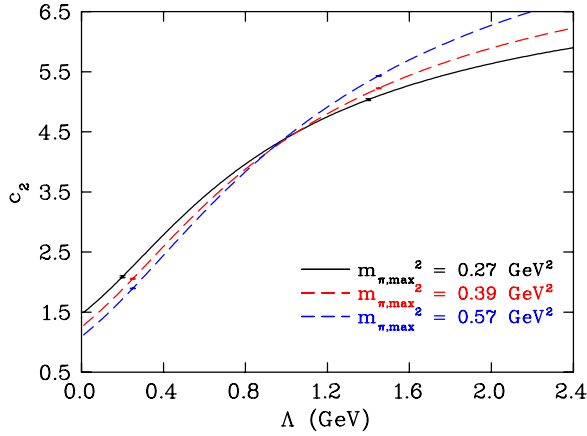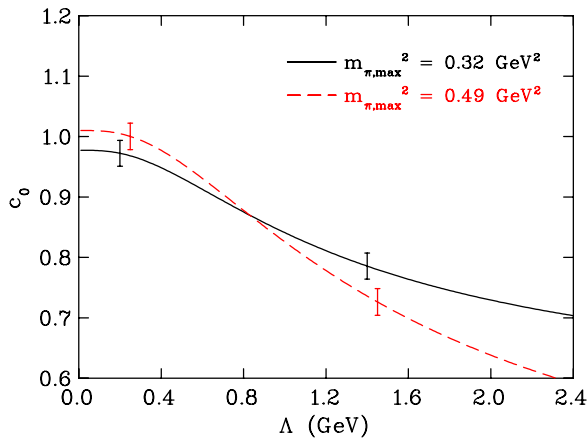


FIG. 27 (color online). Behavior of $c_2$ vs $\Lambda$, based on CP-PACS data. The chiral expansion is taken to order $\mathcal{O}(m_\pi^3)$ and a doubledipole regulator is used. A few points are selected to indicate the general size of the statistical error bars.
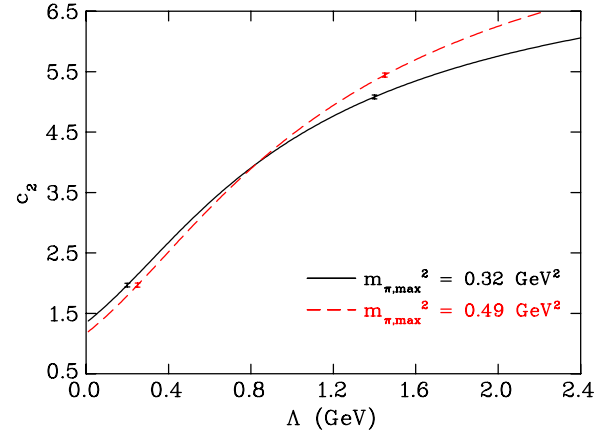
FIG. 28 (color online).   Behavior of $c_0$ vs $\Lambda$, based on JLQCD data. The chiral expansion is taken to order $\mathcal{O}(m_\pi^3)$ and a triple-dipole regulator is used. A few points are selected to indicate the general size of the statistical error bars.



FIG. 29 (color online).   Behavior of $c_2$ vs $\Lambda$, based on JLQCD data. The chiral expansion is taken to order $\mathcal{O}(m_\pi^3)$ and a triple-dipole regulator is used. A few points are selected to indicate the general size of the statistical error bars.



FIG. 30 (color online).   Behavior of $c_0$ vs $\Lambda$, based on PACS-CS data. The chiral expansion is taken to order $\mathcal{O}(m_\pi^3)$ and a triple-dipole regulator is used. A few points are selected to indicate the general size of the statistical error bars.



FIG. 31 (color online).   Behavior of $c_2$ vs $\Lambda$, based on PACS-CS data. The chiral expansion is taken to order $\mathcal{O}(m_\pi^3)$ and a triple-dipole regulator is used. A few points are selected to indicate the general size of the statistical error bars.

the source of the pion dressings of the nucleon. This is a central result of this analysis.

An intrinsic scale of $\Lambda_{\mathrm{dip}}^{\mathrm{scale}} \approx 1.3$ GeV was obtained for the dipole, $\Lambda_{\mathrm{doub}}^{\mathrm{scale}} \approx 1.0$ GeV for the double dipole and $\Lambda_{\mathrm{trip}}^{\mathrm{scale}} \approx 0.9$ GeV for the triple dipole. These values differ because the regulators have different shapes, and different values of $\Lambda^{\mathrm{scale}}$ are required to create a similar suppression of large loop momenta.

## B. Statistical errors

On each renormalization plot in Figs. 16–33 there are many curves, each corresponding to different values of $m_{\pi,\mathrm{max}}^2$. It is of primary interest to what extent these curves match. Therefore, a $\chi_{\mathrm{dof}}^2$ should be constructed, where dof equals the number of curves on each plot minus one for the best fit value of $c_0$ or $c_2$, denoted by $c^T$ in the following.
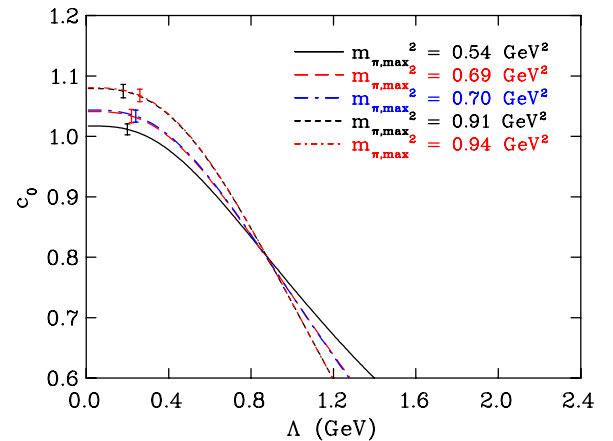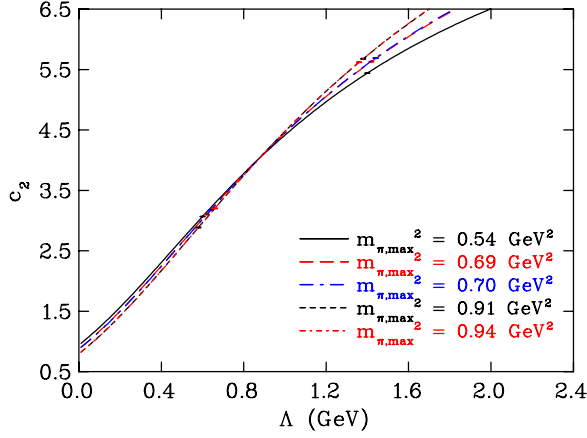


FIG. 32 (color online).   Behavior of $c_0$ vs $\Lambda$, based on CP-PACS data. The chiral expansion is taken to order $\mathcal{O}(m_\pi^3)$ and a triple-dipole regulator is used. A few points are selected to indicate the general size of the statistical error bars.
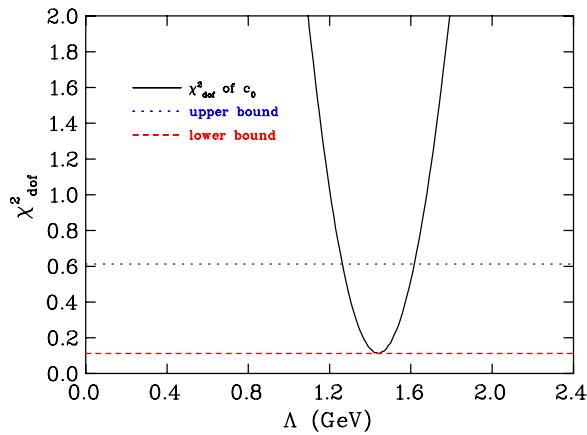
FIG. 33 (color online). Behavior of $c_2$ vs $\Lambda$, based on CP-PACS data. The chiral expansion is taken to order $\mathcal{O}(m_\pi^3)$ and a triple-dipole regulator is used. A few points are selected to indicate the general size of the statistical error bars.

This also serves to quantify the constraint on the intrinsic scale $\Lambda^{\text{scale}}$. The $\chi^2_{\text{dof}}$ is evaluated separately for each renormalized constant $c$ (with error $\delta c$) and regulator value $\Lambda$:

$$\chi^2_{\text{dof}} = \frac{1}{n-1} \sum_{i=1}^{n} \frac{(c_i(\Lambda) - c^T(\Lambda))^2}{(\delta c_i(\Lambda))^2}, \qquad (31)$$

for $i$ corresponding to data sets with differing $m_{\pi,\text{max}}^2$. The theoretical value $c^T$ is given by the weighted mean:

$$c^T(\Lambda) = \frac{\sum_{i=1}^{n} c_i(\Lambda)/(\delta c_i(\Lambda))^2}{\sum_{j=1}^{n} 1/(\delta c_j(\Lambda))^2}. \qquad (32)$$

The $\chi^2_{\text{dof}}$ can be calculated as a function of the regulator parameter $\Lambda$ for each of the renormalization plots of Figs. 16–33. In the case of the PACS-CS data, the minimum of the $\chi^2_{\text{dof}}$ curve will be centered at the intersection

point. In the case of the JLQCD and CP-PACS data, there appears to be a single intersection point on each plot, but in fact there are multiple intersections over a very small window of $\Lambda$. The results for $\chi^2_{\text{dof}}$ will indicate the "best" central value of $\Lambda$. This central value of $\Lambda$ will be taken to be the intrinsic scale. The $\chi^2_{\text{dof}}$ curves for a dipole regulator are shown in Figs. 34–39, the $\chi^2_{\text{dof}}$ curves for the double-dipole case are shown in Figs. 40–45, and the $\chi^2_{\text{dof}}$ curves for the triple dipole are shown in Figs. 46–51.

### C. Higher chiral order

Consider the renormalization of $c_0$ and $c_2$ as a function of $\Lambda$, for chiral order $\mathcal{O}(m_\pi^4 \log m_\pi)$. The results for PACS-CS and CP-PACS data are shown in Figs. 52–55, as an example. In this case, no clear intersection points in the renormalization curves can be found, and so one is unable to specify an intrinsic scale. This certainly should be the



FIG. 35 (color online). Behavior of $\chi^2_{\text{dof}}$ for $c_2$ vs $\Lambda$, based on JLQCD data. The chiral expansion is taken to order $\mathcal{O}(m_\pi^3)$, and a dipole regulator is used.
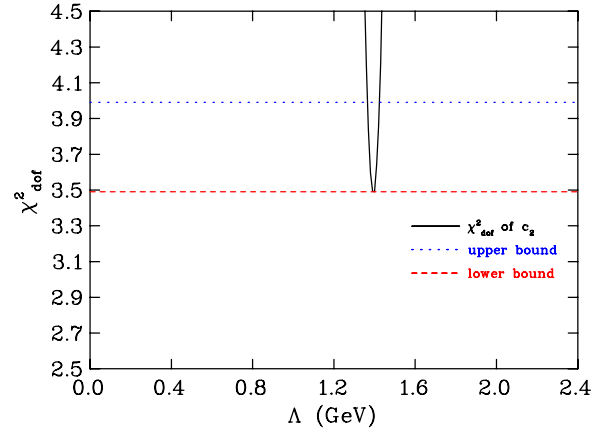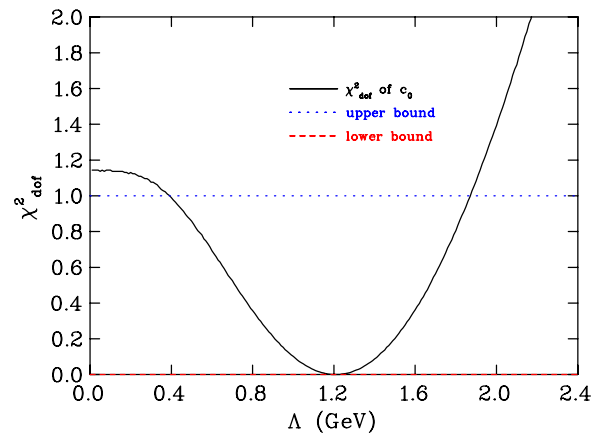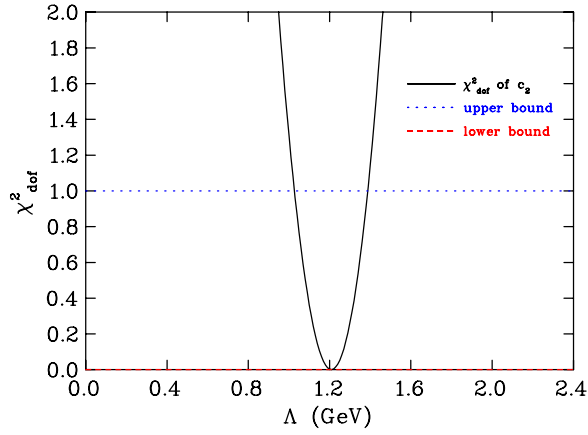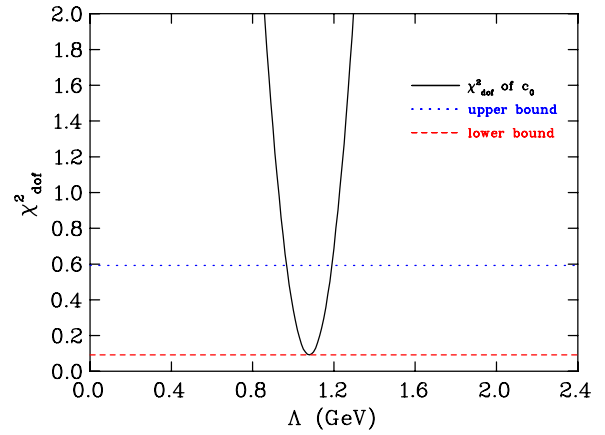


FIG. 34 (color online). Behavior of $\chi^2_{\text{dof}}$ for $c_0$ vs $\Lambda$, based on JLQCD data. The chiral expansion is taken to order $\mathcal{O}(m_\pi^3)$, and a dipole regulator is used.
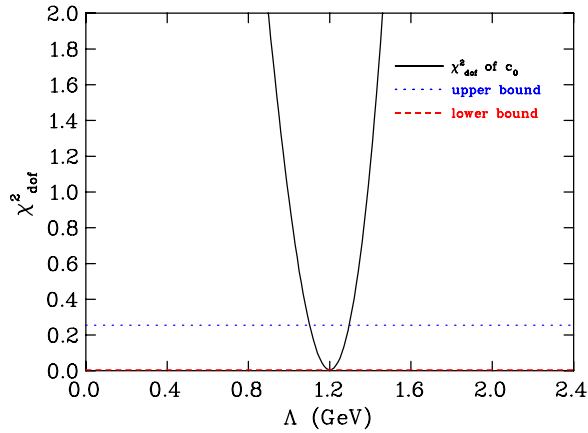


FIG. 36 (color online). Behavior of $\chi^2_{\text{dof}}$ for $c_0$ vs $\Lambda$, based on PACS-CS data. The chiral expansion is taken to order $\mathcal{O}(m_\pi^3)$, and a dipole regulator is used.

FIG. 37 (color online). Behavior of $\chi^2_{\text{dof}}$ for $c_2$ vs $\Lambda$, based on PACS-CS data. The chiral expansion is taken to order $\mathcal{O}(m_\pi^3)$, and a dipole regulator is used.
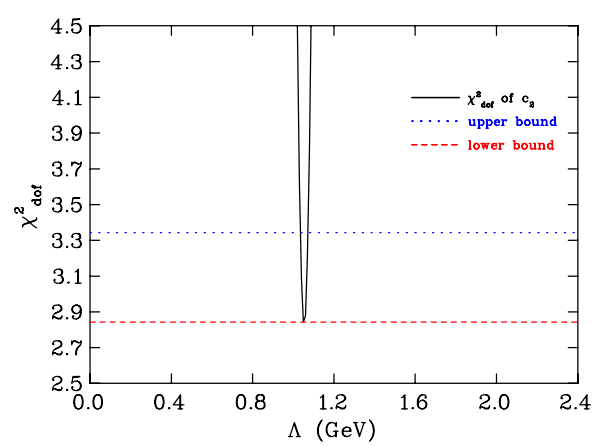


FIG. 40 (color online). Behavior of $\chi^2_{\text{dof}}$ for $c_0$ vs $\Lambda$, based on JLQCD data. The chiral expansion is taken to order $\mathcal{O}(m_\pi^3)$, and a double-dipole regulator is used.
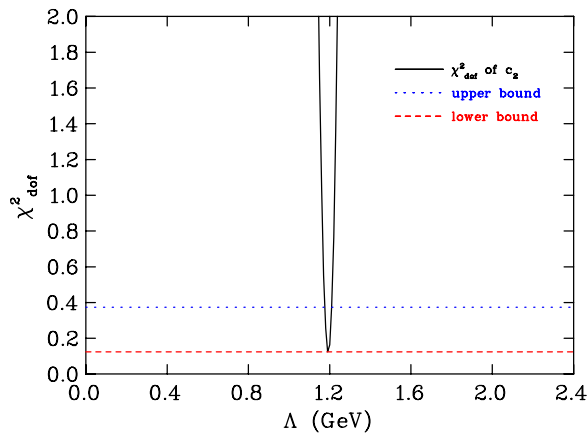


FIG. 38 (color online). Behavior of $\chi^2_{\text{dof}}$ for $c_0$ vs $\Lambda$, based on CP-PACS data. The chiral expansion is taken to order $\mathcal{O}(m_\pi^3)$, and a dipole regulator is used.



FIG. 41 (color online). Behavior of $\chi^2_{\text{dof}}$ for $c_2$ vs $\Lambda$, based on JLQCD data. The chiral expansion is taken to order $\mathcal{O}(m_\pi^3)$, and a double-dipole regulator is used.



FIG. 39 (color online). Behavior of $\chi^2_{\text{dof}}$ for $c_2$ vs $\Lambda$, based on CP-PACS data. The chiral expansion is taken to order $\mathcal{O}(m_\pi^3)$, and a dipole regulator is used.
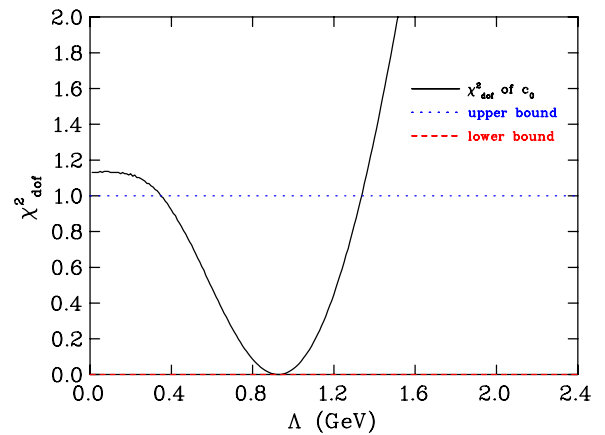


FIG. 42 (color online). Behavior of $\chi^2_{\text{dof}}$ for $c_0$ vs $\Lambda$, based on PACS-CS data. The chiral expansion is taken to order $\mathcal{O}(m_\pi^3)$, and a double-dipole regulator is used.
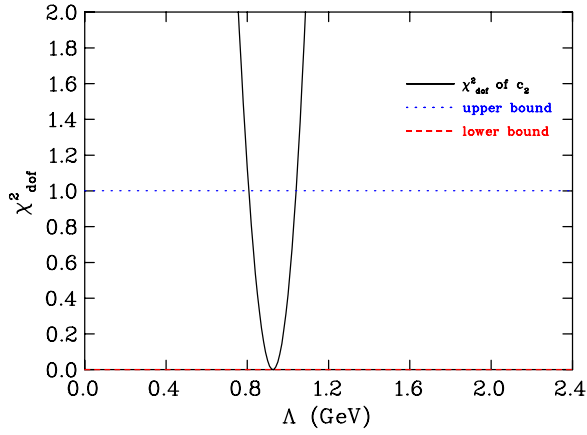
FIG. 43 (color online). Behavior of $\chi^2_{\mathrm{dof}}$ for $c_2$ vs $\Lambda$, based on PACS-CS data. The chiral expansion is taken to order $\mathcal{O}(m_\pi^3)$, and a double-dipole regulator is used.
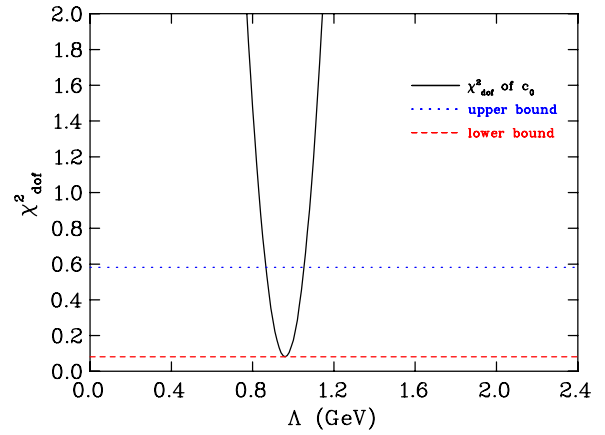


FIG. 46 (color online). Behavior of $\chi^2_{\mathrm{dof}}$ for $c_0$ vs $\Lambda$, based on JLQCD data. The chiral expansion is taken to order $\mathcal{O}(m_\pi^3)$, and a triple-dipole regulator is used.
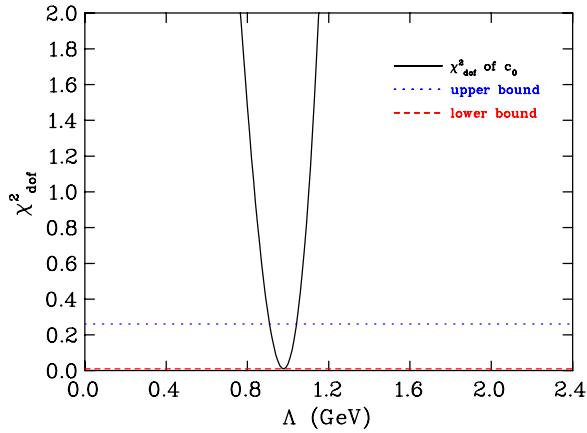


FIG. 44 (color online). Behavior of $\chi^2_{\mathrm{dof}}$ for $c_0$ vs $\Lambda$, based on CP-PACS data. The chiral expansion is taken to order $\mathcal{O}(m_\pi^3)$, and a double-dipole regulator is used.



FIG. 47 (color online). Behavior of $\chi^2_{\mathrm{dof}}$ for $c_2$ vs $\Lambda$, based on JLQCD data. The chiral expansion is taken to order $\mathcal{O}(m_\pi^3)$, and a triple-dipole regulator is used.



FIG. 45 (color online). Behavior of $\chi^2_{\mathrm{dof}}$ for $c_2$ vs $\Lambda$, based on CP-PACS data. The chiral expansion is taken to order $\mathcal{O}(m_\pi^3)$, and a double-dipole regulator is used.
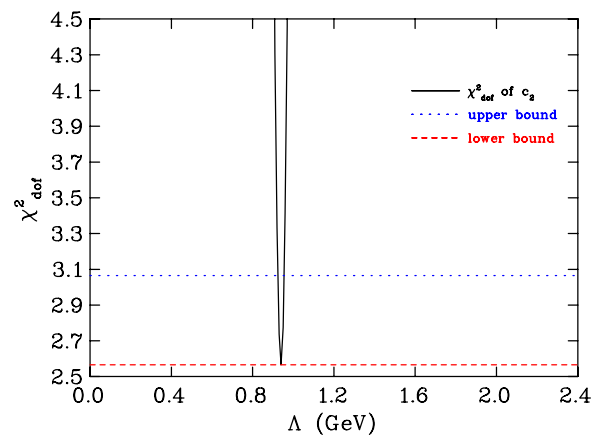


FIG. 48 (color online). Behavior of $\chi^2_{\mathrm{dof}}$ for $c_0$ vs $\Lambda$, based on PACS-CS data. The chiral expansion is taken to order $\mathcal{O}(m_\pi^3)$, and a triple-dipole regulator is used.
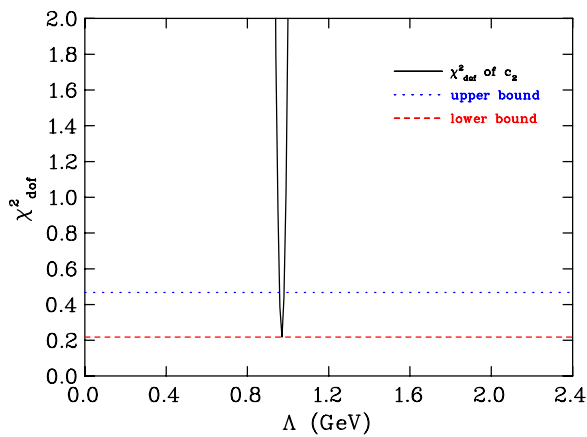
FIG. 49 (color online). Behavior of $\chi^2_{\text{dof}}$ for $c_2$ vs $\Lambda$, based on PACS-CS data. The chiral expansion is taken to order $\mathcal{O}(m_\pi^3)$, and a triple-dipole regulator is used.



FIG. 52 (color online). Behavior of $c_0$ vs $\Lambda$, based on PACS-CS data. The chiral expansion taken to order $\mathcal{O}(m_\pi^4 \log m_\pi)$ and a dipole regulator is used. A few points are selected to indicate the general size of the statistical error bars.



FIG. 50 (color online). Behavior of $\chi^2_{\text{dof}}$ for $c_0$ vs $\Lambda$, based on CP-PACS data. The chiral expansion is taken to order $\mathcal{O}(m_\pi^3)$, and a triple-dipole regulator is used.
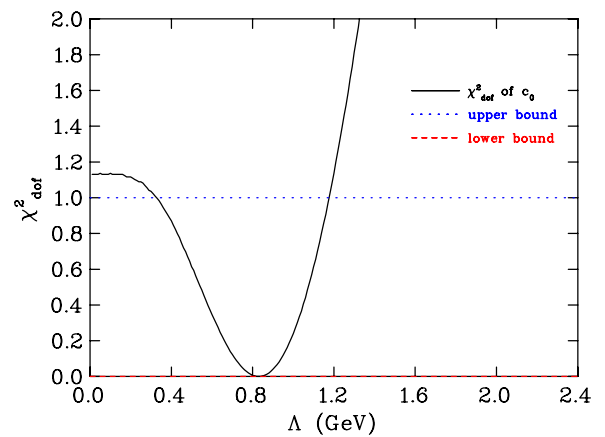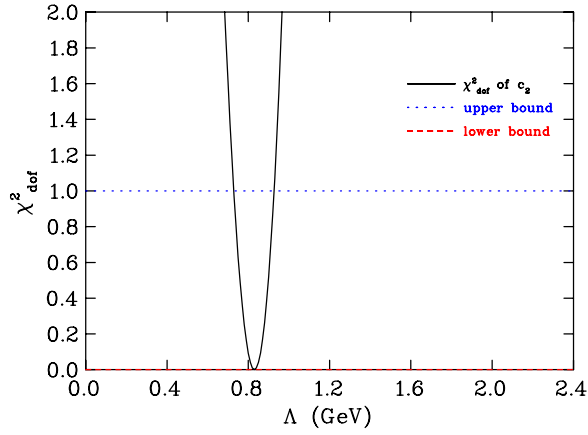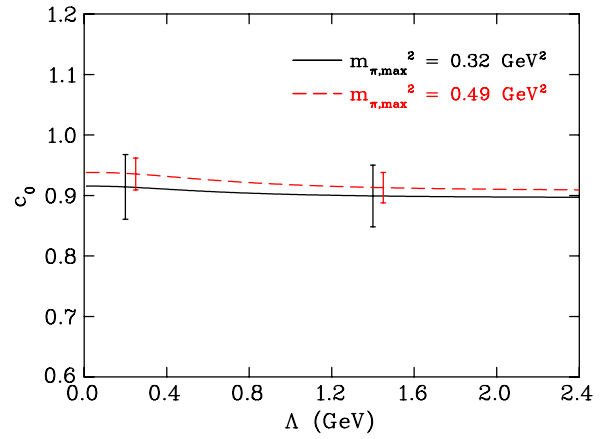


FIG. 53 (color online). Behavior of $c_2$ vs $\Lambda$, based on PACS-CS data. The chiral expansion taken to order $\mathcal{O}(m_\pi^4 \log m_\pi)$ and a dipole regulator is used. A few points are selected to indicate the general size of the statistical error bars.
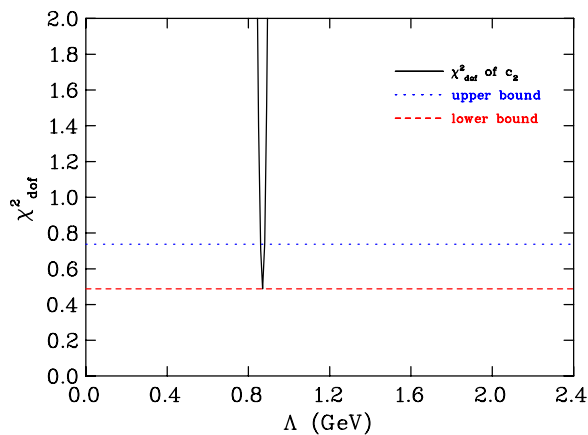


FIG. 51 (color online). Behavior of $\chi^2_{\text{dof}}$ for $c_2$ vs $\Lambda$, based on CP-PACS data. The chiral expansion is taken to order $\mathcal{O}(m_\pi^3)$, and a triple-dipole regulator is used.
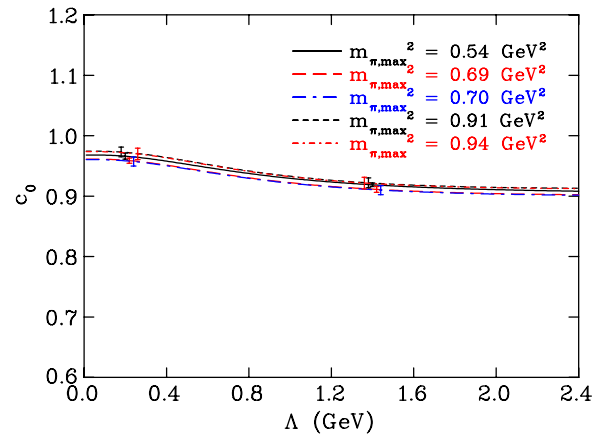


FIG. 54 (color online). Behavior of $c_0$ vs $\Lambda$, based on CP-PACS data. The chiral expansion taken to order $\mathcal{O}(m_\pi^4 \log m_\pi)$ and a dipole regulator is used. A few points are selected to indicate the general size of the statistical error bars.
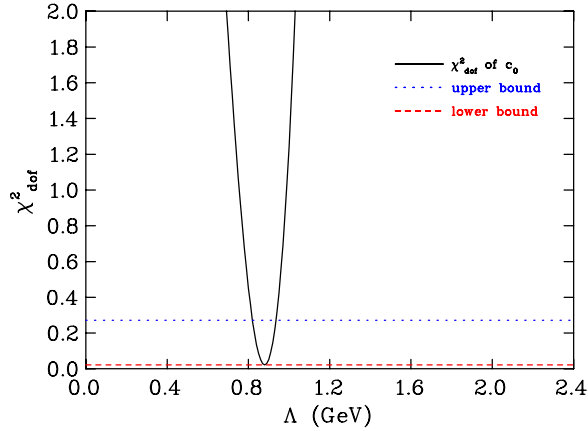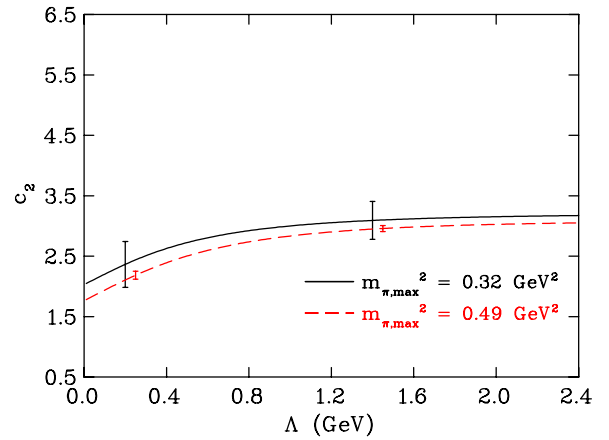
FIG. 55 (color online). Behavior of $c_2$ vs $\Lambda$, based on CP-PACS data. The chiral expansion taken to order $\mathcal{O}(m_\pi^4 \log m_\pi)$ and a dipole regulator is used. A few points are selected to indicate the general size of the statistical error bars.
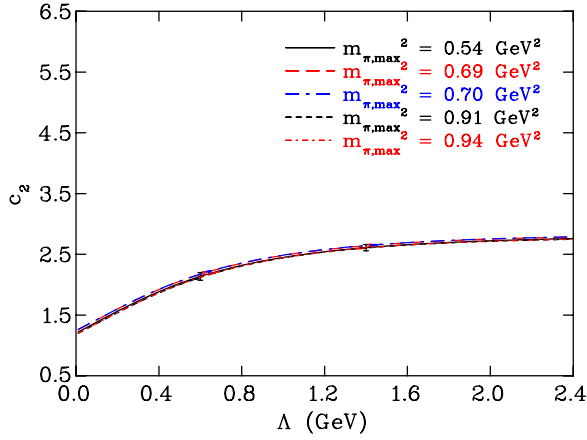
TABLE II. Values of the central $\Lambda$ value in GeV, taken from the $\chi_{\rm dof}^2$ analysis for $c_0$ and $c_2$, based on JLQCD, PACS-CS, and CP-PACS data.

| | | Regulator form | |
|---|---|---|---|
| Optimal scale | Dipole | Double | Triple |
| $\Lambda_{c_0,\rm JLQCD}^{\rm scale}$ | 1.44 | 1.08 | 0.96 |
| $\Lambda_{c_2,\rm JLQCD}^{\rm scale}$ | 1.40 | 1.05 | 0.94 |
| $\Lambda_{c_0,\rm PACS-CS}^{\rm scale}$ | 1.21 | 0.93 | 0.83 |
| $\Lambda_{c_2,\rm PACS-CS}^{\rm scale}$ | 1.21 | 0.93 | 0.83 |
| $\Lambda_{c_0,\rm CP-PACS}^{\rm scale}$ | 1.20 | 0.98 | 0.88 |
| $\Lambda_{c_2,\rm CP-PACS}^{\rm scale}$ | 1.19 | 0.97 | 0.87 |

case when working with data entirely within the PCR, because all renormalization procedures would be equivalent (to a prescribed level of accuracy) and so there would be no optimal regulator parameter. It is known that this is not the case for the data sets used in this study. This is verified by considering the evident scale dependence of $c_0$ and $c_2$ in Figs. 52–55. The fact that $c_0$ and $c_2$ change over the range of $\Lambda$ values indicates that the data are not inside the PCR. Further, since no preferred scale is revealed, any choice of $\Lambda$ appears equivalent at this order. While this is encouraging that the scheme dependence is being weakened by working to higher order, it must be recognized that there is a systematic error associated with the choice of $\Lambda$. In the case of the CP-PACS results shown in Figs. 54 and 55, it can be seen that the statistical errors are substantially smaller than the systematic error associated with a characteristic range, $\Lambda_{\rm lower} < \Lambda < \infty$, where $\Lambda_{\rm lower}$ is the lowest reasonable value of $\Lambda$.

Since it is difficult to identify the intrinsic scale at this chiral order, the results for chiral order $\mathcal{O}(m_\pi^3)$ will be chosen to demonstrate the process of handling the existence of an optimal regulator scale in lattice QCD data. The results for the calculation of the intrinsic scales $\Lambda^{\rm scale}$ for different data sets and regulators are given in Table II. This table simply summarizes the central values from Figs. 34–51. *Such excellent agreement between the $c_0$ analysis and the $c_2$ analysis is remarkable, and indicative of the existence of an instrinsic scale in the data.* There is also consistency among independent data sets. It is important to realize that the value of $\Lambda^{\rm scale}$ is always the order of ~1 GeV, not 10 GeV, nor 100 GeV; nor is it infinity.

In calculating the systematic uncertainty in the observables $c_0$, $c_2$ and the nucleon mass at the physical point due to the intrinsic scale at order $\mathcal{O}(m_\pi^4 \log m_\pi)$, two methods are provided. First, the upper and lower bounds from the $\chi_{\rm dof}^2$ analysis at order $\mathcal{O}(m_\pi^3)$ will be used to constrain $\Lambda$,

and taken to be an accurate estimate of the systematic uncertainty in the contributions of higher-order terms. Second, variation of the observables across the characteristic range of scale values, $\Lambda_{\rm lower} < \Lambda < \infty$ will be used, where $\Lambda_{\rm lower}$ takes the value of 0.6, 0.4, and 0.3 GeV for the dipole, double-dipole, and triple-dipole regulator, respectively. The results from both of these methods are displayed in Table III.

The final results for the calculation of the renormalized constants $c_0$, $c_2$ and the nucleon mass extrapolated to the physical point ($m_{\pi,\rm phys} = 140$ MeV) are summarized in Table IV. The lightest four data points from each of JLQCD, PACS-CS, and CP-PACS lattice QCD data are used. The nucleon mass is calculated at the scale determined by the data.

TABLE III. Results at $\mathcal{O}(m_\pi^4 \log m_\pi)$ for the systematic error due to the intrinsic scale, calculated using two methods, for the values of $c_0$ (GeV), $c_2$ (GeV$^{-1}$), and the nucleon mass $M_N$ (GeV) extrapolated to the physical point ($m_{\pi,\rm phys} = 140$ MeV). The first number in each column is the systematic error due to the intrinsic scale using the upper and lower bound from the $\chi_{\rm dof}^2$ analysis at order $\mathcal{O}(m_\pi^3)$. The second number is the systematic error due to the instrinsic scale across the whole range of $\Lambda$ values from the lowest reasonable value ($\Lambda = \Lambda_{\rm lower}$) obtained from the pseudodata analysis, to the asymptotic value ($\Lambda = \infty$).

| | | Regulator form | | | | |
|---|---|---|---|---|---|---|
| Sys. err. | Dipole | | Double | | Triple | |
| $\delta^\Lambda c_0^{\rm JLQCD}$ | 0.001, | 0.009 | 0.001, | 0.013 | 0.001, | 0.016 |
| $\delta^\Lambda c_0^{\rm PACS-CS}$ | 0.005, | 0.006 | 0.005, | 0.010 | 0.006, | 0.012 |
| $\delta^\Lambda c_0^{\rm CP-PACS}$ | 0.002, | 0.024 | 0.002, | 0.037 | 0.002, | 0.045 |
| $\delta^\Lambda c_2^{\rm JLQCD}$ | 0.02, | 0.31 | 0.03, | 0.38 | 0.01, | 0.48 |
| $\delta^\Lambda c_2^{\rm PACS-CS}$ | 0.18, | 0.25 | 0.16, | 0.33 | 0.14, | 0.43 |
| $\delta^\Lambda c_2^{\rm CP-PACS}$ | 0.02, | 0.40 | 0.02, | 0.58 | 0.02, | 0.73 |
| $\delta^\Lambda M_{N,\rm phys}^{\rm JLQCD}$ | 0.0004, | 0.0051 | 0.0003, | 0.0073 | 0.0003, | 0.0090 |
| $\delta^\Lambda M_{N,\rm phys}^{\rm PACS-CS}$ | 0.0022, | 0.0030 | 0.0025, | 0.0046 | 0.0025, | 0.0058 |
| $\delta^\Lambda M_{N,\rm phys}^{\rm CP-PACS}$ | 0.0012, | 0.0175 | 0.0013, | 0.0270 | 0.0014, | 0.0326 |

TABLE IV.   Results at $\mathcal{O}(m_\pi^4 \log m_\pi)$ for the values of $c_0$ (GeV), $c_2$ (GeV$^{-1}$), and the nucleon mass $M_N$ (GeV) extrapolated to the physical point ($m_{\pi,\text{phys}} = 140$ MeV). WM is the weighted mean of each row. The nucleon mass is calculated at the optimal scale $\Lambda^{\text{scale}}$, which is the average of $\Lambda_{c_0}^{\text{scale}}$ and $\Lambda_{c_2}^{\text{scale}}$ for each data set. The extrapolations are performed at box sizes relevant to each data set: $L_{\text{extrap}}^{\text{JLQCD}} = 1.9$ fm, $L_{\text{extrap}}^{\text{PACS-CS}} = 2.9$ fm, and $L_{\text{extrap}}^{\text{CP-PACS}} = 2.8$ fm. The errors are quoted as the estimate of the statistical error first (based on random bootstrap configurations), and the systematic error obtained from the number of $m_\pi^2$ values used second. Two seperate weighted means are calculated for each row. WM(1) incorporates the systematic error in the intrinsic scale using the upper and lower bound from the $\chi_{\text{dof}}^2$ analysis at order $\mathcal{O}(m_\pi^3)$. The WM(2) incorporates the systematic error due to the intrinsic scale across the whole range of $\Lambda$ values from the lowest reasonable value ($\Lambda = \Lambda_{\text{lower}}$) obtained from the pseudodata analysis, to the asymptotic value ($\Lambda = \infty$). The weighted means also include an estimate of the systematic error in the choice of regulator. All errors are added in quadrature. Note that any order $\mathcal{O}(a)$ errors have not been incorporated into the total error analysis.

|  | | Regulator form | | |
| Parameter | Dipole | Double | Triple | WM(1) | WM(2) |
| --- | --- | --- | --- | --- | --- |
| $c_0^{\text{JLQCD}}$ | 0.873(18)(16) | 0.875(17)(16) | 0.891(17)(16) | 0.880(29) | 0.879(32) |
| $c_0^{\text{PACS-CS}}$ | 0.900(51)(15) | 0.899(51)(14) | 0.898(51)(14) | 0.899(53) | 0.899(55) |
| $c_0^{\text{CP-PACS}}$ | 0.924(3)(8) | 0.914(3)(7) | 0.918(3)(7) | 0.918(13) | 0.920(37) |
| $c_2^{\text{JLQCD}}$ | 3.09(9)(11) | 3.18(9)(12) | 3.20(9)(11) | 3.16(18) | 3.14(43) |
| $c_2^{\text{PACS-CS}}$ | 3.06(32)(15) | 3.15(31)(14) | 3.17(31)(14) | 3.13(39) | 3.12(49) |
| $c_2^{\text{CP-PACS}}$ | 2.54(5)(4) | 2.70(5)(2) | 2.71(5)(3) | 2.66(18) | 2.61(60) |
| $M_{N,\text{phys}}^{\text{JLQCD}}$ | 1.02(2)(9) | 1.02(2)(9) | 1.02(2)(9) | 1.02(9) | 1.02(9) |
| $M_{N,\text{phys}}^{\text{PACS-CS}}$ | 0.967(45)(43) | 0.966(45)(43) | 0.966(45)(43) | 0.966(62) | 0.966(62) |
| $M_{N,\text{phys}}^{\text{CP-PACS}}$ | 0.982(2)(40) | 0.975(2)(43) | 0.978(2)(42) | 0.979(43) | 0.979(50) |

## V. CONCLUSION

In conclusion, it has been demonstrated that chiral effective field theory is an important tool for investigating the chiral properties of hadrons, and for extrapolating lattice QCD results. Because the chiral expansion is only convergent within a PCR, a renormalization scheme such as finite-range regularization should be used for current lattice QCD results, and into the foreseeable future. Renormalization-scheme dependence occurs when lattice QCD data extending outside the PCR are used in the extrapolation. This provides a new quantitative test for determining when lattice QCD data lie within the PCR. As most lattice data extend beyond the PCR, a formalism was developed to determine if there is an optimal regularization scale $\Lambda^{\text{scale}}$ in the finite-range regulator, and to calculate it if it exists. It was concluded that such an optimal scale can be obtained from the data itself by analyzing the renormalization flow curves of the low-energy coefficients in the chiral expansion. The optimal scale is selected by the value for which the renormalized constants are independent of the upper bound of the fit domain. This also means that the renormalized constants are not to be identified with their asymptotic values at large $\Lambda$.

It was revealed that a preferred regularization scheme exists only for data sets extending outside the PCR. Such a preferred regularization scheme is associated with an *intrinsic scale* for the size of the pion dressings of the nucleon. By working to sufficiently high chiral order, it was discovered that the scale dependence was weakened. Nevertheless, the residual scale dependence persists as a significant component of the systematic uncertainty. For efficient propagation of this uncertainty, an interesting future direction would be to consider marginalization over the scale dependence [29]. The described procedure was used to calculate the nucleon mass at the physical point, the low-energy coefficients $c_0$ and $c_2$ and their associated statistical and systematic errors. Several different functional forms of regulator were considered, and lattice QCD data from JLQCD, PACS-CS, and CP-PACS were used. An optimal cutoff scale $\Lambda^{\text{scale}}$ for each set of lattice QCD data was obtained, and the systematic error in the choice of renormalization scheme was calculated.

In summary, the existence of a well-defined intrinsic scale has been discovered. It has also been illustrated how its value can be determined from lattice QCD results.

[1] J. A. McGovern and M. C. Birse, Phys. Lett. B **446**, 300 (1999).
[2] J. A. McGovern and M. C. Birse, Phys. Rev. D **74**, 097501 (2006).
[3] M. R. Schindler, D. Djukanovic, J. Gegelia, and S. Scherer, Phys. Lett. B **649**, 390 (2007).
[4] S. R. Beane, Nucl. Phys. **B695**, 192 (2004).
[5] D. B. Leinweber, A. W. Thomas, and R. D. Young, Nucl. Phys. **A755**, 59 (2005).
[6] M. Gell-Mann, R. J. Oakes, and B. Renner, Phys. Rev. **175**, 2195 (1968).
[7] D. B. Leinweber, A. W. Thomas, and S. V. Wright, Phys. Lett. B **482**, 109 (2000).
[8] S. V. Wright, D. B. Leinweber, and A. W. Thomas, Nucl. Phys. **A680**, 137 (2001).
[9] A. Holl, P. Maris, C. D. Roberts, and S. V. Wright, Nucl. Phys. B, Proc. Suppl. **161**, 87 (2006).
[10] J. F. Donoghue, B. R. Holstein, and B. Borasoy, Phys. Rev. D **59**, 036002 (1999).
[11] R. D. Young, D. B. Leinweber, A. W. Thomas, and S. V. Wright, Phys. Rev. D **66**, 094507 (2002).
[12] R. D. Young, D. B. Leinweber, and A. W. Thomas, Prog. Part. Nucl. Phys. **50**, 399 (2003).
[13] B. Borasoy, B. R. Holstein, R. Lewis, and P. P. A. Ouimet, Phys. Rev. D **66**, 094020 (2002).
[14] D. B. Leinweber, A. W. Thomas, and R. D. Young, Phys. Rev. Lett. **92**, 242002 (2004).
[15] V. Bernard, T. R. Hemmert, and U.-G. Meissner, Nucl. Phys. **A732**, 149 (2004).
[16] D. Djukanovic, M. R. Schindler, J. Gegelia, and S. Scherer, Phys. Rev. D **72**, 045002 (2005).
[17] R. D. Young, D. B. Leinweber, and A. W. Thomas, Phys. Rev. D **71**, 014001 (2005).
[18] D. B. Leinweber *et al.*, Phys. Rev. Lett. **94**, 212001 (2005).
[19] E. E. Jenkins, Nucl. Phys. **B368**, 190 (1992).
[20] R. F. Lebed, Phys. Rev. D **51**, 5039 (1995).
[21] S. R. Beane, Phys. Rev. D **70**, 034507 (2004).
[22] W. Armour, C. R. Allton, D. B. Leinweber, A. W. Thomas, and R. D. Young, J. Phys. G **32**, 971 (2006).
[23] S. Aoki *et al.* (PACS-CS), Phys. Rev. D **79**, 034503 (2009).
[24] A. Ali Khan *et al.* (QCDSF-UKQCD), Nucl. Phys. **B689**, 175 (2004).
[25] R. D. Young, J. M. M. Hall, and D. B. Leinweber, arXiv:0907.0408.
[26] R. D. Young and A. W. Thomas, Phys. Rev. D **81**, 014503 (2010).
[27] H. Ohki *et al.*, Phys. Rev. D **78**, 054502 (2008).
[28] A. Ali Khan *et al.* (CP-PACS), Phys. Rev. D **65**, 054505 (2002).
[29] M. R. Schindler and D. R. Phillips, Ann. Phys. (N.Y.) **324**, 682 (2009).

Hall, J.M.M., Leinweber, D.B. & Young, R.D. (2011) Chiral effective field theory beyond the power-counting regime.
*AIP Conference Proceedings, v. 1354, pp. 78-83*

# Chiral extrapolation beyond the power-counting regime

J. M. M. Hall,[1] F. X. Lee,[2] D. B. Leinweber,[1] K. F. Liu,[3] N. Mathur,[4] R. D. Young,[1] and J. B. Zhang[5]

[1]*Special Research Centre for the Subatomic Structure of Matter (CSSM),*
*Department of Physics, University of Adelaide 5005, Australia*

[2]*Physics Department, The George Washington University, Washington, DC 20052, USA*

[3]*Department of Physics and Astronomy, University of Kentucky, Lexington, KY 40506, USA*

[4]*Department of Theoretical Physics, Tata Institute of Fundamental Research, Mumbai, India*

[5]*ZIMP and Department of Physics, Zhejiang University, Hangzhou, 310027, P. R. China*

Chiral effective field theory can provide valuable insight into the chiral physics of hadrons when used in conjunction with non-perturbative schemes such as lattice quantum chromodynamics (QCD). In this discourse, the attention is focused on extrapolating the mass of the $\rho$ meson to the physical pion mass in quenched QCD (QQCD). With the absence of a known experimental value, this serves to demonstrate the ability of the extrapolation scheme to make predictions without prior bias. By using extended effective field theory developed previously, an extrapolation is performed using quenched lattice QCD data that extends outside the chiral power-counting regime (PCR). The method involves an analysis of the renormalization flow curves of the low-energy coefficients in a finite-range regularized effective field theory. The analysis identifies an optimal regularization scale, which is embedded in the lattice QCD data themselves. This optimal scale is the value of the regularization scale at which the renormalization of the low-energy coefficients is approximately independent of the range of quark masses considered. By using recent precision, quenched lattice results, the extrapolation is tested directly by truncating the analysis to a set of points above 380 MeV, while temporarily disregarding the simulation results closer to the chiral regime. This tests the ability of the method to make predictions of the simulation results, without phenomenologically motivated bias. The result is a successful extrapolation to the chiral regime.

## I. INTRODUCTION

In lattice quantum chromodynamics (QCD), the calculation of observables with light dynamical quarks is computationally intensive, and only in recent times have there been successful attempts to perform calculations of any observable at the physical point ($m_\pi = 140$ MeV) [1–3]. Usually, some extrapolation scheme is needed if one is to compare theoretical calculations with the corresponding physical observables. Utilizing lattice QCD results spread over a larger range of quark masses naturally enables greater statistical precision in the extrapolation.

Quenched QCD (QQCD) was introduced as a way to ameliorate the computational difficulty of simulating dynamical fermions on the lattice. Quenched simulations typically have been superseded by the wide availability of dynamical configurations. Nevertheless, it can still be used as an efficient testing ground. This is particularly true of the chiral extrapolation problem, where the experimentally known values may introduce a prejudice on a chosen form. In QQCD, the physical target point does not exist, and an extrapolation of moderate-mass points to the chiral regime provides an unbiased test of the procedure.

In order to discuss the chiral behaviour of the $\rho$ meson in QQCD, one first constructs an effective field theory describing the relevant low-energy degrees of freedom. The mass of the $\rho$ meson is described by a chiral expansion in the quark mass ($m_q$), which includes analytic terms that are polynomial in $m_q$, and non-analytic terms

arising from chiral loop integrals. These loop integrals are commonly divergent, and thus it is necessary to introduce a regularization procedure. Finite-range regularization (FRR) is selected as a regularization scheme, which introduces a momentum cutoff scale $\Lambda$ into the loop integrals. The properties of FRR allow it to be used with data extending outside the power-counting regime (PCR), at the expense of complete scheme-independence. As has been demonstrated, an optimal choice of regularization scale, $\Lambda_{\text{scale}}$, can be extracted from the lattice simulation results [4]. A systematic uncertainty in $\Lambda_{\text{scale}}$ can also be estimated, which provides a range of suitable values for the scale obtained from the data [5]. Thus the scheme-dependence in using data extending outside the PCR can be quantified in an unbiased fashion.

## II. EXTENDED EFFECTIVE FIELD THEORY

In chiral effective field theory ($\chi$EFT), the diagrammatic formulation can be used to identify the major contributions to the $\rho$ meson mass in QQCD [6, 7]. The leading-order diagrams are the double and single $\eta'$ hairpin diagrams as shown in Figures 1 and 2, respectively. The constant coefficients of these loop integrals are endowed with an uncertainty to encompass the possible effects of smaller contributions to order $\mathcal{O}(m_\pi^4)$. Interactions with the flavour-singlet $\eta'$ are the most important contributions to the $\rho$ meson mass in QQCD. This is an artifact of the quenched approximation, where the $\eta'$ also behaves as a pseudo-Goldstone boson, having
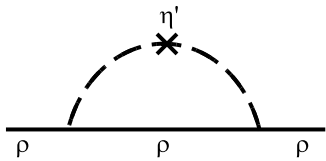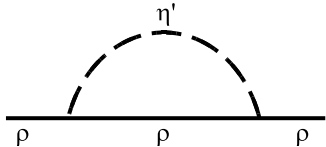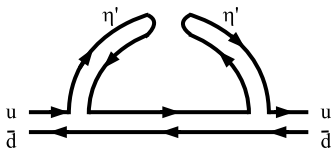
FIG. 1. Double hairpin $\eta'$ diagram.



FIG. 2. Single hairpin $\eta'$ diagram.
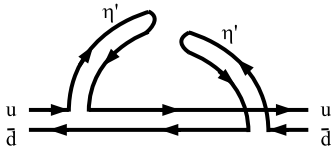


FIG. 3. Double hairpin quark flow diagram.



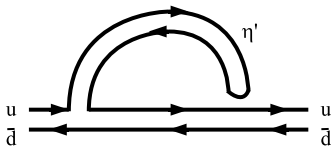FIG. 4. Alternative double hairpin quark flow diagram.



FIG. 5. Single hairpin quark flow diagram.

a "mass" that is degenerate with the pion. The dressing of the $\rho$ meson by the $\eta'$ field is illustrated in Figures 3 through 5. Since the hairpin vertex must be a flavor-singlet, the mesons that can contribute are the $\eta'$ meson, and the $\omega$ meson. The contributions from the $\omega$ meson are insignificant due to OZI suppression and the small $\rho$-$\omega$ mass splitting. However, in QQCD, the $\eta'$ loop behaves much as a pion loop, yet with a slightly modified propagator.

In full QCD however, the $\eta'$ does not play any role in the low-energy dynamics. The physical $\eta'$ acquires a finite mass — which survives in the chiral limit — by resumming the chain of vacuum insertions as depicted in Figure 6. As a "heavy" degree of freedom, the $\eta'$ can
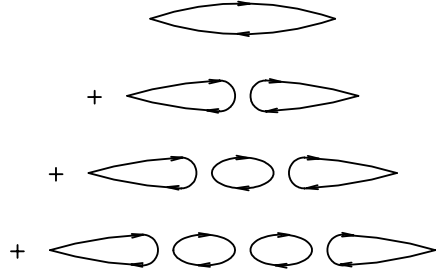


FIG. 6. Diagrammatic representation of $\eta'$ propagator terms.

then be integrated out of the of the effective field theory.

## A. Loop integrals and definitions

Using the Gell-Mann−Oakes−Renner Relation connecting quark and pion masses, $m_q \propto m_\pi^2$ [8], the $\rho$ meson mass extrapolation formula in QQCD can be expressed in a form that contains an analytic polynomial in $m_\pi^2$ plus the chiral loop integrals ($\Sigma^Q$):

$$m_{\rho,Q}^2 = a_0 + a_2 m_\pi^2 + a_4 m_\pi^4 \\ + \Sigma_{\eta'\eta'}^Q(m_\pi^2, \Lambda) + \Sigma_{\eta'}^Q(m_\pi^2, \Lambda) + \mathcal{O}(m_\pi^5). \quad (1)$$

The coefficients $a_i$ are the 'residual series' coefficients, which correspond to direct quark-mass insertions in the underlying Lagrangian of chiral perturbation theory. However, the non-analytic behaviour of the expansion arises from the chiral loop integrals. Upon renormalization of the divergent loop integrals, these will correspond with low-energy constants of the quenched $\chi$EFT. The extraction of these parameters from lattice QCD results will now be demonstrated.

By convention, the non-analytic terms from the double and single hairpin integrals are $\chi_1 m_\pi$ and $\chi_3 m_\pi^3$, respectively. The coefficients $\chi_1$ and $\chi_3$ of the leading-order non-analytic terms are scheme-independent constants that can be estimated from phenomenology. The low-order expansion of the loop contributions takes the following form:

$$\Sigma_{\eta'\eta'}^Q = b_0^{\eta'\eta'} + \chi_1 m_\pi + b_2^{\eta'\eta'} m_\pi^2 + \chi_3^{\eta'\eta'} m_\pi^3 + b_4^{\eta'\eta'} m_\pi^4 \\ + \mathcal{O}(m_\pi^6), \quad (2)$$

$$\Sigma_{\eta'}^Q = b_0^{\eta'} + b_2^{\eta'} m_\pi^2 + \chi_3^{\eta'} m_\pi^3 + b_4^{\eta'} m_\pi^4 + \mathcal{O}(m_\pi^6), \quad (3)$$

The coefficient $\chi_3$ is obtained by adding the contributions from both integrals, $\chi_3 = \chi_3^{\eta'\eta'} + \chi_3^{\eta'}$. Each integral has a solution in the form of a polynomial expansion analytic in $m_\pi^2$ plus non-analytic terms, of which the leading-order term is of greatest interest. The coefficients $b_i$ are scale-dependent and therefore scheme-dependent. In order to achieve an extrapolation based on an optimal FRR scale, first the scale-dependence of the low-energy expansion must be removed through renormalization. The

renormalization program of FRR combines the scheme-dependent $b_i$ coefficients from the chiral loops with the scheme-dependent $a_i$ coefficients from the residual series at each chiral order $i$. The result is a scheme-independent coefficient $c_i$:

$$c_0 = a_0 + b_0^{\eta'\eta'} + b_0^{\eta'}, \tag{4}$$

$$c_2 = a_2 + b_2^{\eta'\eta'} + b_2^{\eta'}, \tag{5}$$

$$c_4 = a_4 + b_4^{\eta'\eta'} + b_4^{\eta'}, \text{ etc.} \tag{6}$$

That is, the underlying $a_i$ coefficients undergo a renormalization from the chiral loop integrals. The renormalized coefficients $c_i$ are an important part of the extrapolation technique. A stable and robust determination of these parameters forms the core of determining an optimal scale $\Lambda^{\text{scale}}$.

The loop integrals can be expressed in a convenient form by taking the non-relativistic limit and performing the pole integration for $k_0$. Renormalization is achieved by subtracting the relevant terms in the Taylor expansion of the loop integrals and absorbing them into the corresponding low-energy coefficients, $c_i$:

$$\tilde{\Sigma}_{\eta'\eta'}^Q(m_\pi^2;\Lambda) = \frac{-\chi_{\eta'\eta'}}{3\pi^2}\int d^3k \frac{(M_0^2k^2 + \frac{5}{2}A_0k^4)u^2(k;\Lambda)}{(k^2+m_\pi^2)^2}$$
$$- b_0^{\eta'\eta'} - b_2^{\eta'\eta'}m_\pi^2 - b_4^{\eta'\eta'}m_\pi^4, \tag{7}$$

$$\tilde{\Sigma}_{\eta'}^Q(m_\pi^2;\Lambda) = \frac{\chi_{\eta'}}{2\pi^2}\int d^3k \frac{k^2u^2(k;\Lambda)}{k^2+m_\pi^2} - b_0^{\eta'} - b_2^{\eta'}m_\pi^2$$
$$- b_4^{\eta'}m_\pi^4. \tag{8}$$

The tilde ( ˜ ) denotes that the integrals are written out in renormalized form to chiral order $\mathcal{O}(m_\pi^4)$. The coefficients $\chi_{\eta'\eta'}$ and $\chi_{\eta'}$ are related to the coefficients of the leading-order non-analytic terms by:

$$\chi_1 = M_0^2\,\chi_{\eta'\eta'}, \tag{9}$$

$$\chi_3 = \chi_3^{\eta'\eta'} + \chi_3^{\eta'} = A_0\,\chi_{\eta'\eta'} + \chi_{\eta'}. \tag{10}$$

These couplings are discussed in detail below. The function $u(k;\Lambda)$ is a finite-range regulator with cutoff scale $\Lambda$, which must be normalized to 1 at $k^2 = 0$, and must approach 0 sufficiently fast to ensure convergence of the loop. Different functional forms of $u(k;\Lambda)$ are equivalent within the PCR [9, 10]. Different choices of $u(k;\Lambda)$ for this investigation are discussed in Sec. II B.

With the loop integrals specified, Eq. (1) can be rewritten in terms of the renormalized coefficients $c_i$:

$$m_{\rho,Q}^2 = c_0 + c_2m_\pi^2 + c_4m_\pi^4 + \tilde{\Sigma}_{\eta'\eta'}^Q(m_\pi^2;\Lambda)$$
$$+ \tilde{\Sigma}_{\eta'}^Q(m_\pi^2;\Lambda) + \mathcal{O}(m_\pi^5) \tag{11}$$
$$\approx c_0 + \chi_1m_\pi + c_2m_\pi^2 + \chi_3m_\pi^3 + c_4m_\pi^4$$
$$+ \mathcal{O}(m_\pi^5). \tag{12}$$

Eq. (11) will be used as the extrapolation formula for $m_{\rho,Q}$ at infinite lattice volume. The fit coefficients are

$c_0$, $c_2$ and $c_4$, and $m_{\rho,Q}$ is obtained by taking the square root of Eqs. (11). It is important to note that the formula in Eq. (12) holds only in the chiral regime. At larger pion masses, the higher order terms encoded in the integrals of Eq. (11) cannot be neglected. Therefore, beyond the PCR, the formula in Eq. (12) is not equivalent to that of Eq. (11), and is included only to indicate the ordering of the terms in the chiral expansion.

Since lattice simulations are necessarily carried out on a discrete spacetime, any extrapolations performed should take into account finite-volume effects. The low-energy effective field theory is ideally suited for characterising the leading infrared effects associated with the finite volume. In order to achieve this, each of the three-dimensional integrals can be transformed to its form on the lattice using a finite sum of discretized momenta, following Armour *et al.* [7], for instance:

$$\int d^3k \rightarrow \frac{(2\pi)^3}{L_xL_yL_z}\sum_{k_x,k_y,k_z}. \tag{13}$$

Each momentum component is quantized in units of $2\pi/L$, that is $k_i = n_i 2\pi/L$ for integers $n_i$. Finite-volume corrections $\delta^{\text{FVC}}$ can be written simply as the difference between the finite sum and the corresponding integral. It is known that the finite-volume corrections saturate to a fixed result for large values of the regularization scale [4]. Following the example set by this article, the value $\Lambda' = 2.0$ GeV is chosen to evaluate all finite-volume corrections independent of the FRR cutoff scale $\Lambda$ in Eqs. (7) and (8). The finite-volume version of Eq. (11) can thus be expressed:

$$m_{\rho,Q}^2 = c_0 + c_2m_\pi^2 + c_4m_\pi^4 + (\tilde{\Sigma}_{\eta'\eta'}^Q(m_\pi^2;\Lambda)$$
$$+ \delta_{\eta'\eta'}^{\text{FVC}}(m_\pi^2;\Lambda')) + (\tilde{\Sigma}_{\eta'}^Q(m_\pi^2;\Lambda) + \delta_{\eta'}^{\text{FVC}}(m_\pi^2;\Lambda'))$$
$$+ \mathcal{O}(m_\pi^5). \tag{14}$$

The convention used for defining the values of $\chi_1$, $\chi_3$, and the various coupling constants that occur in each, follows Booth [11]. For the possible different values that coupling constants can take, definitions by Chow & Rey [6], Armour *et al.* [7] and Sharpe [12] are used. The types of vertices available are shown in Figure 7, where $g_2$ and $g_4$ occur explicitly in the two diagrams considered here. Booth suggests naturalness for $g_2 \sim 1$, and that $g_4 \sim 1/N_c$. These quenched coupling constants can be connected with the experimental value of $g_{\omega\rho\pi}$ as per Lublinsky [13] by the relation:

$$g_2 = \frac{1}{2}g_{\omega\rho\pi}f_\pi, \tag{15}$$

where $g_{\omega\rho\pi} = 14 \pm 2$ GeV$^{-1}$ and the pion decay constant takes the value $f_\pi = 0.0924$ GeV. Thus $g_2$ is chosen to be $0.65 \pm 0.09$ GeV and $g_4$ is chosen to be approximately $g_2/3$. The coupling between the separate legs of the double hairpin diagram are approximated by the massive constant $M_0^2 \propto m_{\eta'}^2$. The next-order correction to $M_0$
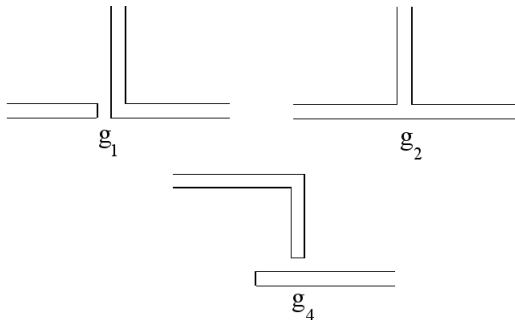
FIG. 7. Coupling types following convention introduced by Booth [11].

in momentum $k$ defines the coupling to be $-M_0^2 + A_0 k^2$. These constants can be connected to the full QCD $\eta'$ meson mass $m_{\eta'}$ by considering the geometric series of terms as previously illustrated in Figure 6. As a result, $M_0^2$ is taken to be $0.6 \pm 0.2$ GeV$^2$ and $A_0$ is taken to be $0 \pm 0.2$.

The coefficients $\chi_{\eta'\eta'}$ and $\chi_{\eta'}$ can be specified in terms of the relevant coupling constants:

$$\chi_{\eta'\eta'} = -2\,\overset{\circ}{m}_\rho \frac{g_2^2}{4\pi f_\pi^2},$$
$$\chi_{\eta'} = -2\,\overset{\circ}{m}_\rho \frac{g_2 g_4}{6\pi f_\pi^2}, \qquad (16)$$

where the couplings are defined relative to $\overset{\circ}{m}_\rho$ representing the $\rho$ meson mass in the chiral limit, which is taken to be 770 MeV.

### B. Finite-range regularization

In FRR, regulator functions $u(k; \Lambda)$ with characteristic scale $\Lambda$ are inserted into the loop integrals to control the ultraviolet divergences that occur in the loop integrals encountered. For some choices of regulator, extra regulator-dependent non-analytic terms arise in the chiral expansion of Eq. (12). Since the correct non-analytic terms of the chiral expansion are regularization scale-independent terms, the extra non-analytic terms within working chiral order must be removed. All scale-dependence should be absorbed into the analytic fit parameters $a_i$. For example, if a dipole regulator is chosen, the extra terms $b_3^{(1)} m_\pi^3$, $(b_5^{(1)} + b_5^{(3)}) m_\pi^5$ and higher-order terms occurring at odd powers of $m_\pi$ feature in Eq. (12). One can avoid this by choosing a regulator that does not generate these extra terms, up to working-order $\mathcal{O}(m_\pi^4)$. Since the step function $u^2(k; \Lambda) = \theta(\Lambda - k)$ introduces inconvenient finite-volume artifacts, a 'triple-dipole' form factor will be chosen, defined by:

$$u(k; \Lambda) = \left(1 + \left[\frac{k^2}{\Lambda^2}\right]^3\right)^{-2}. \qquad (17)$$

### III. LATTICE SIMULATION DETAILS

The calculation is performed on a $20^3 \times 32$ lattice with 197 gauge configurations generated with the Iwasaki gauge action [14] at $\beta = 2.264$, and the quark propagators are calculated with overlap fermions and a wall-source technique. The lattice spacing is 0.153 fm, as determined from the Sommer scale parameter.

The massive overlap Dirac operator is defined [15] in the following way so that at tree-level there is no mass or wavefunction renormalization [16]:

$$D(m) = \rho + \frac{m}{2} + (\rho - \frac{m}{2})\gamma_5 \epsilon(H), \qquad (18)$$

where $\epsilon(H)$ is the matrix sign function of an Hermitian operator $H$. $\epsilon(H) \equiv H_W/|H_W| = H_W/(H_W^\dagger H_W)^{1/2}$ is chosen, where $H_W(x, y) = \gamma_5 D_W(x, y)$. Here $D_W$ is the usual Wilson-Dirac operator on the lattice, except with a negative mass parameter $-\rho = 1/2\kappa - 4$ in which $\kappa_c < \kappa < 0.25$. Taking $\kappa = 0.19$ in the calculation corresponds to $\rho = 1.368$ [17, 18].

In Figure 8 the simulation results for the vector meson mass are shown for a range of quark masses.

The data displayed in Figure 8 are split into two parts. All the data left of the solid vertical line is unused for extrapolation and kept in reserve. Indeed, the authors performing the extrapolation were blind to these data. This is so that the extrapolation can be checked against these known data points once the extrapolation is established. In other words, the results of the chiral extrapolation are genuine *predictions* of the hidden lattice results. Only the data points to the right of the solid vertical line are used for extrapolation. The full set of data is also listed in Table I.

To estimate finite-volume effects using overlap fermions, quenched lattices of volumes $16^3 \times 28$ and $12^3 \times 28$ with $a = 0.2$ fm are used. For a pion mass of 180 MeV, $m_{PS}L \approx 3$, and the finite-volume correction is approximately 2.7 MeV: about 1.5% of the pion mass [17]. The current $20^3 \times 32$ lattice with $a = 0.153$ fm is about the same physical size as that of a $16^3 \times 28$ lattice and a similar finite-volume correction is expected. To estimate the finite-volume correction of the lowest $\rho$ meson mass at $m_\pi \approx 200$ MeV, the same percentage of error is used, and a shift of $\delta_L m_\rho \approx 13$ MeV to the $\rho$ mass is calculated for the $\rho$ meson mass of $m_\rho \approx 917$ MeV. This is about half of the statistical error of the lattice data. It should be noted that the data that will be used in chiral extrapolations are those with pion mass greater than 400 MeV, with $m_{PS}L > 6.2$. The predictions are extended to the region with pion mass less than 400 MeV and compared with the lattice data.

The enhancement of zero modes effects in QQCD primarily affects the pseodoscalar and scalar mesons. Since all the zero modes appear in one chiral sector in each gauge configuration, the pseudoscalar and scalar mesons will have a leading $1/m^2$ singularity from the zero modes.

TABLE I. Quenched lattice QCD data for the $\rho$ meson mass $m_\rho$ at various pion mass squared values $m_\pi^2$. The lattice size is $20^3 \times 32$, with a lattice spacing of 0.153 fm. Entries below the line (underneath $m_\pi^2 = 0.143$ GeV$^2$) remained hidden until the extrapolation was determined.

| $m_\pi^2$(GeV$^2$) | $m_\rho$(GeV) | $m_\pi L$ |
|---|---|---|
| 1.329 | 1.399(2) | 17.88 |
| 1.212 | 1.354(2) | 17.08 |
| 1.062 | 1.294(2) | 15.98 |
| 0.867 | 1.214(3) | 14.44 |
| 0.743 | 1.162(4) | 13.37 |
| 0.676 | 1.133(4) | 12.75 |
| 0.610 | 1.103(5) | 12.12 |
| 0.515 | 1.060(5) | 11.13 |
| 0.422 | 1.016(6) | 10.07 |
| 0.347 | 0.985(7) | 9.13 |
| 0.288 | 0.960(8) | 8.32 |
| 0.241 | 0.938(8) | 7.62 |
| 0.204 | 0.926(9) | 7.00 |
| 0.172 | 0.914(11) | 6.43 |
| 0.143 | 0.908(14) | 5.87 |
| 0.114 | 0.899(15) | 5.24 |
| 0.094 | 0.899(16) | 4.75 |
| 0.080 | 0.896(18) | 4.38 |
| 0.068 | 0.898(20) | 4.04 |
| 0.059 | 0.902(22) | 3.77 |
| 0.053 | 0.903(26) | 3.58 |
| 0.047 | 0.907(28) | 3.37 |
| 0.041 | 0.913(32) | 3.15 |



FIG. 8. (color online). Quenched lattice QCD data for the $\rho$ meson mass. The dashed vertical line indicates the physical pion mass and the solid vertical line shows how the data set is split into two parts. The lower-mass portion of the data was not known at the time of extrapolation.



FIG. 9. (color online). A test extrapolation based on the four lightest original data points (excluding the low-energy set) as shown. Both the finite- and infinite-volume results are shown for a triple-dipole regulator at $\Lambda = 1.0$ GeV. The dashed vertical line indicates the physical pion mass.

These appear in both the quark and antiquark propagators in the meson correlator [16]. Nevertheless, the vector and axial vector mesons have only a $1/m$ sigularity, which is a less dramatic effect. In either case, the quantity that determines the size of the zero mode effects is $m\Sigma V$ in the $p$-regime [19]. It has been demonstrated that when $m\Sigma V \gtrsim 5$, the zero mode effect is hardly detectable [17, 20]. For the present lattice with pion mass greater than 400 MeV, $m\Sigma V > 6$. Therefore, there is no reason to suggest that there is a zero mode contribution to the $\rho$ meson correlators being studied.

## IV. EXTRAPOLATION RESULTS

### A. Renormalization flow curves

In order to produce an extrapolation to each test value of $m_\pi^2$, a finite-range regularization scale $\Lambda$ must be selected. As an example, one can choose a triple-dipole regulator at $\Lambda = 1.0$ GeV. By using Eq.(14), finite- and infinite-volume extrapolations are shown in Figure 9. Note that the $m_\pi^2$ values selected for the finite-volume
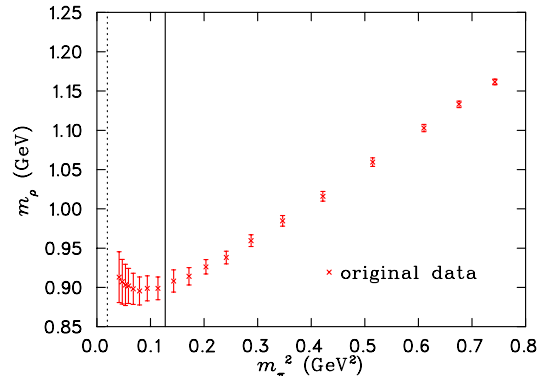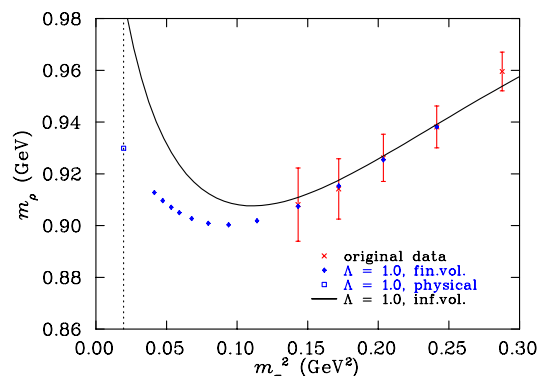
extrapolations exactly correspond to the 'missing' low-energy data points set aside earlier. The physical point $m_\pi^2 = 0.0196$ GeV$^2$ is included as well.

Now the regularization scale-dependence of low-energy coefficients $c_0$, $c_2$ and $c_4$ is investigated for various upper limits of the range of pion masses. The renormalization of these low-energy coefficients is considered for a series of $\Lambda$ values. The aim is to obtain renormalization flow curves, each corresponding to a different value of maximum pion mass, $m_{\pi,\text{max}}^2$. Thus the behaviour of the renormalization of the low-energy coefficients can be examined as lattice data extend further outside the PCR. Figures 10 through 12 show the renormalization flow curves for each of $c_0$, $c_2$ and $c_4$. Note that each data point plotted has an associated error bar, but for the sake of clarity only a few points are selected to indicate the general size of the statistical error bars. Using the procedure described in Ref. [4], the optimal regularization scale is identified by the value of $\Lambda$ that minimizes the discrepancies among the renormalization flow curves. This indicates the value of regularization scale at which the renormalization of $c_0$, $c_2$ and $c_4$ is least sensitive to the truncation of the data. Physically, this value of $\Lambda$ can be associated with
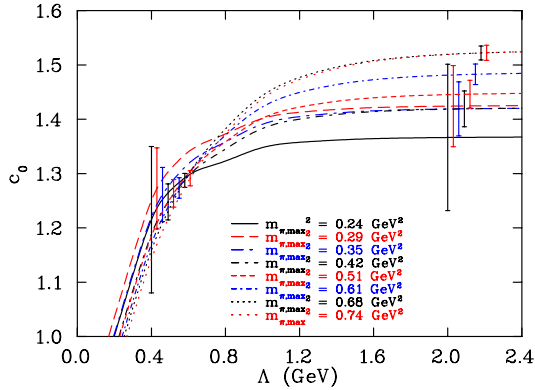
FIG. 10. (color online). Behaviour of $c_0$ vs. $\Lambda$. A few points are selected to indicate the general size of the statistical error bars.
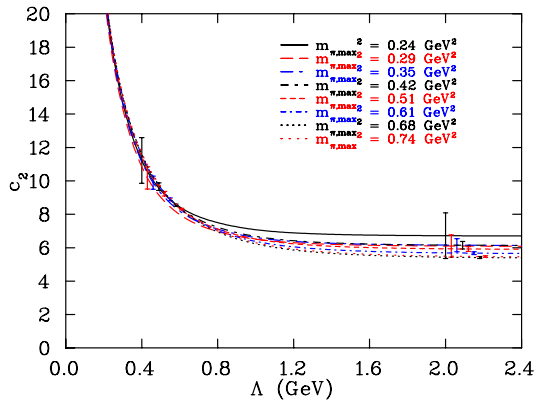


FIG. 11. (color online). Behaviour of $c_2$ vs. $\Lambda$. A few points are selected to indicate the general size of the statistical error bars.
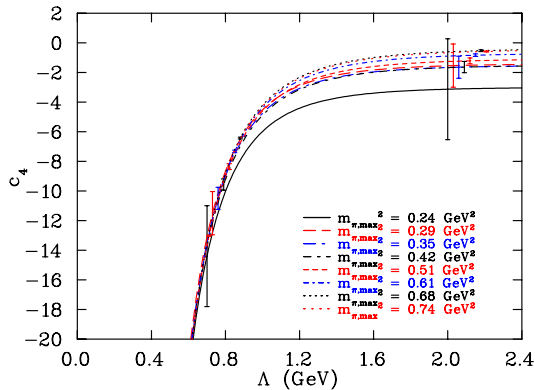


FIG. 12. (color online). Behaviour of $c_4$ vs. $\Lambda$. A few points are selected to indicate the general size of the statistical error bars.

an intrinsic scale related to the size of the source of the pion cloud.

By examining Figures 10 through 12, increasing $m_{\pi,\max}^2$ leads to greater scheme-dependence in the renormalization, since the data sample lies further from the PCR. Complete scheme-independence would be indicated by a horizontal line at the physical point. Since the effective field theory is calculated to a finite chiral order, complete scheme-independence across all possible values of $\Lambda$ will not occur in practice. Note that an asymptotic value is usually observed in the renormalization flow as $\Lambda$ becomes large, indicating that the higher-order terms of

the chiral expansion are effectively zero. However, these asymptotic values of the low-energy coefficients are poor estimates of their correct values, as previously demonstrated in a pseudodata model [4]. Instead, the best estimates of the low-energy coefficients lie in the identification of the intersection point of the renormalization flow of the low-energy coefficients. It is also of note that, for small values of $\Lambda$, FRR schemes break down. The regularization scale must be at least large enough to include the chiral physics being studied.

## B. Optimal regularization scale

The optimal regularization scale $\Lambda^{\text{scale}}$ can be obtained from the renormalization flow curves using a chi-square analysis described below. In addition, the analysis will allow the extraction of a range for $\Lambda^{\text{scale}}$. Knowing how the data are correlated, the systematic uncertainties from the coupling constants and $\Lambda^{\text{scale}}$ will be combined to obtain an error bar for each extrapolation point. Of particular interest are the values of $m_{\rho,Q}$ at the values of $m_\pi^2$ explored in the lattice simulations but excluded in the chiral extrapolation.

To obtain a measure of the uncertainty associated with an optimal regularization scale, a $\chi_{dof}^2$ function is constructed. This function should allow easy identification of the intersection points in the renormalization flow curves, and a range associated with this central regularization scale. The first step is to plot $\chi_{dof}^2$ against a series of $\Lambda$ values. The relevant data are the extracted low-energy coefficients with differing values of $m_{\pi,\max}^2$. A plot of $\chi_{dof}^2$ is constructed separately for each renormalized coefficient $c$ (with uncertainty $\delta c$):

$$\chi_{dof}^2 = \frac{1}{n-1} \sum_{i=1}^{n} \frac{\left(c(i\,;\Lambda) - c^T(\Lambda)\right)^2}{\left(\delta c(i\,;\Lambda)\right)^2}, \qquad (19)$$

for $i$ corresponding to fits with differing values of $m_{\pi,\max}^2$ ($n = 8$). The theoretical value $c^T$ is given by the weighted mean:

$$c^T(\Lambda) = \frac{\sum_{i=1}^{n} c(i\,;\Lambda)/\left(\delta c(i\,;\Lambda)\right)^2}{\sum_{j=1}^{n} 1/\left(\delta c(j\,;\Lambda)\right)^2}. \qquad (20)$$

The $\chi_{dof}^2$ plots using a triple-dipole regulator are shown in Figures 13 through 15. The optimal regularization scale $\Lambda^{\text{scale}}$ is taken to be the central value $\Lambda_{\text{central}}$ of each plot. The upper and lower bounds obey the condition $\chi_{dof}^2 < \chi_{dof,min}^2 + 1/(dof)$. The results for the optimal regularization scale and the upper and lower bounds are shown in Table II. It is remarkable that each low-energy coefficient leads to the same optimal value of $\Lambda$, i.e. $\Lambda_{\text{central}} = 0.67$ GeV. By averaging the results among $c_0$, $c_2$, and $c_4$, the optimal regularization scale $\Lambda_{\text{scale}}$ for the quenched $\rho$ meson mass can be calculated for this data set: $\Lambda_{\text{scale}} = 0.67^{+0.09}_{-0.08}$ GeV.
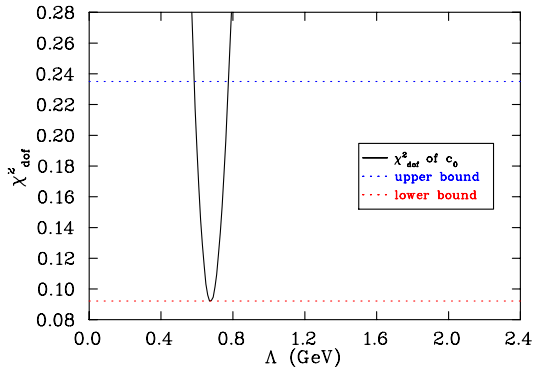
FIG. 13. (color online). $\chi_{dof}^2$ for $c_0$ versus $\Lambda$, corresponding to the renormalization flow curves displayed in Figure 10.
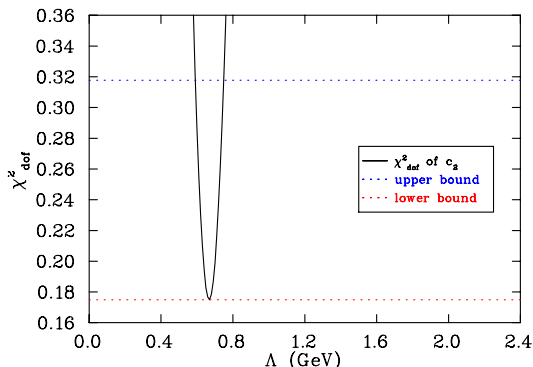


FIG. 14. (color online). $\chi_{dof}^2$ for $c_2$ versus $\Lambda$, corresponding to the renormalization flow curves displayed in Figure 11.
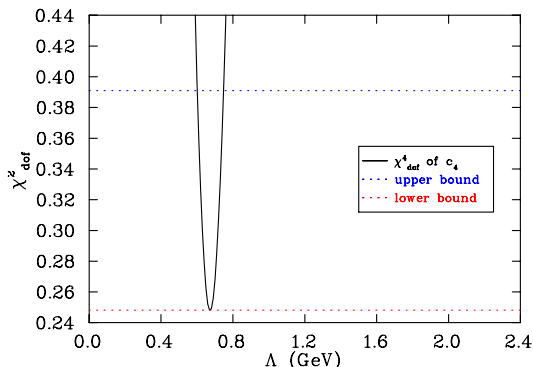


FIG. 15. (color online). $\chi_{dof}^2$ for $c_4$ versus $\Lambda$, corresponding to the renormalization flow curves displayed in Figure 12.

The result of the final extrapolation, using the estimate of the optimal regularization scale $\Lambda_{\text{scale}} = 0.67^{+0.09}_{-0.08}$ GeV, and using the initial data set to predict the low-energy data points, is shown in Figure 16. The extrapolation to the physical point obtained for this quenched data set is: $m_{\rho,Q}^{\text{ext}}(m_{\pi,\text{phys}}^2) = 0.925^{+0.053}_{-0.049}$ GeV, an uncertainty of less than 6%.

Note that each extrapolation point displays two error bars. The inner error bar corresponds to the systematic uncertainty in the parameters only, and the outer error bar corresponds to the systematic and statistical uncertainties of each point added in quadrature. Also, the infinite-volume extrapolation curve is displayed in order to illustrate the effect of finite-volume corrections to the

TABLE II. Values of the central, upper and lower regularization scales, in GeV, obtained from the $\chi_{dof}^2$ analysis of $c_0$, $c_2$ and $c_4$, displayed in Figures 13 through 15.

| scale (GeV) | $c_0$ (Fig.13) | $c_2$ (Fig.14) | $c_4$ (Fig.15) |
| --- | --- | --- | --- |
| $\Lambda_{\text{central}}$ | 0.67 | 0.67 | 0.67 |
| $\Lambda_{\text{upper}}$ | 0.78 | 0.75 | 0.75 |
| $\Lambda_{\text{lower}}$ | 0.58 | 0.59 | 0.60 |

loop integrals.

In Figure 17, the extrapolation predictions are compared against the actual simulation results, which were not included in the fit. Note that both the extrapolations and the simulation results display the same non-analytic curvature near the physical point. Figure 18 shows the data plotted with error bars correlated relative to the lightest data point in the original set, $m_\pi^2 = 0.143$ GeV$^2$. To highlight the importance of this application of an extended $\chi$EFT, a simple linear fit is included in Figure 18. By ignoring low-energy chiral physics, the linear fit is statistically incorrect at the physical point. Note also that all of the missing original data points are consistent within the extrapolations' systematic uncertainties. After statistical correlations are subtracted, the extrapolated points correspond to an error bar almost half the size of that of the lattice data points. In order to match this precision at low energies, the time required in lattice simulations would increase by approximately four times.

In order to check if scheme-independence is recovered using data within the PCR, the low-energy data that were initially excluded from analysis can now be treated in the same way. That is, renormalization flow curves can be constructed as a function of $\Lambda$ for sequentially increasing $m_{\pi,\text{max}}^2$. The results are shown in Figures 19 through 21. Clearly, the renormalization flow curves for each plot corresponding to $c_0$, $c_2$ and $c_4$ are flatter than those of the initial analysis, indicating a reduction in the regularization scale-dependence due to the use of data closer to the PCR. One is not able to extract an optimal regularization scale from these plots, as shown in the behaviour of $\chi_{dof}^2$, displayed in Figures 22 through 24. However, each $\chi_{dof}^2$ curve provides a lower bound for the regularization scale, where FRR breaks down [4], as discussed in Section IV A. These lower bounds are: $\Lambda_{\text{lower}}^{c_0} = 0.39$ GeV, $\Lambda_{\text{lower}}^{c_2} = 0.52$ GeV and $\Lambda_{\text{lower}}^{c_4} = 0.59$ GeV.

The statistical error bars of the low-energy coefficients corresponding to a small number of data points in Figures 19 through 21 is large, and a statistical difference among the curves does not appear until $m_{\pi,\text{max}}^2 \approx 0.11$ GeV$^2$. Thus the identification of an optimal regularization scale will be aided by incorporating data corresponding to even larger values of $m_{\pi,\text{max}}^2$. By considering *all* of the available data, the behaviour of $\chi_{dof}^2$, as displayed in Figures 25 through 27, resolve precise optimal regularization scales: $\Lambda_{\text{central}}^{c_0} = 0.72$ GeV, $\Lambda_{\text{central}}^{c_2} = 0.71$ GeV
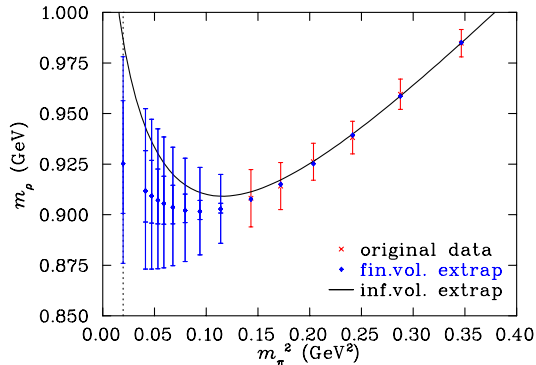
FIG. 16. (color online). Extrapolation at $\Lambda_{\text{scale}} = 0.67^{+0.09}_{-0.08}$ GeV based on Kentucky Group data, and using the optimal number of data points, corresponding to $\hat{m}^2_{\pi,\text{max}} = 0.35$ GeV$^2$. The inner error bar on the extrapolation points represents purely the systematic error from parameters. The outer error bar represents the systematic and statistical error estimates added in quadrature.
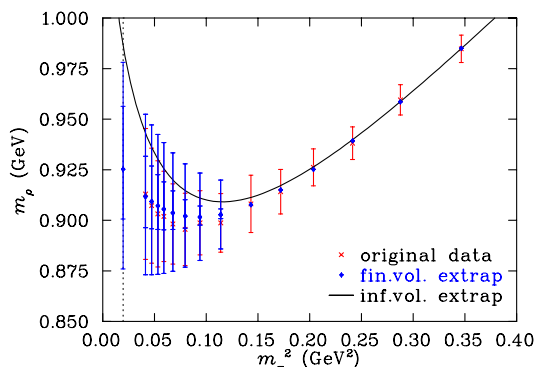


FIG. 17. (color online). Comparison of chiral extrapolation predictions (blue diamond) with Kentucky Group data (red cross). Extrapolation is performed at $\Lambda_{\text{scale}} = 0.67^{+0.09}_{-0.08}$ GeV, and using the optimal number of data points, corresponding to $\hat{m}^2_{\pi,\text{max}} = 0.35$ GeV$^2$. The inner error bar on the extrapolation points represents purely the systematic error from parameters. The outer error bar represents the systematic and statistical error estimates added in quadrature.
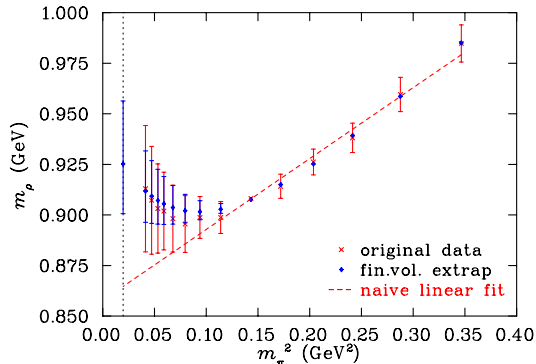


FIG. 18. (color online). Comparison of chiral extrapolation predictions (blue diamond) with Kentucky Group data (red cross), with errors correlated relative to the point at $m^2_\pi = 0.143$ GeV$^2$. Extrapolation is performed at $\Lambda_{\text{scale}} = 0.67^{+0.09}_{-0.08}$ GeV, and using the optimal number of data points, corresponding to $\hat{m}^2_{\pi,\text{max}} = 0.35$ GeV$^2$. The error bar on the extrapolation points represents the systematic error only. A simple linear fit, on the optimal pion mass region, is included for comparison.
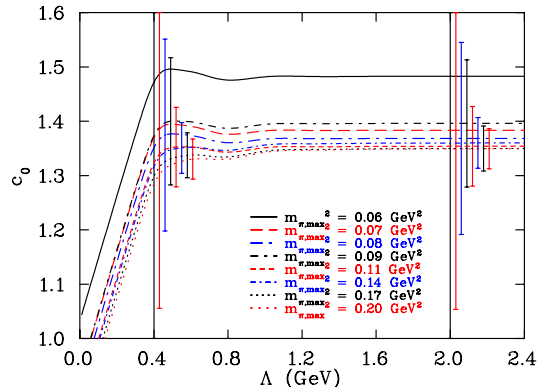


FIG. 19. (color online). Behaviour of $c_0$ vs. $\Lambda$ including the initially excluded low-energy data. A few points are selected to indicate the general size of the statistical error bars.



FIG. 20. (color online). Behaviour of $c_2$ vs. $\Lambda$ including the initially excluded low-energy data. A few points are selected to indicate the general size of the statistical error bars.



FIG. 21. (color online). Behaviour of $c_4$ vs. $\Lambda$ including the initially excluded low-energy data. A few points are selected to indicate the general size of the statistical error bars.

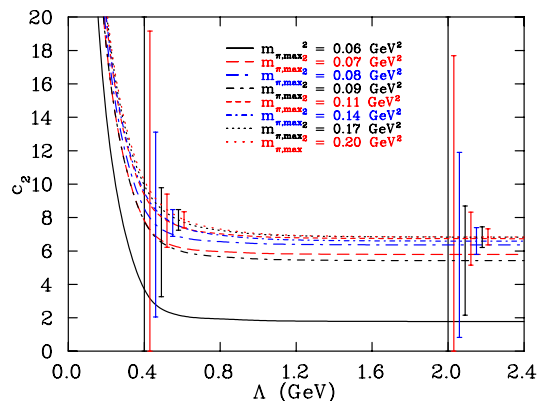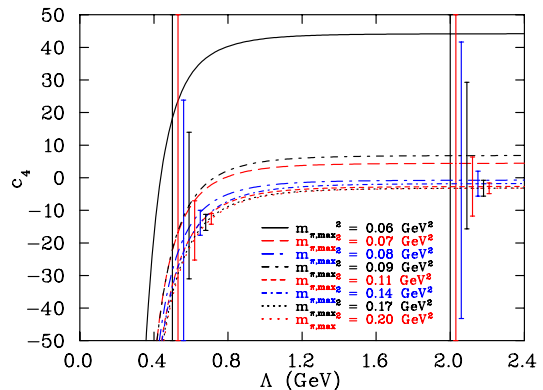and $\Lambda^{c_4}_{\text{central}} = 0.71$ GeV. The systematic errors obtained from each $\chi^2_{dof}$ curve seem arbitrarily constrained as a consequence of including more data points, which extend well outside the chiral regime, and possibly outside the applicable region of FRR techniques. This issue is addressed in the ensuing section.
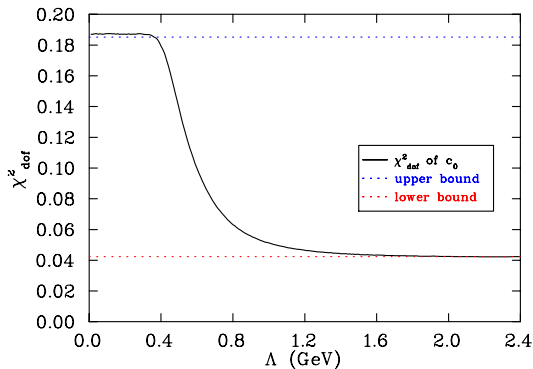
FIG. 22. (color online). $\chi^2_{dof}$, for $c_0$ versus $\Lambda$, corresponding to the renormalization flow curves displayed in Figure 19. A lower bound for the regularization scale is found: $\Lambda^{c0}_{lower} = 0.39$ GeV.



FIG. 23. (color online). $\chi^2_{dof}$, for $c_2$ versus $\Lambda$, corresponding to the renormalization flow curves displayed in Figure 20. A lower bound for the regularization scale is found: $\Lambda^{c2}_{lower} = 0.52$ GeV.



FIG. 24. (color online). $\chi^2_{dof}$, for $c_4$ versus $\Lambda$, corresponding to the renormalization flow curves displayed in Figure 21. A lower bound for the regularization scale is found: $\Lambda^{c4}_{lower} = 0.59$ GeV.
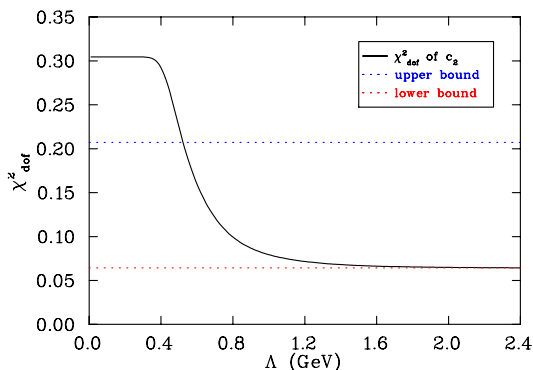


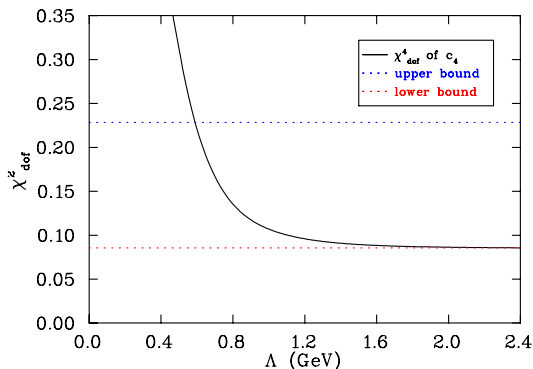FIG. 25. (color online). $\chi^2_{dof}$, for $c_0$ versus $\Lambda$, corresponding to all available data, including the low-energy set.



FIG. 26. (color online). $\chi^2_{dof}$, for $c_2$ versus $\Lambda$, corresponding to all available data, including the low-energy set.



FIG. 27. (color online). $\chi^2_{dof}$, for $c_4$ versus $\Lambda$, corresponding to all available data, including the low-energy set.

## C.  Optimal pion mass region

In this section, a robust method for determining an optimal range of pion masses is presented. This range corresponds to an optimal number of simulation results to be used for fitting. First, consider the extrapolation of the quenched $\rho$ meson mass, which can now be completed. The statistical uncertainties in the values of $c_0$, $c_2$, $c_4$ are dependent on $m^2_{\pi,max}$. As a consequence, the uncertainty in the extrapolated $\rho$ meson mass $m^{ext}_{\rho}$ must also be dependent on $m^2_{\pi,max}$. Since the estimate of the
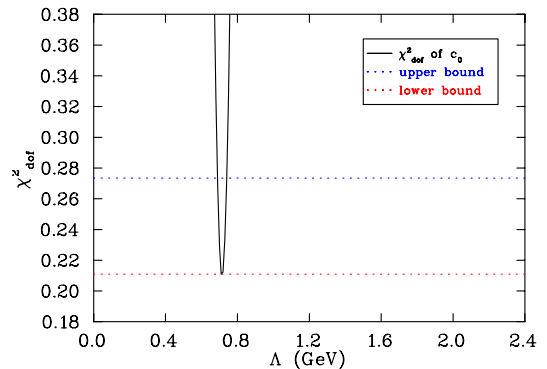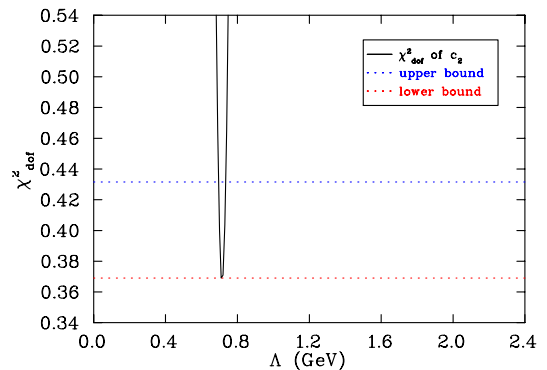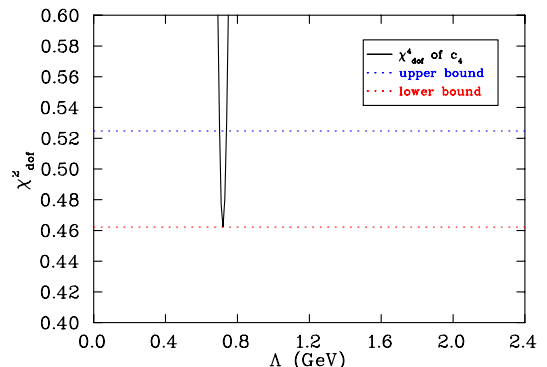
statistical uncertainty in an extrapolated point will tend to decrease as more data are included in the fit, one might naïvely choose to use the largest $m^2_{\pi,max}$ value possible in the data set. However, at some large value of $m^2_{\pi,max}$, FRR $\chi$EFT will not provide a valid model for obtaining a suitable fit. At this upper bound of applicability for FRR $\chi$EFT, the uncertainty in an extrapolated point is dominated by the systematic error in the underlying parameters. This is due to a greater scheme-dependence in extrapolations using data extending outside the PCR, meaning that the extrapolations are more sensitive to changes in the parameters of the loop integrals. Thus there is a balance point $m^2_{\pi,max} = \hat{m}^2_{\pi,max}$, where the statistical and systematic uncertainties (added in quadra-

ture) in an extrapolation are minimized.

In order to obtain this value $\hat{m}_{\pi,\mathrm{max}}^2$, consider the behaviour of the extrapolation of the $\rho$ meson mass to the physical point $m_{\rho,Q}^{\mathrm{ext}}(m_{\pi,\mathrm{phys}}^2)$, as a function of $m_{\pi,\mathrm{max}}^2$. Treating the parameters $g_2$, $g_4$, $M_0^2$, $A_0$ and $\Lambda^{\mathrm{scale}}$ as independent, their systematic uncertainties from these sources are added in quadrature. In addition, the systematic uncertainty due to the choice of the regulator functional form is roughly estimated by comparing the results using the double-dipole and the step function. These functional forms are the two most different forms of the various regulators considered, since the dipole was excluded due to the extra non-analytic contributions it introduces. The results for the initial and complete data sets are shown in Figures 28 and 29, respectively. Figure 28 indicates an optimal value $\hat{m}_{\pi,\mathrm{max}}^2 = 0.35$ GeV$^2$, which will be used in the final extrapolations, in order to check the results of this method with the low-energy data. By using only the data contained in the optimal pion mass region, constrained by $\hat{m}_{\pi,\mathrm{max}}^2$, an estimate of the optimal regularization scale may be calculated with a more generous corresponding systematic uncertainty. The value $\Lambda^{\mathrm{scale}} = 0.64$ GeV is the average of $\Lambda_{c_0}^{\mathrm{scale}}$, $\Lambda_{c_2}^{\mathrm{scale}}$ and $\Lambda_{c_4}^{\mathrm{scale}}$ using this method. The $\chi_{dof}^2$ analysis does not provide an upper or lower bound at this value of $\hat{m}_{\pi,\mathrm{max}}^2$. Note that these two estimates of the optimal regularization scale are consistent with each other. Both shall be used and compared in the final analysis. Figure 29 indicates an optimal value $\hat{m}_{\pi,\mathrm{max}}^2 = 0.20$ GeV$^2$ for the complete data set, which includes the low-energy data. A higher density of data in the low-energy region serves to decrease the statistical error estimate of extrapolations to the low-energy region. The corresponding value of $\Lambda^{\mathrm{scale}}$ is unconstrained in this case, since the data lie close to the PCR.

The values of $c_0$, $c_2$ and $c_4$ for both the original data set and the complete data set are shown in Table III, with statistical error estimate quoted first and systematic uncertainty due to the parameters $g_2$, $g_4$, $M_0^2$, $A_0$, $\Lambda^{\mathrm{scale}}$ and the regulator functional form quoted second. In the case of the original data set, the value of $c_4$ is not well-determined, due to the small number of data points used. In the case of the complete data set, the results are dominated by statistical uncertainty and also results in an almost unconstrained value of $c_4$. The coefficients of the complete set are less well-determined due to the fact that $\hat{m}_{\pi,\mathrm{max}}^2 = 0.20$ GeV$^2$, leaving only low-energy results with large statistical uncertainties for fitting.

The result using the estimate of the optimal regularization scale $\Lambda^{\mathrm{scale}} = 0.64$ GeV, with the systematic uncertainty calculated by varying $\Lambda$ across all suitable values, and using the initial data set, is shown in Figure 30. The extrapolation to the physical point obtained for this quenched data set is: $m_{\rho,Q}^{\mathrm{ext}}(m_{\pi,\mathrm{phys}}^2) = 0.922_{-0.060}^{+0.065}$ GeV, an uncertainty of approximately 7%. Figure 31 shows the data plotted with error bars correlated relative to the lightest data point in the original set, $m_\pi^2 = 0.143$ GeV$^2$, using $\Lambda_{\mathrm{scale}} = 0.64$ GeV, and varying $\Lambda$ across its



FIG. 28. (color online). Behaviour of the extrapolation of the quenched $\rho$ meson mass to the physical point $m_{\rho,Q}^{\mathrm{ext}}(m_{\pi,\mathrm{phys}}^2)$ vs. $m_{\pi,\mathrm{max}}^2$ using the initial data set, which excludes the lowest mass data points. In each case, $c_0$ is obtained using the scale $\Lambda_{\mathrm{central}}$ (for a triple-dipole regulator) as obtained from the $\chi_{dof}^2$ analysis. The error bars include the statistical and systematic uncertainties in $c_0$ added in quadrature. The optimal value $\hat{m}_{\pi,\mathrm{max}}^2 = 0.35$ GeV$^2$.
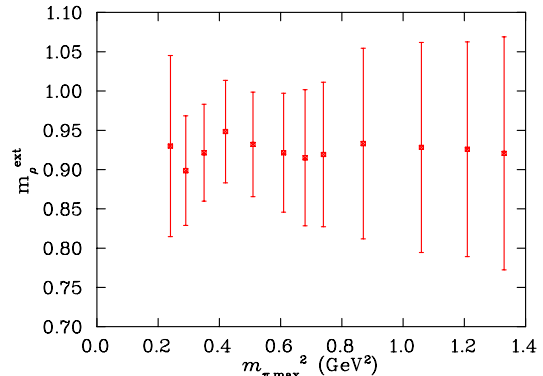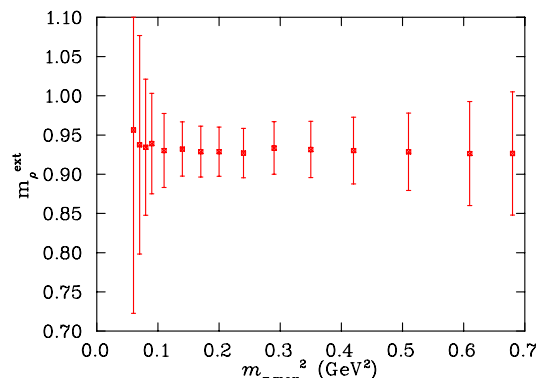


FIG. 29. (color online). Behaviour of the extrapolation of the quenched $\rho$ meson mass to the physical point $m_{\rho,Q}^{\mathrm{ext}}(m_{\pi,\mathrm{phys}}^2)$ vs. $m_{\pi,\mathrm{max}}^2$ using the complete data set, which includes the lowest mass data points. In each case, $c_0$ is obtained using the scale $\Lambda_{\mathrm{central}}$ (for a triple-dipole regulator) as obtained from the $\chi_{dof}^2$ analysis. The error bars include the statistical and systematic uncertainties in $c_0$ added in quadrature. The optimal value $\hat{m}_{\pi,\mathrm{max}}^2 = 0.20$ GeV$^2$.

full range of values. This naturally increases the estimate of the systematic uncertainty of the extrapolations, but also serves to demonstrate how closely the results from lattice QCD and $\chi$EFT match.

## V. CONCLUSION

A technique for isolating an optimal regularization scale, established in Ref. [4], was tested in quenched QCD through an examination of the quenched $\rho$ meson mass. The result is a successful extrapolation based on an extended effective field theory procedure. By using quenched lattice QCD results that extended beyond the power-counting regime, an optimal regularization scale was obtained from the renormalization flow of the low-energy coefficients.

An optimal value of the maximum pion mass to be used for fitting was also calculated, and this resulted in

TABLE III. The values of $c_0$, $c_2$ and $c_4$ as obtained from both the original data set and the complete set, which includes the low-energy data. In each case, the coefficients are evaluated using the scale $\Lambda_{\text{central}}$ (for a triple-dipole regulator) as obtained from the $\chi^2_{dof}$ analysis. The value of $m^2_{\pi,\max}$ used is that which yields the smallest error bar in adding statistical and systematic uncertainties in quadrature. For the initial data set, $\hat{m}^2_{\pi,\max} = 0.35$ GeV$^2$. For the complete data set, $\hat{m}^2_{\pi,\max} = 0.20$ GeV$^2$. The statistical uncertainty is quoted in the first pair of parentheses, and the systematic uncertainty is quoted in the second pair of parentheses. For the original data set, $c_4$ is not well-determined, with only a small number of data. For the complete data set, large statistical uncertainties result in an almost unconstrained value of $c_4$. The coefficients of the complete set are less well-determined due to the fact that $\hat{m}^2_{\pi,\max} = 0.20$ GeV$^2$, leaving only low-energy results with large statistical uncertainties for fitting.

|  | $c_0$(GeV$^2$) | $c_2$ | $c_4$(GeV$^{-2}$) |
| --- | --- | --- | --- |
| original set | 1.31(5)(17) | 7.9(4)(26) | $-16.2(8)(382)$ |
| complete set | 1.35(4)(241) | 6.8(5)(31) | $-3.3(17)(361)$ |

an alternative estimate of the value of the optimal regularization scale, which was consistent with the first result. The mass of the $\rho$ meson was calculated in the low-energy region, including the physical point, using each estimate of the optimal regularization scale, and both results were compared. The results of extrapolations using $\chi$EFT, and the results of lattice QCD simulations, were demonstrated to be consistent. The extrapolation correctly predicts the low-energy curvature that was observed when the low-energy lattice simulation results were revealed.

In full QCD, using dynamical fermions, the process $\rho \to \pi\pi$ contributes to the $\rho$ meson mass. This means that the pion energy increases as the chiral limit is approached, and therefore is not amenable to the methods of low-energy expansions, as entailed by $\chi$PT. Therefore, one needs to resort to alternative techniques, such as FRR.

However, since there exists no experimental value for the mass of a particle in the quenched approximation, this analysis demonstrates the ability of the technique to make predictions without phenomenologically motivated bias. The results clearly indicate a successful procedure for using lattice QCD data outside the power-counting regime to extrapolate an observable to the chiral regime.

[1] S. Aoki et al. (PACS-CS Collaboration), Phys.Rev. **D79**, 034503 (2009), 0807.1661.
[2] Y. Kuramashi, PoS **LATTICE2008**, 018 (2008), 0811.2630.
[3] S. Durr, Z. Fodor, C. Hoelbling, S. Katz, S. Krieg, et al. (2010), * Temporary entry *, 1011.2711.
[4] J. M. M. Hall, D. B. Leinweber, and R. D. Young, Phys. Rev. **D82**, 034010 (2010), 1002.4924.
[5] R. D. Young, J. M. M. Hall, and D. B. Leinweber (2009), 0907.0408.
[6] C.-K. Chow and S.-J. Rey, Nucl. Phys. **B528**, 303 (1998), hep-ph/9708432.
[7] W. Armour, C. R. Allton, D. B. Leinweber, A. W. Thomas, and R. D. Young, J. Phys. **G32**, 971 (2006), hep-lat/0510078.
[8] M. Gell-Mann, R. J. Oakes, and B. Renner, Phys. Rev. **175**, 2195 (1968).
[9] R. D. Young, D. B. Leinweber, and A. W. Thomas, Prog. Part. Nucl. Phys. **50**, 399 (2003), hep-lat/0212031.
[10] D. B. Leinweber, A. W. Thomas, and R. D. Young, Nucl. Phys. **A755**, 59 (2005), hep-lat/0501028.
[11] M. Booth, G. Chiladze, and A. F. Falk, Phys. Rev. **D55**, 3092 (1997), hep-ph/9610532.
[12] S. R. Sharpe, Nucl. Phys. Proc. Suppl. **53**, 181 (1997), hep-lat/9609029.
[13] M. Lublinsky, Phys. Rev. **D55**, 249 (1997), hep-ph/9608331.
[14] Y. Iwasaki, Nucl. Phys. **B258**, 141 (1985).
[15] H. Neuberger, Phys. Rev. **D57**, 5417 (1998), hep-lat/9710089.
[16] S. J. Dong et al., Phys. Rev. **D65**, 054507 (2002), hep-lat/0108020.
[17] Y. Chen et al., Phys. Rev. **D70**, 034502 (2004), hep-lat/0304005.
[18] J. B. Zhang et al., Phys. Rev. **D72**, 114509 (2005), hep-lat/0507022.
[19] H. Leutwyler and A. V. Smilga, Phys.Rev. **D46**, 5607 (1992).
[20] A. Li et al. (xQCD Collaboration), Phys.Rev. **D82**, 114501 (2010), 1005.5424.
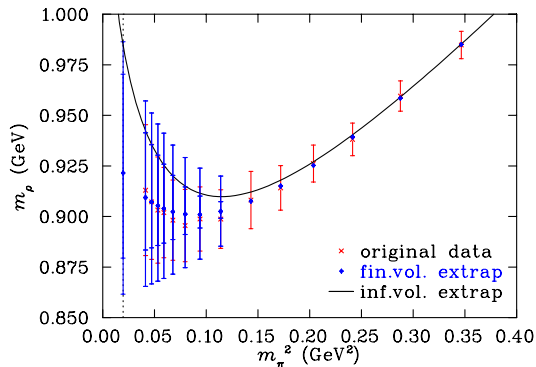
FIG. 30. (color online). Comparison of chiral extrapolation predictions (blue diamond) with Kentucky Group data (red cross). Extrapolation is performed at $\Lambda_{\text{scale}} = 0.64$ GeV, varied across the whole range of $\Lambda$ values, and using the optimal number of data points, corresponding to $\hat{m}_{\pi,\text{max}}^2 = 0.35$ GeV$^2$. The inner error bar on the extrapolation points represents purely the systematic error from parameters. The outer error bar represents the systematic and statistical error estimates added in quadrature.
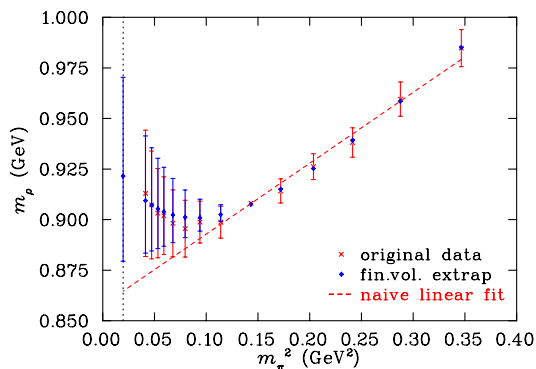


FIG. 31. (color online). Comparison of chiral extrapolation predictions (blue diamond) with Kentucky Group data (red cross), with errors correlated relative to the point at $m_\pi^2 = 0.143$ GeV$^2$. Extrapolation is performed at $\Lambda_{\text{scale}} = 0.64$ GeV, varied across the whole range of $\Lambda$ values, and using the optimal number of data points, corresponding to $\hat{m}_{\pi,\text{max}}^2 = 0.35$ GeV$^2$. The error bar on the extrapolation points represents the systematic error only. A simple linear fit, on the optimal pion mass region, is included for comparison.

# Chiral extrapolations for nucleon magnetic moments

J.M.M. Hall, D.B. Leinweber, and R.D. Young

*Special Research Centre for the Subatomic Structure of Matter (CSSM),*
*Department of Physics, University of Adelaide 5005, Australia*

Chiral effective field theory is a model-independent approach to connecting lattice quantum chromodynamics (QCD) results with experiment. Within the power-counting regime (PCR) of the chiral expansion, the result of a chiral effective field theory calculation is independent of the regularization scheme. However, since few lattice QCD results in the literature are constrained entirely within the PCR, it is useful to extend effective field theory in a model-independent way to take full advantage of the lattice QCD results available. By considering the magnetic moment of the isovector nucleon using a finite-range regularization scheme and using lattice QCD results that may extend outside the PCR, any emerging scheme-dependence can be quantified and handled by the identification of an intrinsic scale. By analyzing the renormalization flow of the low-energy coefficients, the intrinsic scale can be obtained from the lattice QCD results themselves, which provide guidance on the selection of an optimal regularization scale. This optimal scale, for a given functional form, is consistent with the result from the nucleon mass, and thus provides evidence for the existence of an intrinsic scale in the nucleon.

## I. INTRODUCTION

The analysis of the magnetic moment of the nucleon provides an excellent check for the identification of an intrinsic scale in the nucleon-pion interaction. Using chiral effective field theory ($\chi$EFT), it has been demonstrated that lattice quantum chromodynamics (QCD) results for the nucleon mass have an energy scale embedded within them [1]. This property is a consequence of the small size of the power-counting regime (PCR), where the expansion formulae of chiral perturbation theory ($\chi$PT) formally hold. Since a selection of lattice QCD results reasonable for fitting an extrapolation invariably extend outside the restrictive PCR [2], the validity of a formal scheme for extrapolation, and for identifying the leading-order terms in the chiral expansion, is compromised. Fortunately, a finite-range regularization (FRR) scheme, in conjunction with $\chi$EFT, provides a robust method for achieving an extrapolation to physical quark masses, and identifying an intrinsic scale embedded within lattice QCD results.

This extended effective field theory proceeds by analyzing the behaviour of the renormalization of one or more low-energy coefficients of the chiral expansion as a function of the FRR scale. Ideally, that is, with lattice QCD results constrained entirely within the PCR, the renormalized coefficients should be independent of regularization scale. However, in practice, a scale-dependence is observed; particularly for data sets including data points corresponding to large quark masses. By truncating the lattice QCD results at different points corresponding to an $m_{\pi,\mathrm{max}}^2$, an optimal FRR scale can be identified. This optimal scale is the value of $\Lambda$ at which the low-energy coefficient is least senstive to the truncation of the lattice results. Due to consistent results among the analysis of the magnetic moment and the various analyses of the nucleon mass using the same technique [1], this provides

evidence for an intrinsic scale in the nucleon.

The magnetic moment is of interest because of the physical significance of its anomalous component, obtained from the Pauli form factor. Because electrically charged pions with non-zero angular momentum *dress* the bare nucleon, they contribute non-trivially to its magnetic moment, altering the value from its semi-classical Dirac value.

In lattice QCD, the isovector combination of the nucleon $(p - n)$ is often calculated. Feynman diagrams including any photons coupling to sea-quark loops cancel in the case of the isovector. This is fortunate, since the calculation of the disconnected loops is computationally expensive. As a result, the lattice QCD data analyzed from the QCDSF Collaboration will be isovector nucleon data for two-flavor $\mathcal{O}(a)$-improved Wilson quark action.

## II. CHIRAL EFFECTIVE FIELD THEORY

In an effective field theory of the electromagnetic properties of baryons such as the nucleon, the matrix element for the baryon-photon interaction can be parameterized by the Dirac and Pauli form factors, $F_1$ and $F_2$, respectively. In the non-relativistic limit, this can be written as:

$$\langle B(p')|J_\mu|B(p)\rangle =$$
$$\bar{u}^{s'}(p')\left\{\gamma_\mu\,F_1(Q^2) + \frac{i\sigma_{\mu\nu}q^\nu}{2m_B}\,F_2(Q^2)\right\}u^s(p)\,. \quad (1)$$

$Q^2$ is a positive momentum transfer $Q^2 = -(p'-p)^2$. The Sachs electromagnetic form factors $G_{E,M}$ are the linear combinations of $F_1$ and $F_2$ defined by:

$$G_E(Q^2) = F_1(Q^2) - \frac{Q^2}{4m_B^2}F_2(Q^2)\,, \quad (2)$$

$$G_M(Q^2) = F_1(Q^2) + F_2(Q^2)\,. \quad (3)$$

By considering the behavior of the Sachs magnetic form factor of the nucleon at zero momentum transfer, $G_M(Q^2 = 0)$, one obtains the magnetic moment as two separate pieces: an anomalous component due to the finite-size of hadron interactions, and unity due to charge conservation:

$$\mu_n = G_M^v(Q^2 = 0) \tag{4}$$
$$= 1 + \kappa_n. \tag{5}$$

For the leading-order contributions to the magnetic moment, the standard first-order interaction Lagrangian from heavy-baryon chiral perturbation theory is used [3–8]:

$$\mathcal{L}_{\chi PT}^{(1)} = 2D \operatorname{Tr}\left[\bar{B}_{\text{v}} S_{\text{v}}^\mu \{A_\mu, B_{\text{v}}\}\right] + 2F \operatorname{Tr}\left[\bar{B}_{\text{v}} S_{\text{v}}^\mu [A_\mu, B_{\text{v}}]\right]$$
$$+ \mathcal{C}\left(\bar{T}_{\text{v}}^\mu A_\mu B_{\text{v}} + \bar{B}_{\text{v}} A_\mu T_{\text{v}}^\mu\right), \tag{6}$$
$$(S_v^\mu = \frac{i}{2}\gamma_5 \sigma^{\mu\nu} v_\nu), \tag{7}$$

where the pion fields are encoded as the adjoint representation of $\mathrm{SU}(3)_L \otimes \mathrm{SU}(3)_R$, and forming an axial vector combination $A_\mu$:

$$\xi \equiv \exp\left\{\frac{i}{f_\pi}\tau^a \pi^a\right\}, \tag{8}$$
$$A_\mu = \frac{1}{2}(\xi\,\partial_\mu\,\xi^\dagger - \xi^\dagger\,\partial_\mu\,\xi). \tag{9}$$

By the convention presented here, $f_\pi = 92.4$ MeV. The values for the couplings in the interaction Lagrangian are obtained from the $\mathrm{SU}(6)$ flavor-symmetry relations [5, 9] and from phenomenology: $D = 0.76$, $F = \frac{2}{3}D$ and $\mathcal{C} = -2D$.

From the full Lagrangian, the chiral behaviour of the magnetic moment can be written in terms of an ordered expansion in pion mass squared, through use of the Gell-Mann−Oakes−Renner Relation, $m_q \propto m_\pi^2$ [10]:

$$\mu_n = a_0^\Lambda + a_2^\Lambda m_\pi^2 + \mathcal{T}_N(m_\pi^2\,;\Lambda) + \mathcal{T}_\Delta(m_\pi^2\,;\Lambda) + \mathcal{O}(m_\pi^4). \tag{10}$$

This expansion contains an analytic polynomial in $m_\pi^2$ plus the leading-order chiral loop integrals ($\mathcal{T}_{a,b}$), from which non-analytic behaviour arises. The coefficients $a_i$ are the 'residual series' coefficients, which correspond to direct quark-mass insertions in the full Lagrangian. Upon renormalization of the divergent loop integrals, these will correspond with low-energy coefficients of $\chi$EFT. In this instance, only two free parameters are chosen in the residual series, since the non-analytic contributions are included only to order $\mathcal{O}(m_\pi^4 \log m_\pi)$. The leading-order included in this investigation are simply the 1-pion loops, in $N_f = 2$ QCD, as shown in Figures 1 and 2.

## A. Finite-range regularization

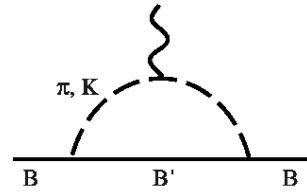A finite-range regularized effective field theory handles divergences in the ultraviolet region of the loop integrals



FIG. 1. The pion/kaon loop contributions to the magnetic moment of an octet baryon $B$, allowing a transition to a baryon $B'$, with photon attachment, which provides the leading non-analytic contribution. All charge conserving transitions are implicit.
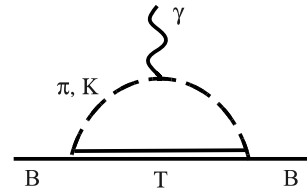


FIG. 2. The pion/kaon loop contribution to the magnetic moment of an octet baryon $B$, with photon attachment, allowing transitions to the nearby and strongly-coupled decuplet baryons $T$.

by introducing a regulator function as part of the coupling to each vertex of the diagram. The regulator function $u(k\,;\Lambda)$ introduces a cutoff scale $\Lambda$, and should satisfy $u|_{k=0} = 1$ and $u|_{k\to\infty} = 0$. The exact functional form chosen for the regulator should be independent of the result of calculation, so long as the lattice QCD results are constrained within the PCR. In order to avoid obfuscating the calculation with inconvenient finite-volume artifacts, a smooth attenuating dipole form is chosen for this investigation:

$$u(k\,;\Lambda) = \left(1 + \frac{k^2}{\Lambda^2}\right)^{-2}, \tag{11}$$

though, detailed analyses exist for a range of alternative forms [1, 2].

It has been suggested that a sharp cutoff FRR scheme should be chosen to ensure the preservation of the chiral Ward Identities [11]. In this investigation, chiral symmetry may be maintained by including the necessary vertex corrections at higher-order, in order to suppress any extra scheme-dependent non-analytic terms induced by the regulator [12]. However, since the renormalization of a single observable at any time is considered in this analysis, the issue is not so urgent.

## B. Loop integrals and definitions

Each loop integral has a solution in the form of a polynomial expansion analytic in $m_\pi^2$ plus a non-analytic

term:

$$\mathcal{T}_N(m_\pi^2\,;\Lambda) = b_0^N + \chi_N\, m_\pi + b_2^N\, m_\pi^2 + \mathcal{O}(m_\pi^3)\,, \qquad (12)$$

$$\mathcal{T}_\Delta(m_\pi^2\,;\Lambda) = b_0^\Delta + b_2^\Delta\, m_\pi^2 + \chi_\Delta\, m_\pi^2 \log m_\pi/\mu + \mathcal{O}(m_\pi^3)\,, \qquad (13)$$

where $\mu$ is an implicit mass scale, chosen here to be 1 GeV. The coefficients of the polynomial, $b_i^{N,\Delta}$ are entirely regulator-dependent and therefore scheme-dependent. In order to achieve an extrapolation based on some optimal FRR scale, first the scale-dependence of the low-energy expansion must be removed through renormalization. The renormalization program of FRR combines the scheme-dependent $b_i$ coefficients from the chiral loops with the scheme-dependent $a_i$ coefficients from the residual series at each chiral order $i$. The result is a scheme-independent coefficient $c_i$:

$$c_0 = a_0^\Lambda + b_0^N + b_0^\Delta\,, \qquad (14)$$

$$c_2 = a_2^\Lambda + b_2^N + b_2^\Delta\,,\ \text{etc.} \qquad (15)$$

This means the underlying $a_i$ coefficients undergo a renormalization from the chiral loop integrals. The renormalized coefficients $c_i$ are an important part of the extrapolation technique. A stable and robust determination of these parameters forms the heart of determining an optimal scale $\Lambda^{\text{scale}}$.

The loop integrals can be expressed in a convenient form by taking the non-relativistic limit and performing the pole integration for $k_0$. Renormalization is achieved by subtracting the relevant $b_0^\Lambda$ term from the integral, effectively absorbing it into the corresponding renormalized coefficient $c_0$. The integrals take the form [8, 13]:

$$\tilde{\mathcal{T}}_N(m_\pi^2\,;\Lambda) = \frac{-\chi_N}{3\pi^2}\int \mathrm{d}^3k\,\frac{k^2 u^2(k\,;\Lambda)}{(k^2+m_\pi^2)^2} - b_0^N\,, \qquad (16)$$

$$\tilde{\mathcal{T}}_\Delta(m_\pi^2\,;\Lambda) = \frac{-\chi_\Delta}{3\pi^2}\int \mathrm{d}^3k\,\frac{k^2(2\omega(k)+\Delta)\,u^2(k\,;\Lambda)}{2\omega^3(k)\,[\omega(k)+\Delta]^2} - b_0^\Delta\,, \qquad (17)$$

where $\hat{q}$ is the direction of the external momentum introduced by the incoming photon. The chiral coefficients $\chi_N$ and $\chi_\Delta$ are constants in terms of the chiral Lagrangian of Eq.(6) and the relevant Clebsch-Gordan coefficients:

$$\chi_N^p = -\frac{m_N}{8\pi f_\pi^2}(D+F)^2 = -\chi_N^n\,, \qquad (18)$$

$$\chi_\Delta^p = -\frac{m_N}{8\pi f_\pi^2}\frac{2\mathcal{C}^2}{9} = -\chi_\Delta^n\,. \qquad (19)$$

Since lattice simulations are necessarily carried out on a discrete spacetime, any extrapolations performed should take into account finite volume effects. The low-energy EFT is ideally suited for characterising the leading infrared effects associated with the finite volume. In order to achieve this, each of the 3-dimensional integrals can be transformed to its form on the lattice using a finite-sum of discretized momenta, see Allton *et al.* [14] for

instance:

$$\int \mathrm{d}^3k \to \frac{(2\pi)^3}{L_x L_y L_z}\sum_{k_x, k_y, k_z}. \qquad (20)$$

On the finite-volume lattice, each momentum component is quantized in units of $2\pi/L$, that is $k_i = 2\pi n_i/L$ for integers $n_i$. Finite volume corrections $\delta^{\text{FVC}}$ can be written simply as the difference between the finite sum and the corresponding integral. It is known that the finite volume corrections saturate to a fixed result for large values of regularization scale [1]. The value $\Lambda' = 2.0$ GeV is chosen to evaluate all finite volume corrections independent of the integral cutoff scale $\Lambda$ in Eqs.(16) and (17). The finite-volume version of Eq.(10) can thus be expressed:

$$\mu_n = c_0 + a_2^\Lambda\, m_\pi^2 + (\tilde{\mathcal{T}}_N(m_\pi^2\,;\Lambda) + \delta_N^{\text{FVC}}(m_\pi^2;\Lambda'))$$
$$+ (\tilde{\mathcal{T}}_\Delta(m_\pi^2\,;\Lambda) + \delta_\Delta^{\text{FVC}}(m_\pi^2;\Lambda')) + \mathcal{O}(m_\pi^4)\,. \qquad (21)$$

### III. RESULTS

The QCDSF results for the isovector magnetic moment at a variety of $m_\pi^2$ values are displayed in Figure 3. The lattice sizes of each data point vary from 1.43 to 3.04 fm using $N_f = 2$ and $\mathcal{O}(a)$-improved Wilson quark action. A simple linear fit is included in this plot, which does not take into account the chiral loop integrals, nor the finite-volume corrections to the data. Therefore, it is not surprising that the linear fit does not reach the experimental value of the magnetic moment at the physical pion mass. Since the lattice QCD results extend outside the PCR, the result of an extrapolation will be regulator-dependent. However, scheme-dependence can be handled by obtaining an optimal regularization scale in the extrapolations, as described in Ref. [1].

#### A. Renormalization flow analysis

In order to obtain the optimal regularization scale, the low-energy coefficient $c_0$ from Eq.(21) will be calculated across a range of $\Lambda$ values. Thus the renormalization flow can be constructed. Multiple renormalization flow curves may be obtained by constraining the fit window by a maximum, $m_{\pi,\text{max}}^2$, and sequentially adding data points to extend further outside the PCR. The renormalization flow curves for a dipole regulator are plotted on the same set of axes in Figure 4. As more data are included in the fit, a greater degree of regulator-dependence is observed. Note that there is a reasonably well-defined $\Lambda$ value at which the renormalization of $c_0$ is least sensitive to the truncation of the data. This indicates that there exists an optimal regularization scale embedded in the lattice QCD results themselves.

The optimal regularization scale for a dipole form can be extracted from Figure 4 using a $\chi_{dof}^2$ analysis. Such an
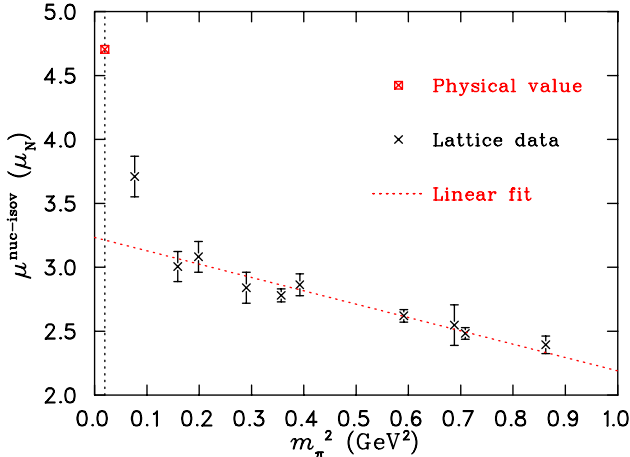
FIG. 3. (color online). Lattice QCD data for $\mu^{\text{isov}}$ from QCDSF, with physical value from experiment as marked.



FIG. 4. (color online). The renormalization flow of $c_0$ for $\mu^{\text{isov}}$ obtained using a dipole regulator, based on lattice QCD data from QCDSF.

analysis will also provide a measure of the systematic uncertainty in the optimal regularization scale. By plotting $\chi^2_{dof}$ against $\Lambda$, where $dof$ equals the number of curves $n$ minus one, a measure of the spread of the renormalization flow curves can be calculated, and the intersection point obtained. A plot of $\chi^2_{dof}$ is constructed at each value of $\Lambda$ for $c_0$ (with uncertainty $\delta c_0$):

$$\chi^2_{dof} = \frac{1}{n-1} \sum_{i=1}^{n} \frac{\left(c_0^i(\Lambda) - \bar{c}_0(\Lambda)\right)^2}{\left(\delta c_0^i(\Lambda)\right)^2}, \qquad (22)$$

$$\bar{c}_0(\Lambda) = \frac{\sum_{i=1}^{n} c_0^i(\Lambda)/\left(\delta c_0^i(\Lambda)\right)^2}{\sum_{j=1}^{n} 1/\left(\delta c_0^j(\Lambda)\right)^2}. \qquad (23)$$

The indices $i$ and $j$ correspond to data sets with differing $m^2_{\pi,\text{max}}$. The $\chi^2_{dof}$ plot corresponding to Figure 4 is shown in Figure 5. The optimal regularization scale $\Lambda^{\text{scale}}$ is taken to be the central value $\Lambda_{\text{central}}$ of the plot, and the upper and lower bounds obey the condition $\chi^2_{dof} < \chi^2_{dof,min} + 1/(dof)$. Thus the optimal regularization scale for a dipole form is $\Lambda^{\text{scale}} = 1.13^{+0.22}_{-0.20}$ GeV. This value is consistent with the optimal regularization scale obtained for the nucleon mass using a dipole form [1], based on lattice QCD results from JLQCD [15], PACS-CS [16] and CP-PACS [17]. This is strong evidence that, for a given functional form, the optimal regularization scale is associated with an intrinsic scale, which characterizes the size of the nucleon, as probed by the pion.

## IV. CHIRAL EXTRAPOLATIONS

Using the optimal regularization scale, extrapolations can be made to any quark mass. Consider the behaviour of the magnetic moment as a function of the quark mass as shown in Figure 6 (in physical units). Here, the finite-volume expansion of Eq.(21) is constrained by the lattice results from several different volumes. Extrapolation
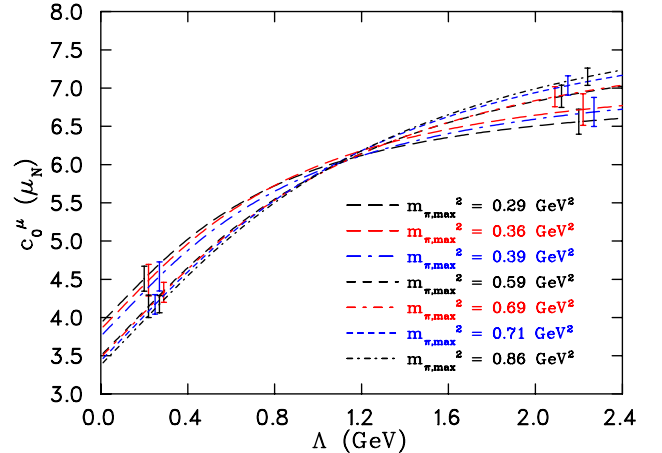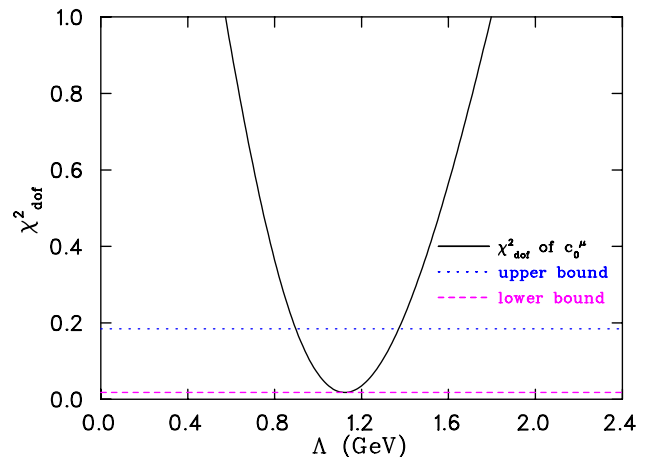


FIG. 5. (color online). $\chi^2_{dof}$ for the renormalization flow of $c_0$ for $\mu^{\text{isov}}$ obtained using a dipole regulator, based on lattice QCD data from QCDSF.

curves are then plotted for infinite-volume and a variety of finite-volumes at which current lattice QCD results are produced. For each curve, only the values for which $m_\pi L > 3$ are plotted, provisionally, to avoid undesired effects of the $\epsilon$-regime. The infinite-volume extrapolation to the physical point is within 2% of the experimentally derived value. The finite-volume extrapolations are also useful for estimating the result of a lattice QCD calculation at certain box sizes. This can also provide a benchmark for estimating the outcome of a lattice QCD simulation at larger and untested box sizes. Note that even a relatively standard 3 fm lattice box length will differ significantly from the experimental value at the physical point. Since the data points in Figure 6 are at differing finite volumes, the infinite-volume corrected data points are displayed in Figure 7.
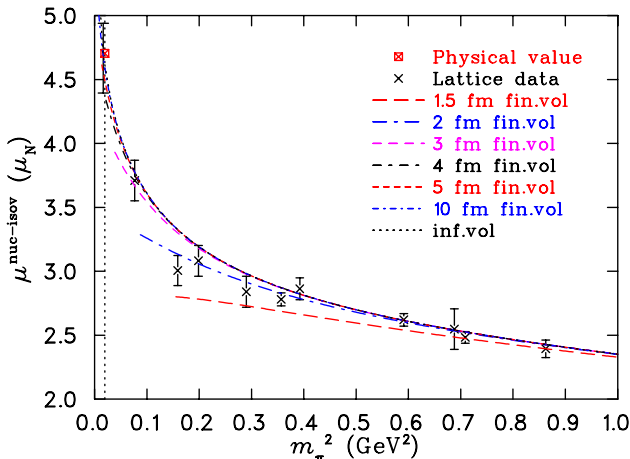
FIG. 6. (color online). Extrapolations of $\mu^{\text{isov}}$ at different finite volumes and infinite volume, using a dipole regulator, based on lattice QCD data from QCDSF, lattice sizes: $1.43 - 3.04$ fm. The provisional constraint $m_\pi L > 3$ is used. The physical value from experiment is marked. An estimate in the uncertainty in the extrapolation due to $\Lambda^{\text{scale}}$ has been calculated from Figure 5, and is indicated at the physical value of $m_\pi^2$.



FIG. 7. (color online). Extrapolations of $\mu^{\text{isov}}$ at different finite volumes and infinite volume, using a dipole regulator, based on lattice QCD data from QCDSF, lattice sizes: $1.43 - 3.04$ fm. The provisional constraint $m_\pi L > 3$ is used. The infinite-volume corrected data points are shown. The physical value from experiment is marked. An estimate in the uncertainty in the extrapolation due to $\Lambda^{\text{scale}}$ has been calculated from Figure 5, and is indicated at the physical value of $m_\pi^2$.

## V. CONCLUSION

The technique for obtaining an optimal regularization scale from lattice QCD data has been investigated in the context of the magnetic moment of the isovector nucleon. By using recent precision lattice QCD results from QCDSF, an optimal regularization scale for a dipole form was obtained. This was achieved by analyzing the renormalization flow of the low-energy coefficient $c_0$ with respect to the scale $\Lambda$, whilst extending the data beyond the power-counting regime. A regularization scale was discovered where the renormalization of $c_0$ is least sen-
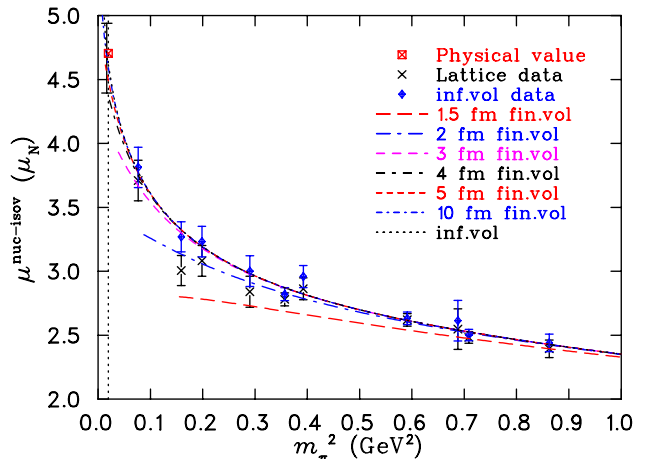
sitive to the truncation of the lattice QCD data. The value of the optimal regularization scale was consistent with results from the nucleon mass. Thus an intrinsic scale has been uncovered, which characterizes the energy scale of the nucleon-pion interaction.

Using the value of the intrinsic scale, the extrapolation of the magnetic moment to the physical pion mass and infinite-volume lattice box size is consistent with experiment. The finite-volume extrapolations provide a benchmark for estimating the outcome of a lattice QCD simulation at realistic or optimistic box sizes.

The results clearly indicate a successful procedure for using lattice QCD data to extrapolate an observable to the chiral regime.

[1] J. M. M. Hall, D. B. Leinweber, and R. D. Young, Phys. Rev. **D82**, 034010 (2010), 1002.4924.

[2] D. B. Leinweber, A. W. Thomas, and R. D. Young, Nucl. Phys. **A755**, 59 (2005), hep-lat/0501028.

[3] E. E. Jenkins and A. V. Manohar (1991), talk presented at the Workshop on Effective Field Theories of the Standard Model, Dobogoko, Hungary, Aug 1991.

[4] E. E. Jenkins and A. V. Manohar, Phys. Lett. **B255**, 558 (1991).

[5] E. E. Jenkins, Nucl. Phys. **B368**, 190 (1992).

[6] J. N. Labrenz and S. R. Sharpe, Phys. Rev. **D54**, 4595 (1996), hep-lat/9605034.

[7] A. Walker-Loud, Nucl. Phys. **A747**, 476 (2005), hep-lat/0405007.

[8] P. Wang, D. B. Leinweber, A. W. Thomas, and R. D. Young, Phys. Rev. **D75**, 073012 (2007), hep-ph/0701082.

[9] R. F. Lebed, Phys. Rev. **D51**, 5039 (1995), hep-ph/9411204.

[10] M. Gell-Mann, R. J. Oakes, and B. Renner, Phys. Rev. **175**, 2195 (1968).

[11] V. Bernard, T. R. Hemmert, and U.-G. Meissner, Nucl. Phys. **A732**, 149 (2004), hep-ph/0307115.

[12] D. Djukanovic, M. R. Schindler, J. Gegelia, and S. Scherer, Phys. Rev. **D72**, 045002 (2005), hep-ph/0407170.

[13] P. Wang, D. B. Leinweber, A. W. Thomas, and R. D. Young (2008), 0810.1021.

[14] W. Armour, C. R. Allton, D. B. Leinweber, A. W. Thomas, and R. D. Young, J. Phys. **G32**, 971 (2006), hep-lat/0510078.

[15] H. Ohki et al., Phys. Rev. **D78**, 054502 (2008), 0806.4744.

[16] S. Aoki et al. (PACS-CS) (2008), 0807.1661.

[17] A. Ali Khan et al. (CP-PACS), Phys. Rev. **D65**, 054505 (2002), hep-lat/0105015.

# Finite volume corrections to charge radii

J.M.M. Hall, D.B. Leinweber, R.D. Young

*Special Research Centre for the Subatomic Structure of Matter (CSSM), Department of Physics,*
*University of Adelaide 5005, Australia*

## Abstract

Lattice quantum chromodynamics (QCD) provides important non-perturbative techniques for the analysis of observables. Nevertheless, in order to compare lattice simulation results with experiment, an extrapolation to infinite volume is required. The electric charge radius is of particular interest when considering the implementation of finite-volume corrections. It is standard practice in the literature to transform electric form factors on the lattice into charge radii prior to analysis. However, there is a fundamental difficulty with using these charge radii results in a finite-volume extrapolation. The subtleties are a consequence of the absence of a well-defined continuous derivative, which is required to define the charge radius. In this discourse, a procedure is outlined for handling finite-volume corrections, which should be applied directly to the electric form factors rather than to the charge radii themselves.

## 1. Introduction

Extrapolations of lattice QCD simulation results are a useful tool in examining the chiral properties of observables. Reliable extrapolations take into account leading-order chiral loop corrections and account for finite-volume effects. In many cases, calculating the finite-volume corrections poses no essential problems. Examples of chiral effective field theory analyses accounting for finite-volume effects are in Refs. [1, 2].

However, the treatment of the electric charge radius is more challenging. Once form factors have been extracted from the lattice simulation, they are typically converted directly into charge radii, The essential difficulty lies in the definition

1

of the charge 'radius' at finite volume (more precisely, the slope of the electric form factor). In order to define the radius, a $Q^2$ derivative must be applied to the electric form factor, for small momentum transfer $Q^2 = \vec{q}^2 - q_0^2$. This approach breaks down on the lattice, where only discrete momentum values are allowed.

In this discourse, a method is outlined for handling finite-volume corrections to a given lattice simulation result. It will be shown that the finite-volume corrections to the loop integrals must be applied before the conversion from form factor to charge radius. By applying the finite-volume corrections directly to the electric form factor, and ensuring that the procedure preserves the electric charge normalization, an extrapolation in $Q^2$ may be used to construct an infinite-volume charge radius. The infinite-volume charge radius can be defined as normal. A finite-volume charge radius may also be defined, so long as an allowed value of momentum $q$ is used in the conversion from infinite to finite volume.

## 2. Effective field theory

In electromagnetic chiral perturbation theory ($\chi$PT), it is usual to define the Sachs electromagnetic form factors $G_{E,M}$, which parameterize the matrix element for the quark current $J_\mu$:

$$\langle B(p')|J_\mu|B(p)\rangle =$$

$$\bar{u}^{s'}(p')\left\{v_\mu\, G_E(Q^2) + \frac{i\epsilon_{\mu\nu\rho\sigma}v^\rho\, S_v^\beta\, q^\gamma}{m_B}\, G_M(Q^2)\right\}u^s(p), \tag{1}$$

where $Q^2$ is the positive momentum transfer $Q^2 = -q^2 = -(p'-p)^2$. Lattice QCD results are often constructed from an alternative representation, using the form factors $F_1$ and $F_2$, which are called the Dirac and Pauli form factors, respectively. The Sachs form factors are simply linear combinations of $F_1$ and $F_2$:

$$G_E(Q^2) = F_1(Q^2) - \frac{Q^2}{4m_B^2}F_2(Q^2)\,, \tag{2}$$

$$G_M(Q^2) = F_1(Q^2) + F_2(Q^2)\,. \tag{3}$$

In the heavy-baryon formulation of Eq.(1), the covariant spin operator $S_v^\mu = -\frac{1}{8}\gamma_5[\gamma^\mu, \gamma^\nu]v_\nu$ has the useful properties that its commutation and anti-commutation rules depend only on the 4-velocity $v_\mu$.

The external-momentum-dependent electric form factor $G_E(Q^2)$ allows a charge radius, or (strictly speaking) the slope of the form factor, to be defined in the usual

manner:

$$\langle r^2 \rangle_E = \lim_{Q^2 \to 0} -6 \frac{\partial G_E(Q^2)}{\partial Q^2}. \tag{4}$$

The first challenge involves the definition of the electric charge radius in terms of this derivative in Eq.(4). Since only certain, discrete values of momenta are allowed on the lattice, the derivative may only be constructed from these allowed momenta when calculating finite-volume corrections. This crucial observation becomes apparent when a comparison is made beween the loop integrals evaluated at allowed, and unallowed, values of momentum transfer $q$, respectively. The comparision is shown in Figures 1 and 2. Note that, if there is a momentum-translation in the loop integrals $k \to k - q/2$, the choice of $q = q_{\min} = (2\pi/L)$ is no longer an allowed value on the lattice, and the finite-volume corrections will be inconsistent with the untranslated result. Under such a momentum-translation, external momenta $q_i/2$ flow through the loop integral, and one must choose at least a value of $q = 2q_{\min}$ if one is to define a consistent discrete derivative for use in Eq.(4). This situation differs from the infinite-volume calculation of loop integrals, where true momentum-translation invariance is restored, and a continuous derivative may be used as normal.

## 3. Loop integral definitions

Though loop integrals in the continuum limit are invariant under momentum translations $k \to k + c\,q$, $c \in \mathbb{Z}$ (for internal loop momentum $k$), a finite volume loop sum must not include any values of $q$ less than $q_{\min} = (2\pi/L)$. Therefore, to obtain a sensible definition of the charge radius one chooses a definition of the loop integrals such that no factors of $\vec{q}/2$ appear. In fact, as long as no fractions of $\vec{q}$ appear in the integrand, the finite-volume version will converge correctly to the infinite-volume version as $L \to \infty$, for $q = (2\pi n/L)$, $n \in \mathbb{Z}$. The loop integrals in the heavy-baryon approximation that correspond to the leading-order diagrams in Figures 3 through 5 are:

$$\mathcal{T}_N(Q^2) = \frac{\chi_N}{3\pi} \int d^3 k \frac{(k^2 - \vec{k} \cdot \vec{q})}{\omega_{\vec{k}} \omega_{\vec{k}-\vec{q}} (\omega_{\vec{k}} + \omega_{\vec{k}-\vec{q}})}, \tag{5}$$

$$\mathcal{T}_\Delta(Q^2) = \frac{\chi_\Delta}{3\pi} \int d^3 k \frac{(k^2 - \vec{k} \cdot \vec{q})}{(\omega_{\vec{k}} + \Delta)(\omega_{\vec{k}-\vec{q}} + \Delta)(\omega_{\vec{k}} + \omega_{\vec{k}-\vec{q}})}, \tag{6}$$

$$\mathcal{T}_{\text{tad}}(Q^2) = \frac{\chi_t}{\pi} \int d^3 k \frac{1}{\omega_{\vec{k}} + \omega_{\vec{k}-\vec{q}}}, \tag{7}$$
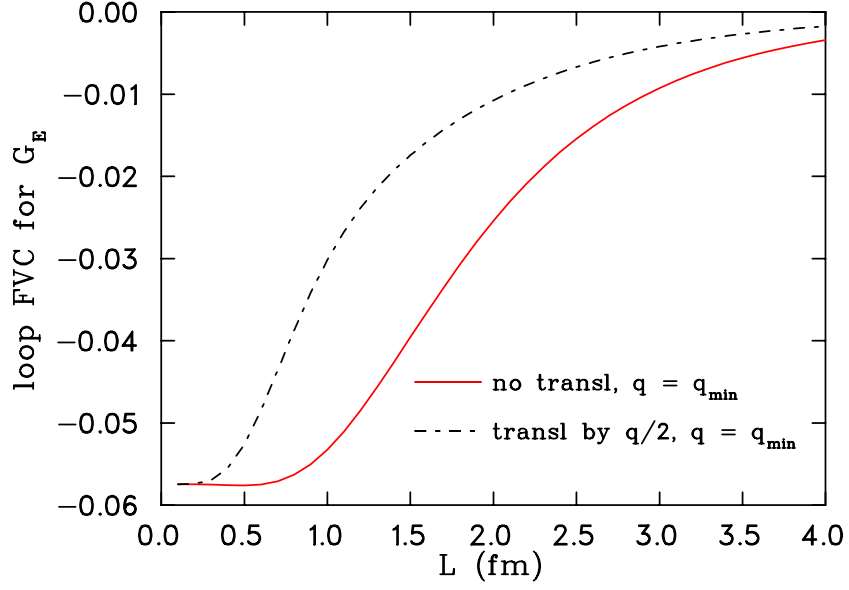
Figure 1: (color online). Finite-volume correction for the loop integral contributing to $G_E$, with $q = q_{\min}$. The choice of $q/2 = q_{\min}/2$ is not an allowed value on the lattice. The momentum translated and untranslated behaviour of the finite-volume correction are inconsistent with each other.
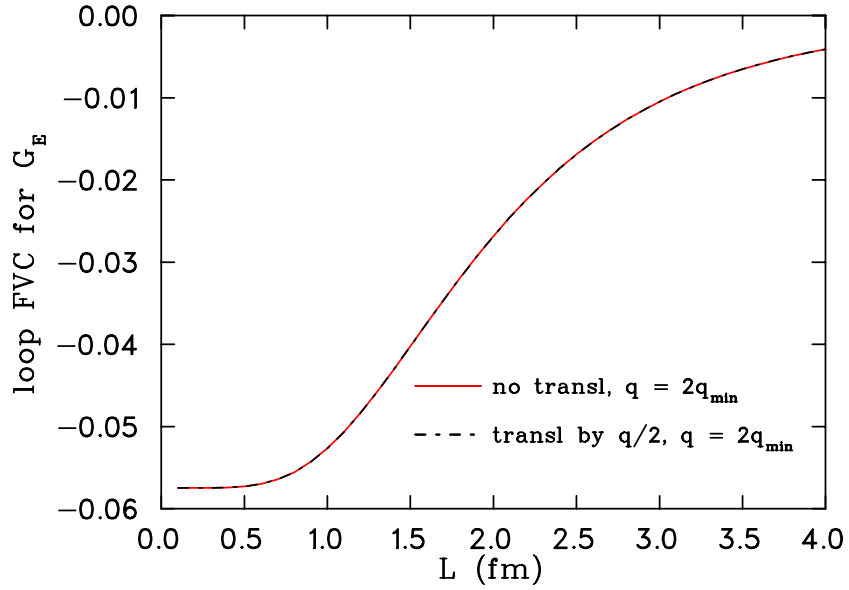


Figure 2: (color online). Finite-volume correction for the loop integral contributing to $G_E$, with $q = 2q_{\min}$. The choice of $q/2 = q_{\min}$ is an allowed value on the lattice. Therefore, the momentum translated and untranslated behaviour of the finite-volume correction is identical.

4

where $\omega_{\vec{k}} = \sqrt{\vec{k}^2 - m_\phi^2}$, $m_\phi$ is the pion or kaon mass, and $\Delta$ is the baryon mass splitting. The finite-volume correction is defined through the convention:

$$\delta_L[\mathcal{T}] = \chi \left[ \frac{(2\pi)^3}{L_x L_y L_z} \sum_{k_x, k_y, k_z} - \int d^3k \right] \mathcal{I} \,, \qquad (8)$$

for integrand $\mathcal{I}$. The integrals which contribute to the electric charge radius, denoted $(T)$, are exactly analogous to the integrals $(\mathcal{T})$ defined in Eqs.(5) and (7), that correspond to the electric form factor $G_E$. To obtain the integrals that contribute to the charge radius, one simply takes the derivative with respect to momentum transfer $Q^2$ at vanishingly small values of $Q^2$. This is allowed in the infinite-volume limit:

$$T = \lim_{Q^2 \to 0} -6 \frac{\partial \mathcal{T}(Q^2)}{\partial Q^2}. \qquad (9)$$

Note that the ensuing procedure for calculating the finite-volume corrected electric charge radius uses only the infinite-volume versions of the integrals $(\mathcal{T})$. Fitting methods need only be applied at infinite volume. Thus, the external momentum derivative in Eq.(9) need not be discretized, but may remain a continuous derivative.

## 4. Procedure for obtaining the charge radius at finite volume

As emphasized already, Figures 1 and 2 show that the finite-volume corrections cannot be applied directly to the charge radius itself. The momentum discretization ruins the circular symmetry in $q$ except at the values coinciding with lattice momentum values $(2\pi n/L)$, $n \in \mathbb{Z}$. The finite-volume corrections should be applied to the electric form factor $G_E(Q^2)$ instead. A momentum convention in the loop integral is chosen such that $q$ may be chosen to be $q_{\min} = (2\pi n/L)$. The procedure for achieving the correct finite-volume corrections is outlined below.

First, the lattice finite-volume charge radius $\langle r^2 \rangle_E^L$ is converted into a finite-volume form factor $G_E^L(Q^2)$, using $q = q_{\min} = (2\pi/L)$. This is achieved through use of an extrapolation in $Q^2$. As an example, a dipole Ansatz yields the following formula:

$$G_E^L(Q_{\min}^2) = \left( 1 + \frac{Q_{\min}^2 \langle r^2 \rangle_E^L}{12} \right)^{-2}, \qquad (10)$$

respectively, where $Q_{\min}^2 = \vec{q}_{\min}^2 - (E_N - M_N)^2$. In many cases, this simply reverses the steps used to convert lattice results to charge radii. Ideally, one should start
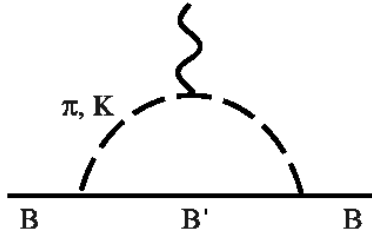
Figure 3: The pion/kaon loop contributions to the self energy of an octet baryon $B$, allowing a transition to a baryon $B'$, with photon attachment, providing the leading nonanalytic contribution to the electric charge radius. All charge conserving transitions are implicit.
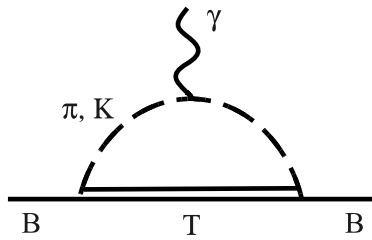


Figure 4: The pion/kaon loop contribution to the self-energy of an octet baryon $B$, with photon attachment, allowing transitions to the nearby and strongly-coupled decuplet baryons $T$.
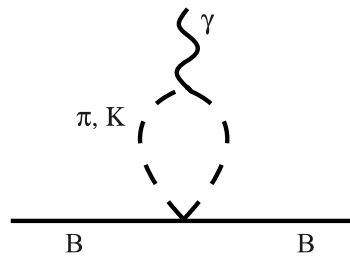


Figure 5: Tadpole contributions at $O(m_q)$ to the octet baryon self energy, with photon attachment.

with the form factors as extracted from the lattice, and only convert them into radii using an Ansatz after correcting for lattice finite-volume effects. The next step is to transform the finite-volume form factor $G_E^L(Q_{\min}^2)$ to an infinite-volume form factor $G_E^\infty(Q_{\min}^2)$, so that the infinite-volume charge radius can be calculated. This is achieved by subtracting the electric charge symmetry-preserving finite-volume correction, defined by:

$$\Delta_L(Q_{\min}^2, 0) = \delta_L \left[ \mathcal{T}(Q_{\min}^2) - \mathcal{T}(0) \right]. \tag{11}$$

The second term of Eq.(11) ensures that both infinite- and finite-volume form factors are correctly normalized, i.e. $G_E^{L,\infty}(0) = 1$. Thus, the infinite-volume electric form factor can be calculated using the equation:

$$G_E^\infty(Q_{\min}^2) = G_E^L(Q_{\min}^2) - \Delta_L(Q_{\min}^2, 0). \tag{12}$$

The infinite-volume charge radius $\langle r^2 \rangle_E^\infty$ can be recovered from the form factor by using the extrapolation in $Q^2$. Once the infinite-volume charge radius has been obtained, a chiral extrapolation can be performed if needed. The chiral loop integrals corresponding to the charge radius are those defined by Eq.(9).

Finally, the finite-volume charge radius can be evaluated by adding the finite-volume correction to the form factor at any box length $\tilde{L}$, and corresponding momentum transfer on the lattice, $\tilde{Q}_{\min}^2$:

$$G_E^{\tilde{L}}(\tilde{Q}_{\min}^2) = G_E^\infty(\tilde{Q}_{\min}^2) + \Delta_{\tilde{L}}(\tilde{Q}_{\min}^2, 0). \tag{13}$$

The finite-volume charge radii are obtained from the chosen extrapolation formula at box size $\tilde{L}$. Thus, an electric charge radius may be calculated at any desired value of box length, based on lattice QCD simulation results. In doing so, the finite-volume behaviour of the charge radius may be analyzed.

## 5. Conclusion

It was discovered that finite-volume corrections for charge radii are not well defined on the lattice. The use of continuous derivatives in constructing the electric charge radius leads to inconsistent results in the finite-volume corrections. Furthermore, finite-volume corrections must be applied to the electric form factors rather than to the charge radii directly. Therefore, a procedure was developed to apply finite-volume corrections to the electric form factor, strictly involving momenta available on the lattice. The resultant finite-volume-corrected form factor may then be converted into a charge radius using an extrapolation in $Q^2$.

[1] Beane, S.R.. Nucleon masses and magnetic moments in a finite volume. Phys Rev 2004;D70:034507. doi:10.1103/PhysRevD.70.034507. `hep-lat/0403015`.

[2] Hall, J.M.M., Leinweber, D.B., Young, R.D.. Power Counting Regime of Chiral Effective Field Theory and Beyond. Phys Rev 2010;D82:034010. doi:10.1103/PhysRevD.82.034010. `1002.4924`.

# Chiral extrapolations for nucleon electric charge radii

J.M.M. Hall, D.B. Leinweber, and R.D. Young

*Special Research Centre for the Subatomic Structure of Matter (CSSM),*
*Department of Physics, University of Adelaide 5005, Australia*

Chiral effective field theory allows the extrapolation of lattice quantum chromodynamics (QCD) simulation results to the infinite-volume limit and the chiral regime. The electric charge radius of the nucleon affords an opportunity to explore the subtleties of both these extrapolations. To achieve an extrapolation to infinite-volume electric charge radii, the finite-volume corrections must be applied directly to the electric form factors. Additionally, since lattice QCD results typically reside outside the chiral power-counting regime of chiral effective field theory, care must be taken in performing a chiral extrapolation. Using finite-range regularized chiral effective field theory, one can obtain an optimal regularization scale by analyzing the scale-flow of the renormalization of the chiral coefficients. Thus, effective field theory is extended beyond the PCR. This optimal regularization scale is retrieved from the lattice QCD results themselves. A comparison of this optimal scale with previous analyses of the mass and magnetic moment of the nucleon demonstrates consistency in the value of the optimal scale. This provides evidence for the existence of an intrinsic energy scale in the nucleon-pion interaction, as calculated from lattice QCD results. Using the optimal scale, chiral extrapolations and infinite-volume corrections are presented. Extrapolations to a variety of finite lattice box sizes are also included, which are useful for predicting the outcome of lattice simulations in a finite volume.

## I. INTRODUCTION

The analysis of the electric charge radius of the nucleon provides an important test case for extrapolations to the infinite-volume limit and the physical point. Since the finite box size of the lattice entails undesirable finite-volume effects in the simulated behaviour of the hadrons, it is important to be able to quantify these effects with a reliable infinite-volume extrapolation. In order to avoid model-dependence in the result, one should ideally use lattice simulations that lie within the chiral power-counting regime (PCR). The PCR is defined by the range of quark or pion masses at which a $\chi$EFT calculation is independent of regularization scheme, up to some tolerance [2]. Within the PCR, the chiral expansion of an observable converges, and the result is independent of any resummation of the higher-order terms of the expansion.

In finite-range regularization (FRR), a regulator is introduced into the chiral loop integrals, which serves to suppress the ultraviolet divergences of the effective field theory. The selection of the momentum cutoff scale $\Lambda$ is arbitrary within the PCR, but outside the PCR the results of $\chi$EFT calculations are scale-dependent. Since lattice QCD results typically extend outside the PCR, one is restricted by the available data when performing an extrapolation. However, using the techniques developed in Refs. [1], the extent of scale-dependence in chiral exptrapolations can be quantified. This is achieved by identifying an optimal regularization scale $\Lambda^{\text{scale}}$ embedded within the lattice data themselves. The optimal scale is realized by analyzing the renormalization scale-flow of the coefficients of the chiral expansion.

This optimal scale can be compared with previous results for an optimal scale derived from lattice QCD data for the nucleon mass and the magnetic moment. If the values of the optimal scales are consistent, this lends credence to the notion that one can obtain an intrinsic scale for the nucleon-pion interaction from lattice QCD simulations. Moreover, the resultant scale $\Lambda^{\text{scale}}$ can be used to perform chiral extrapolations in which any scheme-dependence in the result has been handled, and incorporated into the systematic uncertainty in the choice of $\Lambda^{\text{scale}}$.

In lattice QCD, the isovector combination of the nucleon $(p - n)$ is often calculated to avoid the computationally expensive disconnected loops that occur in full QCD. Quark-flow diagrams including any photons coupling to sea-quark loops cancel in the case of the isovector. Isovector nucleon data for two-flavor $\mathcal{O}(a)$-improved Wilson quark action from the QCDSF Collaboration is used in this analysis, which is displayed in Figure 1.

## II. CHIRAL EFFECTIVE FIELD THEORY

In electromagnetic chiral perturbation theory ($\chi$PT), it is usual to define the Sachs electromagnetic form factors $G_{E,M}$, which parameterize the matrix element for the quark current $J_\mu$. In the non-relativistic limit, this can be written as:

$$\langle B(p')|J_\mu|B(p)\rangle =$$
$$\bar{u}^{s'}(p') \left\{ \text{v}_\mu\, G_E(Q^2) + \frac{i\epsilon_{\mu\nu\rho\sigma}\text{v}^\rho\, S_\text{v}^\beta\, q^\nu}{m_B}\, G_M(Q^2) \right\} u^s(p).$$

$Q^2$ is defined as positive momentum transfer $Q^2 = -q^2 = -(p' - p)^2$. Lattice QCD results are often constructed from an alternative representation, using the form factors
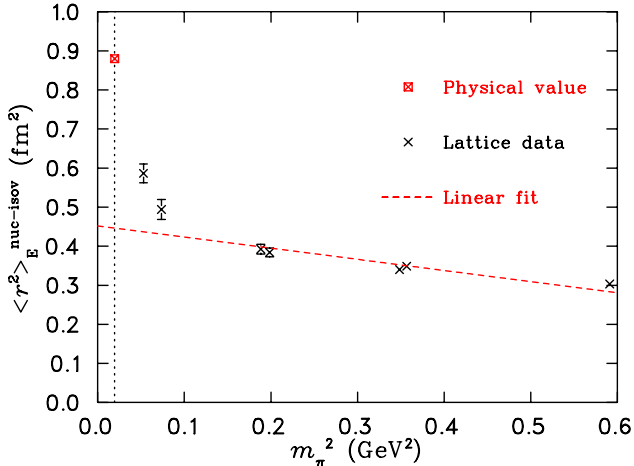
FIG. 1. (color online). Lattice QCD data for $\langle r^2 \rangle_E$ from QCDSF, with physical value from experiment as marked.

$F_1$ and $F_2$, which are called the Dirac and Pauli form factors, respectively. The Sachs form factors are simply linear combinations of $F_1$ and $F_2$:

$$G_E(Q^2) = F_1(Q^2) - \frac{Q^2}{4m_B^2} F_2(Q^2), \qquad (2)$$

$$G_M(Q^2) = F_1(Q^2) + F_2(Q^2). \qquad (3)$$

In the heavy-baryon formulation of Eq.(1), the covariant spin operator $S_v^\mu = -\frac{1}{8}\gamma_5[\gamma^\mu, \gamma^\nu]v_\nu$ has the useful properties that its commutation and anti-commutation rules depend only on the 4-velocity $v_\mu$. The external-momentum-dependent electric form factor $G_E(Q^2)$ allows a charge radius (more precisely, the slope of the electric form factor) to be defined in the usual manner:

$$\langle r^2 \rangle_E = \lim_{Q^2 \to 0} -6 \frac{\partial G_E(Q^2)}{\partial Q^2}. \qquad (4)$$

For the leading-order contributions to the electric form factor, the standard first-order interaction Lagrangian from heavy-baryon chiral perturbation theory is used [3–8]:

$$\mathcal{L}_{\chi PT}^{(1)} = 2D \, \text{Tr} \left[ \bar{B}_v S_v^\mu \{A_\mu, B_v\} \right] + 2F \, \text{Tr} \left[ \bar{B}_v S_v^\mu [A_\mu, B_v] \right]$$
$$+ \mathcal{C} \left( \bar{T}_v^\mu A_\mu B_v + \bar{B}_v A_\mu T_v^\mu \right), \qquad (5)$$

where the pion fields are encoded as the adjoint representation of $SU(3)_L \otimes SU(3)_R$, and forming an axial vector combination $A_\mu$:

$$\xi \equiv \exp \left\{ \frac{i}{f_\pi} \tau^a \pi^a \right\}, \qquad (6)$$

$$A_\mu = \frac{1}{2}(\xi \, \partial_\mu \, \xi^\dagger - \xi^\dagger \, \partial_\mu \, \xi). \qquad (7)$$

By the convention presented here, $f_\pi = 92.4$ MeV. The values for the couplings in the interaction Lagrangian are obtained from the SU(6) flavor-symmetry relations [5, 9] and from phenomenology: $D = 0.76$, $F = \frac{2}{3}D$ and $\mathcal{C} = -2D$.
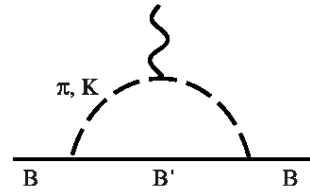


FIG. 2. The pion/kaon loop contributions to the electric charge radius of an octet baryon $B$, allowing a transition to a baryon $B'$, with photon attachment. All charge conserving transitions are implicit.
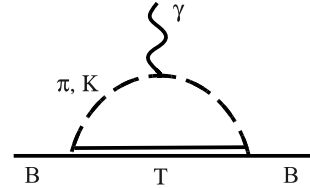


FIG. 3. The pion/kaon loop contribution to the electric charge radius of an octet baryon $B$, with photon attachment, allowing transitions to the nearby and strongly-coupled decuplet baryons $T$.
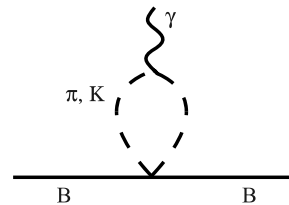


FIG. 4. The tadpole contribution at $\mathcal{O}(m_q)$ to the electric charge radius of an octet baryon $B$, with photon attachment.

### A. Finite-range regularization

In finite-range regularized effective field theory, regulator functions $u(k\,;\Lambda)$, with characteristic momentum scale $\Lambda$, are inserted into the loop integrals. The regulators should be chosen such that they satisfy $u|_{k=0} = 1$ and $u|_{k\to\infty} = 0$. The exact functional form chosen for the regulator should be independent of the result of calculation, so long as the lattice QCD results are constrained within the PCR. In order to avoid obfuscating the calculation with inconvenient finite-volume artifacts, a smooth attenuating dipole form is chosen for this investigation:

$$u(k\,;\Lambda) = \left(1 + \frac{k^2}{\Lambda^2}\right)^{-2}, \qquad (8)$$

though detailed analyses exist for a range of alternative forms [1, 2]. Further discussion of the subtleties involved in choosing a regulator can be found in Refs. [10, 11].

### B. Loop integrals and definitions

The leading-order loop integral contributions to the electric form factor, corresponding to the diagrams in

Figures 2 through 4, can be simplified to a convenient form by taking the heavy-baryon limit, and performing the pole integration for $k_0$:

$$\mathcal{T}_N^E(Q^2) = \frac{\chi_N^E}{5\pi} \int d^3k \frac{(k^2 - \vec{k} \cdot \vec{q})\, u(\vec{k}\,;\Lambda)\, u(\vec{k} - \vec{q}\,;\Lambda)}{\omega_{\vec{k}} \omega_{\vec{k}-\vec{q}}(\omega_{\vec{k}} + \omega_{\vec{k}-\vec{q}})}, \tag{9}$$

$$\mathcal{T}_\Delta^E(Q^2) = \frac{\chi_\Delta^E}{5\pi} \int d^3k \frac{(k^2 - \vec{k} \cdot \vec{q})\, u(\vec{k}\,;\Lambda)\, u(\vec{k} - \vec{q}\,;\Lambda)}{(\omega_{\vec{k}} + \Delta)(\omega_{\vec{k}-\vec{q}} + \Delta)(\omega_{\vec{k}} + \omega_{\vec{k}-\vec{q}})}, \tag{10}$$

$$\mathcal{T}_{\rm tad}^E(Q^2) = -\frac{\chi_t^E}{\pi} \int d^3k \frac{u^2(\vec{k}\,;\Lambda)}{\omega_{\vec{k}} + \omega_{\vec{k}-\vec{q}}}, \tag{11}$$

where $\omega_{\vec{k}} = \sqrt{\vec{k}^2 - m_\phi^2}$, $m_\phi$ is the pion or kaon mass, and $\Delta$ is the baryon mass splitting.

The chiral coefficients $\chi_N^E$, $\chi_\Delta^E$ and $\chi_t^E$ are constants in terms of the chiral Lagrangian of Eq.(5) and the relevant Clebsch-Gordan coefficients, as summarized by Wang [12]:

$$\chi_N^{E,p} = \frac{5}{16\pi^2 f_\pi^2}(D + F)^2 = -\chi_N^{E,n}, \tag{12}$$

$$\chi_\Delta^{E,p} = -\frac{5}{16\pi^2 f_\pi^2}\frac{4\mathcal{C}^2}{9} = -\chi_\Delta^{E,n}, \tag{13}$$

$$\chi_t^{E,p} = -\frac{1}{16\pi^2 f_\pi^2} = -\chi_t^{E,n}. \tag{14}$$

### C. Finite-volume corrections

Finite-volume corrections cannot be applied directly to the charge radius itself. Instead, the electric form factors $G_E(Q^2)$ are corrected to infinite-volume using an extrapolation in $Q^2$, such as a dipole Ansatz. The integrals which contribute to the electric charge radius, denoted $(T^E)$, are exactly analogous to the integrals $(\mathcal{T}^E)$, defined in Eqs.(9) through (11), that correspond to the electric form factor $G_E$. To obtain the integrals that contribute to the charge radius, one simply takes the derivative with respect to momentum transfer $Q^2$ at vanishingly small values of $Q^2$. This is allowed in the infinite-volume limit:

$$T^E = \lim_{Q^2 \to 0} -6\frac{\partial \mathcal{T}^E(Q^2)}{\partial Q^2}. \tag{15}$$

Note that the ensuing procedure for calculating the finite-volume corrected electric charge radius uses only the infinite-volume versions of the chiral loop integrals.

The finite-volume correction to the electric form factors is achieved by subtracting the electric charge symmetry-preserving finite-volume correction, defined by:

$$\Delta_L(Q_{\rm min}^2, 0) = \delta_L\left[\mathcal{T}^E(Q_{\rm min}^2) - \mathcal{T}^E(0)\right], \tag{16}$$

where the functional $\delta_L$ is defined through the convention:

$$\delta_L[\mathcal{T}^E] = \chi\left[\frac{(2\pi)^3}{L_x L_y L_z} \sum_{k_x, k_y, k_z} - \int d^3k\right]\mathcal{I}, \tag{17}$$

for integrand $\mathcal{I}$. The second term of Eq.(16) ensures that both infinite- and finite-volume electric form factors are correctly normalized, ie. $G_E^{L,\infty}(0) = 1$. Thus, the infinite-volume electric form factor can be calculated using the equation:

$$G_E^\infty(Q_{\rm min}^2) = G_E^L(Q_{\rm min}^2) - \Delta_L(Q_{\rm min}^2, 0). \tag{18}$$

The infinite-volume charge radius $\langle r^2 \rangle_E^\infty$ can be recovered from the form factor by using the extrapolation in $Q^2$.

Once the lattice data have been converted into infinite-volume charge radii, the chiral behaviour of the electric charge radius can be written in terms of an ordered expansion in pion mass squared, through use of the Gell-Mann−Oakes−Renner Relation, $m_q \propto m_\pi^2$ [13]:

$$\langle r^2 \rangle_E^\infty = \{a_0^\Lambda + a_2^\Lambda m_\pi^2\} + T_N^E + +T_\Delta^E + T_{\rm tad}^E + \mathcal{O}(m_\pi^3). \tag{19}$$

This expansion contains an analytic polynomial in $m_\pi^2$ plus the leading-order chiral loop integrals, from which non-analytic behaviour arises. The scale-dependent coefficients $a_i^\Lambda$ are the 'residual series' coefficients, which correspond to direct quark-mass insertions in the full Lagrangian. Since the residual coefficients $(a_i)$ are expected to be volume-independent quantities, fitting methods need only be applied at infinite volume. Upon renormalization of the divergent loop integrals, these will correspond with low-energy coefficients of $\chi$EFT. In this instance, only two free parameters are chosen in the residual series, since the non-analytic contributions are included only to order $\mathcal{O}(m_\pi^3)$.

### D. Renormalization

In order to obtain the renormalized chiral coefficients $c_0$ and $c_2$, one must add the terms from each of the loop integrals in Eqs.(9) through (11) to the residual coefficients $a_0^\Lambda$ and $a_2^\Lambda$:

$$c_0 = a_0^\Lambda + b_0^{\Lambda,N} + b_0^{\Lambda,\Delta} + b_0^{\Lambda,t}, \tag{20}$$

$$c_2 = a_2^\Lambda + b_2^{\Lambda,N} + b_2^{\Lambda,\Delta} + b_2^{\Lambda,t}. \tag{21}$$

The coefficients $b_i^\Lambda$ are the coefficients of the polynomial terms obtained from calculating the relevant loop integrals. The resultant $c_0$ is $\Lambda$-independent within the PCR, where the chiral series converges and the renormalization scheme is successful. By evaluating the loop integrals, the fully-renormalized chiral expansion can be written in terms of a polynomial in $m_\pi^2$ and non-analytic terms:

$$\langle r^2 \rangle_E^\infty = c_0^{(\mu)} + (\chi_N^E + \chi_t^E) \log \frac{m_\pi}{\mu} + \mathcal{O}(m_\pi^2). \tag{22}$$

Since the chiral expansion of Eq.(22) contains a logarithm, the value of $c_0$ can only be extracted relative to some mass scale $\mu$, which is chosen to be 1 GeV. To achieve a chiral extrapolation, it is convenient to subtract the coefficients $b_0^\Lambda$ from the respective loop integrals:

$$\tilde{T}_N^E = T_N^E - b_0^{\Lambda,N}, \tag{23}$$

$$\tilde{T}_\Delta^E = T_\Delta^E - b_0^{\Lambda,\Delta}, \tag{24}$$

$$\tilde{T}_{\text{tad}}^E = T_{\text{tad}}^E - b_0^{\Lambda,t}. \tag{25}$$

This removes the $\Lambda$-dependence from the lowest-order fit parameter of the chiral expansion. Thus, in renormalized form, the chiral expansion used for fitting may be written:

$$\langle r^2 \rangle_E^\infty = \{c_0^{(\mu)} + a_2^\Lambda m_\pi^2\} + \tilde{T}_N^E + \tilde{T}_\Delta^E$$
$$+ \tilde{T}_{\text{tad}}^E + \mathcal{O}(m_\pi^3), \tag{26}$$

and the renormalization flow of the coefficient $c_0$ will be considered.

### III. RESULTS

The QCDSF results for the electric charge radius of the isovector nucleon are displayed, with the experimental value marked, in Figure 1. The lattice sizes of each data point vary from 1.92 to 3.25 fm using $N_f = 2$ and $\mathcal{O}(a)$-improved Wilson quark action. A simple linear fit is included in this plot, which does not take into account the non-analytic behaviour of the chiral loop integrals, nor the finite-volume corrections to the data. Therefore, it is not surprising that the linear fit does not reach the experimental value of the electric charge radius at the physical pion mass. Since the lattice QCD results extend outside the PCR, the result of an extrapolation will be scale-dependent. However, the scheme-dependence may be ameliorated using a procedure that obtains an optimal regularization scale and an estimate of its systematic uncertainty, constrained by the lattice results.

#### A. Renormalization flow analysis

In order to obtain an optimal regularization scale, the low-energy coefficient $c_0$ from Eq.(26) will be calculated across a range of regularization scale values. Multiple renormalization flow curves may be obtained by constraining the fit window by a maximum, $m_{\pi,\max}^2$, and sequentially adding data points to extend further outside the PCR. The renormalization flow curves for a dipole regulator are plotted on the same set of axes in Figure 5. Note that, unlike the analysis of the nucleon mass [1] and the magnetic moment, there is no distinct intersection point in the renormalization flow curves. In addition, the scale-dependence of the coefficient $c_0$ is very slight, so long as the regularization scale is not too small. (A discussion of the best estimate for a lower bound on

the regularization scale can be found in Ref. [1].) This lack of scale-dependence is a natural consequence of the logarithm in the chiral expansion of Eq.(22), which is slowly-varying with respect to the regularization scale.

The optimal dipole regularization scale can be extracted from Figure 5 using a $\chi_{dof}^2$ analysis. Such an analysis will also provide a measure of the systematic uncertainty in the optimal scale. By plotting $\chi_{dof}^2$ against the regularization scale $\Lambda$, where $dof$ equals the number of curves $n$ minus one, a measure of the spread of the renormalization flow curves can be calculated, and the intersection point obtained. A plot of $\chi_{dof}^2$ is constructed at each value of $\Lambda$ for $c_0$ (with uncertainty $\delta c_0$):

$$\chi_{dof}^2 = \frac{1}{n-1} \sum_{i=1}^n \frac{\left(c_0^i(\Lambda) - \bar{c}_0(\Lambda)\right)^2}{\left(\delta c_0^i(\Lambda)\right)^2}, \tag{27}$$

$$\bar{c}_0(\Lambda) = \frac{\sum_{i=1}^n c_0^i(\Lambda)/\left(\delta c_0^i(\Lambda)\right)^2}{\sum_{j=1}^n 1/\left(\delta c_0^j(\Lambda)\right)^2}. \tag{28}$$

The indices $i$ and $j$ correspond to data sets with differing values of $m_{\pi,\max}^2$. The $\chi_{dof}^2$ plot corresponding to Figure 5 is shown in Figure 6. The value of the optimal regularization scale $\Lambda^{\text{scale}}$ is taken to be the central value $\Lambda^{\text{central}}$ of the plot, and the upper and lower bounds obey the condition $\chi_{dof}^2 < \chi_{dof,min}^2 + 1/(dof)$. Thus the optimal dipole scale is $\Lambda^{\text{scale}} = 1.67_{-0.33}^{+0.66}$ GeV. This value is consistent with the optimal dipole regularization scale values obtained for the nucleon mass, using lattice QCD data from JLQCD [14], PACS-CS [15] and CP-PACS[16], and the magnetic moment, using lattice QCD data from QCDSF. This is strong evidence that, for a given functional form, the optimal regularization scale is associated with an intrinsic scale, which characterizes the size of the nucleon, as probed by the pion.

### IV. CHIRAL EXTRAPOLATIONS

Using the optimal regularization scale, a reliable chiral extrapolation can be performed, with the systematic uncertainty in the optimal scale taken into account. Consider the behaviour of the electric charge radius as a function of the quark mass as shown in Figure 7 (in physical units). Extrapolation curves are then plotted for infinite-volume and a variety of finite-volumes at which current lattice QCD results are produced. For each curve, only the values for which $m_\pi L > 3$ are plotted, provisionally, to avoid undesired effects of the $\epsilon$-regime. The infinite-volume extrapolation to the physical point differs from the experimentally derived value: $\langle r^2 \rangle_E^{\text{isov}} = 0.88$ fm$^2$, by merely 0.5%. The finite-volume extrapolations are also useful for estimating the result of a lattice QCD calculation at certain box sizes. This can also provide a benchmark for estimating the outcome of a lattice QCD simulation at larger and untested box sizes. Note that even a relatively standard 3 fm lattice box length will differ significantly from the experimental value at the physical
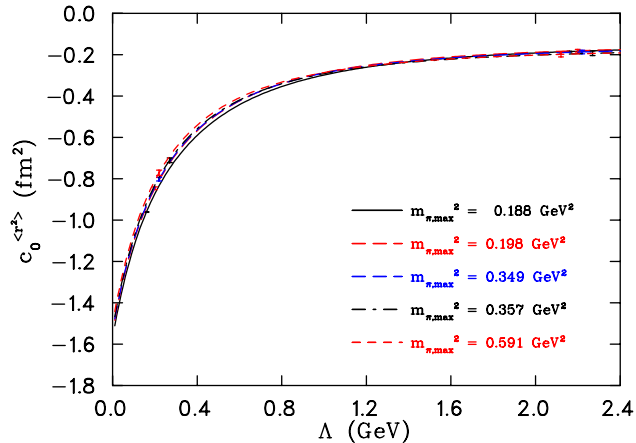
FIG. 5. (color online). The renormalization flow of $c_0$ for $\langle r^2 \rangle_E$ obtained using a dipole regulator, based on lattice QCD data from QCDSF. $c_0$ is calculated relative to the energy scale $\mu = 1$ GeV.
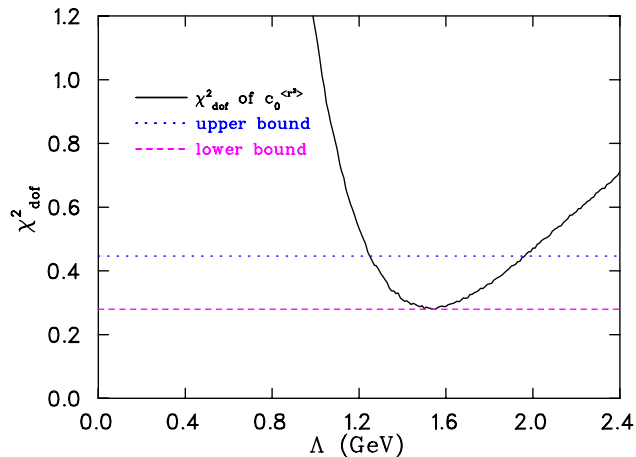


FIG. 6. (color online). $\chi^2_{dof}$ for the renormalization flow of $c_0$ for $\langle r^2 \rangle_E$ obtained using a dipole regulator, based on lattice QCD data from QCDSF. $c_0$ is calculated relative to the energy scale $\mu = 1$ GeV.



FIG. 7. (color online). Extrapolations of $\langle r^2 \rangle_E$ at different finite volumes and infinite volume, using a dipole regulator, based on lattice QCD data from QCDSF, lattice sizes: $1.92 - 3.25$ fm. The provisional constraint $m_\pi L > 3$ is used. The physical value from experiment is marked.



FIG. 8. (color online). Extrapolations of $\langle r^2 \rangle_E$ at different finite volumes and infinite volume, using a dipole regulator, based on lattice QCD data from QCDSF, lattice sizes: $1.92 - 3.25$ fm. The provisional constraint $m_\pi L > 3$ is used. The infinite-volume corrected data points are shown. The physical value from experiment is marked.

point. Since the data points in Figure 7 are at differing finite volumes, the infinite-volume corrected data points are displayed in Figure 8.

To highlight the insensitivity of the extrapolation to the regularization scale $\Lambda^{\text{scale}}$, an estimate of the systematic uncertainty in the extrapolation to the physical point solely due to $\Lambda^{\text{scale}}$ is displayed in Figure 9. The size of the error bar at the physical point is comparable to that due to statistical uncertainty, as shown in Figure 10. This indicates that, in the case of the electric charge radius, the identification of an intrinsic scale is borderline, due to the dominance of the logarithm in the chiral expansion, and its slowly varying property in the large $m_\pi$ regime. Thus, chiral extrapolations of the electric charge radius are more robust, in the sense that the scale-dependence in the result is suppressed, and the identification of an intrinsic scale is not so vital as in the case of the nucleon mass or magnetic moment.
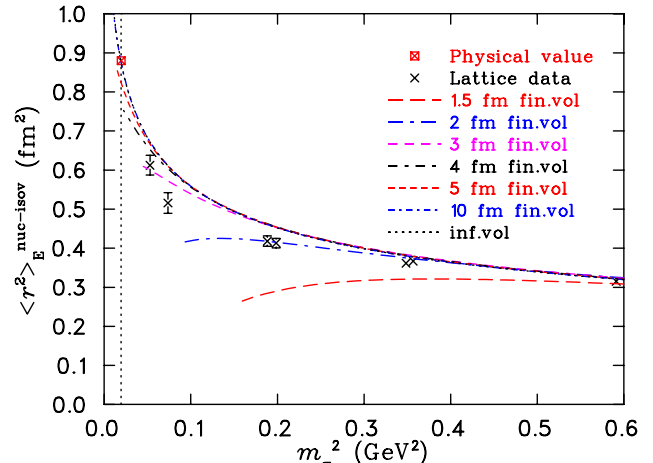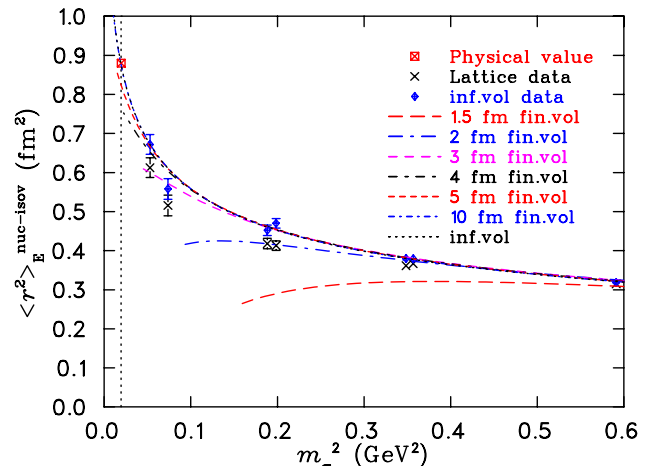
## V. CONCLUSION

The technique for obtaining an optimal regularization scale from lattice QCD data has been investigated in the context of the electric charge radius of the isovector nucleon. By using recent precision lattice QCD results from QCDSF, an optimal regularization scale for a dipole form was obtained. This was achieved by analyzing the renormalization flow of the low-energy coefficient $c_0$ with respect to the scale $\Lambda$, whilst extending the data beyond the power-counting regime. A regularization scale was discovered where the renormalization of $c_0$ is least sensitive to the truncation of the lattice QCD data. The value of the optimal regularization scale was consistent with results from the nucleon mass and the magnetic moment
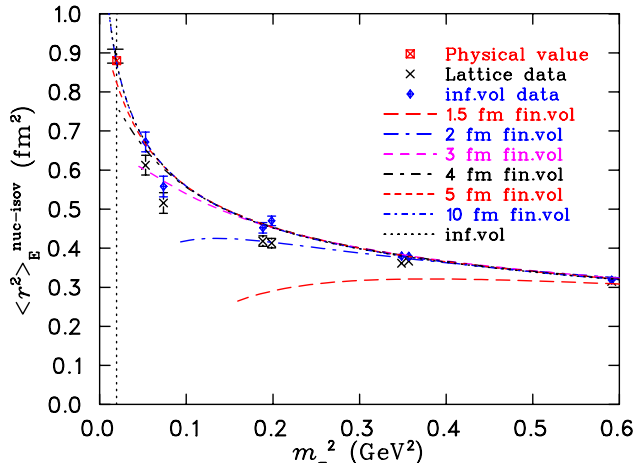
FIG. 9. (color online). Extrapolations of $\langle r^2 \rangle_E$ at different finite volumes and infinite volume, using a dipole regulator, based on lattice QCD data from QCDSF, lattice sizes: $1.92 - 3.25$ fm. The provisional constraint $m_\pi L > 3$ is used. The infinite-volume corrected data points are shown. The physical value from experiment is marked. An estimate in the uncertainty in the extrapolation, due to $\Lambda^{\rm scale}$, has been calculated from Figure 6, and is indicated at the physical value of $m_\pi^2$.

of the isovector nucleon. Thus an intrinsic scale has been uncovered, which characterizes the size of the nucleon, as probed by the pion.

Using the value of the intrinsic scale, the extrapolation of the electric charge radius to the physical pion mass and

infinite-volume lattice box size is consistent with experiment. The finite-volume extrapolations provide a benchmark for estimating the outcome of a lattice QCD simulation at realistic or currently optimistic lattice sizes.

The results also demonstrates a successful procedure for using lattice QCD data to extrapolate an observable to the low-energy region of QCD.
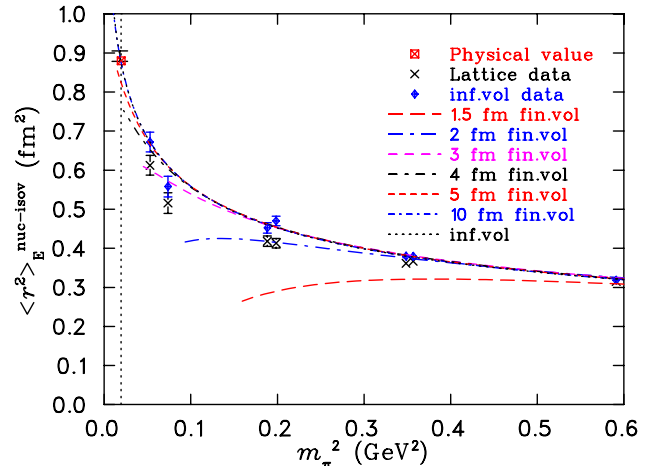


FIG. 10. (color online). Extrapolations of $\langle r^2 \rangle_E$ at different finite volumes and infinite volume, using a dipole regulator, based on lattice QCD data from QCDSF, lattice sizes: $1.92 - 3.25$ fm. The provisional constraint $m_\pi L > 3$ is used. The physical value from experiment is marked. An estimate of the statistical uncertainty in the extrapolation is marked at the physical value of $m_\pi^2$.

[1] J. M. M. Hall, D. B. Leinweber, and R. D. Young, Phys. Rev. **D82**, 034010 (2010), 1002.4924.
[2] D. B. Leinweber, A. W. Thomas, and R. D. Young, Nucl. Phys. **A755**, 59 (2005), hep-lat/0501028.
[3] E. E. Jenkins and A. V. Manohar (1991), talk presented at the Workshop on Effective Field Theories of the Standard Model, Dobogoko, Hungary, Aug 1991.
[4] E. E. Jenkins and A. V. Manohar, Phys. Lett. **B255**, 558 (1991).
[5] E. E. Jenkins, Nucl. Phys. **B368**, 190 (1992).
[6] J. N. Labrenz and S. R. Sharpe, Phys. Rev. **D54**, 4595 (1996), hep-lat/9605034.
[7] A. Walker-Loud, Nucl. Phys. **A747**, 476 (2005), hep-lat/0405007.
[8] P. Wang, D. B. Leinweber, A. W. Thomas, and R. D. Young, Phys. Rev. **D75**, 073012 (2007), hep-ph/0701082.
[9] R. F. Lebed, Phys. Rev. **D51**, 5039 (1995), hep-ph/9411204.
[10] V. Bernard, T. R. Hemmert, and U.-G. Meissner, Nucl. Phys. **A732**, 149 (2004), hep-ph/0307115.
[11] D. Djukanovic, M. R. Schindler, J. Gegelia, and S. Scherer, Phys. Rev. **D72**, 045002 (2005), hep-ph/0407170.
[12] P. Wang, D. B. Leinweber, A. W. Thomas, and R. D. Young (2008), 0810.1021.
[13] M. Gell-Mann, R. J. Oakes, and B. Renner, Phys. Rev. **175**, 2195 (1968).
[14] H. Ohki et al., Phys. Rev. **D78**, 054502 (2008), 0806.4744.
[15] S. Aoki et al. (PACS-CS) (2008), 0807.1661.
[16] A. Ali Khan et al. (CP-PACS), Phys. Rev. **D65**, 054505 (2002), hep-lat/0105015.